

Alma Mater Studiorum – Università di Bologna

DOTTORATO DI RICERCA IN
AUTOMOTIVE PER UNA MOBILITÀ INTELLIGENTE

Ciclo 34

Settore Concorsuale: 09/C1 – MACCHINE E SISTEMI PER L'ENERGIA E L'AMBIENTE

Settore Scientifico Disciplinare: ING-IND/08 – MACCHINE A FLUIDO

DEVELOPMENT OF NUMERICAL METHODOLOGIES TO PREDICT THE
LIQUID FUEL SPRAYS – WALL INTERACTION TO OPTIMIZE THE MIXING
PROCESS OF DIRECT INJECTION SPARK IGNITION ENGINES

Presentata da: Valerio Mariani

Coordinatore Dottorato

Nicolò Cavina

Supervisore

Gian Marco Bianchi

Esame finale anno 2022

*A mia madre Franca,
baluardo dell'espressione più virtuosa dell'essere umano, integra, nonostante ogni cosa.
Il buono ed il giusto che mi hai donato insegnandomi; la mia forza per sempre.*

Abstract

Nowadays the development of new Internal Combustion Engines is mainly driven by the following needs: i) reduce the tailpipe emissions of pollutants e.g., Nitrogen Oxides, Carbon Monoxide, Unburned Hydrocarbons, soot; ii) reduce the emissions of Green-House Gases e.g., Carbon Dioxide; iii) avoid the fossil fuels wasting. In both stand-alone (pure thermal) and hybrid (electric + thermal) engine configurations, the design of dimension and shape of the combustion chamber together with the implementation of different injection strategies e.g., injection timing, spray targeting, higher injection pressure, play a key role in the accomplishment of the aforementioned targets. As far as the match between the fuel injection and evaporation and the combustion chamber shape is concerned, the assessment of the interaction between the liquid fuel spray and the engine walls is crucial. It must be remembered that if the liquid fuel spray hits the engine walls, the interaction of the fuel droplets with the solid walls and with the lubricant oil layer may occur. As a consequence, effects on several aspects of the engine performance and emissions are concerned. The use of numerical simulations is an acknowledged technique to support the study of new technological solutions such as the design of new gasoline blends and of tailored injection strategies to pursue the target mixture formation. The current simulation framework lacks a well-defined best practice for the liquid fuel spray interaction simulation, which is a complex multi-physics problem. The main scope of the present thesis is the presentation of a research focused on the development of robust methodologies to approach the numerical simulation of the liquid fuel spray interaction with walls and lubricants. The accomplishment of this task was divided into three tasks:

- T-1) setup and validation of three-dimensional CFD spray simulations focused on the after-impingement liquid film formation and the Leidenfrost effect; In this section, the values of some coefficients will be not declared being confidential data of the used commercial CFD software.
- T-2) development of a one-dimensional model describing the liquid fuel – lubricant oil interaction.
- T-3) development of a machine learning based algorithm aimed to define which mixture of known pure components mimics the physical behaviour of the real gasoline for the simulation of the liquid fuel spray interaction.

Each operational step was developed according to different sub-steps and the results were validated against experimental data from the literature. As a result, each operational step has contributed to improve the current spray simulation state of the art by providing different guidelines and perspectives regarding the setup and the tuning of the spray sub-models in CFD simulations and new tools for the modeling of real fuels and their interaction with lubricants.

Nomenclature

Due to the large number of equations that are present in this thesis, in the document each variable would be associated to multiple meanings, so in the Nomenclature. Therefore, for the sake of clarity, in the Nomenclature the different meanings of each variable are associated to the corresponding chapter, which is reported next in square brackets.

Abbreviations

AEOI: After End Of Injection

AL-PIONA: Alcohol – n-Paraffins i-Paraffins Olefins Naphthenes Aromatics

AMD: Average Mean Diameter

ANN: Artificial Neural Network

ARE: Absolute Relative Error

BDC: Bottom Dead Center

BEV: Battery Electric Vehicles

BMEP: Brake Mean Effective Pressure

BNN: Bayesian Neural Network

C: number of carbon atoms

CFD: Computational Fluid Dynamics

CFL: Courant-Friedrichs-Lewy

CHT: Conjugate Heat Transfer

CO: carbon monoxide

CO₂: carbon dioxide

DHA: Detailed Hydrocarbon Analysis

DI: Direct Injection

DOE: Design Of Experiment

EGR: Exhaust Gas Recirculation

EOI: End Of Injection

E-PIONA: Ethanol – n-Paraffins i-Paraffins Olefins Naphthenes Aromatics

ETRF: Ethanol Toluene Reference Fuel

GCI: Gasoline Compression Ignition

GDI: Gasoline Direct Injection

GDP: Gross Domestic Product

GP: Gaussian Process

HC: unburned hydrocarbons

HCCI: Homogeneous Charge Compression Ignition

HEV: Hybrid Electric-thermal engine Vehicle

HFI: High Frequency Ignition

Nomenclature

HFR: Hydraulic Flow Rate
HNN: Hybrid Neural Network
ICE: Internal Combustion Engine
IVC: Intake Valve Closing
IVO: Intake Valve Opening
LCA: Life-Cycle Assessment
LGI: Liquid-Gas Interface
LIF: Laser Induced Fluorescence
LLE: Liquid-Liquid Equilibrium
LSPI: Low-Speed Pre-Ignition
LTC: Low Temperature Combustion
MARE: Mean Absolute Relative Error
MARS: Monotone Advection and Reconstruction Scheme
MON: Motor Octane Number
NBP: Normal Boiling Point
NEDC: New European Driving Cycle
NLTE: Non-Local Thermal Equilibrium
NO_x: nitrogen oxides
ON: Octane Number
PDF: Probability Density Function
PDI: Port Direct Injection
PDPA: Phase Doppler Particle Analysis
PEMS: Portable Emissions Measurements System
PFI: Port Fuel Injection
PISO: Pressure-Implicit with Splitting Operators
PM: Particulate Matter
PN: Particulate Number
PPS: Purchasing Power Standards
PR: Peng-Robinson
PRF: Primary Reference Fuel
Ra: mean surface roughness
RANS: Reynolds Average Navier-Stokes
RDE: Real Driving Emission
RIM: Refractive Index Matching
RK: Redlich-Kwong
RON: Research Octane Number
RSME: Root Squared Mean Error
RVP: Reid Vapor Pressure
SA: Spark Advance
SACI: Spark Assisted Compression Ignition

Nomenclature

SI: Spark Ignition
SKR: Soave-Redlich-Kwong
SLI: Solid-Liquid Interface
SMD: Sauter Mean Diameter
SOI: Start Of Injection
TDC: Top Dead Center
TGDI: Turbo Gasoline Direct Injection
TRF: Toluene Reference Fuel
TTW: Tank-To-Wheel
TX: Distillation temperature at X% volume evaporated
UCB: Upper Confidence Bound
UDF: User Defined Function
VLE: Vapor-Liquid Equilibrium
WLTP: Worldwide harmonized Light Vehicles Test Procedure
WTW: Well-To-Wheel

Variables

α : thermal diffusivity (m^2/s) [3], SKR pure component parameter (-) [4]
 β : SKR pure component parameter (-) [4]
 Γ : generic diffusive transport term [1]
 γ : splash ratio coefficient (-) [2], compatibility parameter (%) [4]
 δ : non-dimensional liquid film thickness (-) [2], film shrinking (m) [3]
 ε : turbulent energy dissipation (m^2/s^3) [2]
 ζ : Kernel hyperparameter [4]
 η : evaporation ratio (-) [3]
 θ : droplet trajectory angle ($^\circ$) [2], generic hyperparameter [4]
 λ : normalized air-fuel ratio (-) [1] [2], L2 regularizer coefficient (-) [3]
 μ : dynamic viscosity ($\text{Pa}\cdot\text{s}$) [1] [2], (cP) [3]
 ξ : liquid mass volume concentration (kg/m^3) [3]
 ρ : density (kg/m^3) [1] [2] [3] [4]
 Σ : std deviation function [4]
 σ : surface tension (N/m) [1] [2] [3], std deviation (-) [3]
 ϕ : generic quantity [2], fugacity coefficient (-) [4]
 φ : liquid volume fraction (-) [4]
 φ_D : distilled liquid volume fraction (-) [4]
 τ : non-dimensional time interaction parameter (-) [2]
 τ^* : non-dimensional secondary breakup time (-) [2]
 τ_{BU} : breakup characteristic time scale (s) [2]
 τ_{d-d} : droplet-droplet interaction time (s) [2]

Nomenclature

τ_{res} : droplet residence time (s) [2]
 τ_t : turbulent characteristic time scale (s) [2]
 v : Kernel hyperparameter (-) [4]
 ω : acentric factor (-) [4]
 A : area (m²) [2], SKR mixture parameter (-) [4]
 A_{UCB} : acquisition function [4]
 a : association factor (-) [3], SKR mixture parameter (-) [4]
 a_i : SKR pure component parameter (-) [4]
 B : engine bore (m) [3], SKR mixture parameter (-) [4]
 b : bias [1], SKR mixture parameter (-) [4]
 b_i : SKR pure component parameter (-) [4]
 C : heat capacity (J/K) [3]
 C_C : contraction coefficient (-) [2]
 C_D : discharge coefficient (-) [2]
 C_f : friction factor (-) [3]
 C_k : kinetic parameter (-) [2]
 C_v : velocity reduction coefficient (-) [2]
 C_{ix} : breakup coefficients (-) [2]
 C_{ij} : SKR cross interaction coefficients (-) [4]
 C_x : generic constant [2] [3]
 Ca : capillary number (-) [2]
 Co : Courant number (-) [2]
 c_p : specific heat (J/kg/K) [3]
 D : diffusion coefficient (m²/s) [3], solution domain [4]
 D_0 : infinite dilution diffusion coefficient (m²/s) [3]
 d : droplet diameter (m) [1] [2]
 d_{10} : average mean diameter (μm) [2]
 d_{32} : Sauter mean diameter (μm) [2]
 d_G : geometric minimum nozzle diameter (m) [2]
 d_s : stable droplet diameter (m) [2]
 E : droplet energy factor (-) [2]
 E_k : kinetic energy (J) [1] [2]
 E_s : surface energy (J) [1] [2]
 e : relative error (%) [4]
 F : generic objective function [4]
 f_{UR} : under-relaxation coefficient (-) [1]
 G : Gaussian distribution function [3] [4]
 H : heat transfer coefficient (W/m²/K) [3]
 H_v : latent heat of vaporization (J/kg) [3]
 h : height (m) [2] [3]

Nomenclature

I: generic input variable [1]
J: intermolecular forces correction factor (-) [3]
 j_H : heat transfer Chilton-Colburn factor (-) [3]
 j_M : mass transfer Chilton-Colburn factor (-) [3]
K: Sommerfeld number (-) [2], Kernel function [4]
 K_X : ONERA coefficients (-) [2]
k: turbulent kinetic energy (m^2/s^2) [2], thermal conductivity (W/m/K) [3], equilibrium ratio (-) [4]
 L_t : turbulent characteristic length scale (m) [2]
 L_{d-d} : droplet-droplet interaction length (m) [2]
 La : Laplace number (-) [2]
 Le : Lewis number (-) [3]
M: mass transfer coefficient (m/s) [3], Mean function [4]
MW: molecular weight (g/mol) [3]
m: mass (kg) [2] [3] [4]
N: number of droplets in the statistical sample [2], number of surrogate components [4]
NP: number of components in the palette [4]
 N_t : number of optimization targets [4]
n: ONERA exponent [2]
 Oh : Ohnesorge number (-) [1] [2]
P: generic probability function [3]
 P_n : generic polynomial function of degree n [2]
 Pr : Prandtl number (-) [3]
pressure (Pa) [4]
 p_b : back pressure (Pa) [2]
 p_{inj} : injection pressure (Pa) [2]
 p_{sat} : saturation pressure at given temperature (Pa) [3] [4]
Q: injector mass flow rate (kg/s) [2]
q: variational form of the posterior distribution function [3]
R: residual liquid amount (mol) [4]
 R^2 : coefficient of determination (-) [3]
 R_0 : universal gas constant (J/mol/K) [4]
 R_i : gas constant (J/kg/K) [4]
 Re : Reynolds number (-) [1] [2]
 R_v : molar volume ratio (-) [3]
r: residual liquid change (mol) [3]
 r_s : Spearman correlation coefficient (-) [3]
S: generic source term [1]
 Sc : Schmidt number (-) [3]
T: temperature (K) [2] [3] [4]
 T_1 : generic temperature at ambient pressure (K) [2]

Nomenclature

T_b : normal boiling temperature (K) [4]
 T_H : head distillation temperature (K) [4]
 T_{inj} : injection temperature (K) [2]
 T_K : kettle distillation temperature (K) [4]
 T_L : Leidenfrost temperature (K) [1] [2]
 T_N : Nukiyama temperature (K) [1] [2]
 T_{sat} : saturation temperature at given pressure (K) [1] [2] [4]
 T_W : wall temperature (K) [2]
TX: distillation temperature at distillate X %vol [4]
t: time (s) [1] [2] [3]
U: velocity magnitude (m/s) [1] [2]
 \bar{U} : velocity array (m/s) [2]
 U^* : non dimensional droplet velocity (-) [2]
 U_P : mean piston speed (m/s) [3]
 U_t : turbulent fluctuating velocity component (m/s) [2]
V: molar volume (cm³/mol) [3], geometric volume (m³) [4]
 V_b : molar volume at the normal boiling temperature (cm³/mol) [3]
 V_c : engine displacement (m³) [3]
v: diffusion volume (L/mol) [3]
W: splashing parameter (-) [2], assigned weight (-) [1] [3] [4]
w: liquid mass fraction (-) [3] [4]
 We : Weber number (-) [1] [2]
X: array of observations [3], fuel molar composition array (-) [4]
 X_s : splash-incident mass ratio (-) [2]
x: liquid mole fraction (-) [3] [4]
Y: generic output variable [1]
y: vapor molar fraction (-) [4]
Z: compressibility factor (-) [4]

Sub/Super-scripts

1: solvent [3]
2: solute [3]
A: air [3]
AL: alcohol [4]
C: critical [2] [4]
D: deposition [2]
F: fuel [2] [3]
G: gaseous phase [1] [2] [3]
H: head [4]

Nomenclature

I: incident [2]

K: kettle [4]

L: liquid phase [1] [2] [3] [4]

MAX: maximum [2] [4]

n: normal component [1] [2]

O: oil [3]

opt: optimum [4]

R: rebound [2]

S: splashed [2], solid [3]

V: vapor [4]

t: tangential component [2]

TH: theoretical [2]

Index

1	Introduction	1
1.1	Internal combustion engines scenario	1
1.2	Gasoline Direct Injection: Overview	7
1.3	Phases of the liquid fuel spray	11
1.3.1	Spray primary breakup	13
1.3.2	Spray secondary breakup	15
1.3.3	Spray-wall impingement.....	16
1.4	Aims and methods	23
2	Fuel spray-wall impingement simulation	29
2.1	State of the art and original contribution	29
2.2	Methodology	32
2.2.1	Reference validation benchmark.....	32
2.2.2	General setting.....	34
2.2.3	Injection setting	36
2.2.4	Free spray setting	39
2.2.5	Wall impingement modeling	44
2.3	Results.....	59
2.3.1	Free spray validation	59
2.3.2	Wall impingement validation.....	63
3	After-impingement oil-fuel dilution simulation	75
3.1	State of the art and original contribution	75
3.2	Methodology	77
3.2.1	Oil-Fuel dilution model	77
3.2.2	Diffusion coefficient	84
3.3	Results.....	84
3.3.1	Predicting oil-fuel diffusion coefficient	84
3.3.2	Oil-fuel dilution simulation	88
4	Liquid fuel evaporative behaviour simulation.....	93
4.1	State of the art and original contribution	93
4.2	Methodology	95

4.2.1	Palette definition.....	95
4.2.2	Target properties.....	97
4.2.3	Searching strategy	108
4.3	Results.....	116
4.3.1	Distillation model validation	116
4.3.2	Optimum surrogate identification.....	119
4.3.3	Surrogate unicity analysis	127
5	Conclusions and perspectives.....	131
	References	137

List of contents

Figures

Figure 1-1: Comparison of Gross Domestic Product per capita and Motor vehicles per 1000 inhabitants for the EU countries (data from [1]).	1
Figure 1-2: Comparison between different anthropic sectors in terms of air poisoning (CO, HC, NO _x , PM) and CO ₂ emissions in 2018 (data from [2]).	2
Figure 1-3: Vehicle speed against test time in NEDC (top) and WLTP (bottom) cycles. UDC is Urban Driving Cycle, EUDC is Extra-Urban Driving Cycle. Pictures from [4].	4
Figure 1-4: Product share of the gasoline DI technique in light-duty vehicles, data from [13].	6
Figure 1-5: Comparison between the share of the gasoline DI light-duty vehicles for the main car manufacturers in 2017, data from [14].	6
Figure 1-6: Schemes of Port Fuel Injection (a) and Gasoline Direct Injection (b) engine configurations, image from [15].	7
Figure 1-7: Sketch of two Gasoline Direct Injection configurations showing the solid spray cones: a) wide-spacing (side-mounted injector); b) narrow-spacing (central-mounted injector). Spark plug is shown in transparency.	7
Figure 1-8: HCCI-SACI-SI mode transition for different EGR ratio and spark timing in the case of homogeneous charge (a) and stratified charge (b). Pictures from [19].	9
Figure 1-9: Scheme of the PDI gasoline engine proposed by Toyota, picture from [20].	10
Figure 1-10: Injection timespan for PFI and GDI configurations with respect to a reference engine cycle. The Intake Valve (IV) lift (solid), the Exhaust Valve (EV) lift (dashed) and the Top Dead Center (TDC, solid purple) are reported.	10
Figure 1-11: Cross section view of a solenoid driven GDI injector (top) with detailed view of the needle lift system (top right) and the nozzle-holes region (bottom right), picture from [23].	12
Figure 1-12: Scheme of the liquid fuel spray main phenomena: primary and secondary breakup; spray-wall impingement, pictures from [24].	12
Figure 1-13: Number of new published papers by keyword "gasoline wall impingement" for different journals and years.	13
Figure 1-14: Primary breakup regimes diagram. The experimental image of the breakup regime taken from [27] is associated to the corresponding zone of the diagram.	14
Figure 1-15: Representation of the secondary breakup regimes, pictures from [29].	16
Figure 1-16: Experimental pictures of some possible impact regimes using water: a) deposition; b-e) different splash modes; f) rebound. Images taken from [30].	17
Figure 1-17: Comparison between the kinematic viscosity of a nowadays commercial gasoline and three different typical engine oils.	19
Figure 1-18: Sketch of the Leidenfrost effect for an impacting droplet, edited from [34].	20
Figure 1-19: Water droplets floating over the Leidenfrost-induced water vapor layer, solid plate at 197°C.	20
Figure 1-20: Representation of liquid-wall heat flux (top) and droplet lifetime (bottom) behaviour for increasing wall temperature with focus on the four vaporization regimes.	21

Figure 1-21: Sketch of perpendicular impact angle and diagonal impact angle (top) and behaviour of the non-dimensional Leidenfrost temperature (TL^*) against the incidence angle.....	22
Figure 1-22: Schematic view of a sample neural network with two hidden layers and multiple outputs.....	25
Figure 1-23: Schematic view of the input elaboration performed in a sample layer of the neural network.....	25
Figure 1-24: Most common activation functions for neural network applications.....	26
Figure 1-25: Timeline of the PhD research project.....	27
Figure 2-1: Sketch of the wall-impingement experimental vessel domain.....	33
Figure 2-2: Representation of the computation domain as subset of the real experimental vessel.....	34
Figure 2-3: Schematic view of the computation domain including the simulated spray with the section detail of the mesh grading applied.....	35
Figure 2-4: Bosch HDEV5 6-hole spray pattern at 30 mm downstream the nozzle tip.....	37
Figure 2-5: Assumed injection profile (solid line) of the Bosch HDEV5 injector for two test injection pressure and corresponding injected mass (dashed line). Experimental target injected mass in dashed-dotted gray line.....	38
Figure 2-6: Example of tip spray cloud in CFD simulations for a generic spray (100 bar vs 1 bar).....	39
Figure 2-7: Schematic representation of the blob injection assumption.....	40
Figure 2-8: Example of the results from a chi-squared diameter distribution.....	42
Figure 2-9: Wall impingement maps according to the Bai-ONERA model for dry (magenta boundaries) and wet (blue boundaries) surfaces.....	49
Figure 2-10: Splash ratio behaviour with respect to non-dimensional temperature for different values of the tuning exponent γ according to Bai-ONERA.....	52
Figure 2-11: Wall impingement maps according to the Senda model for cold (top left: dry; top right: wet) and hot (bottom) states. The dependence on the interaction time (τ), non-dimensional film thickness (δ), non-dimensional temperature (T^*) are shown respectively. Sketches of the rim, cluster, column splash modes are also shown.....	53
Figure 2-12: Splash ratio behaviour with respect to both non-dimensional film thickness (bottom x) and film height (top x) according to Senda assuming a diameter of the incident parcel of 7 μm	56
Figure 2-13: Comparison between different methods to predict the Leidenfrost temperature and experimental data [36] for i-octane at different gas pressure (0.5; 1; 2.4 bar). The i-octane equilibrium temperature (gray) is also shown as a reference.....	59
Figure 2-14: Comparison between different methods to predict the Nukiyama temperature and experimental data [36] for i-octane at different gas pressure (0.5; 1; 2.4; 4.4; 7.7 bar). The i-octane equilibrium temperature (gray) is also shown as a reference.....	59
Figure 2-15: Behaviour of the parcel diameter against different values of the two tuning coefficients of the breakup model. Results referred to the case of i-octane injection under 150 bar - 1 bar pressure difference.....	60
Figure 2-16: Spray shape comparison at 0.5 ms ASOI between experimental shots (picture left side) and numerical simulation (picture right side) for different injection (50, 150, 300 bar) and environmental conditions (80°C, 1 bar, 3 bar, 6 bar).....	61
Figure 2-17: Spray shape comparison at injection pressure of 150 bar between experimental shots (picture left side) and numerical simulation (picture right side) for different environmental conditions (1 bar - 80°C, and 3 bar - 140°C) and record timing....	61

Figure 2-18: Droplet diameter (AMD and SMD) comparison between experimental and simulated data against increasing injection pressure for three different back-pressure conditions (1 bar, 3 bar, 6 bar) at 80°C.....	62
Figure 2-19: Simulated spray wall impingement morphology for the Bai-ONERA and the Senda models at different time ASOI. Injection performed at 150 bar in a vessel at 1 bar, 80°C.....	63
Figure 2-20: Simulated spray wall impingement morphology for the Bai-ONERA and the Senda models at different time ASOI. Injection performed at 300 bar in a vessel at 1 bar, 80°C.....	64
Figure 2-21: Simulated jet wall impingement footprints and droplets for the Bai-ONERA and the Senda models at different time ASOI. Injection performed at 150 bar in a vessel at 1 bar, 80°C.....	65
Figure 2-22: Simulated jet wall impingement footprints and droplets for the Bai-ONERA and the Senda models at different time ASOI. Injection performed at 300 bar in a vessel at 1 bar, 80°C.....	65
Figure 2-23: Simulated distribution over time of the injected fuel mass among vapours, liquid droplets, liquid film (injection at 150 bar on the left, 300 bar on the right) for the Bai-ONERA and the Senda wall impingement models. Solid lines represent the fuel mass, dashed lines represent the percentage of each contribution with respect to the instantaneous injected mass.	66
Figure 2-24: Comparison between experimental and simulated (Senda, and Bai-ONERA models) liquid film mass at 5 ms ASOI based on the footprint of a single jet.....	67
Figure 2-25: Comparison between experimental and simulated (Senda, and Bai-ONERA models) liquid film area at 5 ms ASOI based on the footprint of a single jet.	67
Figure 2-26: Experimental (dashed line) and simulated (solid lines) effect of the wall temperature on the liquid film formed at 150 vs 1 bar injection conditions. The film mass is taken at 5 ms ASOI for a single footprint. The saturation temperature of the test fuel (i-octane, 99°C) is also reported in red.	68
Figure 2-27: Experimental (dashed line) and simulated (solid lines) effect of the wall temperature on the liquid film formed at 300 vs 1 bar injection conditions. The film mass is taken at 5 ms ASOI for a single footprint. The saturation temperature of the test fuel (i-octane, 99°C) is also reported in red.	69
Figure 2-28: Liquid film mass (left y-axis) and After-splash deposited droplet mass (red, right y-axis) for different tested values of the splash tuning coefficient at given non-dimensional temperature ($T^* = 0.36$, transition boiling).....	70
Figure 2-29: Experimental (dashed line) and simulated (solid lines) effect of the gas pressure on the liquid film formed at 80 °C, 150 bar injection pressure. The film mass is taken at 5 ms ASOI for a single footprint. The saturation pressure of the test fuel (i-octane, 0.56 bar) is also reported in red.	71
Figure 2-30: Experimental (dashed line) and simulated (solid lines) effect of the gas pressure on the liquid film formed at 80 °C, 300 bar injection pressure. The film mass is taken at 5 ms ASOI for a single footprint. The saturation pressure of the test fuel (i-octane, 0.56 bar) is also reported in red.	71
Figure 2-31: Liquid film morphology comparison between experiments (left column, LIF images) and simulation (central column: Senda, right column: Bai-ONERA) at 5 ms ASOI.	72
Figure 3-1: Pressure vs non-dimensional temperature maps of liquid iso-octane vaporization regimes for different wall temperatures.	75
Figure 3-2: Sketch of the oil-fuel dilution domain at the simulation start (a) and stop (b) times.	78

Figure 3-3: Scheme of the algorithm adopted to update the liquid boundary cell and the domain size because of the fuel evaporation.....	80
Figure 3-4: Comparison between different thermo-physical liquid properties (thermal conductivity, density, specific heat, thermal diffusivity) of sample lubricant oil and gasoline against temperature.....	82
Figure 3-5: Solvent-solute distribution of some key properties (dynamic viscosity (a), molar volume (b), molecular weight (c), latent heat of vaporization (d)) of the liquids included in the database for predicting the liquid phase diffusion coefficient.	84
Figure 3-6: Schematic workflow of the Hybrid Neural Network methodology for predicting the liquid phase diffusion coefficients.	84
Figure 3-7: Results of the Spearman rank-order analysis on the set of primary and secondary features considered as relevant dependencies for the diffusion coefficient (heat of vaporization (H_v), dynamic viscosity (μ), molecular weight (MW), molar volume (V), density (ρ), number of carbons and oxygens ($\#C$, $\#O$) for both solvent (1) and solute (2)).	84
Figure 3-8: Parity plot of the experimental and HNN predicted diffusion coefficients for train, test, and validation sets.	84
Figure 3-9: Comparison between four literature correlations and the combined HNN+BNN methodology in terms of Absolute Relative Error distribution over the dataset.	84
Figure 3-10: Bayesian neural network predicted value (red markers) and its confidence (yellow band) for different solutes identified by increasing number of carbons in n-heptane (solvent). Experimental reference values (black markers) are available for the first mixtures whilst x-axis points without reference represent conceptual mixtures.....	84
Figure 3-11: Diffusion coefficient against solvent viscosity for different solvent-solute combinations: generic HC oils-n-hexane experimental (black) and predicted (blue) data, SAE oils-gasolines/i-octane (red).....	85
Figure 3-12: Comparison between calculated (solid blue, zero-dimensional model) and experimental (black dotted) pressure trace of the engine under review.....	89
Figure 3-13: Predicted time temperature profile at the solid-liquid interface (solid gray) and for the average liquid film (solid black). Fixed coolant temperature and the film deposition (injection) temperature are also shown as a reference.	90
Figure 3-14: Predicted oil viscosity degradation (solid black) and oil pollution (dashed) at different x-location along the cylinder-piston clearance.	90
Figure 3-15: Predicted foreign oil presence in the non-evaporated liquid film, available to be scraped from the top land ring.	90
Figure 3-16: Potential oil scraped per unit film area recorded at half of compression stroke for baseline conditions and three different solution attempts to reduce LSPI.....	91
Figure 3-17: Oil viscosity degradation and average oil pollution recorded at half of compression stroke for baseline conditions and three different solution attempts to reduce LSPI.....	92
Figure 4-1: Example of gas chromatography data for gasoline [186].....	96
Figure 4-2: Sketch of an experimental distillation rig, measure probes placed for head temperature (dark blue) and kettle temperature (dark orange) recording.	99
Figure 4-3: Sample experimental distillation curves [188] of a base gasoline and two its blends with 5%vol (E5) and 10%vol (E10) ethanol.	99
Figure 4-4: Scheme of the division of the distillation ambient into the three modeling steps.	100
Figure 4-5: Schematic view of the fuel vapours heat exchange domain update.	105

Figure 4-6: Experimental distillation curves [196] of a base gasoline, gasoline(15%vol)-butanol(85%vol) blend and pure butanol. The normal boiling temperature of butanol is also reported.	107
Figure 4-7: Effect of the oxygenate addition on a generic gasoline fuel considering predicted by the chosen tuned reference correlation by Anderson [197].	108
Figure 4-8: Example of prior and posterior distributions by a Gaussian Process on single variable.	111
Figure 4-9: Example of Bayesian optimization by means of the joint use of Gaussian Process and Upper Confidence Bound driven searching strategy. Pictures edited from the original in [198].	112
Figure 4-10: RSME profile in the searching process of the optimum surrogate composition according to the Gaussian Process - Upper Confidence Bound Bayesian optimization. .	113
Figure 4-11: Evolution of the kettle distillation temperature for the surrogate formulation attempts (gray curves), optimized surrogate (black line) and reference experimental data (red markers).	113
Figure 4-12: Example of the solutions pool returned by the Bayesian iterative algorithm reporting optimum surrogate (blue), bounding surrogate (black), acceptable surrogates pool (red), other minor surrogate options (green).	116
Figure 4-13: Comparison between experimental (markers) and predicted (dashed lines) kettle temperature-based distillation curves for the six validation mixtures.	117
Figure 4-14: Absolute relative error profile in predicting the distillation curves of the six validation mixtures. Single profiles in dashed dotted lines, average profile in solid gray line.	118
Figure 4-15: Comparison between experimental ([200], blue markers) and predicted (magenta dotted line) head distillation temperatures and the associated kettle temperatures (yellow markers).	118
Figure 4-16: Volumetric composition of the four validation gasolines and their associated optima surrogates. Macro-composition is displayed via colours for both real and surrogate fuels, micro-composition is shown via patterns for surrogates only.	120
Figure 4-17: Comparison between experimental (markers) and surrogate (solid line) distillation curves for the validation gasoline A. Normal boiling temperature of the surrogate's components (dashed line) ad their molar percentage are also reported.	122
Figure 4-18: Comparison between experimental (markers) and surrogate (solid line) distillation curves for the validation gasoline B. Normal boiling temperature of the surrogate's components (dashed line) ad their molar percentage are also reported.	122
Figure 4-19: Comparison between experimental (markers) and surrogate (solid line) distillation curves for the validation gasoline C. Normal boiling temperature of the surrogate's components (dashed line) ad their molar percentage are also reported.	123
Figure 4-20: Comparison between experimental (markers) and surrogate (solid line) distillation curves for the validation gasoline D. Normal boiling temperature of the surrogate's components (dashed line) ad their molar percentage are also reported.	123
Figure 4-21: Temperature difference between experimental and surrogate distillation curve for the four validation gasolines.	124
Figure 4-22: Comparison between different properties (RON, MON, RVP, density (ρ), aromatics volume, ethanol volume, T10, T50, T90) of the reference A gasoline (dashed polygon) and its optimum surrogate (filled polygon).	125
Figure 4-23: Comparison between different properties (RON, MON, RVP, density (ρ), aromatics volume, ethanol volume, T10, T50, T90) of the reference B gasoline (dashed polygon) and its optimum surrogate (filled polygon).	125

Figure 4-24: Comparison between different properties (RON, MON, RVP, density (ρ), aromatics volume, ethanol volume, T10, T50, T90) of the reference C gasoline (dashed polygon) and its optimum surrogate (filled polygon).	126
Figure 4-25: Comparison between different properties (RON, MON, RVP, density (ρ), aromatics volume, ethanol volume, T10, T50, T90) of the reference D gasoline (dashed polygon) and its optimum surrogate (filled polygon).	126
Figure 4-26: Overall and E-PIONA composition compatibility for optimum and bounding surrogates of the four validation gasolines.....	127
Figure 4-27: Parity plot between reference gasoline and surrogate density values for the four validation gasolines. The surrogate density is reported for both the optimum (circle) and the bounding (cross), for which the value of the compatibility is reported next.	128
Figure 4-28: RVP parity plot between reference gasoline and surrogate RVP values for the four validation gasolines. The optimum (circle) and the bounding (cross, and associated compatibility) surrogates are shown.	129
Figure 4-29: Distillation temperatures parity plot between reference gasoline and surrogate distillation temperatures values for the four validation gasolines. The optimum (circle) and the bounding (cross, and associated compatibility) surrogates are shown.	129
Figure 4-30: Chemical composition parity plot between reference gasoline and surrogate ethanol and aromatics volumes for the four validation gasolines. The optimum (circle) and the bounding (cross, and associated compatibility) surrogates are shown.	129

Tables

Table 1-1: Evolution of the emissions regulations per car for passenger vehicles spark ignition engines (data from [3]).	3
Table 1-2: Evolution of the CO ₂ emissions regulation per car for light-duty vehicles.....	3
Table 1-3: Main differences between the NEDC and the WLTP tests.	4
Table 1-4: Main differences between Wide-spacing and Narrow-spacing Gasoline Direct Injection configurations.	8
Table 1-5: Group of the non-dimensional numbers used to describe the breakup phenomenon.....	15
Table 1-6: Brief description and characteristics of the main possible impact regimes.	16
Table 2-1: Data of the reference injector.	33
Table 2-2: List of the values of the under-relaxation factor applied to the solution equations in vessel spray simulations.	36
Table 2-3: Secondary breakup model possible outcomes.	43
Table 2-4: Comparison among the macroscopic features of six recognized literature impingement models.....	46
Table 2-5: Models comparative analysis in terms of correlation strength between engine parameters (drivers) and the associated modeling feature.	48
Table 2-6: Fitted values of the Bai-ONERA model coefficients.	50
Table 2-7: Thermodynamics boundary of the wall impingement models at different wall temperature values.	68
Table 2-8: Thermophysical properties of the present impact wall (fused silica) and two typical piston crown materials.	69
Table 2-9: Thermodynamics boundary of the wall impingement models at different gas pressure values.	70
Table 3-1: Tuning values for the coefficients of the Woschni heat transfer coefficient.	83

Table 3-2: Comparison between experimental and calculated values of the NBP molar volume (cm^3/mol), relative error in parenthesis calculated as $(\text{calculated} - \text{experimental})/\text{experimental} \times 100$.	84
Table 3-3: Solvent-solute combinations included in the validation set for the validation of the hybrid neural network methodology and their experimental liquid phase diffusion coefficient.	84
Table 3-4: Hybrid-standard neural networks comparison in terms of coefficient of determination (R^2), Mean Absolute Relative Error (MARE), Root Mean Squared Error (RSME) with respect to the experimental data of different datasets.	84
Table 3-5: Hybrid neural network methodology optimum configuration setup.	84
Table 3-6: Mass fraction composition % and relevant properties of the two tested engine oils.	85
Table 3-7: Mass fraction composition % and relevant properties of the four tested gasolines and i-octane.	87
Table 3-8: Bayesian neural network prediction for the mean value and the confidence band of two gasoline-SAE oil mixtures.	87
Table 3-9: List of the relevant engine data of the reference validation case from [44].	88
Table 4-1: Compounds included in the initial palette for the surrogate definition and their properties.	96
Table 4-2: Geometrical data and thermo-physical properties of distillation flask.	106
Table 4-3: List of the optimized setting of the Bayesian optimization algorithm.	115
Table 4-4: Composition of six validation mixtures simulated at the distillation bench model.	116
Table 4-5: Available properties of the four validation gasolines.	119
Table 4-6: Composition of the optimum surrogate for each of the four validation gasolines.	121

1 Introduction

1.1 Internal combustion engines scenario

The application of the Internal Combustion Engine (ICE) to power light duty vehicles has improved the lifestyle and the mobility of the human being. As a matter of fact, owning a passenger vehicle is still an increasing need in order to accomplish everyday tasks. **Figure 1-1** shows the data regarding the Gross Domestic Product (GDP) in Purchasing Power Standards (PPS) per capita (left column) and the number of personal motor vehicles per 1000 inhabitants (right column) for the European states for the period 2010-2020 [1]. As visible in **Figure 1-1** the number of motor vehicle's owners is increasing slightly in higher GDP countries, whilst a strong increase can be seen in medium and lower GDP countries. It must be remembered that in the framework of conventional vehicles the propulsion produced by the ICE relies on the release of the chemical energy contained within the carbon-based fuel due to the combustion reactions with the oxidizing, namely air. Depending on the thermodynamics and the mixing conditions, which in turn depend on the adopted engine technological solution, the complex chemico-physical phenomena involved in combustion lead to the formation of different substances, some of whom are strongly harmful to the environment and to the public health. Therefore, as far as the wide spreading of the ICE for passenger vehicles is concerned, the corresponding increase of harmful tailpipe emissions must be taken into account. The harmful combustion products released by the ICE can be divided into two main categories according to their impact-time on the air pollution: i) substances that may cause the air poisoning by high level short-term exposure e.g., unburned hydrocarbons (HC), nitrogen oxides (NO_x), soot, carbon monoxide (CO); ii) substances that may cause effects by long-term exposure due to accumulation in the atmosphere (CO₂). Short-term impact substances are responsible for health problems such as respiratory diseases, cancer, and blood stream pollution with concerns on hearth and brain [2]. Furthermore, NO_x emissions are known to promote environmental issues such as acid rain and haze and visibility issues [2].

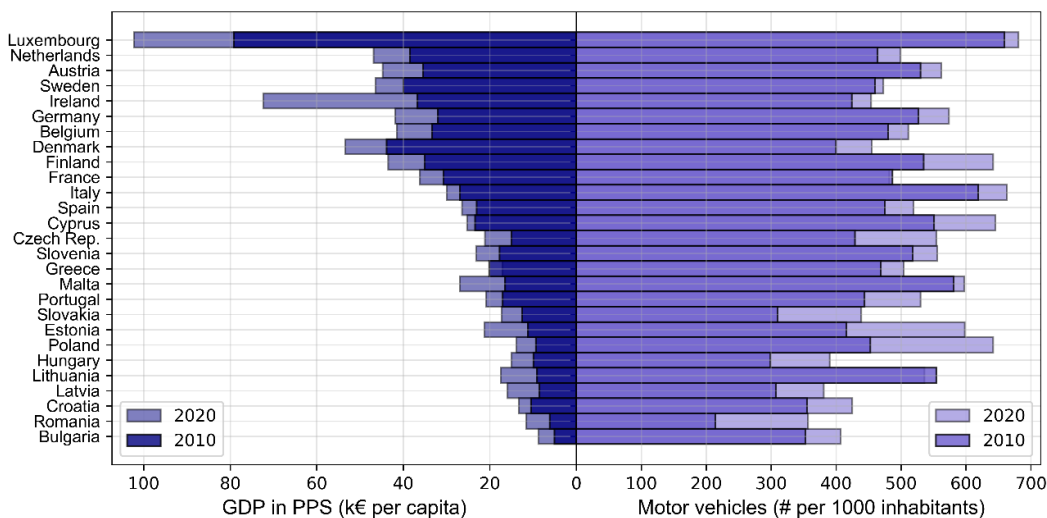


Figure 1-1: Comparison of Gross Domestic Product per capita and Motor vehicles per 1000 inhabitants for the EU countries (data from [1]).

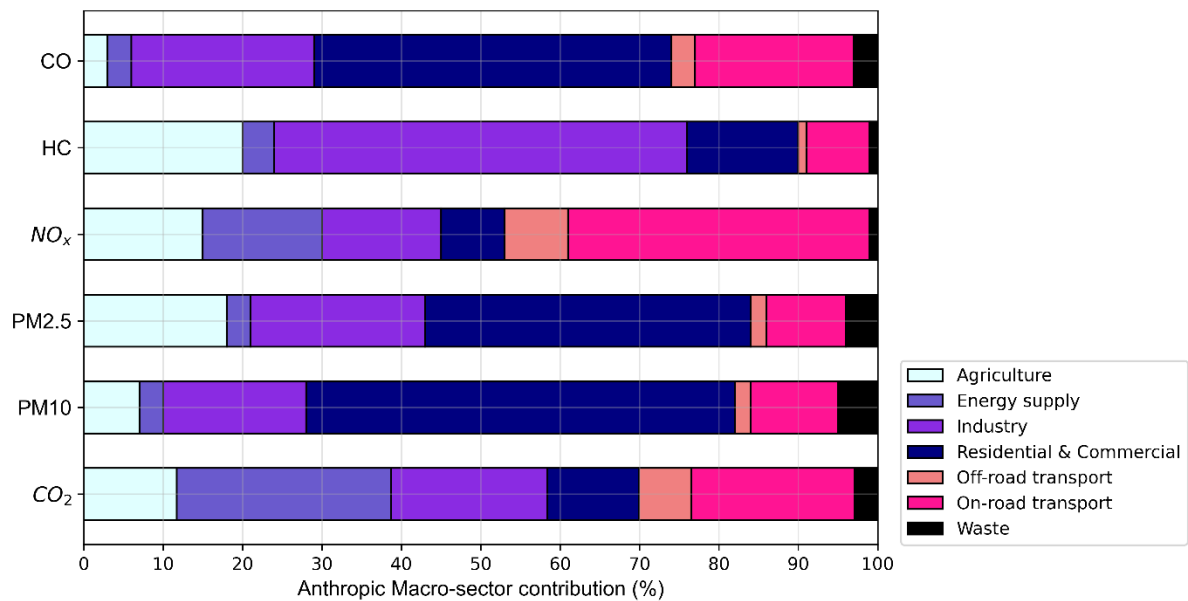


Figure 1-2: Comparison between different anthropic sectors in terms of air poisoning (CO, HC, NO_x, PM) and CO₂ emissions in 2018 (data from [2]).

Among the long-term impact substances, anthropic CO₂ has gained increasing attention since it has been recognized as the greater contributor to the climate change caused by the enhancement of the green-house effect [2]. It is well known that the on-road transport sector, which comprises both light-duty and heavy-duty engines for passenger and commercial application, highly contributes to the emission of the afore-mentioned pollutants. **Figure 1-2** displays the contribution of the anthropic macro-sectors to the emissions of CO, non-methane volatile organic compounds (labelled as HC), NO_x, particulate matter (PM) for two representative particle-size i.e., 2.5 μm and 10 μm, CO₂ in 2018. As visible in **Figure 1-2**, the most significant emissions shares of the ICE for on-road transportation are CO (20%), NO_x (39%), CO₂ (20.6%). While the production of CO by the ICE can be easily maintained at low levels, the continuous reduction of NO_x and CO₂ emissions is the hard challenge to face-off with for both industry and academia. Moreover, it must be considered that avoiding the conventional engine fuel wasting, being fossil fuels non-renewable energy sources, is also a primary target. Therefore, the development of new low-impact and low-consumption engines is mandatory in order to fulfil the increasing need of comfortable long-range personal mobility while accomplishing both the improvement of the air quality and the slowing down of the global warming.

Thanks to the social attention and the visibility gained by the air quality issue in urban areas and the climate change, since the early 2000s the legislation has pushed towards increasingly stringent emission regulations and low-carbon solutions. Focusing on gasoline-powered vehicles, which account for the 42% of the new registered cars, **Table 1-1** shows the evolution of the target emission limits for passenger vehicles powered by gasoline engines [3]. It is visible that since EU3 (early 2000s) the CO, HC, NO_x limits to fulfil to place the vehicles on the market were halved. It must be noticed that since EU5 the particulate matter emissions are constrained as well, i.e., Particulate Mass (PM) and Particulate Number (PN). The presence of limits for the particulate matter, which were typical emissions of Diesel engines, are correlated to the implementation of the gasoline direct injection solution to comply with the regulations of the CO₂ emissions that will be discussed in the following.

Table 1-1: Evolution of the emissions regulations per car for passenger vehicles spark ignition engines (data from [3]).

Regulation	Year	CO	HC	HC + NO _x	NO _x	PM	PN
		g/km				particles/km	
EU1	1992	2.72	-	0.97	-	-	-
EU2	1996	2.2	-	0.5	-	-	-
EU3	2000	2.3	0.2	-	0.15	-	-
EU4	2005	1.0	0.1	-	0.08	-	-
EU5	2011	1.0	0.1	-	0.06	0.005	-
EU6	2014	1.0	0.1	-	0.06	0.005	6 x 10 ¹¹

In the EU the first proposal of CO₂ mandatory emissions standards to comply with was introduced only in 2009. The evolution of those standards and the corresponding date for the accomplishment are shown in **Table 1-2**. It must be remembered that in the case of the lack of the achievement of the CO₂ limit, the placement of the vehicle on the market is not denied, instead the manufacturer must pay a tax of 95 € per each additional g/km over the threshold produced per car.

Table 1-2: Evolution of the CO₂ emissions regulation per car for light-duty vehicles.

Vehicles/Regulation	Mass (kg)	Deadline 2015	Deadline 2021	Deadline 2025
		g/km		
Average fleet	1400	131	95	68-78 (expected)

In the past years, the contribution of fuel-powered vehicles to the emission of CO₂ was evaluated by means of the direct emissions approach i.e., simply the tailpipe emissions are taken into account according to the Tank-To-Wheel (TTW) concept, namely only the conversion processes occurring from the fuel tank to the brake torque were considered. As Battery Electric Vehicles (BEVs) and Hybrid Electric-thermal engine Vehicles (HEVs) pushed into the market, the direct emission meter has become outdated with the perspective to compare those technologies with classical ICE vehicles for environmental impact evaluation purposes. Indeed, at the homologation cycle step, based on the tailpipe emissions, BEVs show zero emissions of green-house gases whilst HEVs are characterized by levels that can be well below those of classical ICEs due to both the presence of the electric unit and the use of the ICE mainly in high efficiency points of the operative map. However, it must be underlined that the electricity to charge the electric unit is usually produced from energy systems in plants emitting green-house gases. In the current discussion on CO₂ emissions from vehicles, the Well-To-Wheel (WTW) approach can describe the carbon balance of the different technological options for transportation extensively. In particular, the WTW concept takes under consideration the equivalent carbon dioxide emission due to the production phase processes upstream the power unit, including feedstock production and transportation, fuel/battery distribution in addition to the TTW path. Beyond WTW, a more comprehensive approach to perform a fair comparison of technological options is the Life-Cycle Assessment (LCA), which bases the CO₂ evaluation on the overall carbon balance of the power unit from making the power source (fuel, battery) to disposing the materials (e.g. battery).

A further step towards sustainable mobility was the introduction of new test procedures for the new registered vehicles, which are based on test conditions that are more representative of the real driving conditions.

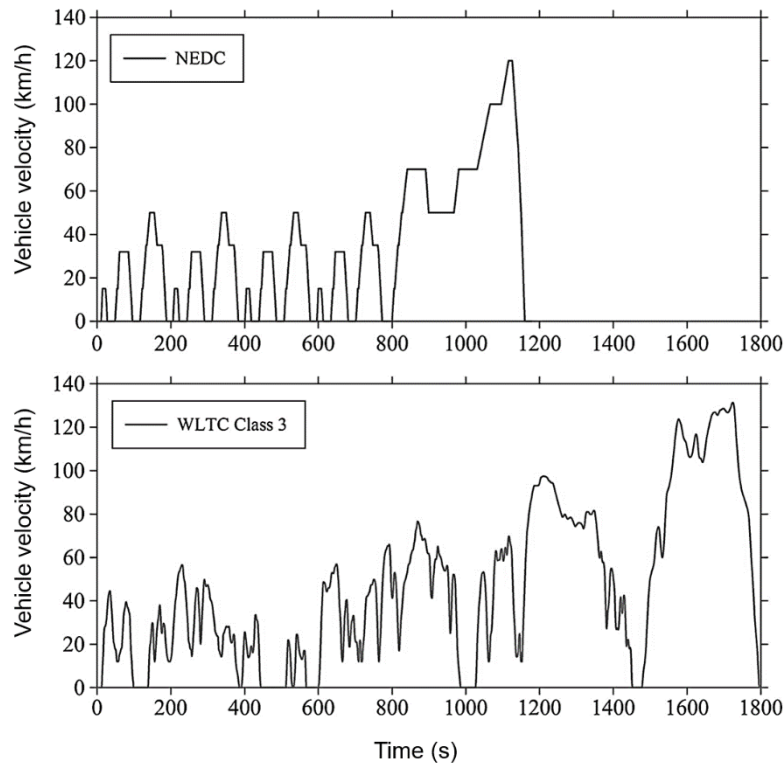


Figure 1-3: Vehicle speed against test time in NEDC (top) and WLTP (bottom) cycles. UDC is Urban Driving Cycle, EUDC is Extra-Urban Driving Cycle. Pictures from [4].

In 2017 the new laboratory test procedure called Worldwide harmonized Light Vehicles Test Procedure (WLTP) was proposed in place of the previous standard laboratory New European Driving Cycle (NEDC) (**Figure 1-3**, [4]). The main changes adopted in the definition of the WLTP cycle with respect to the NEDC [4] are the longer duration, the higher mean velocity and speed variability, the higher test mass. The main differences between the two procedures are listed in **Table 1-3**. In addition, the WLTP test is supported by the so-called Real Driving Emission (RDE) system, which consists in the use of the on-board Portable Emissions Measurements System (PEMS) to measure NO_x and PN emissions during on-road driving in urban, rural and motorways roads.

Table 1-3: Main differences between the NEDC and the WLTP tests.

Parameters	NEDC	WLTP
Start condition	Cold – 23°C	Cold – 14°C
Test mass	Unladen vehicle	Unladen vehicle + optional equipment
Gear shift	Fixed point	Variable per vehicle
Duration	1180 s	1800 s
Distance	11.03 km	23.27 km
Mean velocity	33.6 km/h	46.5 km/h
Maximum velocity	120 km/h	131.3 km/h
Stop phase	23.7%	12.6%
Constant driving phase	40.3%	3.7%
Acceleration phase	20.9%	43.8%
Deceleration phase	15.1%	39.9%

In order to fulfil the new regulations for gasoline-powered light-duty vehicles, two main technological solutions have been adopted: i) the use of full-electric and hybrid thermal-electric engines; ii) the use of new stand-alone ICE configurations that are operated with non-conventional devices, fuels, strategies. Focusing on the latter, new stand-alone configurations are based on the implementation of solutions able to overcome the two curses of gasoline-powered engines, namely the Spark Ignition (SI) system and the occurrence of knocking combustions, allowing the significant improvement of the engine thermal efficiency, thus, the reduction of fuel consumption and CO₂ production. Worth mentioning solutions adopted for new stand-alone configurations are briefly reported:

- Use of different ignition mechanisms and devices, e.g., High Frequency Ignition (HFI) by means of the corona discharge effect [5]–[7]. When using a corona-plug a Non-Local Thermal Equilibrium (NLTE) plasma is created at the discharge time. The main advantages of the NLTE plasma with respect to the thermal plasma created by classical spark devices are [8]: i) lower voltage required at the electrode; ii) the initial reactive volume is around three order of magnitude larger than that associated to classical spark devices; iii) the characteristic ignition time is shorter than that typical of classical spark devices (μs instead of ms); iv) in the NLTE plasma the electrons are highly ionized (12,000-18,000 K) while ions remains almost at ambient temperature, resulting in lower heat losses.
- Blending the gasoline fuel with oxygenates additives e.g., ethanol, propanol-isomers, butanol-isomers, in order to suppress knock events due to: i) the enhancement of the intake charge cooling effect due to the higher heat of vaporization of alcohols (800-900 kJ/kg) with respect to that of hydrocarbons (300-400 kJ/kg); ii) octane rating boosting effect. Furthermore, oxygenates can be produced by means of biological pathways, thus, they contribute to fuel the engine as a renewable energy source reducing the fossil fuel wasting. It is also highlighted that the addition of alcohols helps to reduce the direct emission of the main pollutants.
- Implementation of operating strategies such as: i) non-conventional engine cycles e.g., the Miller cycle, operated with specific Intake Valve Timing and Lift in order to cool down the intake charge [9]; ii) Low Temperature gasoline Combustion (LTC) modes e.g., Gasoline Compression Ignition (GCI), gasoline Homogeneous Charge Compression Ignition (HCCI), Spark Assisted Compression Ignition (SACI), providing Diesel-like engine efficiency or above, and good NO_x-soot emission balance under optimized conditions [10]; iii) the use of the fuel Direct Injection (DI) technique i.e., the implementation of one or multiple injection events directly into the combustion chamber in order to use the heat of vaporization of the liquid fuel phase change to cool-down the intake air and to directly control the ignition features [11], [12]. The penetration of DI on the market is clearly visible in **Figure 1-4** ([13]), **Figure 1-5** ([14]).

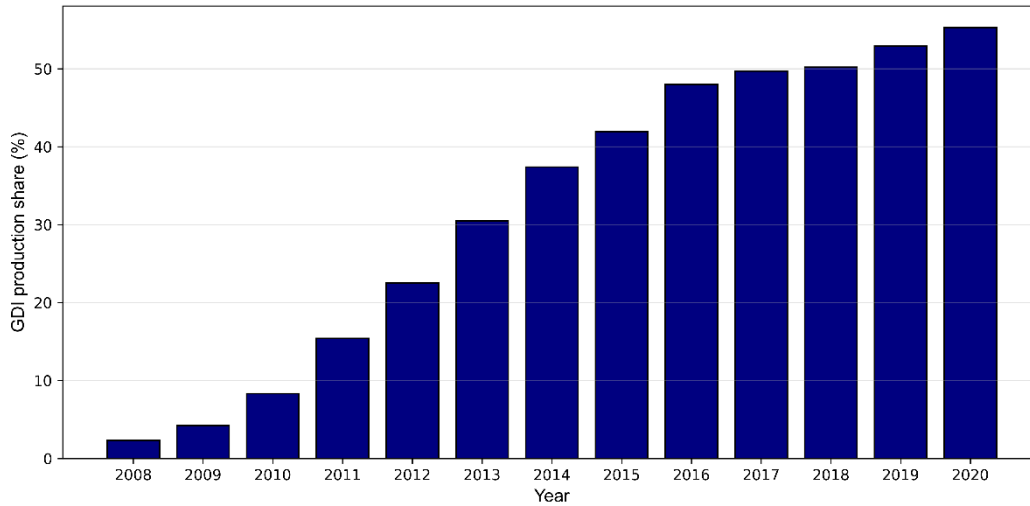


Figure 1-4: Product share of the gasoline DI technique in light-duty vehicles, data from [13].

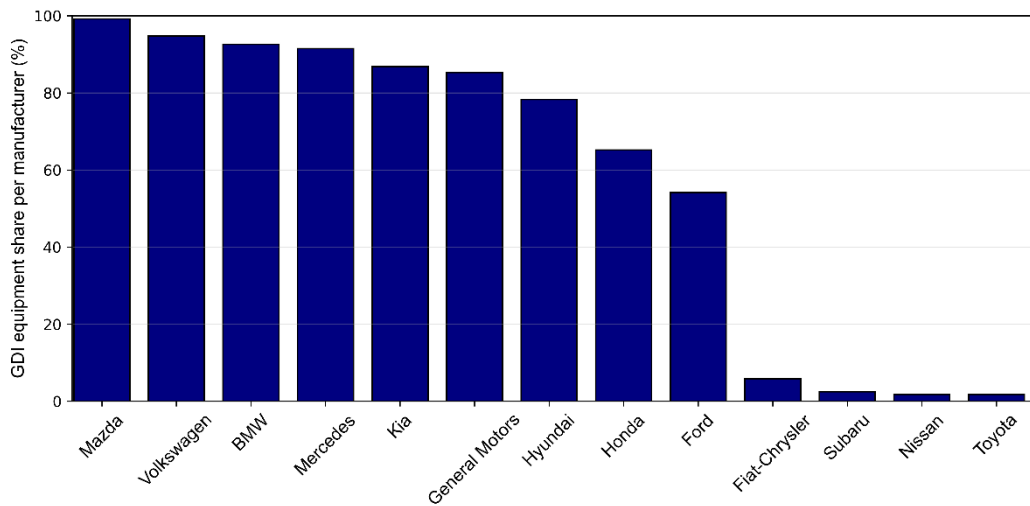


Figure 1-5: Comparison between the share of the gasoline DI light-duty vehicles for the main car manufacturers in 2017, data from [14].

1.2 Gasoline Direct Injection: Overview

Since the EU3 regulation, the conventional injection system is based on the multipoint Port Fuel Injection (PFI), namely the fuel injector is mounted on the intake port, the injector tip is pointed towards the intake valve (**Figure 1-6a**, [15]). The injection timing is chosen in order to ensure the full vaporization of the liquid fuel into the intake port before the Intake Valve Opening (IVO). In the DI configuration the Gasoline Direct Injector (GDI) is mounted on the cylinder head, the injector tip is pointed towards the combustion chamber (**Figure 1-6b**, [15]). The two most common injector mounting options in the DI configuration are two: i) wide spacing (**Figure 1-7a**) if the injector is side-mounted (usually the intake side is preferred because of the lower local temperature); ii) narrow spacing (**Figure 1-7b**) if the injector is central-mounted next to the spark plug.

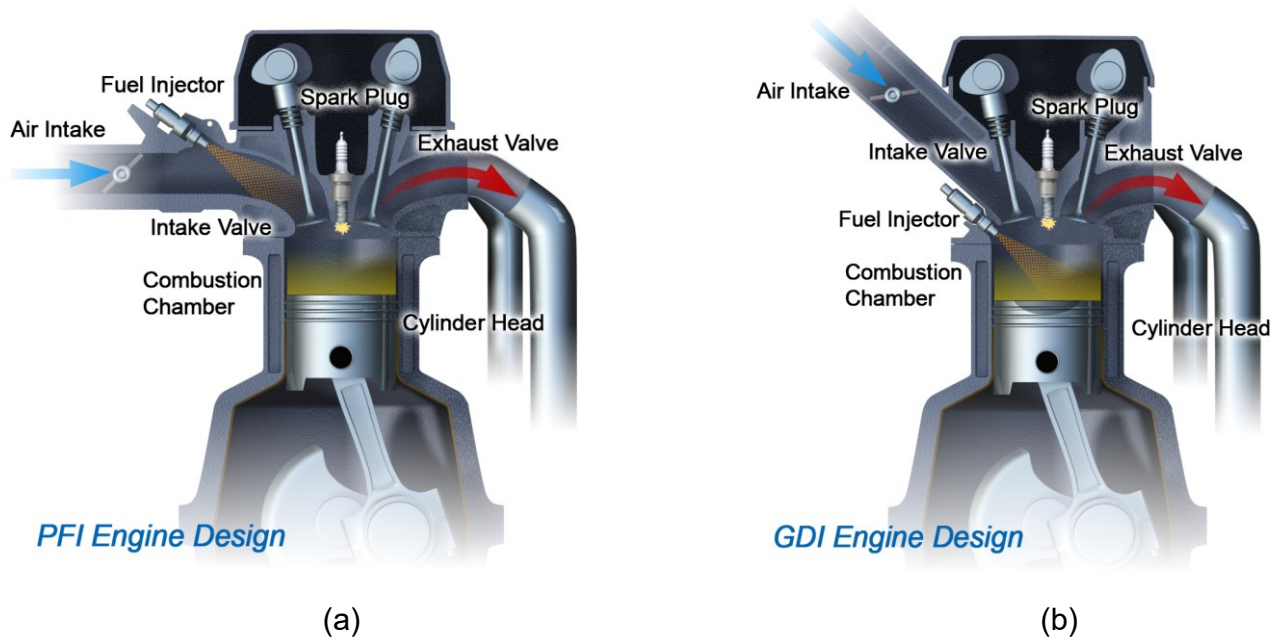


Figure 1-6: Schemes of Port Fuel Injection (a) and Gasoline Direct Injection (b) engine configurations, image from [15].

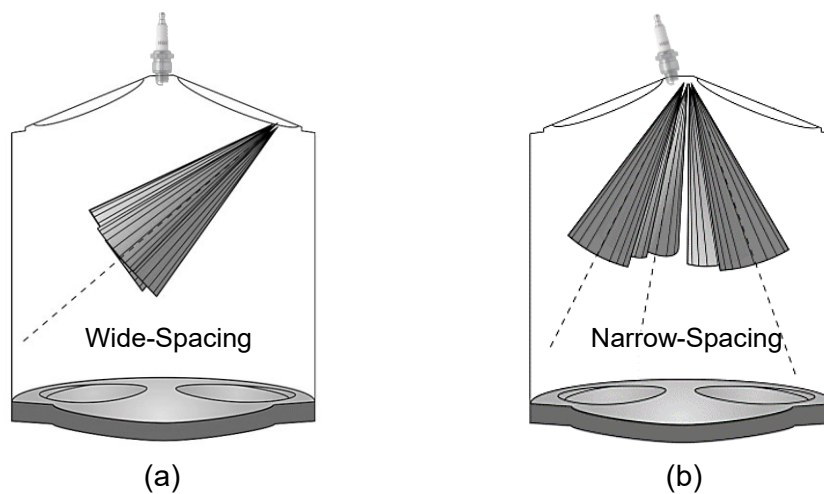


Figure 1-7: Sketch of two Gasoline Direct Injection configurations showing the solid spray cones: a) wide-spacing (side-mounted injector); b) narrow-spacing (central-mounted injector). Spark plug is shown in transparency.

The main differences between wide spacing and narrow spacing configurations regard manufacturing and operating characteristics, which are resumed in **Table 1-4**. From **Table 1-4** it is visible that the wide-spacing option allows for greater manufacturing flexibility and longer components lifetime. Adopting the wide-spacing solution, the injector housing-hole does not limit the design of the cylinder head, namely the spacing between the intake valves and that between the spark plug, and the intake valves are optimized to fulfil geometrical and mechanical constraints. If the narrow-spacing solution is adopted, the need to install both the spark plug and the injector on the center of the pent-roof cylinder head limits the range of the available dimensions and spacing. Moreover, the narrow-spacing option affects the cost and the lifetime of the injector due to the higher local temperature (around 1000 K) caused by the spark plug proximity with respect to the wide-spacing option. Furthermore, in narrow-spacing configurations the proximity between the injector and the spark plug together with the high temperature may promote the spark plug fouling due to leaky fuel clouds and carbon deposits with concerns on the reliability of the spark plug [16]. On the other hand, the wide-spacing architecture may suffer from mixing concerns e.g., the spray angle and the spray pattern are limited due to the need to avoid the impact of the liquid fuel spray with the plate and the stem of the valves; for the most wide-spacing configuration i.e., intake side-mounted injector, the liquid jet is shot against the tumble vortex direction, resulting in the decrease of the tumble motion intensity.

Table 1-4: Main differences between Wide-spacing and Narrow-spacing Gasoline Direct Injection configurations.

Characteristics	Wide-spacing	Narrow-spacing
Valves and Valves-Spark plug spacing		>
Thermal stress		<
Spark-plug fouling		<
Spray angle range		<
Tumble counter-flow		>

It must be underlined that in PFI operations the heat of vaporization of the liquid fuel is wasted towards the intake port's wall, instead, under GDI operations the heat of vaporization is released upon the intake air. As a consequence, the DI promotes the intake charge cool-down leading to two advantages: i) the gas temperature at the Intake Valve Closing (IVC) is lower than that of the corresponding PFI configuration contributing to the knock mitigation; ii) since the gas density increases due to the cool-down, the mass trapped at the IVC for a fixed displacement would be greater, thus, higher specific performances can be achieved. Furthermore, it must be highlighted that the DI technique allows for the achievement of different levels of mixture stratification by implementing different injection timing and number of events.

The DI, due to the positive effect on knock mitigation and charge loading, has proven the potential to effectively support the so-called downsizing technique i.e., the use of smaller displacement volume in order to reduce the weight of the ICE. As a result, lower inertia and reduced mass of the vehicle can be achieved, resulting in lower emissions of CO₂ and fuel consumption. However, it must be considered that the smaller is the displacement, the lower is the geometrical capacity of trapping the gaseous mass, thus, downsized engines may not be capable to fulfil the whole range of the power-demand required by the customer. The application of the DI and the turbocharging (Turbo Gasoline Direct Injection (TGDI)) to downsized engines allows to overcome the lack of performance thanks to the cool-down of the intake charge (DI) and the increase of the intake air pressure (turbocharger). Moreover, in TGDI downsized engines the knock risk induced by the initial higher pressure promoted

by the turbocharger can be balanced by the cool-down effect introduced by the DI. Therefore, the DI is a fundamental technique to support the operations of downsized SI engines in order to reduce fuel consumption and CO₂ emissions while accomplishing the performance requirements.

As mentioned in 1.1, recently the application of LTC modes to gasoline-powered engines has been considered as a promising and attractive solution to significantly increase the thermal efficiency of the engine. The main cause of the improved engine efficiency shown by LTC modes is the low temperature of walls and gases during the combustion phase. The LTC relies on two key aspects: i) the combustion is not based on the formation and growth of the plasma kernel and the development of the flame front as typically observed in gasoline SI engines. Instead, the combustion is fully or mainly driven by the multi-point no-knock auto-ignition of the gasoline as described by chemical kinetics simulations; ii) the combustion environment under LTC modes is highly diluted, thus, the operating mixture is typically lean and rich in Exhaust Gas Recirculation (EGR) gases. Despite the advantages of the implementation of LTC modes in gasoline-powered engines, the gasoline no-knock auto-ignition in those engines is characterized by combustion-control issues, namely the abrupt pressure rise rate and heat release rate in the cylinder. Among different solutions adopted to approach those technical issues, fuel stratification has shown a great potential. In literature experimental works [17], [18] the Authors have proven that in gasoline HCCI engines the stratification of the mixture due to the fuel targeted distribution leads to the stratification of temperature due to the latent heat of vaporization of the fuel. The Authors described the fuel stratification as an effective control strategy of the in-cylinder heat release rate and pressure rise rate. Moreover, the experiments showed that the tailored fuel stratification is an effective technique to extend HCCI operations towards high loads while maintaining a well balance between NO_x emissions and pressure rise rate. In the comprehensive work of Zhou et al. [19] experiments were carried out under SI, HCCI and SACI modes with the same test engine. The Authors reported that fuel stratification helps to suppress knock events in the end-gas and to mitigate the burn rate, resulting in smoother HCCI (low load) – SACI (medium load) transitions and SACI (medium load) – SI (high load) transitions (**Figure 1-8a** vs **Figure 1-8b**). Moreover, fuel stratification under SACI operations improves combustion stability of mixtures that are richer in EGR and earlier spark timings. The achievement of the target fuel distribution in stratified operations is based on the use of the DI, which allows a high level of control by means of the application of tailored injection splits i.e., number of injection events, and the corresponding injection timing i.e., Start Of Injection (SOI) – End Of Injection (EOI).

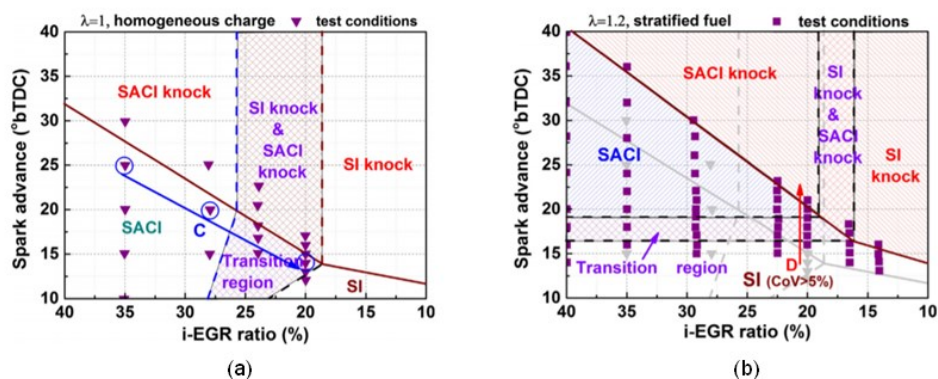


Figure 1-8: HCCI-SACI-SI mode transition for different EGR ratio and spark timing in the case of homogeneous charge (a) and stratified charge (b). Pictures from [19].

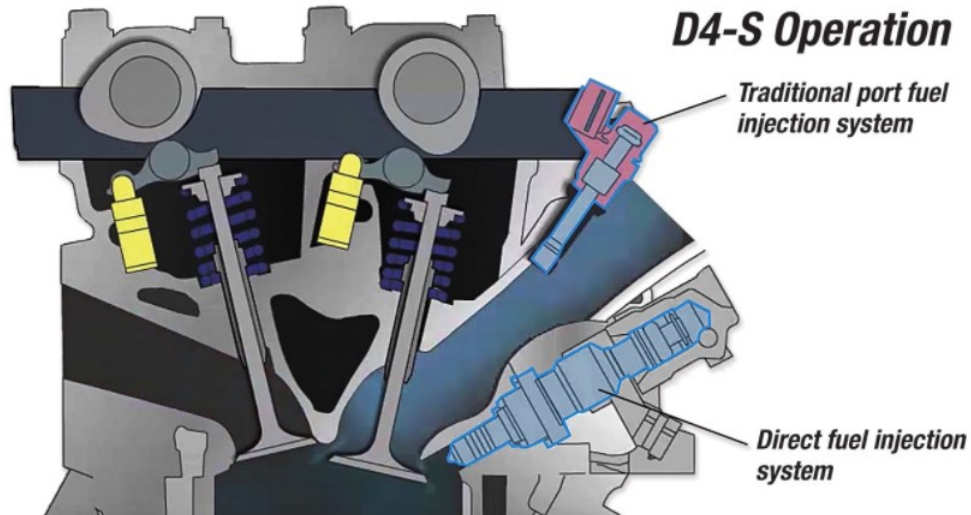


Figure 1-9: Scheme of the PDI gasoline engine proposed by Toyota, picture from [20].

It is underlined that it possible to put both the PFI system and the GDI system in the same engine configuration named Port-Direct-Injection (PDI). In PDI configurations the choice of the active injection system depends on the engine operating point (i.e., load and speed) with the aim of maximizing the advantages of both the techniques. It is common that the DI system is used as stand-alone at high load and high speed due to the knock mitigation promoted by the charge cooling effect. At low load and low speed, and at low-medium transitions one can use the PFI system as stand-alone or the combination of PFI and GDI. The transition from the DI stand-alone strategy is mainly driven by the fuel wasting and the poor mixing that may occur if the DI is used at low operating points due to the reduced turbulence intensity and the lower temperature. The PDI combination can be used to speed-up the cat-heating phase by implementing a main injection by means of the PFI system and a late injection by means of the DI system with the aim to stratify the charge and operate a delayed spark timing. Since there is not a solid best-practice for the DI-to-PFI or the DI-to-PDI transition, the PDI strategy strongly depends on the manufacturer. **Figure 1-9** shows the D4-S PDI gasoline engine by Toyota [20].

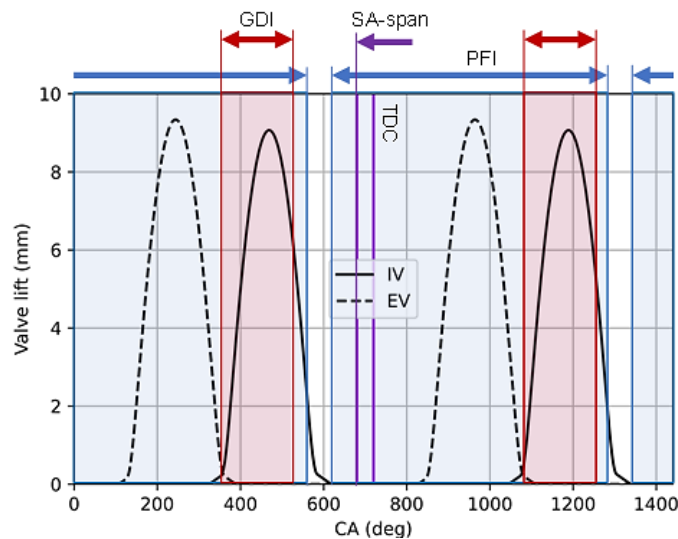


Figure 1-10: Injection timespan for PFI and GDI configurations with respect to a reference engine cycle. The Intake Valve (IV) lift (solid), the Exhaust Valve (EV) lift (dashed) and the Top Dead Center (TDC, solid purple) are reported.

Despite the fact that the DI plays a key role in the development of low-impact engines, the introduction of the fuel liquid phase directly into the combustion chamber and the following liquid phase-change remains a concern. In PFI operations the maximum timespan available for the injection is around the whole engine cycle (**Figure 1-10**, blue) starting from the IVC. In GDI operations the injection event must be placed in order to ensure the liquid phase-change and the target charge distribution (homogeneous or stratified) before the ignition timing (typical Spark-Advance (SA) values are in the range 680-700 CA deg), thus, typically the DI timing is mainly placed in the compression stroke (**Figure 1-10**, red). Moreover, it must be considered that in PFI operations the back pressure is around the ambient pressure whilst in GDI operations the back pressure is that of the in-cylinder, which can be significantly higher than the ambient pressure depending on the engine load. As reported in [21], the higher is the back pressure, the larger is the size of the injected liquid particles, resulting in slower vaporization. Therefore, since the liquid-phase change in GDI operations is more complex with respect to PFI operations due to the shorter time available for the evaporation and the lower evaporation rate promoted by the higher back-pressure, the application of ever higher injection pressure is mandatory in order to both speed-up the injection event and improve the control of the mixture formation. In the earlier application of the GDI the injection pressure could be in the range 50-200 bar, on the other hand typical injection pressure values in PFI operations were 5-10 bar. Currently fuel injection pressures up to 350 bar are available on the market, values of 600-700 bar can be achieved for specific application e.g., the Magneti Marelli injection system implemented in the Skyactiv-X by Mazda [22]. There are several aspects that strongly affect the behavior of the liquid phase-change, thus, the mixture formation e.g., the shape of the combustion chamber, the thermodynamic conditions of the gases, the interaction with the charge motion, the interaction with the solid walls of the combustion chamber and with the lubricant oil film which wet the moving walls e.g., the clearance between the cylinder liner and the piston. Therefore, the deep understanding of the spray phases is fundamental in order to fully enhance the advantages of DI.

1.3 Phases of the liquid fuel spray

Thanks to the use of the fuel injector, the fuel is introduced into the ambient gas as a pressurized liquid that flows through a small orifice i.e., the nozzle-hole, by means of the mechanical action of the needle (**Figure 1-11**, [23]). As a result, the injected fuel is provided in the spray state, namely a two-phase cloud composed of both the fuel vapor phase and the fuel liquid phase under the form of small droplets. The phases of the liquid fuel spray that contribute to the mixture formation can be resumed in three steps (**Figure 1-12**, [24]): i) the liquid injection and atomization phase, also called primary breakup; ii) the formation of the fully dispersed spray due to the complete fragmentation of the liquid macro-structures from the atomization, also called secondary breakup; iii) the spray-wall impingement, namely the impact of the non-evaporated liquid droplets against the solid walls.

In the following sections the three afore-mentioned spray phases will be described in the ICE framework. The first two phases, namely the primary breakup and secondary breakup, are briefly presented since the free-spray formation, i.e., the spray development in gaseous environment with no impacts, is one of the most investigated topic in both industry and academia by means of experiments and numerical simulations. The spray-wall impingement phase is the main topic of the present thesis; thus, it will be discussed with more emphasis.

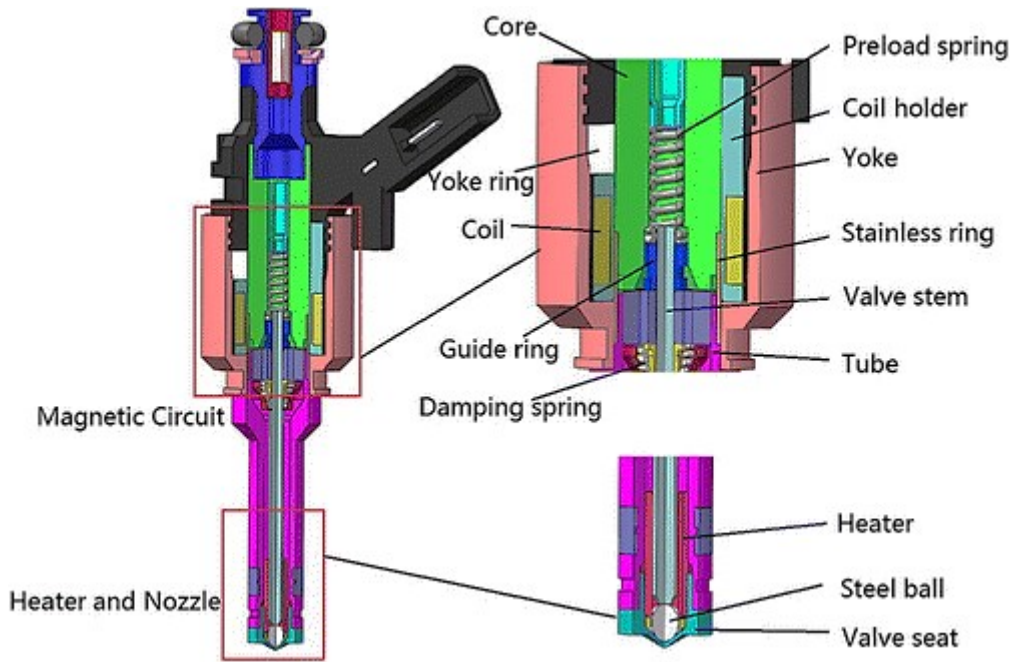


Figure 1-11: Cross section view of a solenoid driven GDI injector (top) with detailed view of the needle lift system (top right) and the nozzle-holes region (bottom right), picture from [23].

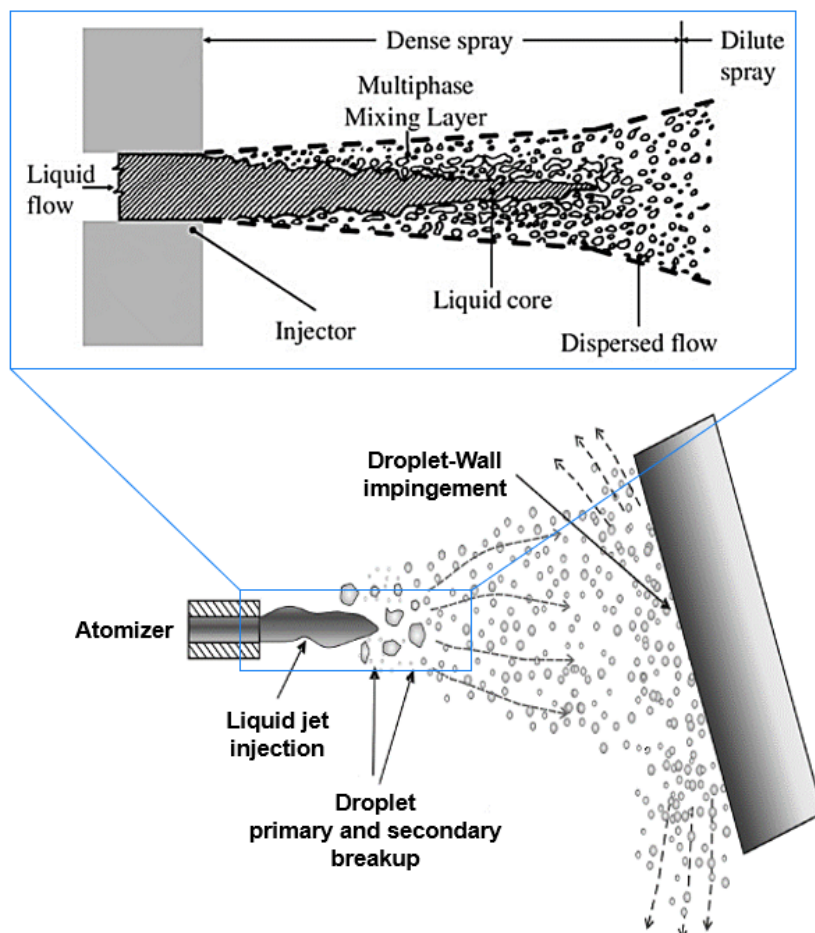


Figure 1-12: Scheme of the liquid fuel spray main phenomena: primary and secondary breakup; spray-wall impingement, pictures from [24].

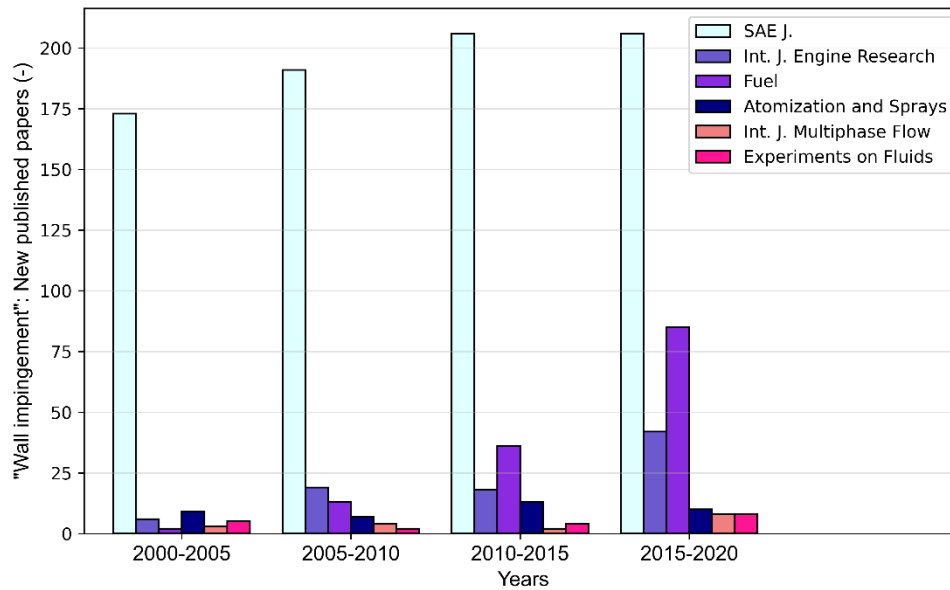


Figure 1-13: Number of new published papers by keyword "gasoline wall impingement" for different journals and years.

As far as the improvement of the fuel economy and of the emission of pollutants is central for the development of the next ICE, the effect of the spray-wall impingement on the mixture formation and burning has gained increasing attention. **Figure 1-13** shows the number of new papers published on different journals i.e., *SAE Journals*, *International Journal of Engine Research*, *Fuel*, *Atomization and Sprays*, *International Journal of Multiphase Flow*, *Experiments on Fluids*, in the last 20 years by searching the keyword 'gasoline wall impingement'. It is visible that since the years of the earlier application of the GDI (2000s), the number of new papers focused on the gasoline spray-wall impingement is increasing, proving the importance of the topic and the need to achieve a deeper knowledge and new reliable methodologies, especially with regards to the engine application (see the bars of *SAE J.*, *Int. J. of Engine Research*, *Fuel*).

1.3.1 Spray primary breakup

The spray primary breakup, also called spray atomization, is a phenomenon consisting of the fragmentation of the coherent liquid jet, also called the 'liquid core'. When the fragmentation of the liquid core occurs, liquid elements such as droplets, ligaments are pinched-off from the liquid core, resulting in a poly-dispersed distribution of the liquid phase. The detachment of such liquid elements from the liquid core is mainly induced by turbulence, which causes the wrinkling of the interface between the liquid jet and the surrounding gases [25], [26]. Besides the high velocity reached by the liquid core, additional sources of turbulence in GDI injector nozzle which enhance the primary breakup are flash boiling and cavitation.

- Flash boiling is encountered if the heated liquid gasoline fuel faces a surrounding pressure which is below its saturation pressure at that liquid temperature. Under those conditions, the formation of fuel vapor under the form of bubbles can be observed, then bubbles rapidly grow up to the collapse. During their lifetime, the evolution of bubbles contributes to the further rupture of the liquid jet, usually resulting in wider spray cone downstream the nozzle tip exit (increased jet-jet mutual interaction) and smaller droplets. As a consequence, induced flash boiling has been taken under consideration as a technique enhance the atomization process allowing to improve mixing and reduce wall-

impingement while limiting the injection pressure [27], [28]. In the framework of boosted high load SI operations (turbocharge active), the achievement of pressure conditions promoting flash boiling is unlikely, whilst if low-intermediate load points (naturally aspirated conditions) and early injection strategy (fuel injection mainly during the intake stroke associated to the pressure decrease due to the positive displacement) are considered, flash boiling should be taken into account.

- Cavitation deals with the formation of pockets of fuel vapor inside the nozzle caused by geometric features of the channel and fluid-dynamics without any thermodynamics concern differently from flash boiling. In general, cavitation occurs due to an abrupt pressure loss by the liquid at almost constant temperature imposed by geometric features of the channel, such as cross-section reduction, up to the saturation pressure. The formation of liquid vacancies is mainly promoted by sharp edges, which are associated to the phenomenon of vena-contracta i.e., occurrence of separated flow with respect to the channel's walls due to the inability of the flow to fit the contact wall shape change. After the cavitation onset, as the liquid phase change develops, the vapor pockets initiated at the edges detach leading to the formation of bubbles that are then transported by the flow up to the collapse along the injector nozzle due to the pressure rise from the saturation value towards the in-cylinder value. As described for flash boiling, the bubbles' growing and collapse have benefit on the liquid core atomization. However, it must be considered that the continuous collapse of bubbles clusters leads to the nozzle hole surface erosion, with concerns on the injector reliability and lifetime [29]. In general, cavitation can be avoided by applying manufacturing solutions such as enhanced rounding of the nozzle entrance and positive nozzle conicity [30].

It was observed that the primary breakup can occur under different rupture modes called breakup regimes, which differ from each other by features such as the length scale of the liquid core consumption, and the shape of the rupture. The breakup regime (which could be Rayleigh regime, 1st wind induced regime, 2nd wind induced regime, atomization) it is commonly identified by means of the breakup regimes diagram (**Figure 1-14**, [31]).

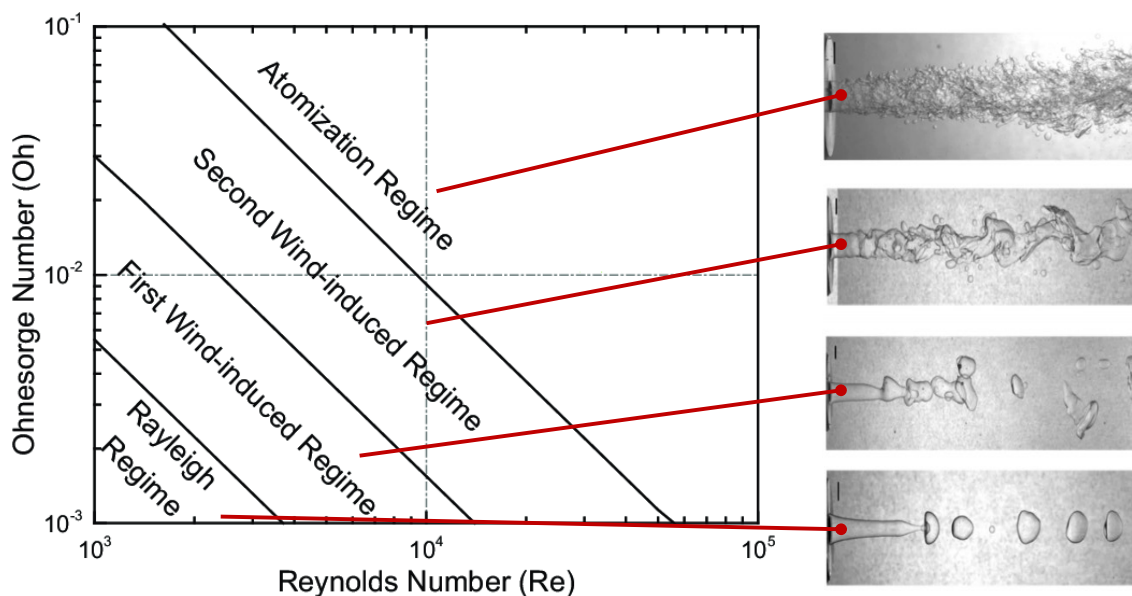


Figure 1-14: Primary breakup regimes diagram. The experimental image of the breakup regime taken from [31] is associated to the corresponding zone of the diagram.

The breakup regime diagram in **Figure 1-14** is defined by means of the non-dimensional group of numbers composed of the Reynolds number (Re), the Weber number (We), the Ohnesorge number (Oh). The meaning of those non-dimensional numbers is resumed in **Table 1-5**, representing the interplay among different forces such as viscous, inertial, capillary and gravitational. In **Table 1-5** ρ is the density, μ is the dynamic viscosity, σ is the surface tension, d is the droplet diameter, U is the magnitude of the droplet velocity.

Table 1-5: Group of the non-dimensional numbers used to describe the breakup phenomenon.

Non-dimensional number	Description	Equation
Reynolds (Re)	Inertia forces vs Viscous forces	$Re = \frac{\rho U d}{\mu}$
Weber (We)	Kinetic energy vs Surface energy	$We = \frac{\rho U^2 d}{\sigma}$
Ohnesorge (Oh)	Viscous forces vs surface and inertia forces	$Oh = \frac{\mu}{\sqrt{\sigma \rho d}} = \frac{\sqrt{We}}{Re}$

In GDI devices the primary breakup begins inside the nozzle-hole, and it lasts until the nozzle-hole exit, then it develops in the gaseous environment for distance of around 5-10 nozzle-hole diameters. In [32] the Authors reported that the liquid fuel spray created by using the DI technique is placed in the atomization breakup regime region for values of the injection pressure ranging from 50 bar to 300 bar. However, it must be underlined that when the injection event is commanded by the engine control unit, the pressure of the liquid at the nozzle inlet surface does not achieve the rail pressure instantaneously, instead the flow pressure at the injection command is that of the in-cylinder. Therefore, in the timespan from SOI to EOI whereas the liquid fuel pressure increases from the in-cylinder pressure to the rail pressure (injection pressure), the liquid fuel spray is subjected to the transition between the different breakup regimes.

1.3.2 Spray secondary breakup

The spray secondary breakup consists of the further rupture of the liquid elements produced by the primary breakup into smaller particles, resulting in the formation of the full dispersion of the liquid phase. As mentioned before, the primary breakup is mainly induced by turbulence, instead the main driver of the secondary breakup is the aerodynamic drag caused by the relative velocity between the liquid elements and the surrounding air. As mentioned in 1.3.1 for the primary breakup, even the secondary breakup-induced rupture can occur in different modes depending on the gas Weber number (Eq. (1-1)) of the droplet.

$$We = \frac{\rho_G \cdot d \cdot U_{G-L}^2}{\sigma_L} \quad (1-1)$$

In Eq. (1-1) ρ_G is the density of the surrounding gas, d is the diameter of the liquid droplet, σ_L is the surface tension of the liquid droplet, U_{G-L} is magnitude of the relative velocity between the liquid droplet and the gas. The features of the different ruptures and the corresponding Weber number values are visible in Figure 1-15 [33].






Rupture mode	Rupture morphology	Weber threshold
Vibrational breakup		≈ 12
Bag breakup		12 - 20
Bag/Streamer breakup		20 - 50
Stripping breakup		50 - 100
Catastrophic breakup		> 100

Figure 1-15: Representation of the secondary breakup regimes, pictures from [33].

1.3.3 Spray-wall impingement

Impact dynamics

The spray-wall impingement occurs if the spray droplets hit a solid wall. Once the impact has occurred, there are three possible fates for the incoming droplet: i) the incident liquid mass may remain stuck to the wall; ii) the incident liquid mass may be scattered back as a polydisperse cloud of smaller and more disperse droplets i.e., the so-called secondary spray; iii) a combination of the two afore-mentioned phenomena. According to the fate of the liquid mass at the strike, three main different impact regimes can be recognized, namely deposition, rebound, splash.

Table 1-6: Brief description and characteristics of the main possible impact regimes.

Impact regime	Description	Promoted by	After-impact features
Deposition	Flattening of the incoming droplet against the wall, resulting in the formation of a thin layer of liquid called wall film	<ul style="list-style-type: none"> Intermediate droplet velocity Low wall temperature 	Thickness of the liquid layer
Rebound	The incoming droplet is bounced-back as a single scattered droplet maintaining the same mass	<ul style="list-style-type: none"> Low droplet velocity 	Scatter velocity; Scatter angle
Splash	Rupture of the incoming droplet with formation of both adhered liquid pool and multiple scattered droplets	<ul style="list-style-type: none"> High droplet velocity Low droplet velocity & wet wall 	Adhered-scattered mass split; scatter number; scatter velocity; scatter angle; scatter diameter

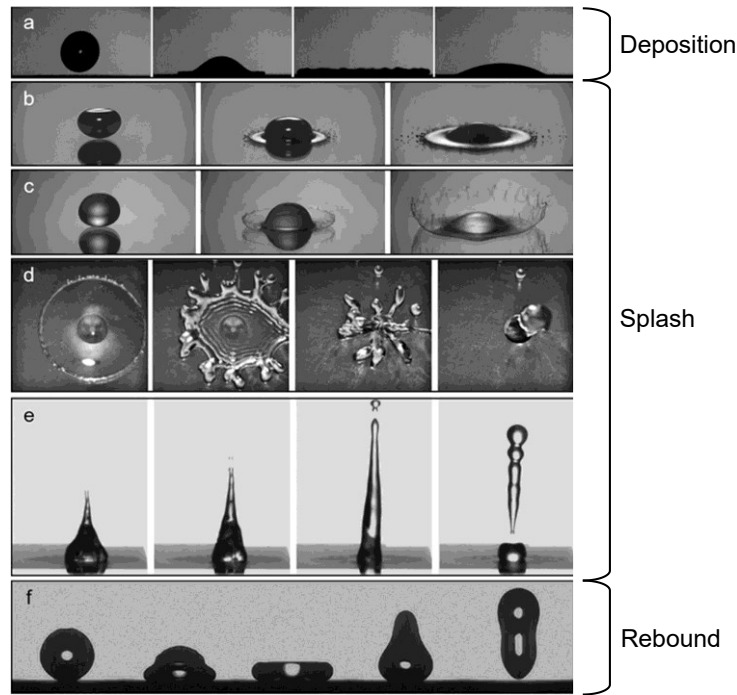


Figure 1-16: Experimental pictures of some possible impact regimes using water: a) deposition; b-e) different splash modes; f) rebound. Images taken from [34].

The description and the main characteristics of the three impact regimes are presented in **Table 1-6**. The morphologies of the impact regimes are reported in **Figure 1-16** [34]. As visible in **Figure 1-16b-e**, the most complex impact regime is the splash due to the multiple possible surface instability-induced rupture morphologies and the corresponding after-impact features such as number, size, direction and velocity of the rupture-induced secondary spray. It is underlined that in the current literature there are impact rupture modes that are considered as stand-alone impact regimes e.g., thermal breakup, receding breakup (**Figure 1-16d**), partial rebound (**Figure 1-16e**). In this work, if the impact results in the split of the incoming droplet into deposited liquid and scattered liquid, the corresponding regime is considered a splash sub-mode. As listed in **Table 1-6**, each impact regime is mainly promoted by specific combinations of the droplet kinetics and the conditions of the solid surface. In **Table 1-6** the droplet kinetics is represented as the droplet velocity however, to be straight the effect of the droplet kinetics on the impact regime depends on the balance between the droplet kinetic energy (Eq. (1-2)) and the surface energy of the droplet (Eq. (1-3)). The kinetic energy of the droplet, resulting from the secondary breakup, will be dissipated due to the strike against the wall, whilst the surface energy represents the cohesion between the molecules of the liquid that shape the droplet, thus, the surface energy is the resistance exhibited by the droplet to the rupture by means of the surface deformation. In both Eq.s (1-2), (1-3) the droplet is assumed as a sphere, $U_{n,L}$ is the normal to the wall component of the velocity of the incoming droplet. As visible in Eq.s (1-2), (1-3) the effect of the droplet kinetics on the impact regime depends on the properties of the liquid composition of the incoming droplet through the density and the surface tension, the size and the velocity of the droplet at the impact. Therefore, the kinetics boundaries between the three mentioned impact regimes are commonly determined by means of the Weber number of the incoming droplet (Eq. (1-4)).

$$E_{K,L} = \rho_L \cdot \frac{4}{3} \pi d^3 \cdot U_{n,L}^2 \quad (1-2)$$

$$E_{S,L} = \sigma_L \cdot 4\pi \cdot d^2 \quad (1-3)$$

$$We = \frac{\rho_L \cdot d \cdot U_{n,L}^2}{\sigma_L} \quad (1-4)$$

Once the incoming liquid type is identified, namely the gasoline in this thesis, the density-surface tension ratio is more or less the same regardless of the specific gasoline. Indeed, for commercial gasolines values ranging from 720 to 740 kg/m³ at 20°C and from 0.019 to 0.022 N/m at 20°C are common for density and surface tension, respectively. Thus, in GDI engines the main drivers of the effect of the droplet kinetics on the impact regime are the size and the velocity of the droplet. In general, the greater are the diameter and the velocity of the droplet at the impact, the higher will be the degree of deformation of the liquid surface due to the discharge of the higher kinetic energy against the surface energy, resulting in the initiation and the propagation of surface instabilities that may induce the formation of different liquid patterns such as sheet, rim, ligament etc. To take some simple examples, if one considers the deposition regime (**Figure 1-16a**), the splat of a droplet against a solid wall with formation of an adhered liquid flat patch requires the dissipation of significant amount of kinetic energy at the impact, instead low kinetic energy impact would promote the sticking of the droplet against the wall with conservation of the droplet dispersed form. If one considers the rebound regime (**Figure 1-16f**), the back scatter of the incoming droplet as a slightly deformed single scatter droplet of equal mass must be the result of a low kinetic energy impact, thus, the surface energy is sufficient to maintain the coherence and the shape of the droplet. If one considers the splash regime (**Figure 1-16b-e**), the split of the liquid mass into adhered pool and scattered polydisperse droplets detached from a characteristic liquid pattern, whose morphology depends on the splash sub-mode, is a clear sign of the complete rupture of the incoming droplet, thus, the kinetic energy at the impact must be significantly greater than the surface energy.

Another key aspect in determining the impact regime is the surface coverage of the impact wall. At the time of the strike, two different wall surface coverage configurations are possible, namely dry wall and wet wall. In GDI engines application, the spray-wall impingement may occur mainly on piston crown, cylinder liner wall, intake valve plate. An example of dry impact surface is the piston crown whilst examples of wet impact surface are: i) the piston crown itself in the case the deposition regime has occurred in certain zones; ii) the cylinder liner wall; iii) the intake valve plate. The latter two are covered in a thin lubricant oil film that allows the upward and downward piston motion within the cylinder (i) and the valves lift off-on against the seat (ii), respectively.

In the case the wall is dry, the kinetic energy is fully dissipated at the strike against the wall. In dry wall impact conditions, the surface roughness may affect the wall impingement, indeed if the average roughness is comparable or larger than the diameter of the incoming droplet, the interaction with ridge-valley lines may cause the stuck in valley and the deformation and rupture against the ridge edge of the droplets. As a consequence, the impact regime against the rough wall would be different than that expected for a smooth wall if the same droplet kinetics is considered. In [35] the Authors conducted vessel iso-octane spray-wall impingement experiments under engine relevant conditions against different surface structures, namely cast surface ($R_a = 15.42 \mu\text{m}$), machined surface ($R_a = 13.42 \mu\text{m}$), polished surface ($R_a = 1.5 \mu\text{m}$). In order to observe the features of the secondary spray after the impact, the Authors equipped the vessel with a Phase Doppler Particle Analyser (PDPA) laser system. The comparison between the secondary spray produced by the impact against the cast and the machined surfaces are quite different due to the finer size of the droplets

produced by the cast surface. On the other hand, the secondary spray size differences between machined and polished surfaces are slight. Considering the high accuracy in the machining of the piston surfaces in engine applications, it is reasonable to assume that the average roughness of the piston crown (order of few micrometers) does not affect the impact regime of the incoming fuel spray droplets (order of dozens of micrometers).

In the case the wall is wet, the impact of the droplet leads to the deformation of the liquid film surface and to the penetration of the droplet into that until a given depth. As a result, the liquid film contributes to the progressive reduction of droplet kinetic energy by viscous damping effect. Consequently, the presence of the liquid film over the impact wall allows the occurrence of low kinetic impact regimes even for given intermediate-high droplet kinetics depending on the thickness and the viscosity of the liquid layer. To take some examples, in the study of the impact regimes proposed by Bai [36], it was observed that for given droplet kinetics and wall temperature, the presence of the liquid film extends the environmental conditions at which the rebound (low kinetics impact regime for dry wall) occurs. In [37] the reference reports that as the liquid film thickens up, the deposition regime (intermediate kinetics impact regime for dry wall) is allowed for ever higher values of the Weber number against the splash regime. Furthermore, it is visible that the presence of the liquid film enables splash sub-modes for low values of the Weber number, indeed at wet wall conditions the deformation and the instability propagation regard both the droplet and the liquid film surfaces likely resulting in the trapping of a given mass of the incoming droplet into the liquid layer and in the breakup of both the droplet and the liquid surface. In the framework of GDI engines the viscous damping effect on the impact regime strongly depends on the coverage of the impact wall. Indeed, as mentioned before the liquid film over the engine walls might be composed of gasoline (piston crown) or oil (cylinder liner wall, valve plate), whose viscosity values highly differ from each other (**Figure 1-17**). Moreover, even the thickness of the fuel and the oil liquid film can be quite different, namely the thickness of oil layer over the cylinder wall varies from tenths μm to $10\ \mu\text{m}$ whilst the thickness of the fuel liquid film formed over the engines walls ranges from few to dozens μm depending on the engine load and the spray pattern.

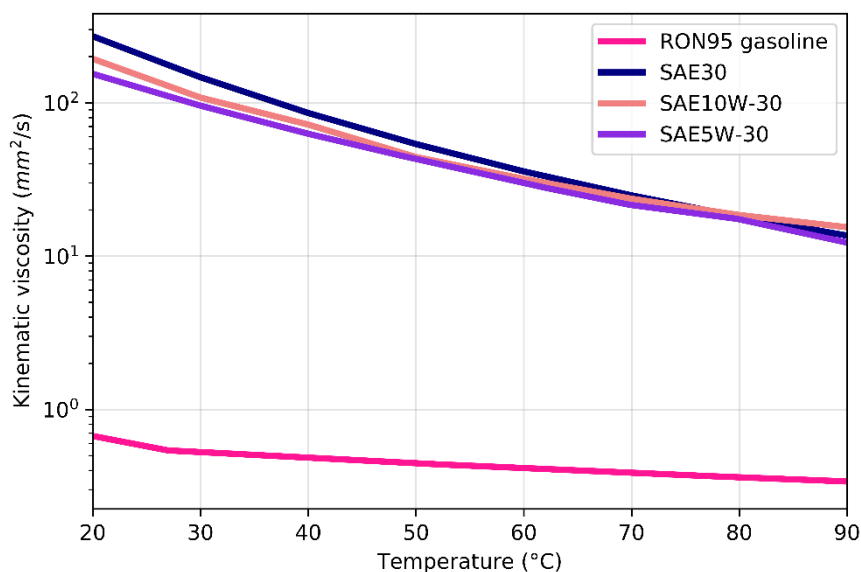


Figure 1-17: Comparison between the kinematic viscosity of a nowadays commercial gasoline and three different typical engine oils.

The Leidenfrost effect

The temperature of the impact wall is the other key parameter that has been mentioned in **Table 1-6**. The high temperature enhances the evaporation reducing the lifetime of the liquid phase e.g., a relatively high wall temperature with respect to the impacting liquid prevents from the formation of the liquid wall film affecting the deposition and the splash regimes. It must be underlined that the relationship between the liquid lifetime and the wall temperature is neither linear nor monotonous due to the so-called Leidenfrost effect. Since the modeling and capture of the Leidenfrost effect is one of the core topics of the present thesis, a comprehensive description of the phenomenon is given in the following section.

The Leidenfrost effect is a physical phenomenon that occurs if liquid droplets hit a solid wall which is heated at temperatures around the so-called Leidenfrost temperature, which mainly depends on the impacting liquid properties and the environmental pressure. The Leidenfrost effect consists of the formation of a thin layer of vapor upon the surface of a heated solid wall caused by the abrupt rising of the evaporation rate of impacting droplets nearby the wall (**Figure 1-18**, [38]).

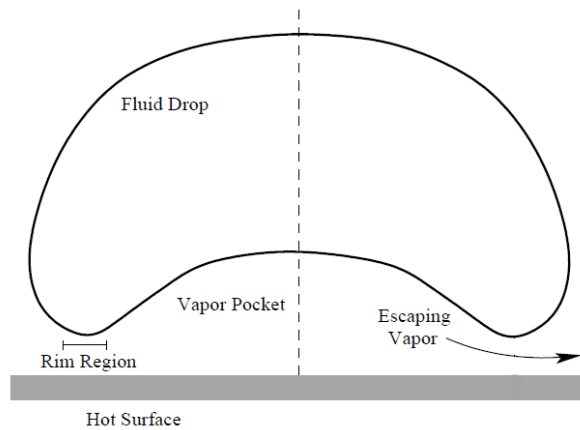


Figure 1-18: Sketch of the Leidenfrost effect for an impacting droplet, edited from [38].

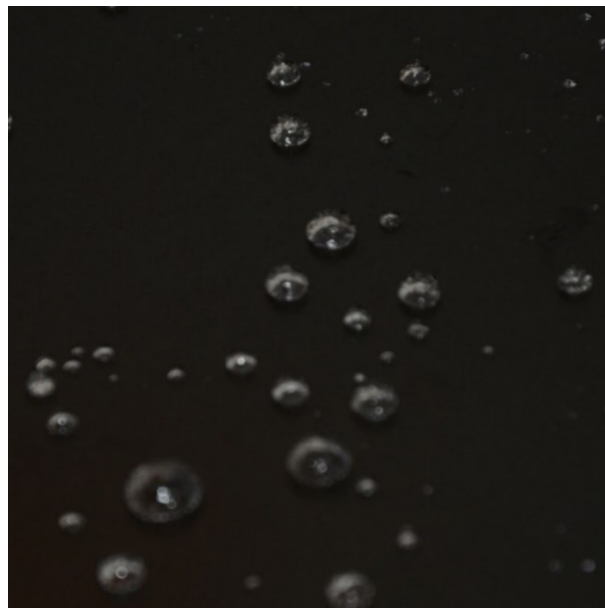


Figure 1-19: Water droplets floating over the Leidenfrost-induced water vapor layer, solid plate at 197°C.

As a result, the vapor layer prevents the direct contact between the wall and the impacting droplets, which instead will interact with the vapor cushion as a floating dispersed liquid (**Figure 1-19**). Therefore, if the Leidenfrost effect occurs the liquid lifetime, namely the time during which the liquid phase can be observed as dispersed phase (droplets), is longer than that typical of the same liquid exposed to wall temperatures higher than its equilibrium temperature.

During the droplet-wall impingement the temperature of the impact wall affects the liquid-solid heat transfer and the fuel phase change according to the so-called droplet lifetime curve (**Figure 1-20**). Four different vaporization regimes can be determined by considering increasing temperatures of the wall [39]: i) *liquid film evaporation* regime (**Figure 1-20, I**), if the surface temperature is below the liquid equilibrium temperature (T_{sat}), the droplet may adhere to the surface leading to liquid film formation; ii) *nucleate boiling* regime (**Figure 1-20, II**), if the surface temperature is between the liquid equilibrium temperature to the so called Nukiyama temperature (T_N). In this temperature range the liquid phase change occurs at the liquid layer in contact with the heated surface, resulting in the formation of vapor pockets within the adhered dispersed liquid. This phase change mechanism determines the condition of maximum heat flux, thus, the maximum droplet consumption rate, which corresponds to the minimum droplet lifetime; iii) *transition boiling* regime (**Figure 1-20, III**), if the surface temperature is in between the aforementioned Nukiyama temperature and the Leidenfrost temperature (T_L). In this range the evaporation rate increases, and the vapor structures grow up until the coalescence into a continuum vapor layer. As mentioned before, the vapour layer, preventing the direct contact between liquid and solid, is the main cause of the droplet lifetime increase; iv) *film boiling* regime (**Figure 1-20, IV), if the surface temperature is above the Leidenfrost temperature the vapor layer fully prevents the contact between liquid and solid. The further heating-up of the wall results in shorter droplet lifetime since the vapor heated by the ever-hotter wall heats significantly the liquid in its turn, thus, the vaporization occurs almost according to the *nucleate boiling* regime.**

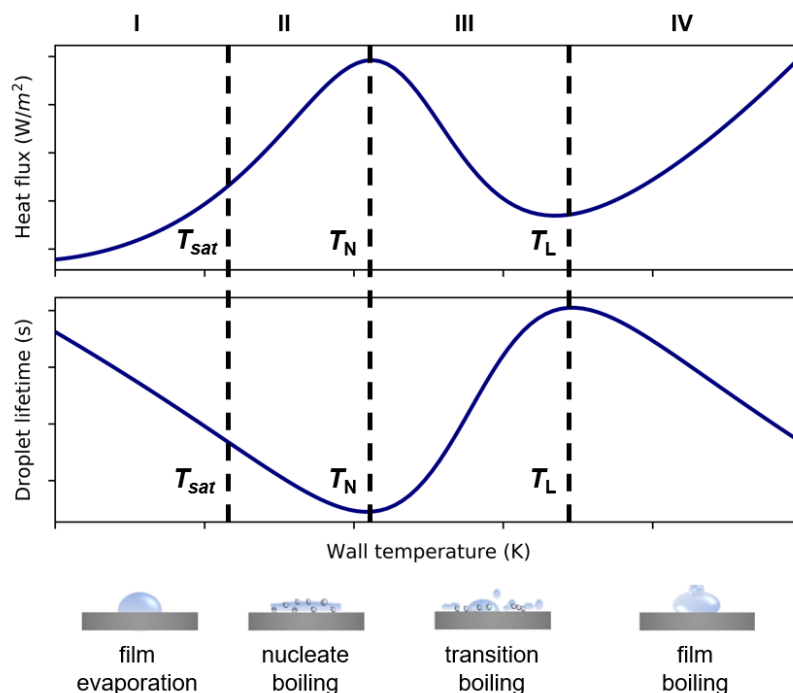


Figure 1-20: Representation of liquid-wall heat flux (top) and droplet lifetime (bottom) behaviour for increasing wall temperature with focus on the four vaporization regimes.

In [40] the Authors highlighted that the higher is the back pressure, the higher is the Leidenfrost temperature, as for the equilibrium temperature of the liquid. Furthermore, the Authors observed that for different hydrocarbons the Leidenfrost effect is not detected for any wall temperature at gas pressure up to 6 bar, which corresponds to high load engine operations supported by the turbocharger. Despite the fact that the Leidenfrost effect is mainly driven by the liquid equilibrium properties and the wall temperature, also the effect of the droplet kinetics must be taken into account.

In [41] the Cai and Yao reported that the incidence angle of the incoming droplet affects the Leidenfrost temperature. Once the vapor layer is formed, the capability of the next droplets to penetrate it depends on the normal-to-wall component of the droplet velocity. Considering a droplet of given kinetic energy, two different scenarios may arise: i) the incidence direction of the droplet is perpendicular to the wall (**Figure 1-21**, $\theta = 90^\circ$), thus, the whole kinetic energy is available for the penetration of the vapor layer; ii) the incidence direction of the droplet is diagonal to the wall (**Figure 1-21**, $\theta < 90^\circ$), thus, the normal component of the velocity contributes to the penetration of the vapor layer whilst the action of the tangential component of the velocity is not relevant. Therefore, in the second scenario (ii), which is the most common in engine applications, only a share of the initial droplet kinetic energy is available for the penetration of the vapor layer with respect to the perpendicular impact. As a consequence, the lower is the incidence angle of the droplet (i.e., the lower is the share of the initial kinetic energy which is effectively used against the vapor layer), the lower is the likelihood that the droplet fully penetrates the vapor layer until the contact with the solid wall. As a result, according to the incidence angle the Leidenfrost temperature is lower than that estimated based on the thermodynamics boundary conditions assuming the perpendicular impact. In other words, a thinner height of the vapor layer (i.e., lower surface temperatures (**Figure 1-21**)) is sufficient to prevent the contact with the wall of a droplet which has a diagonal trajectory with respect to the wall, thus, a weaker kinetic penetration contribution.

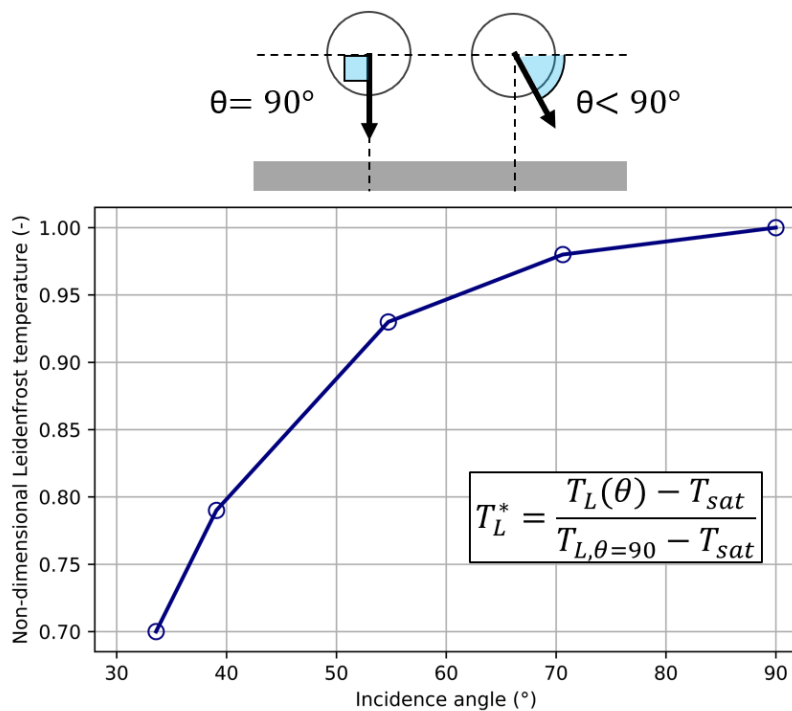


Figure 1-21: Sketch of perpendicular impact angle and diagonal impact angle (top) and behaviour of the non-dimensional Leidenfrost temperature (T_L^*) against the incidence angle.

1.4 Aims and methods

As reviewed in **1.3.3**, the fuel spray-wall impingement is a phenomenon that changes the liquid fuel phase-change dynamics significantly with respect to that typical of free-spray (no droplet-wall impact) conditions. The two main drawbacks of the fuel spray-wall impingement are the following:

- As described in **1.3.3** the fuel liquid wall film is created at the occurrence of deposition and splash regimes, then the vaporization of the liquid adhered as wall film is slowed down with respect to that of the droplets because of different factors: i) the exchange surface of the liquid film is exposed to the solid wall on the one side, which accounts for conductive heat transfer, and to the gas flow on the other side, which accounts for low intensity convective heat transfer due to quasi-zero velocity of the flow near the wall induced by the no-slip conditions. Instead, the surface of the droplets is fully exposed to the airstream, resulting in high intensity convective exchange, which promotes a larger evaporation rate with respect to low-velocity convection and heat conduction; ii) the liquid mass that forms the wall film is larger than that of the single droplet due to the liquid accumulation caused by multiple hits. The delayed evaporation of the fuel under the form of liquid wall film leads to the occurrence of pool flame at the flame arrival. If the latter it is clearly a soot source, the late fuel evaporation is also responsible for the generation of local pockets of rich mixture ($\lambda < 0.5$) which will burn according to a diffusive combustion with soot formation once the flame arrival has raised up the temperature above 1600 K. Therefore, the fuel spray-wall impingement in DI operations is responsible for the engine tailpipe soot emissions, indeed as shown in **Table 1-1** since EU5 the tailpipe soot emissions from gasoline-powered vehicles have been regulated due to the entry in the market of GDI engines. Furthermore, it must be considered that as the fuel spray-wall impingement may change the mixture formation significantly, the assessment of the mixture stratification in GDI engines operated with LTC modes requires the analysis of the droplet impact regimes.
- The fuel spray-wall impingement against the cylinder liner wall leads to the interaction between the liquid fuel and the lubricant oil layer. In the case of deposition and splash impact regimes, patches of liquid fuel remain upon the oil layer resulting in two relevant phenomena: i) the local thickening of the liquid film at the cylinder wall, which then will be larger than the piston-to-wall clearance; ii) the oil-fuel dilution driven by the mutual diffusion of the two liquids with formation of an oil-fuel mixture. At the piston arrival during compression stroke, the thicker part of the non-evaporated oil-fuel film is scraped by the piston top ring into the piston top land crevice [42]. Then, the liquid accumulated into the top land crevice may be scattered into the combustion chamber under the form of flying liquid droplets due to the piston inertia at the end of compression stroke [43]. It is underlined that oil droplets may be carried from the top land crevice to the combustion chamber by the gas upward flow during the blowdown phase [44]. At low engine load, since the lubricant oil is mainly composed of hydrocarbons, those droplets may burn according to diffusive flames contributing to the increase of the PM and PN emissions significantly [45], [46]. Furthermore, there is a general agreement among research and industry engineers that the presence of foreign particles comprising oils into the combustion chamber may lead to pre-ignition events at high loads. In fact, since the lubricant oil is characterized by a higher chemical reactivity, thus, lower characteristic ignition delay time, than that of the fuel [47], those foreign liquid particles may self-ignite before the spark timing leading to the formation of hot spots which can trigger super knock and mega knock events at high load and low speed known as Low Speed Pre-ignition (LSPI) [48]–[51]. Those phenomena are called so since their likelihood is strongly

increased by high gas temperatures (high load) and longer evaporation time available for the oil evaporation before ignition (low speed). As a consequence, severe engine damages such as the piston head crack and the increased spark plug wear are concerned, affecting the engine lifetime and reliability.

For many years now, the use of three-dimensional Computational Fluid Dynamics (CFD) simulations to support the engine development step has been an attractive solution to assess new scenarios, develop new strategies and configurations, address experiments in order to avoid the waste of the high time and cost required for prototyping and bench testing. CFD codes are powerful tools able to perform multi-dimensional simulations of real phenomena by solving the fluid-dynamics equations numerically in a bounded spatial domain discretized for the calculation by using finite volumes. The system can be integrated with different models accounting for the solution of complex phenomena e.g., multi-fluid, multi-phase, reactive flows. Due to the ever more stringent emissions regulations posed by legislation, the improvement of engines is becoming an ever-challenging multi-objective optimization problem, thus, increasing level of accuracy and analysis of micro-scale phenomena are required to simulation engineers. In particular, advances on the simulation of the physico-chemical behavior of real fuels and of the mixture formation (spray formation and evaporation, spray-wall impingement) is becoming central for both industry and academia in the perspective of implementing new fuel blends and engine concepts which relies on DI. In this research project, three-dimensional CFD spray simulations inside vessel domain have been conducted in order to focus the analysis purely on spray models settings and reliability. The setting and run of the CFD simulations have been performed in the commercial CFD code *STAR-CD* v4.28. However, it must be considered that the accomplishment of both high details modeling and fast-response CFD simulations is hard. In fact, due to the fine mesh and time discretization that is necessary in order to reproduce low scale phenomena such as the spray breakup close to the injector tip and the flame kernel growth close to the spark plug electrodes gap, together with the solution of several equations for multiphase flow and different fluids in each cell, typical engine cycle simulation times of two days are usually reached on standard market technology computers. Thus, aiding CFD codes with online and offline tools to reduce the computing power required for a number of sub-tasks is strongly recommended.

Due to the recent advances in computational resources, Artificial Neural Networks (ANN) and machine learning techniques have shown their potential to approach several issues of engineering interest, including the accomplishment of expensive complex optimization tasks and the estimation of fluid properties such as thermal diffusivity [52], void fraction [53], liquid hold-up [54], laminar flame speed [55], mixtures Liquid-Liquid Equilibrium (LLE) [56] and Vapour-Liquid Equilibrium (VLE) [57], diffusion coefficient [58]. A basic feed-forward ANN applied to a regression task is a multi-layer network of simple elements, called neurons, which receive the so-called input features on one end of the network, and provide a predicted value on the other end without any recurrence or matrix manipulation step [59]. Neurons are organized in layers (of any width) connected with each other from the input layer (of the same size as the number of input features), to the output layer. ANNs for deep learning applications are formed by more than three layers. While the presence of input and output layers is mandatory, the number of layers in between depends on the regression task. Those inside layers are called 'hidden layers', they can be seen as the 'active units' of the ANN since they are charged to perform computations for representing data behavior. Input/output layers can be seen as 'passive units', since they are simply charged to take information from the outside world/from the hidden layers unit, and to deploy them to the hidden layers/to the outside world, respectively. For the sake of illustration, the network topology described

before can be seen in **Figure 1-22**. The information is transferred from one layer to the next one via connections among the neurons of variable weights (W), representing the impact of the information conveyed by the connection for the receiving neurons. The values of weights can be optimized during the training step via machine learning algorithms. It must be noticed that the original output elaborated from neurons is linear by definition as it is the weighted sum of the series of input (I) provided to the neuron, that is then shifted by an offset called bias (b). As a matter of fact, neither the linear combination of series of input, nor the scalar addition are suitable for the capture of a non-linear behavior, which is however the most common data pattern in engineering problems. The ability of neural networks to generate predictive models for complex highly non-linear data patterns relies on the use of activation functions, which are functions placed behind neurons that are responsible of the conversion of the natural linear output of neurons into non-linear output information to provide the next layer. For the sake of clarity, the scheme of the information elaboration process by neurons is shown in **Figure 1-23**.

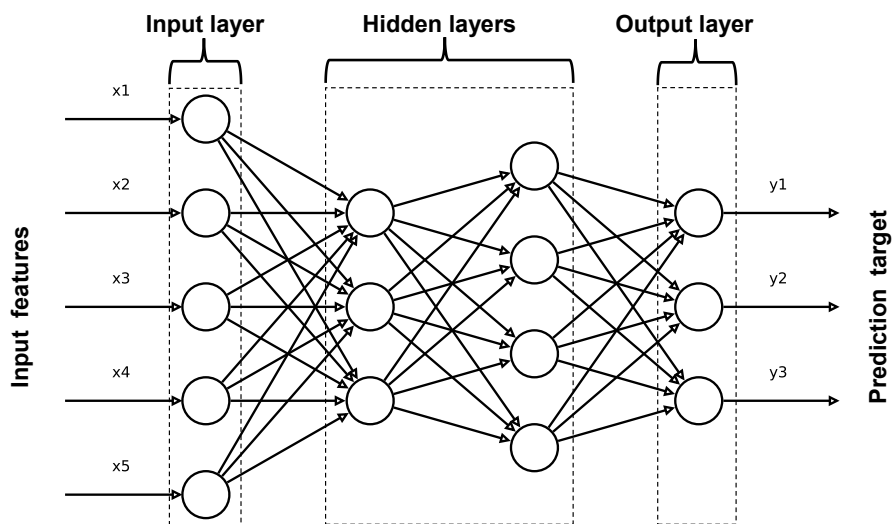


Figure 1-22: Schematic view of a sample neural network with two hidden layers and multiple outputs.

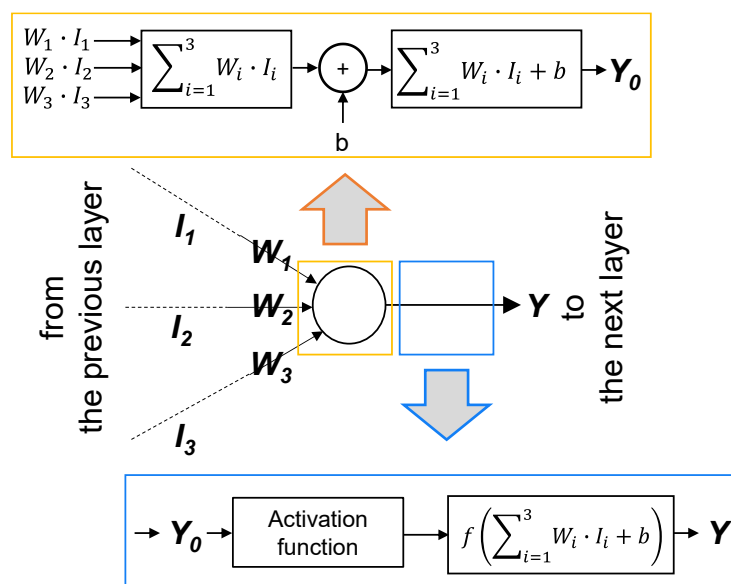


Figure 1-23: Schematic view of the input elaboration performed in a sample layer of the neural network.

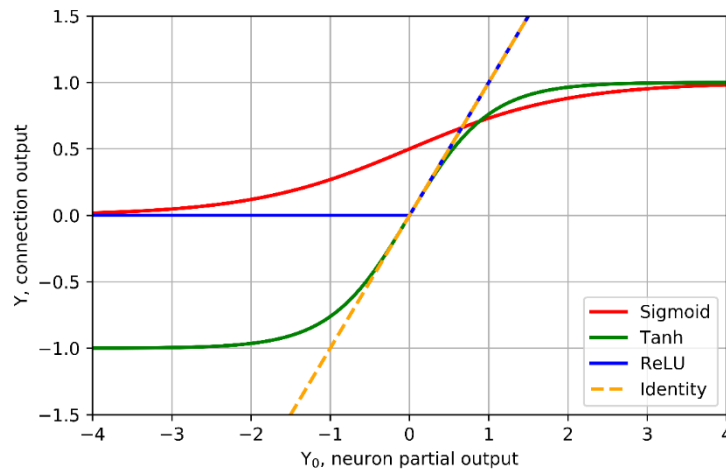


Figure 1-24: Most common activation functions for neural network applications.

Examples of activation functions used in neural network practice are resumed in **Figure 1-24**, namely sigmoid, hyperbolic tangent, ReLU (Rectified Linear Unit), identity. The choice of the proper activation function is not known a-priori since it strongly depends on the specific problem, however, base best-practice are available. For what has been said before on neurons' natural output, it is clear that the presence of identity activation functions in the hidden layers does not provide the ability to tackle non-linear data, instead, identity functions can be applied to the output layer in the case no re-normalization is needed for unbounded output. Hyperbolic tangent (Tanh) is a commonly used sigmoid-shaped function, which relies on a symmetric behavior with output range $-1:1$ against the simple sigmoid, which is not symmetric with respect to input values and returns output in the range $0:1$. However it is known that both those functions, and sigmoid-like in general, suffer from the vanishing gradients issue, which is cause of the weights update convergence slowing down if input information approach high values at which sigmoid-like functions go flat. In fact, in those ranges, the computed gradients that are needed to perform the weights update according to the back-propagation algorithm approach zero. A popular alternative that is not affected by vanishing gradients is ReLU, which sets information to zero if the original input is ≤ 0 and passes it without any modification if the original input is > 0 . The activation functions, together with other additional sets for improving the reliability of the predictions, are called 'hyperparameters', which are the target of the user configuration as the topology of the network (number of layers and neurons per layer). In this research project, the proposed methodologies that involve machine learning and ANN have been implemented in *Python* environment, which was chosen because of different attractive features: i) programs for running *Python* codes are free, allowing to avoid the cost of licenses and the share of programs and advances without requirements of any software limitation; ii) taking the advantage of an extensive pool of open libraries comprising advanced tools for accomplishing several complex tasks i.e., machine learning and neural networks optimizations; iii) high quality and nice graphical output; iv) the wide, active and skilled *Python* community that has been formed thanks to the strong impact of big data on the nowadays society.

The present research project was particularly focused on the improvement of accuracy and predictivity of CFD engine simulations with regards to the mixture formation phase, which is expected to be central for the next fuel and engine technology. The main contribution of this research was the development from scratch of single-task numerical methodologies, and their implementation and testing with as straight as possible scientific approach. The final

aim is to provide the scientific community with reliable tools and settings validated against fundamental experimental analysis from the open literature in order to ensure their robustness as stand-alone tools before being integrated with engine simulations. The contribution of this PhD thesis to the simulation of the liquid fuel spray evaporative behavior and wall impingement in GDI engines can be divided into three different tasks:

- T-1) definition of a best-practice routine for predicting the after-impact liquid fuel film formation in three-dimensional CFD simulations. The accomplishment of the task required the comparison, the combination and the tuning of different droplet-wall impingement models and approaches to estimate the Leidenfrost temperature.
- T-2) development of a one-dimensional oil-fuel dilution numerical model able to predict the level of oil pollution at the cylinder wall and the characteristics of the oil-fuel mixture scraped by the piston. The model was aided by an in-house developed neural network methodology for predicting the oil-fuel diffusion coefficient, whose estimation was greatly improved with respect to the methods adopted in the current literature.
- T-3) design of an algorithm for the definition of fuel surrogate mixtures able to mimic the evaporative behaviour and the liquid phase-change features of real commercial fuel blends. The algorithm was integrated with an in-house developed model of the fuel distillation rig, which was necessary in order to predict the equilibrium properties of the fuel mixture during evaporation. This algorithm was proposed with the aim of providing a reliable and accurate methodology for the identification of the fuel composition to put into CFD simulations to aid the assessment of tailored mixture stratification strategies in non-conventional engine combustions.

The following sections are divided according to the afore-mentioned three main tasks, which are further resumed in **Figure 1-25**. Each section reports the state of the art and the original contribution of the present research project, the numerical methodology, the description of the reference validation case, and the results.

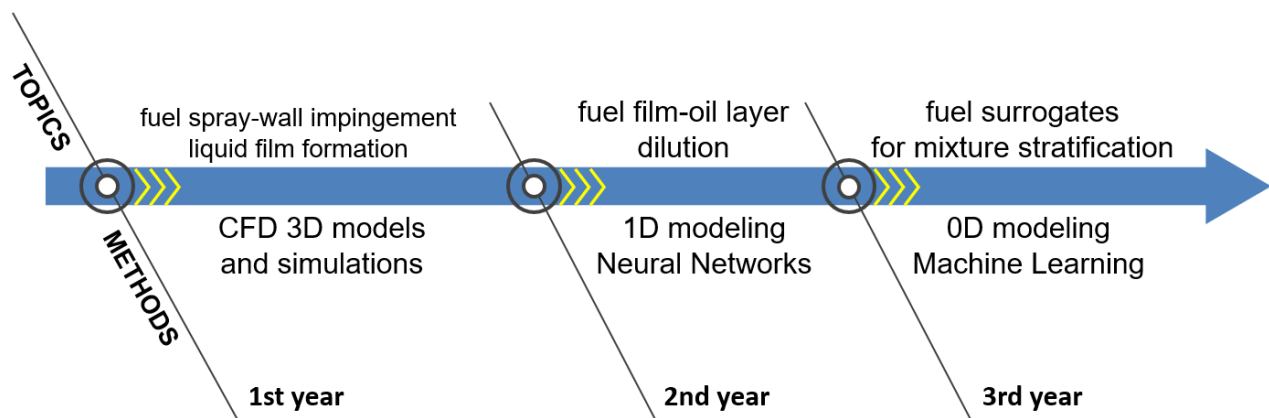


Figure 1-25: Timeline of the PhD research project.

2 Fuel spray-wall impingement simulation

2.1 State of the art and original contribution

The high-pressure DI technology application to gasoline-powered engines has almost replaced the PFI technology in order to fulfil both fuel economy and emission targets. The design of GDI combustion systems for automotive application is a multiple object optimization problem because of the need to match so many different aspects such as chamber geometry, in-cylinder charge motion, injector characteristics, spray pattern, injection timing. Injector nozzle shape and drilling, spray pattern optimization, injection strategy and pressure (currently injection systems operating up to 350 bar are available on market for automotive application), are defined to promote very fast fuel evaporation and minimization of liquid spray interaction with walls, without penalties in air-fuel homogeneous distribution [60]. It must be underlined that the latest injector technology would reduce the wall impingement by improving the nozzle shape, increasing the injection pressure and promoting closed loop injector control, in order to make possible multi-injection strategy under injector ballistic operation. Nevertheless, one of the main drawbacks of the DI technology is still the liquid spray wall impingement in some engine operating points with emphasis on cat-heating, engine cold state at the start of the emissions test cycle and low load conditions, characterized by low air density (longer spray penetration). As mentioned in 1 the injection of gasoline fuel directly into the combustion chamber is responsible for the formation of inhomogeneous mixture spots (rich pockets) and likely for the presence of the fuel liquid phase at the spark time under the form of liquid film. Since it has been shown that those DI-induced issues are responsible for the emission of fine soot at the engine tailpipe, modern gasoline-powered vehicles equipped with the DI system have been subjected to the ever-stringent limitation of PM and PN. Improving the GDI technology is mandatory to comply with the most recent emissions regulation, thus, a deep understanding of the fuel spray phases, and mixture formation is unavoidable. Since detailed optical engine experimental investigations are not affordable in every-day engine design and they are limited to fundamental investigation because of complexity, cost and time requirements, three-dimensional CFD approach can be effective in the investigation of wall impingement and air-fuel mixing.

Since the early 2000s industrial and academia scientists have conducted a number of works aimed at investigating the fuel spray wall impingement at relevant GDI engine conditions in depth by employing both experimental campaigns and numerical three-dimensional CFD simulations. In 2000 Lindgren and Denbratt [61] performed a review of the most recognized droplet-wall impingement models such as the Bai and Gosman [62], [63], the Gavaises [64], the Mundo, Sommerfeld and Tropea [65]–[67], the Senda [68]–[72], the Stanton Rutland [73], the Xu [74]. The analysis had revealed that large differences were present among the models under review mainly with regards to modeling of splashing interaction modes, emulation of the effect of key wall surface conditions e.g., high temperature and wetting. Furthermore, it was posed emphasis on the fact that the models were developed based on experiments conducted on individual impacting droplets of water and diesel fuels under laboratory conditions. As a consequence, uncertainties were highlighted in providing expectations on the predicting performance of those models if considering in-cylinder-like environmental conditions and gasoline fuels. In this respect, in 2010 Moreira et al. [75]

collected data and knowledge from wall impingement works under engine conditions in the open literature, then they presented their critical analysis on the strength of the bond between individual droplet experiments and real spray impingement modeling. The Authors highlighted the fundamental role played by individual droplet experiments in the interpretation and capture the most meaningful features that affect the wall impingement phenomenon. However, it was also pointed out that for given fuel and impact conditions, multiple interacting droplets behave a lot differently than single droplets, especially when hitting a liquid film.

Denbratt and Lindgren conducted an experimental campaign aimed at testing the wall impingement of i-octane injected at 100 bar by a commercial multi-hole GDI device against a flat wall inside a vessel [35]. The experiments included the test of different environmental pressure-temperature combinations (2 bar-177°C; 5 bar-227°C; 15 bar-377°C), temperature of the impact plate (108; 162; 216°C), jet incidence angle (30; 60° with respect to the normal-to-wall direction), surface roughness (1.5; 13.42; 15.42 μm). An optical measure line was implemented in order to record size and velocity data of the after-impingement spray cloud above the wall surface. It was observed that at increasing pressure-temperature gas conditions the difference between incident and scattered diameter distribution becomes negligible likely due to the main occurrence of rebound. At increasing wall temperature, the distribution of the secondary spray's size was shifted towards finer diameter, proving the dominance of splash-like regimes. In [76] the same Authors performed the CFD simulation of the experiments from their previous work in order to compare the wall impingement models of Bai and Gosman [62], [63], Stanton Rutland [73], Mundo Sommerfeld and Tropea [65]–[67], Han [77], Senda [65]–[67], and Kuhnke [78]. A nice reproduction of the scatter angle evolution was reported for any model whilst only the Kuhnke model showed the ability to capture the secondary spray size evolution. Montanaro et al. [79], [80] applied the Schlieren optical technique to record shots of the secondary spray formed after the wall-impingement of the test fuel which was injected by a multi-hole commercial gasoline injector. The images were postprocessed by means of an in-house contouring algorithm which allowed to encode the main features of the after-impact spray into two synthetic quantities, namely the radial and the axial after-impact cloud penetration for both the liquid and the vapor phase. The Authors implemented a wide test matrix including variation of injection pressure (30; 55; 100; 120; 150; 200 bar), wall and gas temperature (25; 100; 200; 300°C), fuel type (i-octane, commercial gasoline) and recorded the morphology, radial and axial penetration of the scattered spray at each test point. The experimental results were used as a benchmark to perform CFD simulations [81], [82] adopting the Bai and Gosman and the Kuhnke models. The simulated spray morphology and vapor penetration at room conditions (1 bar, 30°C) achieved with the Bai and Gosman model at the lower injection pressures (30-100 bar) were in good shape with the experiments. The numerical simulations at the higher temperatures (200; 300°C) and injection pressures (100-200 bar) performed by using the Kuhnke model showed accuracy losses in capturing the temporal behavior of the scatter penetration at 300°C likely due to a poor representation of the film boiling regime. In [83] Catapano et al. set an infrared thermography system to observe the wall impingement-induced cooling of the surface and the consequent increased likelihood of liquid film formation. Furthermore, imaging acquisition and analysis were conducted thanks to the optical accessible vessel. The experiments were conducted in a quiescent vessel where a commercial multi-hole injector fueled with commercial gasoline was mounted. It is noteworthy that the Authors used a real engine piston monitored with different thermocouples as impact wall. Different piston surface temperature (30; 134; 180; 230°C) and injection pressure (30; 50; 100; 120 bar) were tested. The experiments were supported by numerical CFD simulations reproducing the shape of the piston crown and bowl: the

Kuhnke [78] wall impingement model was adopted. The simulated wall temperature evolution is in nice agreement with the experimental measure from the infrared camera at very hot conditions (230°C), especially in the earlier transient cooldown corresponding to the onset of the wall impingement whilst a strong enhancement of the cooldown was shown in the transition boiling regime (180°C) with respect to the experimental data. A general underestimation of the final surface temperature After EOI (AEOI) was observed. Köpple et al. [84] as well applied the infrared thermography to investigate the wall impingement of pure n-heptane and a 3-component mixture (n-hexane, i-octane, n-decane) injected at 150 bar by a multi-hole injector against a flat wall heated at different temperatures (80; 160; 200°C). The experimental temperature time profiles were compared with numerical results achieved with CFD simulations. As in most of the cited works, the Kuhnke wall impingement model was chosen. The results presented by Köpple et al. for pure n-heptane are in line with those reported by Catapano [83], i.e., the Kuhnke modeling approach suffers from a performance degradation in the film boiling regime (test at 160°C) leading to an overall underestimation of the surface temperature drop that got larger AEOI. Furthermore, the limits of the simulation in capturing the temperature profile at any surface temperature in the case of multi-component wall impingement was highlighted. This was likely due to the fact that the capture of the contribution of each single component of a mixture in phase-change phenomena with the sub-models of the wall impingement approach is known to be very challenging.

As it is clear from the presented state of the art, the fuel wall impingement issue has been mainly investigated by focusing on the measure and numerical reproduction of some descriptive features of the rebounded and splashed droplets. Despite the fact that analysis can be helpful in order to identify a reliable numerical methodology that can be then used to predict the in-cylinder size and shape of fuel vapor zones formed by the full evaporation of the scattered droplets, they cannot provide sufficient data on the liquid film, which is the main concern of the wall-impingement. In the current literature, very a few researchers have pushed efforts in providing comprehensive analysis of the after-impingement liquid film features. Maligne et al. [85] were among the first researchers to perform the characterization of the features (thickness, shape) of the liquid film formed after the wall impingement of gasoline-like fuel via optical techniques. The Authors implemented two different optical measure systems i.e., the Refractive Index Matching (RIM) and the Laser Induced Fluorescence (LIF), which return the so-called liquid film footprints at different times. Three different injector types (piezo hollow-cone, swirl hollow-cone, multi-hole full-cone) were tested at 'extreme' environmental conditions i.e., gas pressure between 8-12 bar, gas temperature between 180-400°C. The extreme temperature conditions were obtained by triggering a pre-combustion into the vessel chamber and then cleaning it out until the oxygen fraction achieved the 21%. In [86], [87] Luo et al. conducted RIM wall-impingement in-vessel analyses of toluene injected from a single hole injector against quartz glass with a mean surface roughness comparable to that of the engine piston crown. Furthermore, a Mie scattering optical system was set. The Authors recorded the evolution of liquid film thickness (RIM) and scattered droplets (Mie) over time at different injection pressure (100; 200 bar) - back pressure (1; 5 bar) combinations at room temperature. Synthetic data such as liquid film mass and area were determined thanks to the post-processing of the RIM images. One of the most recent and comprehensive work on the after-impingement liquid film characterization is the series of experimental analyses published by Schulz et al. [88]–[92]. Schulz et al. implemented and calibrated a LIF apparatus to record the footprints generated by the fuel wall impingement against a quartz plate inside a vessel. Information on the liquid film shape, mass, thickness, area, and evaporation time were provided. An extensive test matrix was implemented including different sets of injection pressure (50; 150; 300 bar),

back pressure (0.4; 0.6; 1; 3; 6 bar), gas and wall temperature (80; 140; 180°C); injector-wall distance (25; 35; 50 mm); injected fuel (i-octane, gasoline, 3-component mixture of n-hexane, i-octane, n-decane). To the best knowledge of the present Author, the validation of CFD wall-impingement methodologies against liquid film experimental data at engine relevant conditions is extremely rare. One of the most recent publications on this topic is the work by O'Grover et al. [93] who performed a comparative analysis of different impingement models (Bai and Gosman [62], [63], Gavaises [64], Cossali [94], Stanton and Rutland [73]) with respect to RIM and Mie experimental images. However, it must be underlined that the reference experimental conditions were not consistent with nowadays engine applications. In fact, the fuel (i-octane) was injected with a hollow-cone swirl injector at 100 bar inside a vessel at room conditions (1 bar, 20°C). Furthermore, in spite of the fact that the adopted numerical code allows the user to set the so-called Automatic Mesh Refinement, which is able to refine the computational mesh in the spray zones, the results achieved with any model suffer from a strong over-estimation of the liquid film mass.

Considering the complete analysis of the state of the art, as a matter of fact the current literature lacks proof of predictivity and reliability of CFD simulations in reproducing the fuel liquid film features after the wall impingement. As far as the support of CFD simulations to assess new fuels and mixing solutions is concerned, a deep understanding of the wall impingement simulations to fill the gap between numerical and experimental observations is compulsory in order to achieve predictive results of the mixture formation, combustion evolution and soot tendency of a given engine configuration. The first task of this research project deals with the definition of numerical CFD methodology for the fuel spray-wall impingement simulation based on liquid film data at nowadays engine conditions. The main principal work by Schulz et al. [90] was taken as a benchmark in order to perform an extensive validation of the numerical setup. Two promising different wall impingement models were tested and compared by means of a comprehensive analysis of the effect of the model's workflow on the match with experiments. Best practice and setup guidelines were also provided. A further original contribution of the first task was the application of a practical approach aimed at identifying the most promising wall impingement models based on the connection of their features with key real engine parameters.

2.2 Methodology

2.2.1 Reference validation benchmark

One of the most recent advances on the liquid fuel spray-wall impingement is the extensive experimental campaign conducted by Schulz et al. [90]. In [90] the Authors put their efforts in the analysis of the after-impingement liquid film shape and thickness by means of the LIF optical spectroscopic technique applied in a quiescent vessel under a wide range of TGDI-like environmental conditions. Since this section is aimed at providing the reader with the essential experimental information needed to setup the three-dimensional CFD simulation, only the most meaningful features of the injection, the environment and the image acquisition are briefly described. The punctual description of the techniques adopted in [90] to control the environmental conditions and the choices that were made regarding the tuning of the optical analysis is avoided as it falls outside the main task approached in this chapter. The original Design Of Experiments (DOE) from [90] included: i) the test of three different injection pressures i.e., 50, 150, 300 bar; ii) three different injector tip-impact wall distances in order to reproduce the injector-piston crown distance at different injection timing strategies, i.e. early injection (25 mm), average injection (35 mm), and late injection (50 mm), in an average-sized engine cylinder (450 cm³); iii) five different values of the environmental pressure aimed at simulating homogeneous naturally aspirated low load

engine operating conditions, which rely on the fuel injection during the intake stroke (typically vacuum conditions, 0.4, 0.6, or ambient conditions, 1 bar) as well as turbocharged high load operations (3, 6 bar); iv) three different levels of wall heating in order to simulate both warm-up (80°C) and full load (140, 180°C) conditions. The Authors used a GDI commercial injector with 6 holes uniformly distributed to produce a symmetric full-cones spray, and, for given injection pressure, they adjusted the injection duration in order to inject a fixed fuel mass of i-octane mixed with 3-pentanone (12%vol), which was added as tracer for the LIF measurements. The experimental reference injector data [90] that were implemented in the CFD setting are listed in **Table 2-1**. From previous characterization works, the original Authors have reported that the liquid film mass produced by a single jet differs from the average film mass by 3% of standard deviation. Therefore, only the wall-impingement of one of the six jets was recorded via LIF, thus, the impact wall was equipped with a single quartz window (50 x 50 mm) corresponding to the expected direction of the recorded jet. The temperature of the impact wall was controlled by means of the air temperature, thus, the tested wall temperature is the same as that of the vessel environment. The two main results taken from this validation benchmark [90] were the profile of the liquid film mass against each controlling variable (injection pressure, gas pressure, wall temperature, injector-wall distance) and the liquid film footprints acquired via LIF that provide information on the liquid film thickness, area and shape.

Table 2-1: Data of the reference injector [90].

Injector	Multi-hole Bosch HDEV5
Mechanism	Solenoid-driven
Number of holes	6
Spray type	Symmetric full-cone
Spray including angle	60°
Jet cone angle	16°
Nozzle min. diameter	210 μm
Nozzle length-diameter ratio	1
HFR @100 bar (n-heptane)	20 cm ³ /s
Injection temperature	30°C
Injection duration (at 50,150,300 bar)	2.6,1.5,1.06 ms
Injected mass	21.7 mg (3.62 mg per nozzle)
Fuel (+ tracer)	i-Octane (+ 3-pentanone)

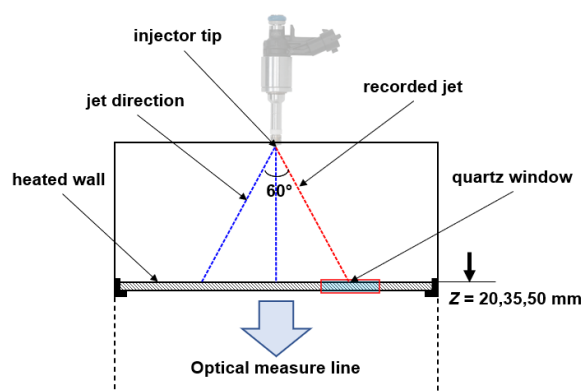


Figure 2-1: Sketch of the wall-impingement experimental vessel domain.

The reported liquid film footprints were observed on 30 x 20 mm ($X \times Y$) grids, and they were acquired 5 ms ASOI. The image acquisition delay was implemented in order to allow the evaporation of the droplets stuck upon the film that would deny a fair comparison between the footprints of points with large droplet evaporation time scale differences (e.g., high against low injection pressure, and high against low wall temperature). Furthermore, it was considered that the presence of residual stuck droplets may affect the measure of the film thickness. For the sake of clarity, a schematic view of the target experimental domain is shown in **Figure 2-1**.

2.2.2 General setting

In order to save computation time a subset of the experimental gaseous domain was considered as computation domain instead of the whole vessel (**Figure 2-2**). As shown in **Figure 2-2** the computation domain is a squared-section box comprised in the vessel domain, furthermore it has been considered that the box is bounded by wall-type conditions. Whilst the wall boundary condition is representative of the real domain at the top and plate faces, vertical boundaries should be inlet-outlet conditions allowing for mass exchange. However, wall boundary conditions have been adopted since the setting of a large number of inlet-outlet conditions is known to induce numerical instability. In order to make negligible the wall boundary effect on the solution, a preliminary spray simulation test has been conducted in order to optimize the $X \times Y$ size of the box according to the trade-off between computation time and the non-interaction conditions between impinging spray-walls and film footprints-walls. As a result, a 100x100xZ mm has been considered ($Z = 25,35,50$ mm).

As mentioned in **1.4**, the simulations have been performed with the commercial software *STAR-CD* v4.28. The computation mesh has been created by using hexahedra of average size of 0.8 mm, which was chosen since it is representative of the typical average cell size used in engine CFD simulations. A three-steps mesh grading has been applied uniformly along the three dimensions. The final mesh shown in **Figure 2-3** is characterized by a refined box around the injector tip (20x20x10 mm) of 0.4 mm cell size which coarsens up to 0.8 mm along $X = \pm 50$ mm, $Y = \pm 50$ mm, Z .

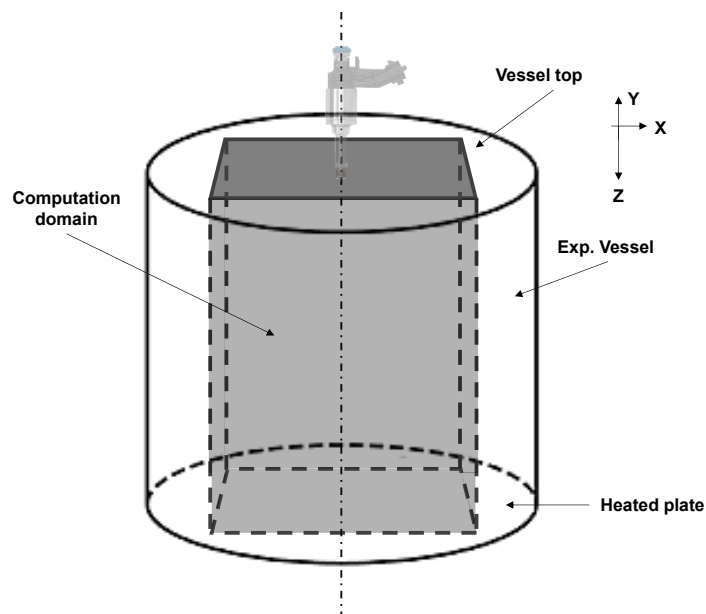


Figure 2-2: Representation of the computation domain as subset of the real experimental vessel.

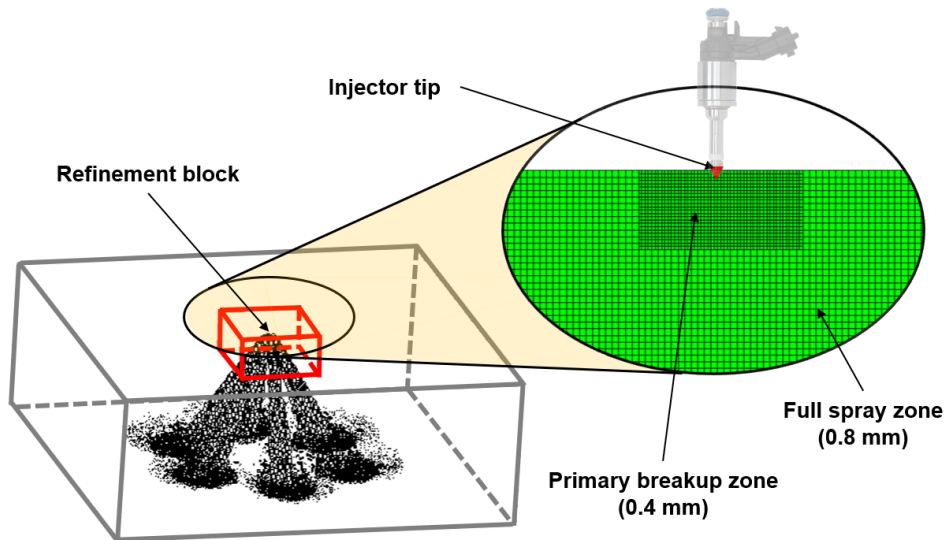


Figure 2-3: Schematic view of the computation domain including the simulated spray with the section detail of the mesh grading applied.

The refinement box around the injector tip has been applied in order to capture with better accuracy the breakup of the initial spray zone which includes the faster droplets. As for the average cell size, the refined cell size was chosen according to the typical mesh refinement adopted in engine simulations and to several Authors who have approached the grid issue for spray simulations following similar criteria [81], [95]–[97]. It must be remembered that super-fine and ultra-fine grids in the injector tip zone should be avoided in order to avoid the likely violation the dispersed liquid hypothesis. The coarsening up to 1.6 mm applied in the outer zone allows to save further computation time without affecting the solution since neither coupled Lagrangian (dispersed droplets) - Eulerian (continuum gaseous phase) multiphase flow, nor low scale phenomena are involved in that zone.

As wall boundary condition, the Dirichlet condition has been adopted by setting a fixed value of the wall temperature at the six bounding faces of the domain. The set value of the boundary condition temperatures as well as those of the initial gas pressure and temperature have been chosen according to the point of the DOE under review. It is remembered that, according to the information provided by the reference experimental works [89], [90], [92], the initial gas temperature is the same as that of the wall boundary condition. Turbulence has been taken into account by means of the RANS (Reynolds Average Navier-Stokes) two-equations eddy-viscosity Realizable k - ε (k , turbulent kinetic energy, and ε , kinetic energy dissipation rate) model which has been coupled with the classical piecewise linear-log wall function to simulate the boundary layer.

According to the characteristic time scales of the multiphase physics i.e., momentum exchange between dispersed (droplets) and continuum (gaseous) phases, a constant time step between 1×10^{-7} and 1×10^{-6} s (depending on the injection pressure) has been set from SOI to EOI. The time-step has been then reduced at 1×10^{-5} from EOI to the end of the simulation (5 ms ASOI according to the first LIF acquisition time) in order to speed-up the simulation once the physical scales are mainly driven by the liquid film shrinking and the exchanges (heat, mass, momentum) between gaseous phase and slow droplets.

The simulation transient run relies on the classical adapted PISO (Pressure-Implicit with Splitting Operators) algorithm for the resolution of the Navier-Stokes equations. Considering the general transport of scalar quantities Eq. (2-1), in which ϕ is a generic scalar e.g., the fuel vapor phase, t is the time, ∇ is the nabla operator accounting for the space derivatives,

ρ is the mean cell density, \bar{U} is the fluid velocity array accounting for the convective transport, Γ is the term accounting for the diffusive transport, S is the source of the scalar ϕ : i) once the PISO algorithm has been selected, the *STAR-CD* software automatically applies a special built-in fully-implicit Euler scheme (backward method) for the discretization of the time derivatives (first term at the left-hand side of Eq. (2-1)) in a manner that ensure that the formal accuracy of the approximation lies between the first and the second order; ii) With regards to the discretization of the space derivatives (second term at the left-hand side of Eq. (2-1)), the *STAR-CD* proprietary scheme called MARS (Monotone Advection and Reconstruction Scheme), which is claimed to be able to handle any mesh structure and skewness without significant accuracy losses. The discretization operated via MARS ensures a second order formal accuracy that is aided by a compression factor comprised between 0 and 1 (set at 0.5 in this methodology) which allows to capture sharp flow discontinuities.

$$\frac{\partial(\rho \phi)}{\partial t} + \nabla \cdot (\rho \bar{U} \phi - \Gamma \nabla \phi) = S_{\phi} \quad (2-1)$$

Finally, for a given time-step each resolved equation is adjusted by means of the so-called under-relaxation factor which applies a correction to the solution computed for the present time-step before moving towards the next. The correction (Eq. (2-2), in which the superscript j indicates the time-step, the superscript $*$ indicates the uncorrected computed solution, f_{UR} the under-relaxation factor, ϕ the generic solution variable) aims at modifying the influence of the solution at the previous time-step based on the solution of the present time-step, realizing the damping of numerical instability-induced oscillations in order to ensure convergence. In the present setup for vessel spray simulations the under-relaxation has been set as reported in **Table 2-2**.

$$\phi^j = f_{UR} \cdot \phi^{j,*} + (1 - f_{UR}) \cdot \phi^{j-1} \quad (2-2)$$

Table 2-2: List of the values of the under-relaxation factor applied to the solution equations in vessel spray simulations.

Equation	Under-relaxation factor
Mass	1.0
Momentum	0.7
Energy	0.95
Turbulence	0.7
Pressure correction	0.5
Lagrangian	0.35

2.2.3 Injection setting

The reference injector produces a six-jet symmetric spray whose pattern is necessary in order to locate the injection points into the computation domain. It is remembered that in coupled Lagrangian-Eulerian RANS CFD simulations the internal nozzle flow is not simulated, instead, it is assumed that the injection point associated to the nozzle hole exit provides dispersed liquid particles whose diameter and velocity distributions are correlated to the in-nozzle phenomena by means of the injector characteristics and the primary breakup model, which will be presented in the following. The pattern has been obtained by placing six injection points uniformly distributed on a circumference of radius 1 mm (**Figure 2-4**).

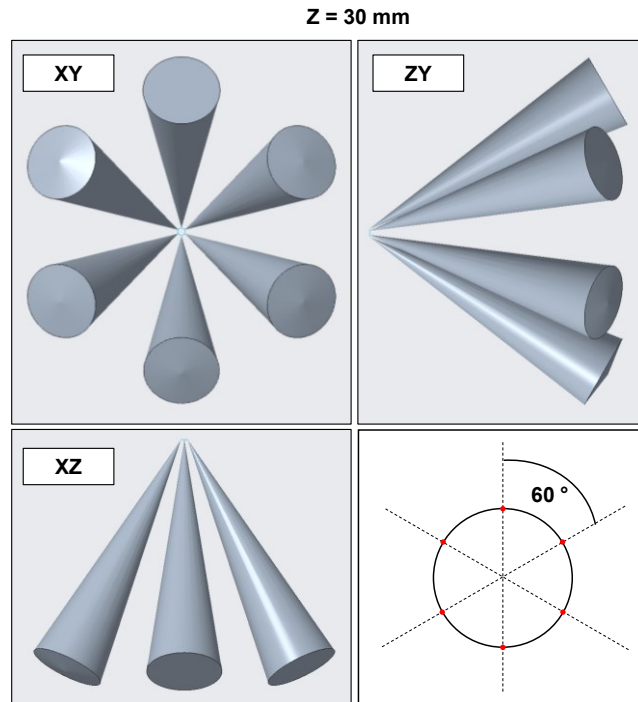


Figure 2-4: Bosch HDEV5 6-hole spray pattern at 30 mm downstream the nozzle tip.

Another key feature of the injector that is necessary to be defined to setup the CFD simulations is the flow rate through the nozzles. Since the experimental injection profile was not available in the reference work, it was determined by using a theoretical approach based on knowing the injected fuel (F), the injection pressure (p_{inj}) – back pressure (p_b) condition, the minimum injector nozzle diameter (d_G), and the Hydraulic Flow Rate (HFR) of the injector at reference test conditions, namely injection of n-heptane under a pressure difference of 100 bar at room temperature conditions for 1 min (steady state flow). The theoretical approach (Eq. (2-3)) relies on the use of the so-called discharge coefficient (C_D), which needs to be determined, to estimate the nozzle steady state mass flow rate (Q_{MAX}) by accounting for the reduction of the maximum theoretical flow rate (Q_{TH}) due to in-nozzle phenomena such as the friction-induced liquid velocity reduction and the reduced cross-section flow caused by vena contracta. As far as the HFR is provided, the ratio between the latter multiplied by the density of n-heptane at room conditions (684 kg/m^3) and the maximum theoretical flow rate calculated at HFR test conditions ($(p_{inj} - p_b) = 100 \text{ bar}$, $\rho_F(T_{inj}) = 684 \text{ kg/m}^3$) for the present nozzle ($d = 210 \mu\text{m}$) provides the value of the discharge coefficient, which is 0.56 for the injector presented in **Table 2-1**. Since the discharge coefficient is a measure of the hydraulic permeability feature of the nozzle, it can be used to calculate the steady state injector flow rate at any condition regardless of the injected fuel and the pressure difference under review. Therefore, the value determined for the discharge coefficient has been used to calculate the mass flow rate of i-octane at 30°C for each injection pressure – back pressure combination that is present in the simulated DOE.

$$Q_{MAX} = C_D \cdot Q_{TH} = C_D \cdot \rho_F(T_{inj}) \cdot \frac{\pi d_G^2}{4} \cdot \sqrt{\frac{2(p_{inj} - p_b)}{\rho_F(T_{inj})}} \quad (2-3)$$

Since it is well known that in GDI injectors the stepwise injection assumption is not realistic, a reasonable injection profile must be assumed. In everyday CFD practice trapezoidal-shaped profiles are typically adopted in order to take into account three main phases: i) the

initial fuel flow rate increase during the transient needle opening (**Figure 1-11**); ii) the achievement of a steady state flow condition (Q_{MAX}); iii) the flow rate drop down during the transient needle closing after the end of the injection signal. In order to produce the trapezoidal-shaped profile model for the present injector, an iterative algorithm has been implemented in *Python* environment. The algorithm is provided with the calculated steady state flow rate, the duration of the injection signal (**Table 2-1**), limiting values of possible time intervals representative of the opening (100-120 μs) and closing (150-200 μs) injection ramps. At each iteration the algorithm tests a couple of opening and closing ramps to create a profile attempt, which is then integrated over the total time by means of the numerical trapezoidal integration rule in order to obtain the injected mass. Thus, the duration of the two ramps is iteratively updated in order to minimize the difference between the computed and the target fuel injected mass provided in the reference experimental work (**Table 2-1**). As a result, time duration values of 110 μs and 150 μs have been achieved for the opening and closing ramps, respectively. Since in the recent years the typical injection pressure in commercial GDI engine application has strongly increased, only points with injection pressure 150 bar and 300 bar have been considered from the experimental DOE for the validation. For the sake of clarity, in **Figure 2-5** is reported the trapezoidal-shaped injection profile of the reference injector for the two tested injection pressure values together with the associated injected mass integral. Those profiles are provided as input to the injector setting file which will be read by the commercial software as a User Defined Function (UDF).

In **Figure 2-5** it is slightly visible that both the injection profiles do not start from a zero-flow rate at the SOI, thus, the final injection profile is quadrilateral. The use of non-zero flow rate at the SOI is a device aimed at preventing a numerical issue in CFD spray simulations under specific conditions. In fact, if a perfect trapezoid profile is adopted, the very first injected dispersed liquid would be characterized by very low velocity magnitude. Therefore, in the case of spray simulation in a quiescent vessel (no strong interaction between the spray and intake air flow) and no inter-droplet collision modeling, those very slow injected particles likely remain around the injection point as flying droplets leading to the formation of a persistent fuel spray cloud (**Figure 2-6**).

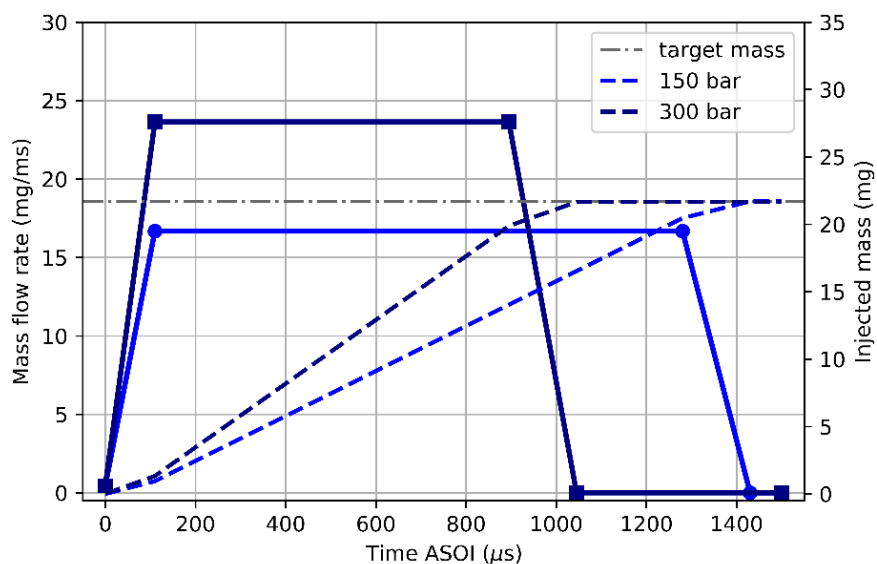


Figure 2-5: Assumed injection profile (solid line) of the Bosch HDEV5 injector for two test injection pressure and corresponding injected mass (dashed line). Experimental target injected mass in dashed-dotted gray line.

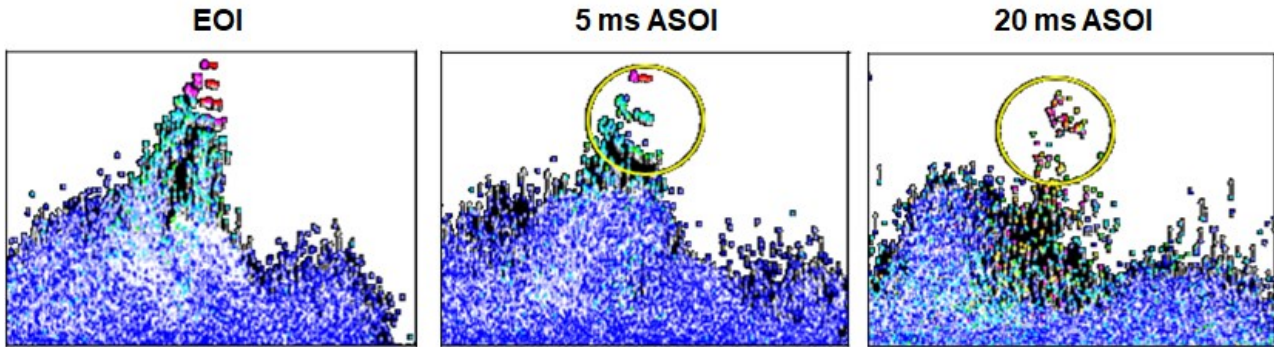


Figure 2-6: Example of tip spray cloud in CFD simulations for a generic spray (100 bar vs 1 bar).

Since there is no evidence of this type of clouds in experiments except for eventual injector leakage from nozzle which is however typically not consistent with the size of the simulation spray cloud, a practical solution must be adopted. Therefore, in the present research project it has been decided to set the injector mass flow rate at the SOI at a non-zero value corresponding to an effective velocity at the nozzle exit of 5 m/s, which has been proven to be a nice compromise value between the production of dispersed liquid that is able to penetrate air independently and the use of a profile that is still realistic at the SOI.

As a simulation fuel, pure i-octane (C_8H_{18}) has been considered and its properties have been runtime update according to the *STAR-CD* built-in NIST database.

2.2.4 Free spray setting

Before moving on the main topic of this task i.e., the liquid fuel spray-wall impingement, it is necessary to ensure that size, velocity and properties of the impinging droplets are in line with the experiments since those characteristics will be responsible for the definition of the impingement regime (1.3.3). Therefore, it was necessary to perform the so-called free spray validation, namely the impact plate is removed so that the vessel provides a free path along the jet direction sufficient for the full development of the spray plume. In free-spray conditions, the reference experimental bench was equipped with a PDPA system able to return the measure of two fundamental indexes for the characterization and the numerical validation of sprays i.e., the Average Mean Diameter (AMD) also called d_{10} (Eq. (2-4)) and the Sauter Mean Diameter (SMD) also called d_{32} (Eq. (2-5)). Whilst d_{10} is simply a weighted average of the droplet diameter on the number of droplets recorded (N) by the system at a given measure station, d_{32} is intended as the ratio between the liquid fuel spray volume and its surface available to exchange with the surrounding air, thus, d_{32} is representative of the evaporative tendency of the spray.

$$AMD = d_{10} = \frac{\sum_i (N_i \cdot d_i)}{\sum_i N_i} \quad (2-4)$$

$$SMD = d_{32} = \frac{\sum_i (N_i \cdot d_i^3)}{\sum_i (N_i \cdot d_i^2)} \quad (2-5)$$

As far as the CFD simulation of the free spray is concerned in order to ensure reliable wall impingement results, the capture of the main features of the free spray such as d_{10} , d_{32} , spray shape is necessary. Since the free spray development is driven by the breakup phase, the tuning and validation of the primary and secondary breakup models must be performed. Despite the fact that several models for the breakup are available, the choice of the breakup models was driven by the experience on the topic gained by the group of researchers which

supported this research project, whom provided their validated breakup model proposal which is also available in literature. As long as the modeling of the spray breakup phase does not fall within the primary objective of this first task, only the used breakup model will be briefly presented and then validated in 2.3 whilst an extensive listing and comparative description of different breakup models is avoided.

Primary breakup modeling

In order to simulate the spray primary breakup phase, a slight modified version of the model by Bianchi et al. [98] has been encoded in a UDF incorporated in *STAR-CD*. The model is based on the Reitz assumption [99] and on the equations proposed by Huh and Gosman [100]. Firstly, the model needs to guess the characteristic distribution and diameter with which the liquid core leaves the nozzle hole. To this aim, according to Reitz it is assumed that the liquid is injected by the injection point under the form of train of blobs (**Figure 2-7**) i.e., parcels initialized in a mono-disperse mode by assigning defined diameter and velocity at the nozzle throat section. In the present model diameter and velocity of the introduced blobs are set to the effective minimum internal nozzle diameter (d_{eff}) and the effective velocity, respectively. Those values can be determined by means of the discharge coefficient split. As mentioned in 2.2.3 the discharge coefficient accounts for the reduction of the nozzle flow rate due to the vena contracta-induced shear layer and the friction losses, thus, the discharge coefficient can be seen as the product between those two contributions, namely the contraction coefficient (C_c) and the velocity reduction coefficient (C_v).

As a result, considering that $C_D = C_c \cdot C_v$, (2-3) can be rewritten as in Eq. (2-6), in which U_{eff} and A_{eff} are the effective velocity and cross section, respectively. Therefore, the velocity and diameter values to be assigned to the monodispersed blobs are calculated as in Eq. (2-7), (2-8). The split of the discharge coefficient has been determined based on previous works conducted by the supporting research group, which performed in-nozzle flow multiphase 3-fluid (liquid fuel, fuel vapor, air) three-dimensional CFD simulations in the commercial software *STAR-CCM+*. The results highlighted that the values of the velocity reduction coefficient for modern GDI injectors lie in the range 0.85-0.95. According to these guidelines, dividing the calculated discharge coefficient (0.56) by the assumed value of the velocity reduction coefficient (0.9), a contraction coefficient of 0.62 is obtained, resulting in a blob diameter of 165.3 μm .

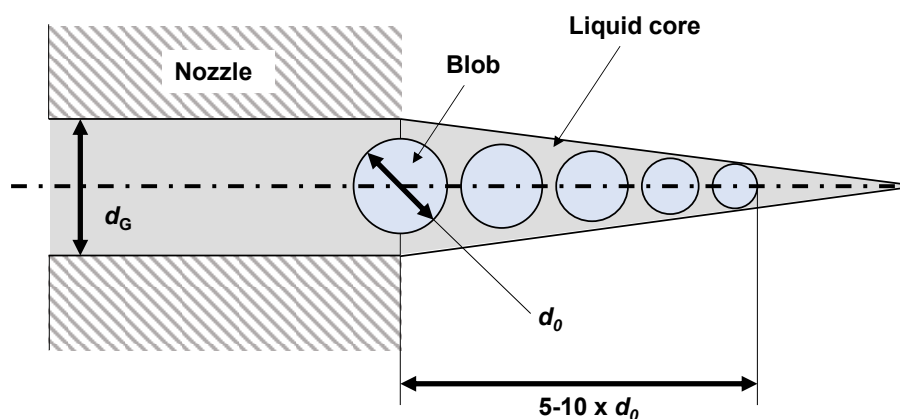


Figure 2-7: Schematic representation of the blob injection assumption.

$$Q = \rho_F(T_{inj}) \cdot \left[C_C \cdot \frac{\pi d_G^2}{4} \right] \cdot \left[C_V \cdot \sqrt{\frac{2(p_{inj} - p_b)}{\rho_F(T_{inj})}} \right] = \rho_F(T_{inj}) \cdot A_{eff} \cdot U_{eff} \quad (2-6)$$

$$U_{eff} = C_V \cdot \sqrt{\frac{2(p_{inj} - p_b)}{\rho_F(T_{inj})}} \quad (2-7)$$

$$d_{eff} = \sqrt{C_C} \cdot d_G \quad (2-8)$$

Once the blob has been introduced into the domain, its size is progressively reduced due to the primary breakup process converging towards the so-called stable diameter, at which the primary breakup induces the rupture of the reduced blob into new multiple particles. It must be remembered that in both Lagrangian-Eulerian and Eulerian-Eulerian multiphase coupled simulations the dispersed liquid form does not identify real droplets, whose large number would require unaffordable computation resources to solve and trace them. Instead of real droplets, the dispersed liquid form in CFD simulations accounts for the so-called ‘parcels’, namely spherical liquid particles each of which is representative of a statistical sample of real droplets. As a result, the evolution of a single parcel is the representation of that occurring for a number of equivalent droplets. It is underlined that at the breakup occurrence, the CFD breakup modeling does not produce a defined number of child parcels (representative of the child droplets), however once the after-breakup diameter has been calculated according to the adopted model, the number of particles is updated in order to comply with the liquid mass conservation. Thus, since between two consecutive time-steps the particle diameter has been strongly reduced, a number of parcels characterized by the new reduced diameter (child parcels) are necessary to match the liquid mass of the larger one at the previous step. The breakup-induced shrinking of the parcel is computed as in Eq. (2-9), in which d_s is the stable diameter at which the droplet tends, d is the diameter of the parcel inherited from the previous time-step, τ_{BU} is the breakup time scale. Thus, at each time-step the simulated effect of the breakup phases on the droplet is completely defined by the couple $(d_s(t), \tau_{BU}(t))$, whose values are computed according to the present model.

$$\frac{d}{dt}(d) = -\frac{d - d_s}{\tau_{BU}} \quad (2-9)$$

In the present model the outcome of the injected blob during the primary breakup depends on the fact that the diameter may fall in three different diameter threshold conditions:

- As long as the first threshold diameter is not exceeded (Eq. (2-10)), the injected blob is progressively reduced without the creation of any child parcel similarly as proposed by Huh and Gosman, however their equations have been slightly modified in order to charge the primary breakup to the in-nozzle turbulence only (Eq. (2-11)).

$$d > C_{I1} \cdot d_{eff} \quad (2-10)$$

$$\frac{d}{dt}d = -\frac{L_t}{\tau_t} \quad (2-11)$$

In Eq. (2-11) L_t and τ_t are the turbulence length and time scales, respectively. The turbulence length scale is that shown in Eq. (2-12) whilst the time scale (Eq. (2-13)) is defined by means of the turbulence length scale, the in-nozzle fluctuating liquid velocity

U_t (Eq. (2-14), in which k is the in-nozzle turbulent kinetic energy estimated by means of the liquid parcel (subscript L) velocity magnitude), a constant coefficient $C_{\beta 3}$. Under this condition, the stable diameter and the breakup time scale needed to define the breakup effect are determined as in Eq.s (2-15), (2-16).

$$L_t = \frac{d_{eff}}{8} \quad (2-12)$$

$$\tau_t = C_{I3} \cdot \frac{L_t}{U_t} \quad (2-13)$$

$$U_t = \sqrt{\frac{2}{3} \cdot k} \quad (2-14)$$

$$d_s = d - \frac{L_t}{\tau_t} \cdot \Delta t \quad (2-15)$$

$$\tau_{BU} = \tau_t \quad (2-16)$$

- If the reduced diameter falls in the second threshold condition (Eq. (2-17)), the atomization of the reduced blob occurs. The diameter of the after-breakup parcel, which will be that assigned to the child parcels, is extracted randomly from a tuned chi-squared Probability Distribution Function (PDF, **Figure 2-8**) centred around a mean diameter (Eq. (2-18)) which was empirically obtained based on the experimental data of modern GDI injectors.

$$C_{I1} \cdot d_{eff} > d > C_{I2} \cdot d_{eff} \quad (2-17)$$

$$d_{mean} = 158 \cdot 10^{-6} \cdot (U_t^{-0.474}) \quad (2-18)$$

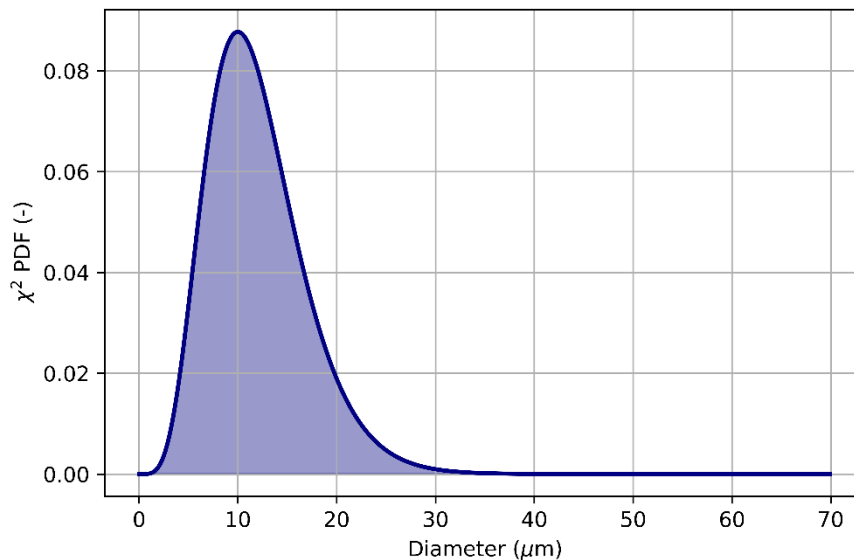


Figure 2-8: Example of the results from a chi-squared diameter distribution.

- Once the diameter of the child parcels has been defined, those parcels evolve tending towards a new stable diameter according to a new breakup time scale that are reported in Eq.s (2-19), (2-20), in which C_{I4} is a tuning coefficient. According to the latter couple of values, the size of the child parcels is progressively reduced until the threshold Eq. (2-21) at which the secondary breakup model is charged to predict the fate of the parcels.

$$d_S = C_{I4} \cdot d_{mean} \quad (2-19)$$

$$\tau_{BU} = C_{I3B} \cdot \tau_t \quad (2-20)$$

$$d < C_{I2} \cdot d_{eff} \quad (2-21)$$

Secondary breakup modeling

As mentioned in 1.3.2 the secondary breakup is driven by the aerodynamics interaction between the after breakup evolved child parcels from the primary breakup phase and the surrounding air. The secondary breakup was modeled via UDF according to a slight modified version of the Bianchi et al. model as well. The present secondary breakup model is strongly based on the one proposed by Pilch and Erdmann [33], which relies on the use of non-dimensional correlations for the breakup time (τ^*) to define the breakup time scale. The breakup non-dimensional time, which is associated to the different recognized breakup regimes (**Figure 1-15**), is chosen depending on the Weber number according to the implementation reported in **Table 2-3**.

The Weber number is determined as in Eq. (1-1), in which the gas-parcel relative velocity is

$$\text{computed as } U_{G-L} = \sqrt{(U_{G,X} - U_{L,X})^2 + (U_{G,Y} - U_{L,Y})^2 + (U_{G,Z} - U_{L,Z})^2}.$$

Table 2-3: Secondary breakup model possible outcomes.

$We = \frac{\rho_G \cdot d \cdot U_{G-L}^2}{\sigma_L}$	$\tau^*(-)$	Breakup regime
< 12	100	Breakup skip
12-18	$6 \cdot (We - 12)^{-0.25}$	Vibrational
18-45	$2.45 \cdot (We - 12)^{0.25}$	Bag
45-351	$14.1 \cdot (We - 12)^{-0.25}$	Bag/streamer
351-2760	$0.766 \cdot (We - 12)^{0.25}$	Stripping
> 2760	5.5	Catastrophic

Once the non-dimensional breakup time at the current time-step has been defined according to **Table 2-3**, the new stable diameter and the breakup time scale are calculated as in Eq.s (2-22), (2-23), in which C_{I5} is a tuning coefficient. The latter couple of values is used to compute the diameter of the second-generation child parcels, then the number of parcels is updated according to the liquid mass conservation constraint as discussed for the primary breakup.

$$d_s = C_{I5} \cdot \frac{12 \cdot \sigma_L}{\rho_G \cdot U_{G-L}^2} \quad (2-22)$$

$$\tau_{BU} = \tau^* \cdot \sqrt{\frac{\rho_L}{\rho_G}} \cdot \frac{d}{U_{G-L}} \quad (2-23)$$

2.2.5 Wall impingement modeling

As described in 2.1 one of the contributions provided by the present research project is the ranking of different recognized wall impingement models based on the comparative analysis among their macroscopic features which can be well correlated with some selected key engine aspects. A fuel spray-wall impingement model is based on the modeling of the outcomes resulting from the impact of a single droplet against a solid wall which is completely defined by: i) the impingement regimes that are accounted for; ii) criteria for the transition among the different impingement regimes; iii) methods for the calculation of the after-impingement characteristics (droplet number, mass, diameter, velocity, trajectory). The recognized literature models by Obermaier and Chaves [101], O'Rourke and Amsden [102], [103], Mundo and Tropea and Sommerfeld [65]–[67], Bai [62], [63], Kuhnke [78], Bai-ONERA [104], [37], Senda [8]–[12], [37] have been reviewed and then ranked. Before moving on the discussion, a few key quantities must be defined. Firstly, it must be remembered that the two fundamental aspects in determining the possible outcomes of the impact of liquid droplets against the wall are the droplet kinetics and the wall surface conditions (mainly temperature and dry/wet status). The droplet kinetics for wall impingement application is typically expressed as function of the non-dimensional group listed in **Table 1-5** accounting for the properties of the liquid droplet at the impact temperature (ρ , μ , σ), the droplet diameter at the impact (d), the normal-to-wall scalar component of the relative velocity between the droplet and the impact wall (e.g. the engine piston) ($U_{L,n}$) at the impact, which is simply the normal-to-wall component of the droplet velocity in vessel spray testing and simulation, which are usually performed with a fixed impact plate. With regards to the wall surface, it is important to define at which conditions the wall can be called hot or cold with respect to the incident liquid. Typically, a sort of superheating coefficient is defined by means of different combinations of the wall temperature (T_w), the fuel equilibrium temperature at the impact environmental conditions (T_{sat}), the Leidenfrost and the Nukiyama temperatures (T_L , T_N). Furthermore, the surface status (dry or wet) is usually taken into account by means of the so-called non-dimensional film thickness δ , which is defined as the ratio between the height of the liquid film (if present, otherwise $\delta = 0$) and the diameter of the incident droplet d . Once those base quantities have been pointed out, more complex indexes used to draw up the boundaries among impingement regimes can be presented. With regards to the droplet kinetics, regardless to the use of the pure droplet Weber number ($We_L = \rho_L \cdot d \cdot U_{L,n}^2 / \sigma_L$), the droplet energy factor E (Eq. (2-24)), the splashing parameter W (Eq. (2-25)), the non-dimensional droplet velocity U^* (Eq. (2-26), in which $Ca = \mu_L \cdot U_{L,n}^2 / \sigma_L$ and $La = \sigma_L \cdot \rho_L \cdot d / \mu_L^2$ are the non-dimensional numbers of capillary and Laplace, respectively), and the Sommerfeld number K (Eq. (2-27)) can be adopted.

$$E = \frac{We_L}{\min(\delta; 1) + \frac{1}{\sqrt{Re_L}}} \quad (2-24)$$

$$W = Oh_L \cdot Re_L^{1.25} \quad (2-25)$$

$$U^* = Ca_L^{5/4} \cdot La_L^{3/4} \quad (2-26)$$

$$K = We_L \cdot Oh_L^{-0.4} \quad (2-27)$$

With regards to the wall surface superheating degree, excluding the use of the absolute wall temperature, the non-dimensional temperatures T_w^* (Eq. (2-28)) and T^* (Eq. (2-29)) can be adopted.

$$T_w^* = \frac{T_w}{T_{sat}} \quad (2-28)$$

$$T^* = \frac{T_w - T_N}{T_L - T_N} \quad (2-29)$$

Furthermore, the key after-impingement parameter called splash-ratio must be introduced. As discussed in **1.3.3**, in this research project it is considered that the splash-regime classification comprises the outcomes that induce the split of the incident droplet into a deposited liquid mass which spreads on the wall and a scattered mass which remains into the gaseous phase under the form of flying secondary droplets. As far as the ability of the models to predict the liquid fuel film is concerned, the capture of the after-splash liquid mass split can be crucial. In order to evaluate this aspect, the ratio between the scattered and the deposited liquid fuel mass after a splash event is represented by the aforementioned splash-ratio (X_s), which can be calculated as in Eq. (2-30) in which the subscript S and I are referred respectively to the single incident droplet, and to the after-splash formed scattered secondary droplets, N_2 is the number of secondary droplets, the denominator is the after-splash deposited liquid mass.

$$X_s = \frac{\sum_{i=1}^{N_2} m_{S,i}}{m_I - \sum_{i=1}^{N_2} m_{S,i}} \quad (2-30)$$

Wall impingement models rank

Once the most significant indexes used to describe the droplet-wall impingement have been given, they can be adopted to critically compare the six selected models. After a detailed review of the original published models and then of their implemented version in CFD codes, the macroscopic characteristics i.e., impact regimes, regime transition criteria, after-impingement computation method are briefly reported in **Table 2-4**. Consider analyzing the differences among the models under review column by column.

Table 2-4: Comparison among the macroscopic features of six recognized literature impingement models.

Model	Impingement regimes	Transition criteria	After-impact velocity	After-impact size	After-impact trajectory
Obermaier	Stick Splash Fragmentation	We	Energy constraint eq.	Empirical	Random
O'Rourke	Deposition Splash	E	PDF	PDF	Empirical + random
Mundo et al.	Deposition Splash	W	Empirical	Empirical	Random
Bai	Deposition Rebound Splash Breakup	(We, T_w)	Energy constraint eq.	Mass constraint eq.	Momentum constraint eq.
Kuhnke	Deposition Rebound Splash Breakup	(U^*, T_w^*)	Empirical	PDF	Empirical + random
Bai-ONERA	Deposition Rebound Splash	(K, T^*)	Energy constraint eq.	Mass constraint eq.	Momentum constraint eq.
Senda et al.	Deposition Rebound Splash	(We, T^*)	Energy constraint eq.	Empirical	Empirical + random

- Regarding the impingement regimes, it is remembered that in the current and next engine framework the ever-higher injection pressure and the liquid film-induced soot emissions at low load have moved the focus of scientists mainly on the prediction of the splash regime (promoted by high droplet kinetics (1.3.3)) and the deposition regime (mainly promoted by low wall temperature (1.3.3)). Therefore, since splash and deposition regimes are both accounted for by the considered models, one can say that there is no practical difference among the models concerning the regimes options. However, it must be underlined that as described in 1.3.3, at engine medium-high load transitions and high load points the incident droplet rebound against the thin vapor layer formed due to the incoming Leidenfrost effect is quite likely. Therefore, in order to extend the predictivity of a wall impingement setup to larger range of engine operations, the modeling of the rebound regime should be also included. As a result, a penalty can be assigned to the models by Obermaier, O'Rourke and Mundo. For the sake of clarity, it is highlighted that **Table 2-4** includes some impingement regimes that have been not described in 1.3.3, namely stick, fragmentation, breakup. The stick regime is a deposition-like regime according to which it is assumed that the incident liquid mass adheres to the wall as undeformed droplet (dispersed form) instead of liquid film (continuum phase). The fragmentation regime describes the conversion of the incident droplet into multiple secondary stucked droplets. Since the conservation smooth deposition and the droplet shape conservation features are not consistent with the typical fuel impact dynamics, the inclusion of those regimes into the models cannot be considered as a plus. On the other hand, the breakup is a splash-like regime that can be induced by extreme droplet kinetics or by high temperatures. Breakup regimes allow for the modeling of splash without deposition, thus, only after-impact scattered droplets can be generated without any contribution to the liquid film. Since the features of breakup regimes can be representative of late injection strategies at high engine load, in order to

realize a local fuel stratification around the spark plug about the Top Dead Center (TDC), extreme kinetics and high temperature scenarios may occur, thus, the modeling of this additional regime can be considered a plus with respect to the Bai-ONERA and the Senda models.

- Focusing on the transition criteria, it is clear that the models by Obermaier, O'Rourke and Mundo are not suitable for engine applications where the boundaries among the impact regimes are strongly dependent by the wall temperature, which may vary significantly over the possible engine operating points e.g., cat-heating, cold states, high loads. However, it is pointed out that the model by O'Rourke is based on a kinetic index (E , Eq. (2-24)) that includes the effect of the non-dimensional liquid film thickness (δ) which provides the potential to reproduce the effect of the film viscous damping on the droplet kinetics and impingement outcomes. As far as the engine application is concerned, regimes boundaries must be defined according to the combination of at least a kinetic index and a thermal index, thus, only the models by Bai, Kuhnke, Bai-ONERA and Senda are taken into account. It is highlighted that the use of the non-dimensional temperature (T^* , Eq. (2-29)) as a thermal index allows the split of the temperature dependency into three different clear scenarios representing the phases of the droplet lifetime curve (**Figure 1-20**), namely $T^* < 0$ (cold state, nucleate boiling), $0 < T^* < 1$ (liquid-wall interaction slope change, transition boiling), $T^* > 1$ (hot state, film boiling). On the other hand, the thermal index proposed by Kuhnke lacks a general interpretability of the impact conditions, being limited to two main scenarios i.e., $T^* < 1$ and $T^* > 1$, thus, performance losses can be expected at the regimes' boundaries.
- Considering the methods implemented in the models under review to compute the after-impingement features (last three columns in **Table 2-4**) it can be seen that both the Bai and Bai-ONERA models rely on an almost pure mathematical approach for the estimation of the two most important after-impact features i.e., size and velocity of the scattered droplets. However, this feature is not necessarily a plus due to the typical super-simplification and hypotheses applied to model such complex phenomena, leading to the loss of accuracy that will be not easily corrected being the computation constrained by given general equations. Instead, the approaches proposed by Kuhnke (statistical distribution) and Senda (empirical correlation) can be more solid in predicting those complex high non-linear phenomena if supported by a comprehensive set of data for tuning. It must be highlighted that the Kuhnke model was developed to meet data regarding SCR (Selective Catalytic Reactor) systems for engine applications whilst the Senda model was continuously improved based on both Diesel and gasoline data, thus, a greater potential can be expected from the latter.

A further rank table is shown in **Table 2-5**, where a score is given to each model with respect to the strength of the correlation between its features and a selection of fundamental variables in engine operations. High scores are represented by double plus (++) in the case the real engine driver is taken into account in a physical manner by the features of the model; positive scores are presented by plus (+) in the case the driver is taken into account through the correction of generally valid features; negative scores are represented by minus (-) in the case the driver is not associated to any feature of the model. Scores have been assigned after the analysis of the implemented algorithm of each model from the handbook of CFD codes.

Table 2-5: Models comparative analysis in terms of correlation strength between engine parameters (drivers) and the associated modeling feature.

Driver	Injection pressure	Dense sprays	Engine load	Engine load	Piston/liner wetting
Feature	Kinetics thresholds	Multiple droplet hits	Wall temperature	Lifetime curve	Viscous damping
Obermaier	+	-	-	-	-
O'Rourke	+	-	-	-	+
Mundo et al.	+	-	-	-	-
Bai	+	-	+	-	-
Kuhnke	++	-	+	-	-
Bai-ONERA	+	-	+	+	+
Senda et al.	+	+	+	+	++

The same score has been assigned to the connection between injection pressure and kinetics threshold of each model, except for the double plus achieved by the Kuhnke model, which allows to represent extreme kinetics scenarios due to the thermal induced breakup kinetic threshold, as discussed earlier. In 2.1 it has been highlighted the fact that most of the impingement models are based on observations conducted on the impact of single droplet or train of droplets with controlled frequency. However, those conditions highly differ from that of the current GDI framework, in which dense sprays and multiple hits play a key role in the wall impingement outcomes. In the Senda's model algorithm (which will be deeply presented later) the effect of multiple hits is implemented by means of the modeling of droplet-droplet collision features at cold ($T^* < 0$) surface conditions, which enables splash events at low and intermediate kinetics promoted by the mutual fragmentation of successive stuck droplets. A further effect that should be accurately reproduced is the liquid film viscous damping on incident droplets, that is enhanced by the thickening of the liquid film. At wall wet and cold states, the algorithm of the Senda model relies on three splash sub-models (which are sometimes called partial rebound regimes) that are based on the interaction between the incident droplet and the liquid film depending on the Weber number and the non-dimensional thickness δ . Even the O'Rourke model and the Bai-ONERA model account for the modification of the impingement outcome for given droplet kinetics and wall temperature by means of corrective features. The O'Rourke model directly modifies the effective kinetics potential of the incident droplet by means of the presence of δ (Eq. (2-24)). The Bai-ONERA model relies on the addition of a regime boundary at wall wet and cold states which sets a generally valid threshold accounting for rebound events for low droplet kinetics conditions. However, since no dependence on the film thickness which wets the surface is included and furthermore simple rebound events do not create liquid film, the adjustment proposed in the Bai-ONERA model may suffer from the under-estimation of liquid film formation.

In light of the results of the ranking analysis, the Bai-ONERA and the Senda wall impingement models have been selected as the most promising options to be tested in spray CFD simulations. Both the models have been tested according to the *STAR-CD* built-in implementation. In this section the features and the impingement regime decision algorithm of the two models are presented and discussed in order to clearly present the practice differences between those two and the expected performance with respect to typical GDI spray conditions.

Bai-ONERA model

The Bai-ONERA model is a *STAR-CD* built-in option [37] which couples a slight modified version of the main algorithm of the ONERA model [104] with some features of the Bai model [62], [63]. The original ONERA model was developed to approach dry smooth surfaces of heated walls by considering the three impingement regimes named deposition, rebound, and splash. As reported in **Table 2-4**, in the Bai-ONERA model the boundaries between those regimes depend on the thermodynamics conditions via the non-dimensional temperature T^* (Eq. (2-29)), and the kinetics of the incident parcel via the Sommerfeld number K (Eq. (2-27)). The transition thresholds were set according to the data fit of experimental results on the impact of i-octane collected by the original Authors. The integration with the Bai model allows for the simulation of dry rough and wet surfaces as well. Furthermore, the coupling with the Bai model affects the approach to deposition and rebound regimes. The wall impingement maps resulting from the use of the Bai-ONERA model are shown in **Figure 2-9** in which K_R is the Sommerfeld boundary threshold between rebound and deposition/splash, and K_S is the Sommerfeld boundary threshold between splash and deposition/rebound. Considering the maps in **Figure 2-9** it is visible that in the Leidenfrost domain (film boiling regime) i.e., values of the non-dimensional temperature higher than 1, only splash and rebound may occur regardless to the status of the surface (dry or wet). The two regimes share the same generally valid constant threshold which loses the dependence from the non-dimensional temperature due to the presence of the vapor layer upon the hot surface. Constant boundary threshold values are given in the nucleate boiling domain as well due to the weak influence of the temperature on the impact at cold states. The temperature dependence can be found in the transition boiling domain with the linear behavior of K_S and the cubic behavior of K_R for both dry and wet surfaces. It is underlined that in dry conditions the splash-deposition boundary can shift within the band depending on the surface mean roughness. For the sake of clarity, the boundary transition conditions are reported in Eq.s (2-31), (2-32). The coefficients included in Eq.s (2-31), (2-32) were tuned by the original Authors of the pure ONERA model against i-octane experimental data and are listed in **Table 2-6**. The calculation of the main after-impingement features is resumed in the following.

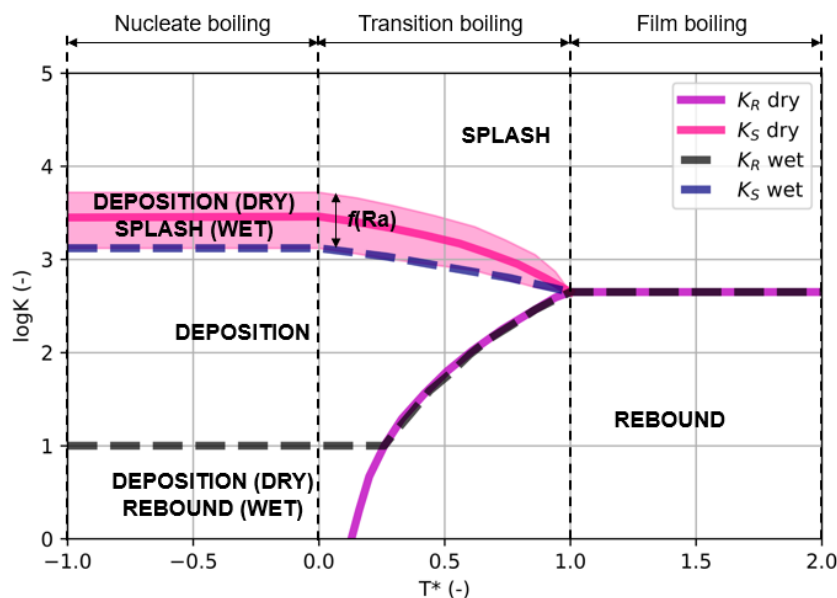


Figure 2-9: Wall impingement maps according to the Bai-ONERA model for dry (magenta boundaries) and wet (blue boundaries) surfaces.

$$K_S = \begin{cases} K_0 & [T^* \leq 0] \\ K_0 + T^* \cdot (K_1 - K_0) & [0 < T^* \leq 1] \\ K_1 & [T^* > 1] \end{cases} \quad (2-31)$$

$$K_R = \begin{cases} K_2 & [T^* \leq 0] \\ K_1 \cdot (T^*)^n & [0 < T^* \leq 1] \\ K_1 & [T^* > 1] \end{cases} \quad (2-32)$$

Table 2-6: Fitted values of the Bai-ONERA model coefficients.

Coefficient	Dry	Wet
K0	$f(Ra)$	3000
K1	450	450
K2	0	$f(La)$
n	3	3

Deposition: in the case of deposition, it is assumed that the incoming parcel is spread on the wall in the form of a disk with a spread diameter d_D (Eq. (2-33)) that accounts for the diameter of the droplet represented by the parcel and its kinetic contribution. The thickness of the formed liquid patch is calculated according to the liquid mass constraint, namely the known incident mass completely spread upon the wall (Eq. (2-34)).

$$d_D = 0.613 \cdot d \cdot f(We) \quad (2-33)$$

$$h = m_I \cdot \frac{4}{\pi \cdot d_D^2} \quad (2-34)$$

Rebound velocity: in the case of rebound, a single parcel with the same mass and diameter of the incident one is scattered off the wall. The magnitude of the scatter velocity (subscript R) can be calculated as the sum of the normal-to-wall and the tangent-to-wall velocity contributions which are determined according to the Bai [36] model by means of the so-called normal and tangent restitution coefficients (Eq. (2-35)).

$$\begin{cases} U_{R,n} = U_I \cdot (0.993 - 1.76 \cdot \theta_I - 0.49 \cdot \theta_I^2) \\ U_{R,t} = U_I \cdot \frac{5}{7} \end{cases} \quad (2-35)$$

Rebound angle: Once the velocity normal and tangent scalar components are known and the magnitude of the scatter velocity U_R has been calculated, the ejection angle (θ_R) is determined from Eq. (2-36).

$$U_R = \sqrt{[U_R \cdot \cos(\theta_R)]^2 + [U_R \cdot \sin(\theta_R)]^2} \quad (2-36)$$

Splash velocity: It must be underlined that in the Bai-ONERA model each splash event leads to the formation of two parcels (subscripts 1,2) of equal mass. As reviewed in **Table 2-4**, the splash velocity is calculated from the overall droplet energy constraint (Eq. (2-37), top) together with a size-velocity correlation for the scattered droplets (Eq. (2-37), bottom). The overall energy balance in (Eq. (2-37), top) describes the conversion of the kinetic energy of the incident parcel ($E_{K,i}$, Eq. (1-2)) into losses for the deformation of the incident liquid mass that is going to detach ($E_{S,i}$, Eq. (1-3)) and then into the cohesion of the splashed droplets

(first term of the right-hand side) and their kinetic energy (second term of the right-hand side), which includes the target velocity magnitudes. N_1 , N_2 are the number of droplets represented by the two splashed parcels.

$$\begin{cases} E_{K,I} - f(We) \cdot X_S \cdot E_{S,I} = \pi \cdot \sigma (N_1 \cdot d_1^2 + N_2 \cdot d_2^2) + \frac{m_S \cdot (U_{R,1}^2 + U_{R,2}^2)}{4} \\ \frac{|U_{R,1}|}{|U_{R,2}|} = \frac{\ln(d_1/d)}{\ln(d_2/d)} \end{cases} \quad (2-37)$$

Splash angle: the ejection angle of one of the two splashed parcels is chosen randomly in the range $(5-50)^\circ$. Then, the ejection angle of the other parcel is computed from the conservation of the tangential momentum constraint (Eq. (2-38)).

$$|U_{R,1}| \cdot \cos(\theta_{R,1}) + |U_{R,2}| \cdot \cos(\theta_{R,2}) = 0 \quad (2-38)$$

Splash diameter: as reviewed in **Table 2-4**, the size of the droplets represented by the splashed parcels is determined by solving the liquid mass conservation (Eq. (2-39), top) together with the constraint of equal mass splashed parcels (Eq. (2-39), bottom).

$$\begin{cases} X_S \cdot d^3 = N_1 \cdot d_1^3 + N_2 \cdot d_2^3 \\ N_1 \cdot d_1^3 = N_2 \cdot d_2^3 \end{cases} \quad (2-39)$$

Splash ratio: the incident parcel mass split into liquid film and splashed droplets is determined as a function of the non-dimensional temperature according to Eq. (2-40). As visible in Eq. (2-40), in the nucleate boiling domain the film/splash mass split is set to 80%/20% as constant whilst in the film boiling domain the model accounts for splash with no film formation due to the Leidenfrost-induced vapor layer similarly to what can be achieved by the breakup impact regime proposed by Kuhnke (**Table 2-4**). In the transition boiling domain the film/splash mass split depends on the non-dimensional temperature with a behavior that depends on the splash exponent coefficient γ , which is a tuning coefficient of the Bai-ONERA model. **Figure 2-10** displays the splashed mass percentage over the non-dimensional temperature domain for different values of the tuning coefficient γ . It is clear that in the case the results from the proposed model suffer from liquid film over-estimation, the tuning coefficient must be reduced whilst if the results suffer from liquid film under-estimation, the tuning coefficient must be increased. It must be underlined that both the nucleate and film boiling regimes are generally valid i.e., no user adjustments are allowed. Only in the transition boiling regime the tuning coefficient γ is present.

$$X_S = \begin{cases} 0.8 & [T^* \leq 0] \\ f(T^*, \gamma) & [0 < T^* \leq 1] \\ 0.0 & [T^* > 1] \end{cases} \quad (2-40)$$

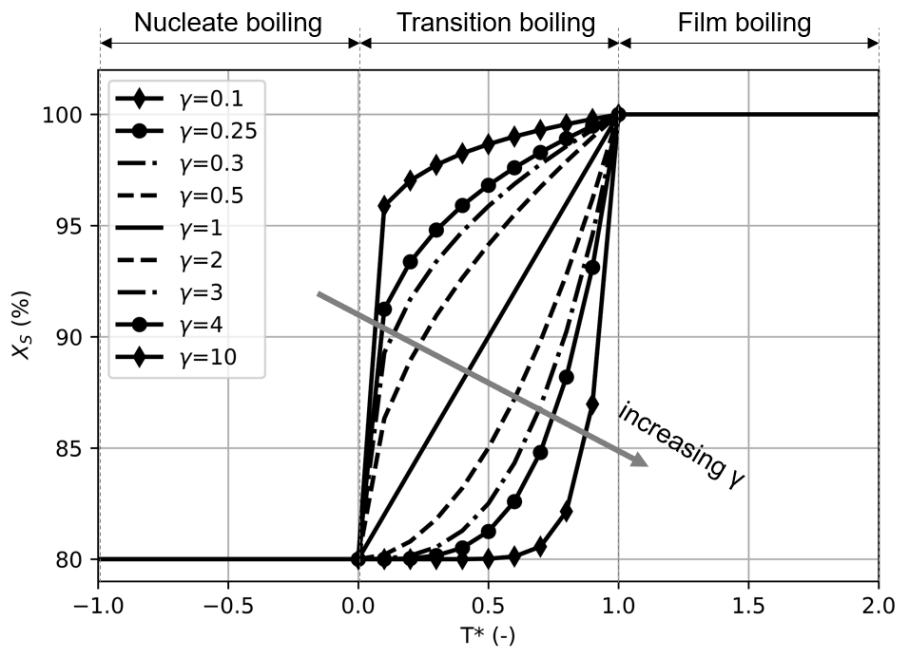


Figure 2-10: Splash ratio behaviour with respect to non-dimensional temperature for different values of the tuning exponent γ according to Bai-ONERA.

Senda model

The *STAR-CD* built-in option for the Senda model [37] is a hybrid wall impingement model that is strongly based on the workflow of the original model by Senda at cold states ($T^* < 0$) whilst hot states $T^* > 0$ are approached by mixing the workflow of Bai-ONERA model with some features of the Bai and the original Senda models. As seen for the Bai-ONERA model, the Senda model as well considers three impingement regimes i.e., deposition, rebound, splash. As reported in **Table 2-4**, the transition between those regimes are drawn up depending on the non-dimensional temperature T^* (Eq. (2-29)) and on the Weber number (Eq. (1-4)). It is highlighted that differently from the Bai-ONERA model, the Senda model relies on different splash sub-models depending on different factors that will be deeply analyzed in the following. Thus, the Senda model has the ability to capture splash events with higher degree of detail with respect to the Bai-ONERA model. The maps of the Senda model are reported in **Figure 2-11**. Since different regimes boundaries were correlated to the Laplace number (La) of the incident droplet, the maps shown in **Figure 2-11** have been drawn up for reference properties of the latter. The liquid properties required by the Laplace number, namely density, dynamic viscosity, surface tension, have been calculated for a commercial-like RON95 gasoline at a reference temperature representative of the typical GDI injection systems (40°C). The diameter of the incident droplet has been set to $7\ \mu\text{m}$ according to the experimental data provided in [21] for injection pressure above 300 bar at distances from the injector tip comprised in the range 20-40 mm. Those reference values are also reported in **Figure 2-11**. The wall Impingement map at the top left of **Figure 2-11** displays that for dry cold surfaces ($T^* < 0$) only splash or deposition may occur depending on the Weber number of the incident droplet and on the non-dimensional time interaction parameter τ (Eq. (2-41), first) which is defined as the ratio between the droplet-droplet interaction time scale (Eq. (2-41), second), and the droplet residence time (Eq. (2-41), third). In Eq. ((2-41), second) L_{d-d} is the approximate center-by-center distance between a pair of parcels along the normal-to-wall direction. Therefore, three main scenarios may occur: i) the time interaction parameter is higher than 1, thus, since the time interval before the droplet-droplet interaction at the wall is longer than the residence time, there is no mutual influence

between the two parcels. As a consequence, cold dry impingement conditions with $\tau > 1$ falls in the simple low kinetics single droplet regime, which creates liquid film via deposition; ii) the time interaction parameter is around zero, thus, the pair of parcels under consideration are extremely close. The pair of parcels interact between each other according to a sort of coalescence mechanism at the wall with a slight mass loss under the form of dispersed liquid caused by the interaction itself. Under this condition ($\tau \approx 0$), the impact is represented by low kinetics splash regime characterized by a quite low splash ratio value; iii) the time interaction parameter lies between 0 and 1, thus, the two parcels collide after the impact of the earlier resulting in the fragmentation of both before the formation of liquid film. This condition ($0 < \tau < 1$) is represented by a low kinetics splash event with a significant splash ratio. This feature helps to simulate the effect of dense sprays.

$$\left\{ \begin{array}{l} \tau = \frac{\tau_{d-d}}{\tau_{res}} \\ \tau_{d-d} = \frac{L_{d-d}}{U_{I,n}} \\ \tau_{res} = \pi \sqrt{\frac{\rho \cdot d^3}{16\sigma}} \end{array} \right. \quad (2-41)$$

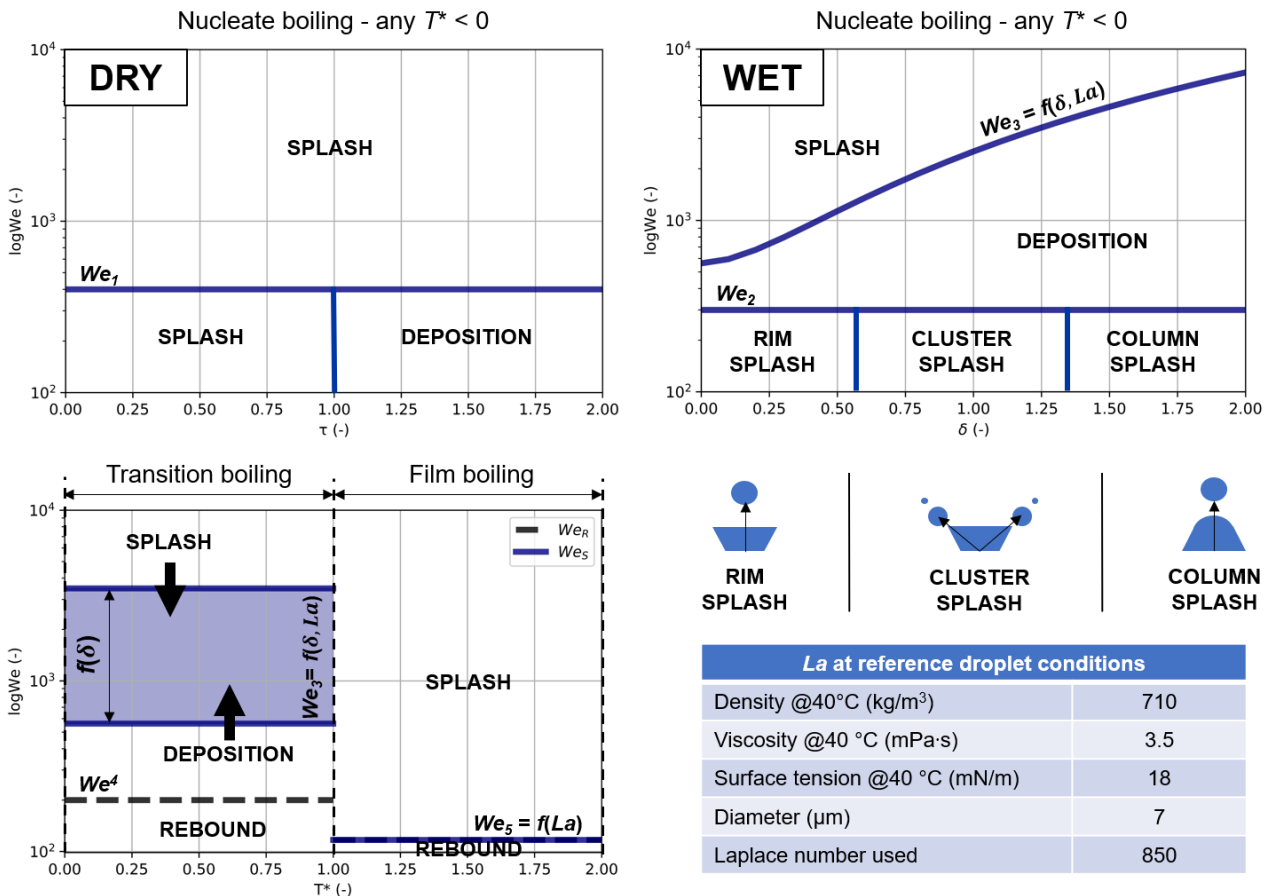


Figure 2-11: Wall impingement maps according to the Senda model for cold (top left: dry; top right: wet) and hot (bottom) states. The dependence on the interaction time (τ), non-dimensional film thickness (δ), non-dimensional temperature (T^*) are shown respectively. Sketches of the rim, cluster, column splash modes are also shown.

In the map at the top right of **Figure 2-11** it is visible that as discussed for dry surfaces, only splash or deposition may occur for wet cold surfaces ($T^* < 0$) with boundaries drawn up with respect to the Weber number and the non-dimensional film thickness δ . It is worth mentioning that in this domain the model relies on the use of three new splash sub-models, namely rim, cluster, and column splash. Those regimes represent the result of the droplet-film interaction at low kinetics depending on the liquid film viscous damping (increasing δ values) and are characterized by unique after-impingement features that will be discussed later. With regards to the hot states displayed at the bottom left of **Figure 2-11**, the boundaries are slightly different with respect to those shown for the Bai-ONERA. In particular, the rebound-deposition boundary has a constant behavior with respect to the non-dimensional temperature as well as the splash-deposition boundary. However, the zone of the $We-T^*$ plane at which the splash-deposition boundary may lie is quite wide (blue band) and, for given reference droplet diameter ($d = 7 \mu\text{m}$ as said before), it depends on the liquid film thickness. The band plotted in **Figure 2-11** accounts for thickness values from 0 (dry wall, lower bound) to $10 \mu\text{m}$ (upper bound), that is the typical range that can be observed in GDI engine simulations. It is clear that if liquid film is present in the transition boiling regime, the model of Senda promotes deposition at high kinetics against splash inducing new incident parcels to join the film. No significant macroscopic differences with respect to the Bai-ONERA model are present in the Leidenfrost regime ($T^* > 1$). For the sake of clarity, the boundary threshold Weber values shown in **Figure 2-11** are reported in Eq. (2-42).

$$\begin{cases} We_1 = 400 \\ We_2 = 300 \\ We_3 = f(\delta) \cdot La^{c_0} \\ We_4 = 200 \\ We_5 = C_1 \cdot La^{c_0} \end{cases} \quad (2-42)$$

In the present model the regimes of deposition and rebound are approached according to the Bai model, thus, their features are the same shown in the description of the Bai-ONERA model (2-33)-(2-36). As a consequence, only the features of the different splash-sub models will be presented. It must be considered that the calculation method of the after-splash velocity depends only on the Weber number, and it is equally applied to all the splash-sub models, thus, it will be reported once. The other features are presented for each different splash sub-model for a generic splashed parcel since in the present model it is assumed that the after-splash parcels have the same mass, diameter and velocity.

Splash velocity: the magnitude of the velocity of the scattered parcels is calculated with two different methods depending on the kinetics of the incident parcel. For given wall conditions (T^* , τ , δ), if the incident parcel has a high kinetics ($We > We_i$, with We_i taken from Eq. (2-42) based on the given wall conditions) the after-splash velocity magnitude is calculated according to the overall energy balance in the first line in Eq. (2-37). Otherwise, for low kinetics parcels ($We < We_i$) the velocity magnitude is calculated from the definition of the Weber number of the scattered parcels (Eq. (2-43), top), which is estimated as the sum of normal ($We_{S,n}$) and tangent ($We_{S,t}$) contributions given by δ -dependent polynomial correlations $P_4(\delta)$ (the subscript indicates the degree of the polynomial).

$$U_S = \sqrt{\frac{\sigma}{\rho \cdot d_i} \cdot \left(\sqrt{We_{S,n}^2 + We_{S,t}^2} \right)} \quad (2-43)$$

Dry cold splash angle: For the set ($T^* < 0$, $\delta = 0$) the calculation method depends on the incident Weber number according to Eq. (2-44). At low kinetics, the ejection angle is calculated by means of the empirical correlation in the first row in Eq. (2-44) in which the

polynomial forms $P_4(\delta)$ for the components of the scatter Weber number account only for the coefficients associated to δ^0 . At high kinetics the ejection angle is a polynomial form $P_1(\theta_I)$ (second row in Eq. (2-44)). At both low and high kinetics, the correlations for the ejection angle are integrated with a random component in order to take into account the aleatoric nature of the complex phenomenon.

$$\theta_s = \begin{cases} \text{atan}\left(\frac{We_{s,n}}{We_{s,t}}\right) + rnd & We < We_1 \\ P_1(\theta_I) + rnd & We > We_1 \end{cases} \quad (2-44)$$

Dry cold splash size: At low kinetics a constant ratio between the diameter of the i-th splashed droplet and the one of the incident parcel is proposed (Eq. (2-45), top) whilst at high kinetics the diameter of the splashed parcels is calculated by means of an empirical correlation (Eq. (2-45), bottom) based on the kinetic parameter $C_k = Oh \cdot Re^{1.25}$.

$$d_i = \begin{cases} C_2 \cdot d & We < We_1 \\ C_3 \cdot C_k^{C_4} & We > We_1 \end{cases} \quad (2-45)$$

Dry cold splash ratio: As mentioned before, the splash mechanics for the set ($T^* < 0, \delta = 0$) at low kinetics strongly depends on the non-dimensional interaction parameter. In those conditions the splash ratio at low kinetics conditions is given by a polynomial piecewise function (Eq. (2-46)) with a maximum achievable value around 40% (corresponding to 60% film). It is underlined that at low kinetics the τ -induced splash creates a single scattered parcel. At high kinetics, two splashed parcels with equal mass are crated according to a constant splash ratio set to 80%.

$$X_s = \begin{cases} P_3(\tau) & 0.0 < \tau < 0.34 \\ P_5(\tau) & 0.34 < \tau < 0.6 \\ \approx 0.4 & 0.6 < \tau < 1.0 \\ 0.0 & \tau > 1.0 \end{cases} \quad (2-46)$$

Wet cold splash angle: For the set ($T^* < 0, \delta > 0$) the ejection angle of the scattered parcels at both low and high kinetics is calculated as for the dry wall conditions.

Wet cold splash size: The size of the scattered parcels is calculated according to a δ -dependent empirical correlation at low kinetics and similarly to what shown in dry cold conditions at high kinetics (Eq. (2-47)).

$$d_i = \begin{cases} P_4(\delta) & We < We_2 \\ C_5 \cdot C_k^{C_6} & We > We_3 \end{cases} \quad (2-47)$$

Wet cold splash ratio: As seen in **Figure 2-11** in wet cold conditions rim, cluster and column splash modes may occur at low kinetics. Each splash sub-model is responsible for the formation of different number of scattered parcels: i) rim splash is expected for $\delta < 0.6$, and it leads to the formation of 1 splashed parcel; ii) cluster splash is expected for $0.6 < \delta < 1.35$, and it leads to the formation of 4 parcels of equal mass, diameter and velocity; iii) column splash is expected for $\delta > 1.35$, and it leads to the formation of 1 splashed parcel. At low kinetics the splash ratio depends on the non-dimensional film thickness with the behavior plotted in **Figure 2-12** whilst at high kinetics a constant splash ratio set to 80% is adopted.

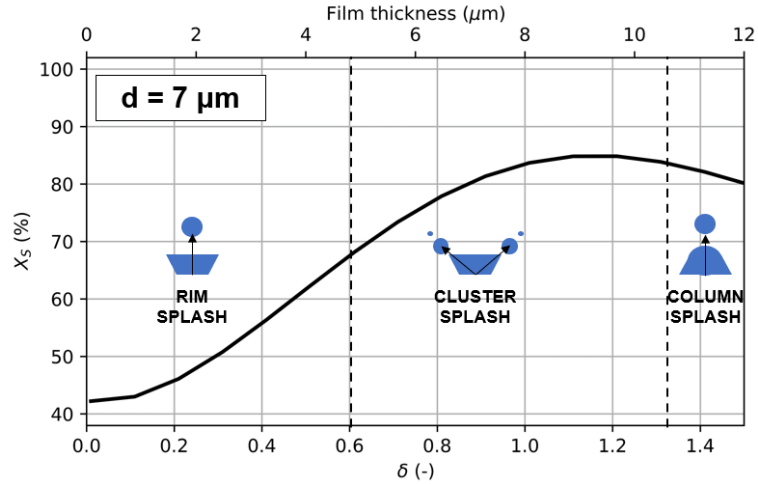


Figure 2-12: Splash ratio behaviour with respect to both non-dimensional film thickness (bottom x) and film height (top x) according to Senda assuming a diameter of the incident parcel of $7 \mu\text{m}$.

In spite of the cold status of the surface ($T^* < 0$, nucleate boiling) and the low kinetics ($We < 300$), those splash modes (in particular the cluster splash) promotes high values of the scattered mass split against the deposited, being able to achieve scattered mass percentage above 80% for a significant range. It is expected that the column splash mode is unlikely due to the fact that its activation requires thick films and/or very small-sized droplets ($d < 5 \mu\text{m}$) at the wall impingement time with respect to those expected in nowadays GDI engine applications.

Hot splash angle: In transition and film boiling regimes the ejection angle of the scattered particles is obtained by scaling the incident angle by a model coefficient (< 1), and then it is adjusted with a random contribution. In the original formulation, there are several values of the scaling coefficients depending on the incident Weber number. After practical engine considerations, the reduced set in Eq. (2-48) has been obtained.

$$\theta_s = \begin{cases} 0.7865 \cdot \theta_I + \text{rnd}(\pm 15) & 0 < T^* < 1 \\ 0.7426 \cdot \theta_I + \text{rnd}(\pm 15) & T^* \geq 1, 100 \leq We < 200 \\ 0.2361 \cdot \theta_I + \text{rnd}(\pm 20) & T^* \geq 1, We \geq 200 \end{cases} \quad (2-48)$$

Hot splash size: the diameter of the splashed parcels is calculated according to empirical Weber correlations (Eq. (2-49)) similarly to what mentioned about the ejection angle.

$$d_i = \begin{cases} 0.30 & 0 < T^* < 1, We < 50 \\ \frac{2.5}{We^{0.3244}} & T^* \geq 1, 50 \leq We < 200 \\ \frac{13.8}{We^{0.6586}} & T^* \geq 1, 200 \leq We < 200 \\ 0.25 & T^* \geq 1, We > 400 \end{cases} \quad (2-49)$$

Hot splash ratio: For $T^* > 0$ (hot surface) two splashed parcels of equal mass, size and velocity are formed. The splash ratio is the same as that of the Bai-ONERA model (Eq. (2-40), **Figure 2-10**), thus, a pure splash without deposition regime is adopted in the Leidenfrost domain, and the tuning splash exponent coefficient γ is the same user coefficient. It must be underlined that even if the Senda and the Bai-ONERA models share the same splash-ratio model, the sensitivity of the simulated liquid film to the tuning

coefficient may differ significantly due to the very different extension of the deposition-splash boundaries implemented in the two models.

Leidenfrost effect

As seen in **1.3.3** the Leidenfrost effect is a fundamental thermophysical phenomenon that promotes the formation of a vapor layer upon a heated wall hit by liquid droplets that is able to prevent the droplet-wall impingement. In light of the deep analysis of the Bai-ONERA and Senda wall impingement models, it is clear that the Leidenfrost effect plays a key role in numerical simulations as well. In fact, both the Nukiyama and the Leidenfrost temperature are necessary to define the non-dimensional temperature (T^* , (2-29)), which is needed by the algorithm to determine the impingement regime for given kinetics of the incoming parcel. Think that even in the case a simulation engineer could rely on advanced trained after-impact sub-models with excellent prediction performance on gasoline-like data, inaccuracy in the estimation of the Leidenfrost and Nukiyama temperatures may lead to unreliable results due to the incorrect placement of the simulation point on the (T^* , $\log K$) or (T^* , We) planes. After a literature review, three different methods to predict the Nukiyama and Leidenfrost temperatures have been considered: i) the Speigler correlation for T_L ; ii) the midpoint rule for T_N ; iii) the Habchi correlation for both T_L and T_N .

In [105] Speigler et al. assumed that a significant bond exists between the Leidenfrost effect inception and the foam limit occurrence. The foam limit temperature was calculated by a simplified mathematical approach by using the Van der Walls equations. The model was applied to a set of experimental data based on different fluids e.g., water, n-heptane, ethanol etc. The best fit results in Eq. (2-50), which is known as Speigler correlation. The main advantage of Eq. (2-50) is its fast and simple use since only the critical temperature of the fluid under review is required. On the other hand, Eq. (2-50) is reliable for values of the ratio between gas pressure and fluid critical pressure about zero i.e., $p \ll p_c$.

$$T_L = \frac{27}{32} \cdot T_c \quad (2-50)$$

As the Speigler correlation, the midpoint rule as well is a simple and fast approach which however aims at predicting the Nukiyama temperature. This method was proposed by Fardad and Ladommatos [106] based on the results from different experiments conducted on hydrocarbons at room conditions. The data had shown that the Nukiyama temperature lies halfway between the normal boiling temperature and the Leidenfrost temperature of the fluid (Eq. (2-51)).

$$T_N = \frac{T_{sat} + T_L}{2} \quad (2-51)$$

One of the most comprehensive work conducted on droplet lifetime phenomena was that by Habchi [107], [108]. The Author introduced a method to predict both the Leidenfrost and the Nukiyama temperatures including the dependence of those key quantities on the gas pressure. In fact, experiments [40] showed that as the gas pressure increases, the droplet lifetime curve shifts towards higher temperatures by mainly following the behavior of the equilibrium temperature. The final correlation developed by Habchi after the fit of experimental results conducted at gas pressure above and below the atmospheric is shown in Eq. (2-52). In Eq. (2-52) the left-hand side term in the first row (T_X) can be the Nukiyama temperature or the Leidenfrost temperature depending on which temperature is set as T_{X1} , which represents the target of the two temperatures at atmospheric conditions. T_{sat1} and T_{sat}

are the normal boiling temperature (T_{sat} at atmospheric pressure) and the equilibrium temperature at the target environmental conditions.

$$\begin{aligned}
 T_x &= T_{sat} + \Delta T \\
 \Delta T &= T_{x1} - T_{sat1} = \Delta T_1 && p \leq 1 \text{ bar} \\
 \Delta T &= \frac{\Delta T_1 - \max[1; T_{x1} - T_c]}{T_c - T_{sat1}} \cdot (T_c - T_{sat}) + \max[1; T_{x1} - T_c] && p > 1 \text{ bar}
 \end{aligned} \tag{2-52}$$

In the case experimental data at atmospheric pressure are available, the T_{N1}, T_{L1} values from the experimental lifetime curves can be provided as input to the Habchi correlation. Those data are usually available for pure compounds or for blends whose full characterization is instead not provided. Therefore, in the case of complex mixtures, the Speigler correlation and the midpoint rule are helpful devices to initiate the computation by using the Habchi correlation.

Considering i-octane for which the experimental lifetime curve is available at different gas pressures in the open literature [109]–[112], a comparison between the experimental and the calculated Nukiyama and Leidenfrost temperatures are shown for different calculation methods. For the Leidenfrost temperature: i) use of the Speigler correlation; ii) use of the Habchi correlation by approximating T_{L1} by using the Speigler correlation; iii) use of the Habchi correlation by providing the experimental T_{L1} value. For the Nukiyama temperature: i) use of the midpoint rule by approximating T_{L1} by using the Speigler correlation (emulating lack of experimental data); ii) use of the Habchi correlation by approximating T_{N1} via the midpoint rule seen in i); iii) use of the Habchi correlation by providing the experimental T_{N1} value. Methods ii) for the Leidenfrost temperature and i)-ii) for the Nukiyama temperature aim at simulating lack of experimental data.

Comparing the results in **Figure 2-13** it is clear that the Speigler correlation applied to i-octane is not fit for predictive estimations under engine high load operations, at which usually the transition and film boiling regimes occur. Regardless of the test fluid, the constant behavior of the Speigler correlation is a weak representation of the real status of the impact wall even though $p < p_c$ are under analysis ($p_{c,i\text{-octane}} = 25.6 \text{ bar}$, $p/p_c = 1 \times 10^{-2} - 1 \times 10^{-1}$). As expectable, the best fit is obtained by combining the Habchi correlation with knowledge on the behavior of the test fluid at a reference point. It is however worth mentioning that the results from the Habchi correlation with approximated reference data are in line with the experimental trend as well. The approximated version of the Habchi correlation gains further reliability if considering the nice match at 0.5 and 2.4 bar. Those validation points play a key role in real engine conditions since the in-cylinder transition to film boiling regime can be driven by both hot walls (typically associated with high engine loads, thus, high in-cylinder pressure induced by the turbocharger) and under-pressure environment (e.g., early injection at low-intermediate engine loads typically associated with low wall temperatures), which are consistent with the two points under discussion. It must be underlined that observing the experimental data, the Leidenfrost effect for i-octane vanishes at gas pressure above 3 bar. Comparing the methods adopted to predict the Nukiyama temperature in **Figure 2-14** it can be noticed that the experimental data-based Habchi correlation is in solid agreement with the experimental validation points. As shown in the Leidenfrost plot, the Habchi correlation suffers from accuracy loss at low pressure environment ($p < 1 \text{ bar}$), however, the prediction performance throughout the high pressure range ($p \geq 1 \text{ bar}$) is almost excellent. Despite the best Habchi option and the approximated Habchi method converge towards the higher pressure (as well as the two Leidenfrost methods), difference around 10°C are present. The poor accuracy of the midpoint rule can be caused by the sum of the errors associated to the two applied simplifications (Speigler and the midpoint approximation).

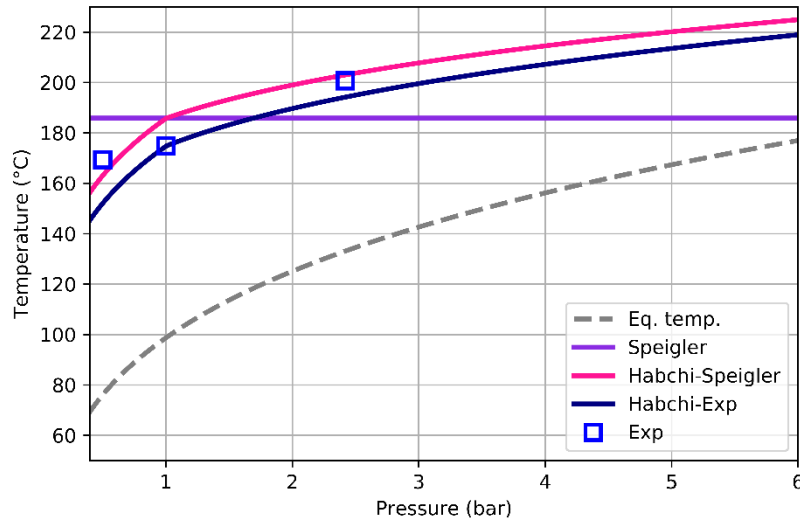


Figure 2-13: Comparison between different methods to predict the Leidenfrost temperature and experimental data [40] for i-octane at different gas pressure (0.5; 1; 2.4 bar). The i-octane equilibrium temperature (gray) is also shown as a reference.

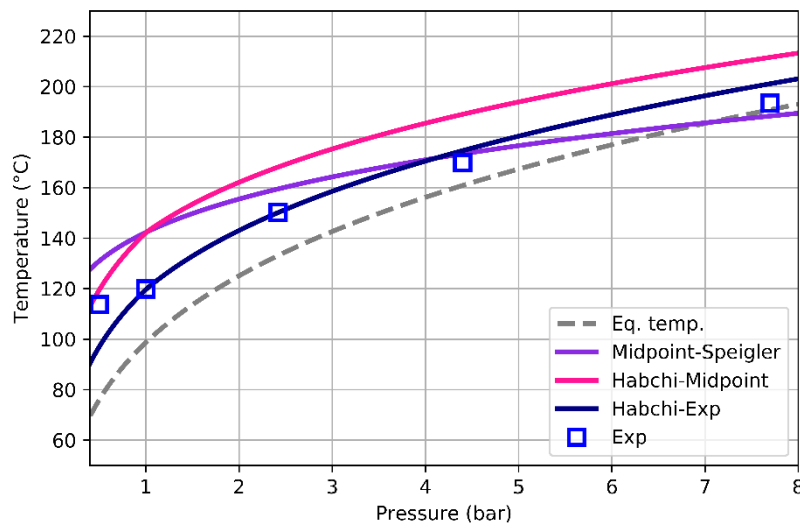


Figure 2-14: Comparison between different methods to predict the Nukiyama temperature and experimental data [40] for i-octane at different gas pressure (0.5; 1; 2.4; 4.4; 7.7 bar). The i-octane equilibrium temperature (gray) is also shown as a reference.

2.3 Results

2.3.1 Free spray validation

As pointed out at the beginning of 2.2.4, before moving on the wall impingement modeling it is necessary to be confident on the free-spray setup. The free spray data provided by the original Author of the reference case have been used as a validation benchmark [21]. The validation data include the values of the droplet d_{10} (AMD) and d_{32} (SMD) captured by means of the PDDA technique at a measure station placed around the axis of the recorded jet (**Figure 2-1**) at 30 mm downstream the nozzle tip, and pictures of the fuel spray recorded at 0.5-0.7-1.0 ms ASOI by means of the shadowgraph optical technique. The reference experimental data were recorded for a subset of injection pressure (50, 150, 300 bar) and back-pressure (1, 3, 6 bar) combinations of the original DOE including 10 points at 80°C and

1 point at 140°C. As a result, a validation matrix of 11 different points has been implemented. The free spray simulation has been set according to the computation mesh and models presented in 2.2.2, however the computation domain was extended along the spray penetration axis to 90 mm in order avoid the influence of the wall impingement against the bottom plate on the free spray results. It is underlined that even the experimental free spray characterization was conducted in a vessel that allows for the full spray plume development. The free spray simulations have been conducted by testing different values of the two tuning coefficients C_{14} , C_{15} that allow to adjust the stable diameter to tend for both the first-generation child parcels, which controls the change from primary to secondary breakup criterion, and the second-generation child parcels. The effect of those coefficients on the spray size has been studied and the results are reported in **Figure 2-15** for a reference validation point, namely the 150 bar vs 1 bar test.

It is assumed that in the untuned version of the model, both the coefficients C_{14} , C_{15} are set to one, thus, the breakup simulation simply relies on the implemented physics and hypotheses. In **Figure 2-15** the red curve is obtained by varying the value of C_{14} while C_{15} is maintained constant at 1, and vice-versa for the blue curve. Focusing on the effect of the coefficient C_{14} it is visible from **Figure 2-15** that increasing the stable diameter by about three times results in a steep increase of the parcel size and the enhancement of the d10-d32 difference. This is due to the fact that higher values of the stable diameter in Eq. (2-19) promote the delayed occurrence of the secondary breakup, which is typically responsible for the final rupture of the spray into small droplets. The effect of increasing C_{14} further on the parcels size gets weaker until it approaches an almost null sensitivity. With regards to the effect of the coefficient C_{15} , it can be seen that the higher is the value of the coefficient, thus the stable diameter in Eq. (2-22), the lower is the particle size. This behavior is due to the fact that increasing the secondary breakup stable diameter leads to slighter step-by-step reduction of the first-generation child parcels (Eq. (2-9)). Therefore, parcels with larger present diameter have larger values of the Weber number as well, thus, they will be subjected to stronger breakup regimes which induce smaller diameter values for the second-generation child parcels. Furthermore, it is worth mentioning that the coefficient C_{15} can be effectively used as a device to enhance or depress the d10-d32 difference.

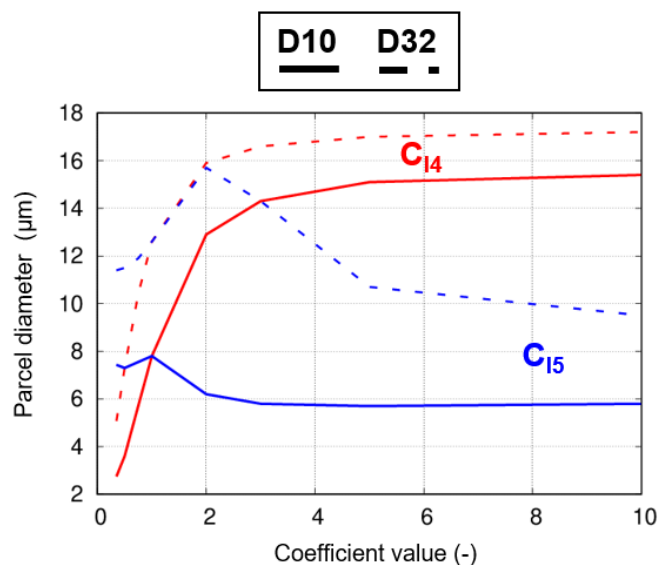


Figure 2-15: Behaviour of the parcel diameter against different values of the two tuning coefficients of the breakup model. Results referred to the case of i-octane injection under 150 bar - 1 bar pressure difference.

The tuned version of the model by Bianchi et al. has been then applied to each point of the validation matrix and the results are reported in the following. It must be underlined that the achievement of a nice accuracy has required a different tuning of the coefficients C_{j4} , C_{j5} for each validation point. **Figure 2-16**, **Figure 2-17** display the spray shape comparison between the experimental shadowgraph image (left side of each picture) and the simulation droplet plot (right side of each picture) for the available experimental combination data. It can be observed that the tuned breakup model and simulation setting is able to reproduce with high fidelity the fuel spray overall morphology. The penetration of the jets along both the axial and the radial direction at the recording times are in good agreement with the experiments. Furthermore, observing the side jet (left experimental, right numerical) it is visible the ability of the model to capture the location of dense and coarse spray zones. The match between experiments and simulations at different timings is also a sign of a reliable reproduction of the spray time evolution.

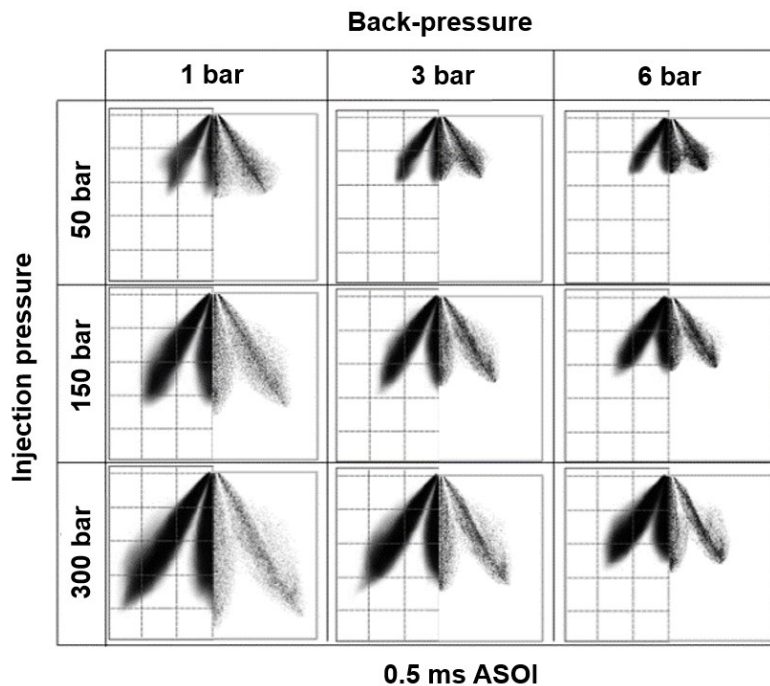


Figure 2-16: Spray shape comparison at 0.5 ms ASOI between experimental shots (picture left side) and numerical simulation (picture right side) for different injection (50, 150, 300 bar) and environmental conditions (80°C, 1 bar, 3 bar, 6 bar).

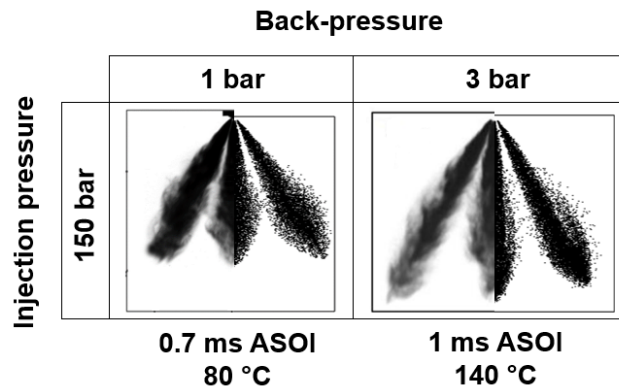


Figure 2-17: Spray shape comparison at injection pressure of 150 bar between experimental shots (picture left side) and numerical simulation (picture right side) for different environmental conditions (1 bar - 80°C, and 3 bar - 140°C) and record timing.

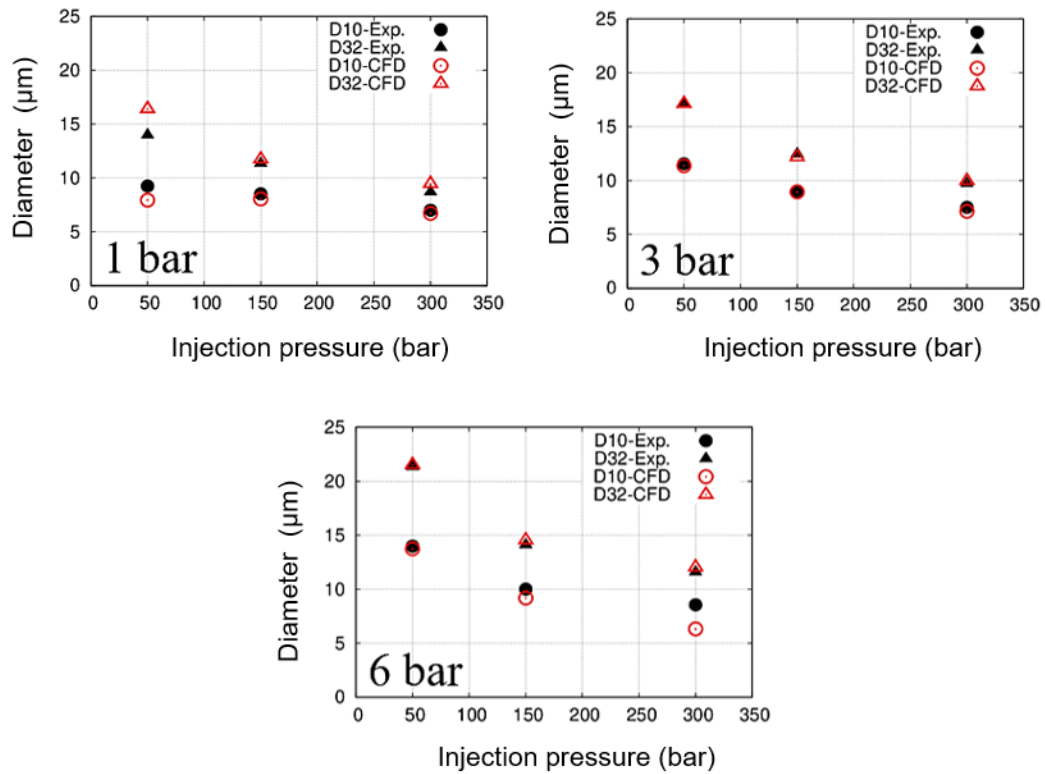


Figure 2-18: Droplet diameter (AMD and SMD) comparison between experimental and simulated data against increasing injection pressure for three different back-pressure conditions (1 bar, 3 bar, 6 bar) at 80°C.

The three plots in **Figure 2-18** show experimental and simulated AMD and SMD for the three tested injection pressure at three different values of the back pressure. Both experimental and simulated data have been obtained by averaging the punctual instantaneous measure over the time interval between the time at which the first droplet hits the measure station (real or virtual) and the EOI. It can be noticed that the tuned breakup model is able to reproduce the dependencies of the droplet size on both injection pressure and back-pressure. Focusing on the earlier, the higher is the injection pressure, the smaller are the droplet size indexes regardless to the back pressure. The capture of this decreasing behavior mainly relies on the primary breakup model, which simulates the enhanced effect of the in-nozzle turbulence due to the higher injection pressure and the resulting earlier rupture (shorter time scale Eq. (2-13)) into smaller parcels. Focusing on the effect of the environmental conditions regardless to the injection pressure, the higher is the back pressure, the larger are the droplet size indexes. In this case the capture of this increasing behavior is mainly due to the secondary breakup model, which is able to take into account the dampen momentum exchange between parcels and surrounding air caused by the increased resistance of the environment to the penetration (greater gas density). An overall nice agreement between experiment and simulation has been achieved except for the d32 at 150 vs 1 bar (**Figure 2-18**, top left) and the d10 at 300 vs 6 bar (**Figure 2-18**, bottom center) for which significant relative errors (10-15%) have been detected. An excellent d10 and d32 prediction performance has been achieved for all the three injection pressures at 3 bar back pressure (relative errors below 4%).

In light of the discussed free spray results, the injector settings and the breakup model have been considered suitable for the fuel spray-wall impingement application.

2.3.2 Wall impingement validation

In this section the fuel spray-wall impingement simulations are discussed in terms of the influence of wall temperature and gas pressure on the liquid film features against experimental data. Since both wall temperature and gas pressure variations are considered with respect to a reference base condition, namely 1 bar-80°C, the main results from the Bai-ONERA and the Senda models at those conditions are presented and compared.

Figure 2-19 displays the front view (plane XZ **Figure 2-4**) of the simulated 150 bar spray at three different moments after the impingement i.e., the instant of the very first hits against the wall, half of the injection duration (DOI), the end of injection: the results of the Bai-ONERA model are placed on the left column whilst those of the Senda model on the right. The spray bottom view (plane XY) has been also provided at the upper left of each picture. The bottom view in the central and lower pictures in **Figure 2-19** show that the Senda model has the tendency to produce a larger number of secondary parcels with respect to the Bai-ONERA model due to both the higher likelihood of splash (splash zone in nucleate boiling is extended to a larger number of kinetics conditions than that of the Bai-ONERA **Figure 2-9, Figure 2-11**) and the presence of the cluster splash sub-model, which produces 4 secondary parcels (**Figure 2-12**). From the front view pictures significant difference can be observed between the Bai-ONERA and the Senda models in terms of morphology and evolution of the secondary spray cloud. The secondary spray cloud predicted by the Bai-ONERA model is characterized by shorter radial penetration and longer axial penetration with respect to those predicted by the Senda model. In fact, at the EOI the secondary spray cloud produced by the Bai-ONERA model has a kinetic content that allowed the scattered parcels to bounce back up to the injector tip. Whilst both the radial and axial penetration resulting from the use of the Bai-ONERA model are due to sparse unshaped groups of parcels, the after-impingement cloud formed using the Senda model shows a mainly coherent motion of the cloud along the radial direction.

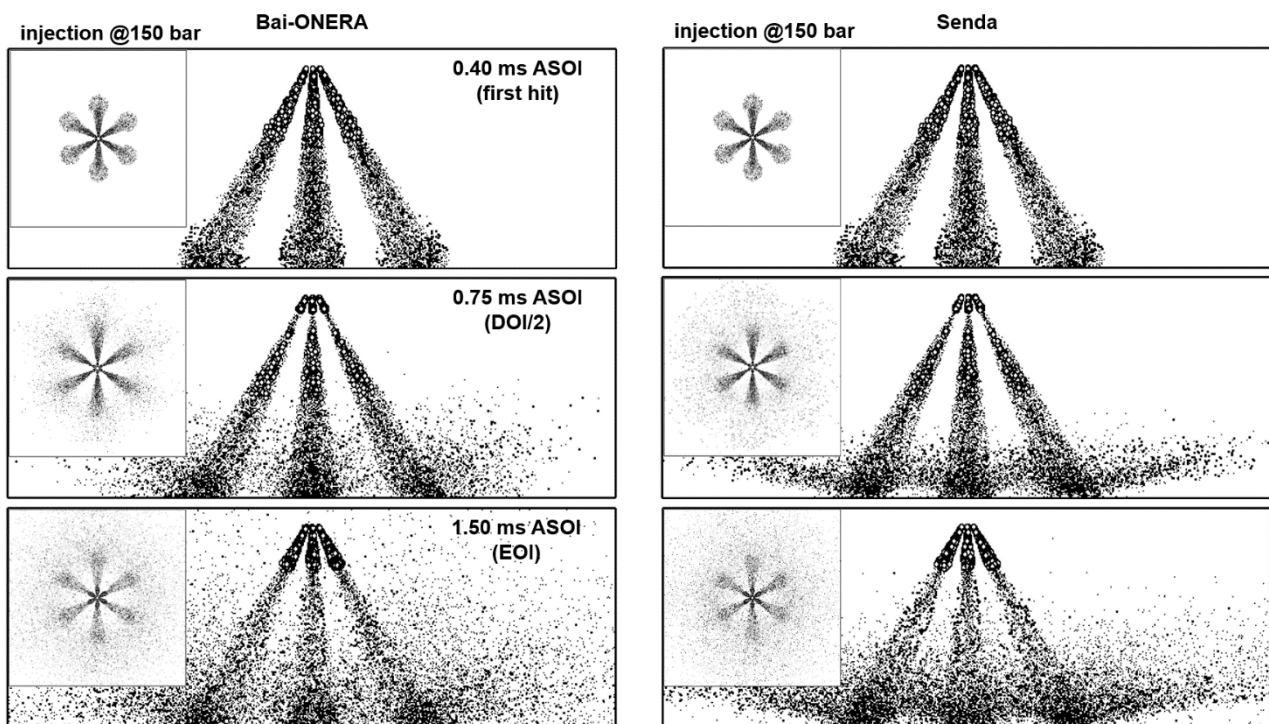


Figure 2-19: Simulated spray wall impingement morphology for the Bai-ONERA and the Senda models at different time ASOI. Injection performed at 150 bar in a vessel at 1 bar, 80°C.

Optical recordings of the test spray [89] and of other commercial GDI injectors [79], [80] showed that the liquid contour during the spray wall impingement is similar to that predicted by the Senda model whilst, to the best knowledge of the present Author, the enhanced axial bounce back predicted by the Bai-ONERA model is not supported by experimental observations. In **Figure 2-20** the same afore-discussed pictures are shown regarding the injection pressure of 300 bar. The overall behavior reported for the case at injection pressure 150 bar is confirmed even at higher injection pressure.

Figure 2-21 shows the bottom view of a single fuel jet overlapped on the liquid film footprint (filled with the film thickness from 0 to 10 μm) formed due to the after-splash and after-deposition fuel accumulation on the surface. From the upper pictures it can be observed that after the very early spray hits on the dry wall, the Bai-ONERA and the Senda models predict around the same shape and thickness of the initial liquid pool. From the Bai-ONERA central and the lower pictures it is visible a local thickening of the liquid film at the center of the footprint corresponding to the direction of the jet axis. The thickening is likely due to the greater kinetics contribution of the droplets associated to the initial liquid core, which lie in the jet direction, that push the deposited liquid at the impingement point towards the boundary of the footprint along the tangential direction, which leads to the accumulation of liquid. The Senda model is less sensitive to the aforementioned effect showing an almost homogeneous thickening of the liquid film throughout the zone that is continuously hit by the spray whilst a thinner profile is detected towards the liquid rim boundary, being the latter formed indirectly from the film wiped by the new incoming droplets on the hit zone. It is highlighted that the lower pictures (EOI) show that the liquid film footprint predicted by the Bai-ONERA model has a slim shape i.e., the thinner zone is mainly developed along tangential direction of the jet, whilst the footprint predicted by the Senda model grows along both length and width. The analysis of the pictures for the injection pressure 300 bar (**Figure 2-22**) confirms what discussed about **Figure 2-21**.

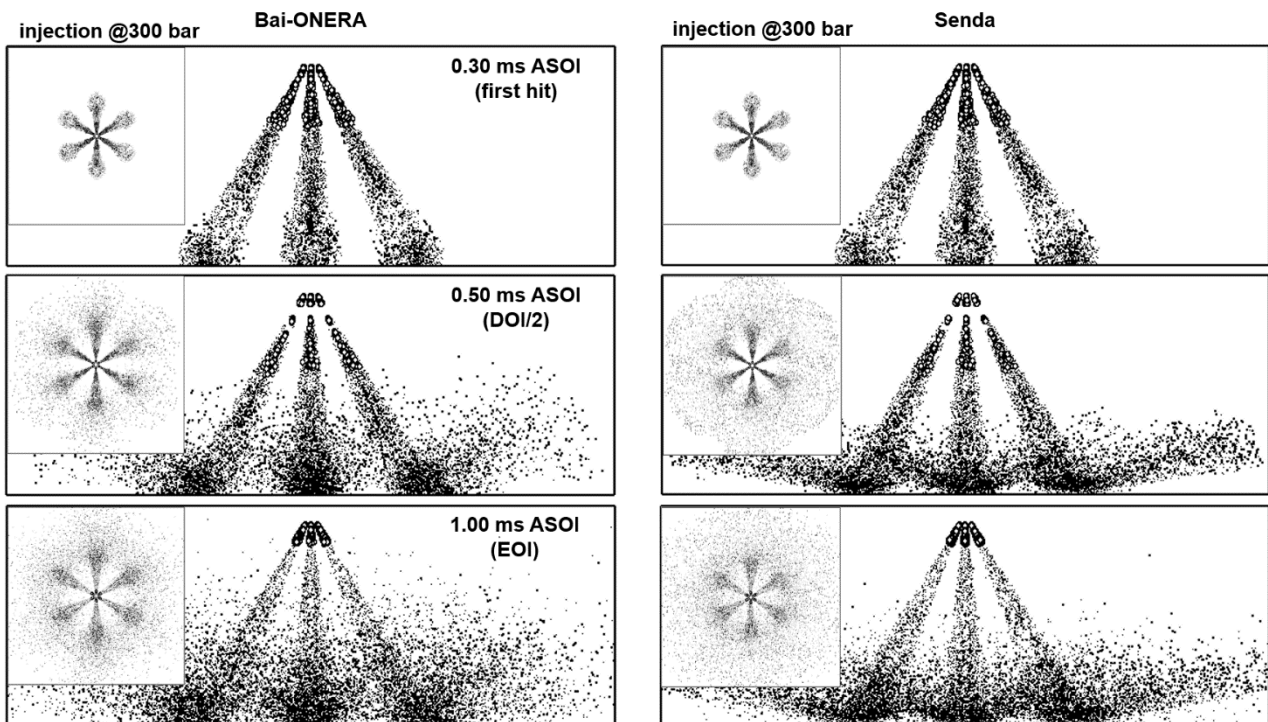


Figure 2-20: Simulated spray wall impingement morphology for the Bai-ONERA and the Senda models at different time ASOI. Injection performed at 300 bar in a vessel at 1 bar, 80°C.

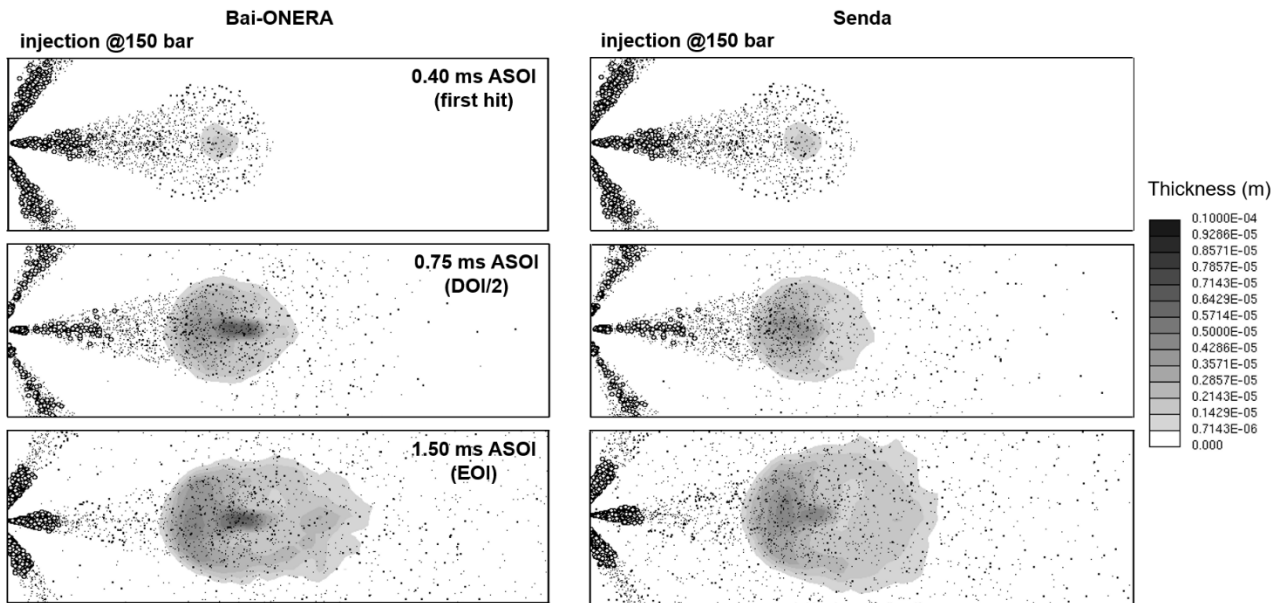


Figure 2-21: Simulated jet wall impingement footprints and droplets for the Bai-ONERA and the Senda models at different time ASOI. Injection performed at 150 bar in a vessel at 1 bar, 80°C.

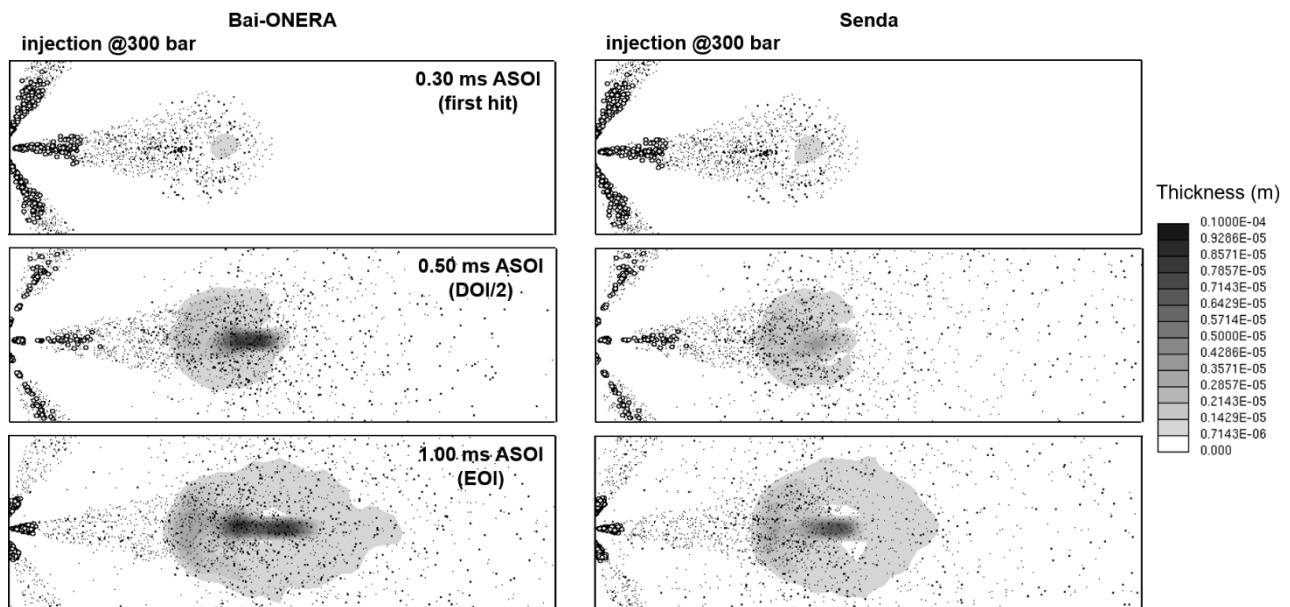


Figure 2-22: Simulated jet wall impingement footprints and droplets for the Bai-ONERA and the Senda models at different time ASOI. Injection performed at 300 bar in a vessel at 1 bar, 80°C.

Comparing **Figure 2-22** with **Figure 2-21** it is clear that the higher is the injection pressure, the smaller is the liquid film footprint because of the high velocity-induced enhanced momentum exchange between droplets and gas, which promotes: i) a faster droplet evaporation, thus there is less mass that reaches the wall; ii) splash in place of deposition, accounting for a smaller part of the incident liquid mass that remains on the wall. It is noteworthy that the higher injection pressure has led to the formation of 'rips' in the footprint (EOI, lower pictures) likely due to the stronger wiping action of the incoming droplets and to the higher impact frequency with respect to that at 150 bar. The presence of those rips is in line with experimental observations that will be shown later.

In **Figure 2-23** the outcomes of the injected liquid mass i.e., evaporation (from both film and spray), dispersed liquid as active droplets, continuum liquid as wall film, are reported for the two analysed injection pressures (left: 150 bar, right: 300 bar). The dashed lines in the upper pictures confirm the afore-mentioned faster evaporation in the case of 300 bar (50-60% vs 60-70% of the present injected liquid). The central pictures reveal that the most significant contribution to the faster evaporation is given from the mass in the form of droplets, whose amount at the end of the simulation (5 ms ASOI, namely the liquid film recording time in the experimental case) is decreased of around 10 percentage points. In the upper pictures it can be observed that the results from the Senda model are characterized by a greater evaporation rate mainly due to the faster conversion of the droplets into the vapour phase (central pictures, from EOI to 5 ms ASOI), which depends on their smaller momentum relaxation scale due to the higher scatter velocity (as noticeable in **Figure 2-19**, **Figure 2-20**). That difference is dampen at the higher injection pressure (picture at the center right). With regards to the liquid film (lower pictures), the fuel deposition clearly begins after the first hit time and linearly increases up to the EOI for both the models at both 150 and 300 bar. After the EOI the liquid film mass is subjected to a significant accumulation due to the impact of the larger and slower droplets introduced by the injector during the simulated needle closing ramp together with the reduced convective intensity.

Considering the reference condition at 150 bar, the two wall impingement models under review are comparable, and they show the same good match with the experimental film mass (**Figure 2-24**). At 300 bar, a slight difference between the film mass predicted by the two models can be observed, however the match with the experimental data is still nice.

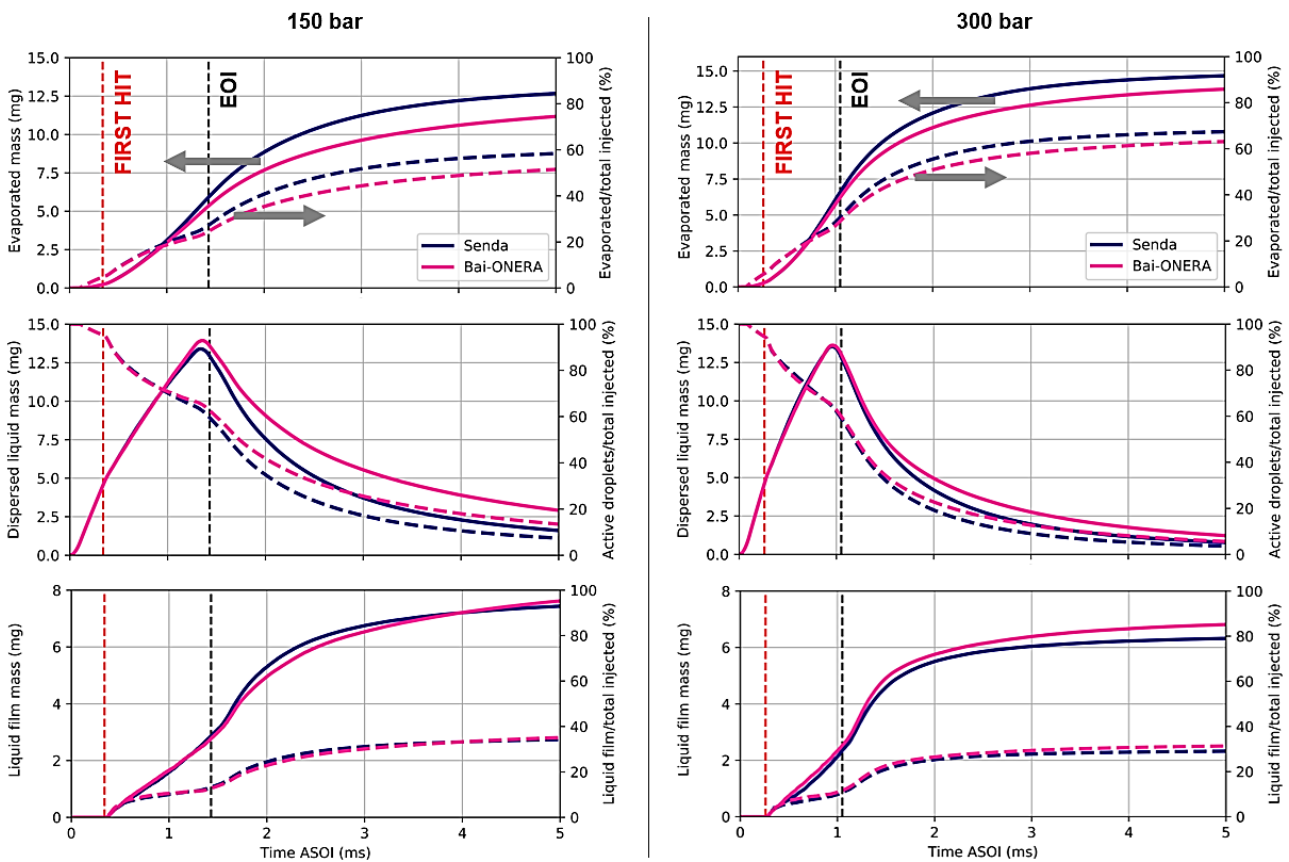


Figure 2-23: Simulated distribution over time of the injected fuel mass among vapours, liquid droplets, liquid film (injection at 150 bar on the left, 300 bar on the right) for the Bai-ONERA and the Senda wall impingement models. Solid lines represent the fuel mass, dashed lines represent the percentage of each contribution with respect to the instantaneous injected mass.

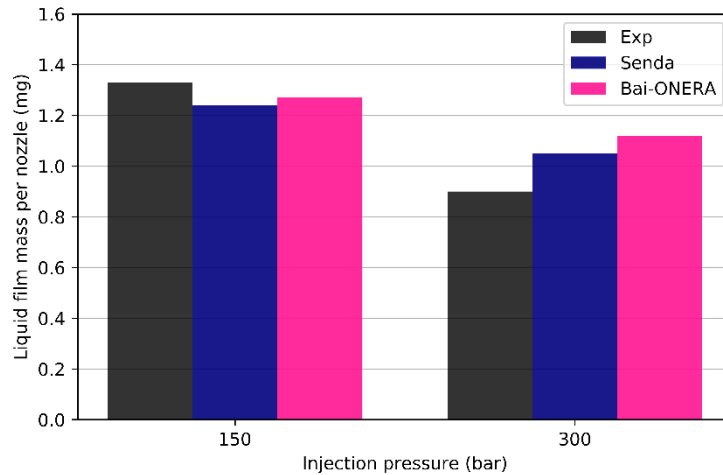


Figure 2-24: Comparison between experimental and simulated (Senda, and Bai-ONERA models) liquid film mass at 5 ms ASOI based on the footprint of a single jet.

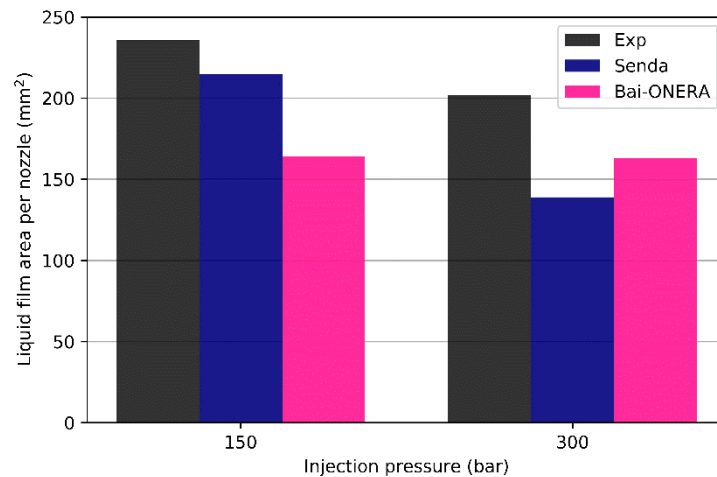


Figure 2-25: Comparison between experimental and simulated (Senda, and Bai-ONERA models) liquid film area at 5 ms ASOI based on the footprint of a single jet.

Figure 2-25 displays also the comparison between the bounding area of the experimental and simulated footprints by considering an equivalent ellipse. It is visible that both the models under-estimate the bounding area of the liquid film, however the decreasing behavior with the injection pressure predicted by the Senda model is more consistent with the experimental observations even though the predicted shrinking from 150 bar to 300 bar is enhanced significantly.

Influence of the wall temperature

In the reference work [90] the test points of interest regarding the influence of the wall temperature were recorded at back pressure of 1 bar. Under those environmental conditions, the non-dimensional temperature and the associated expected evaporation regimes are listed in **Table 2-7**. In **Table 2-7** the saturation temperature of i-octane is taken from [113], the Nukiyama and Leidenfrost have been set at the experimental values from [40]. It is visible that the three tested points are representative of the three main droplet lifetime evaporation regimes (1.3.3), respectively. It must be underlined that considering gas at 1 bar and wall at 180°C, the calculated non-dimensional temperature is very close to the transition boiling - film boiling regimes boundary. However, considering that the experimental

value of the Leidenfrost temperature for i-octane is usually given with associated uncertainty $\pm 5^\circ\text{C}$, the simulated impingement conditions may fall in the transition boiling regime or in the film boiling regime depending on the choice of the user. As a consequence, there concerns on the wall film prediction, being its formation denied if T_L is chosen between $175\text{-}180^\circ\text{C}$ (Leidenfrost effect) whilst it is allowed if T_L is chosen between $180\text{-}185^\circ\text{C}$.

Table 2-7: Thermodynamics boundary of the wall impingement models at different wall temperature values.

	Wall temperature @1 bar		
i-Octane	80°C	140°C	180°C
T_{sat} (°C)	99	99	99
T_N (°C)	120	120	120
T_L (°C)	180	180	180
T^* (-)	-0.72	0.36	1.00
Regime	Nucleate boiling	Transition boiling	Film boiling

Figure 2-26, Figure 2-27 display the residual liquid film mass at 5 ms ASOI at three different increasing environmental (wall and gas) temperature values for injection pressure of 150 bar and 300 bar, respectively. Both the impingement models under review (Senda model and Bai-ONERA model) are able to capture the temperature-dependent behavior of the real liquid film i.e., the higher is the temperature, the lower is the liquid film mass. The first temperature increment from 80°C to 140°C leads to a steep reduction of the presence of liquid film at the recording time due to two key aspects: i) the higher wall temperature (140°C) is greater than the equilibrium temperature of i-octane at ambient pressure (99°C), thus the liquid film consumption is enhanced by the pool boiling contribution in addition to the convective action; ii) at 140°C the transition boiling regime is active, thus, the rebound and splash regimes are promoted in place of deposition for different kinetics conditions of the incident droplets. At the highest test temperature (180°C) the absence of liquid film at the recording time reported by the experimental data is captured due to the activation of the film boiling regime (Leidenfrost effect). As a result, only rebound and splash without deposition are allowed as impact outcomes by both the models.

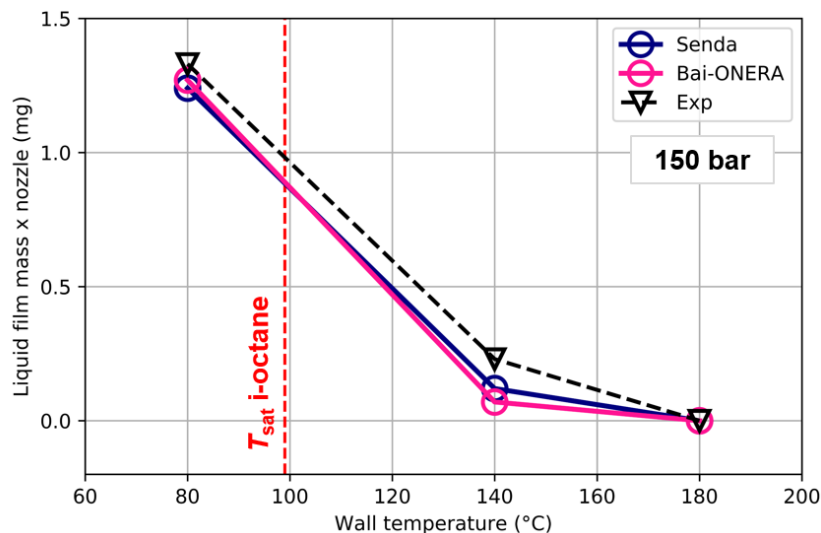


Figure 2-26: Experimental (dashed line) and simulated (solid lines) effect of the wall temperature on the liquid film formed at 150 vs 1 bar injection conditions. The film mass is taken at 5 ms ASOI for a single footprint. The saturation temperature of the test fuel (i-octane, 99°C) is also reported in red.

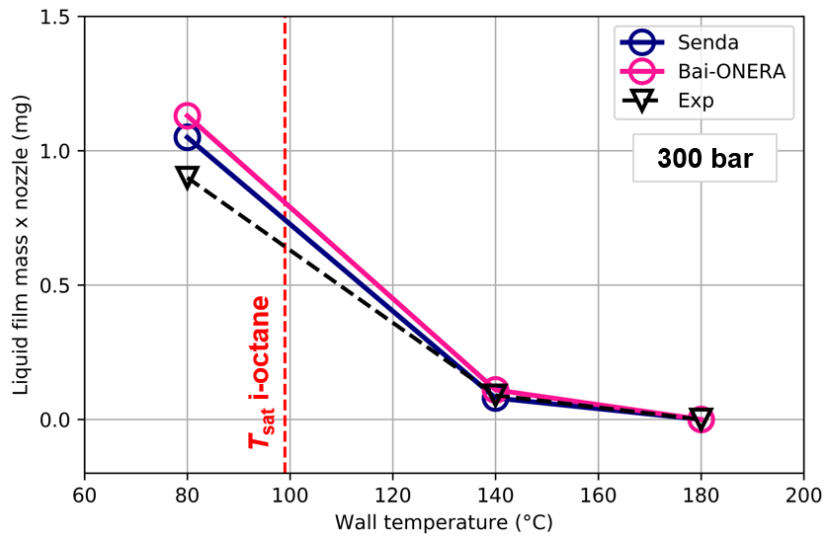


Figure 2-27: Experimental (dashed line) and simulated (solid lines) effect of the wall temperature on the liquid film formed at 300 vs 1 bar injection conditions. The film mass is taken at 5 ms ASOI for a single footprint. The saturation temperature of the test fuel (i-octane, 99°C) is also reported in red.

It must be underlined that in general if the wall temperature is set around the Leidenfrost temperature of the incoming liquid, the complete absence of liquid film is not ensured. In fact, the fuel vapor film created in film boiling regime conditions upon the impact wall boundary induces the local cooling of the wall at the impingement zones. In order to take into account this effect, the so-called one-dimensional CHT (Conjugate Heat Transfer) module must be activated to allow the runtime updating of the boundary condition temperature value. The CHT module is provided with the thermophysical properties and thickness of the solid material, then it solves the heat transfer equations at the wall by using the heat flux returned by the CFD computation step as a constraint. As a result, the local temperature of the wall boundary may fall below the Leidenfrost temperature promoting the activation of the transition boiling regime in which the liquid fuel film formation may occur resulting in non-zero film mass. It is remembered that in the reference case the impact wall is made of quartz in order to allow the LIF visualization. Since as visible in **Table 2-8** the thermal inertia of fused silica is strongly greater than that of typical piston materials (aluminum alloy, steel alloy), the surface is not subjected to significant variation of the initial temperature.

Table 2-8: Thermophysical properties of the present impact wall (fused silica) and two typical piston crown materials.

Material	Density (kg/m ³)	Specific heat (J/kg/K)	Thermal conductivity (W/m/K)	Thermal diffusivity (m ² /s)
Fused silica [114]	2200	750	1.4	8.5x10 ⁻⁷
AlSi alloy [115]	2700	960	155	≈ 6x10 ⁻⁵
Low-C steel [116]	7863	446	74.7	≈ 2x10 ⁻⁵

The simulated effect of the wall temperature is in good agreement with experimental data for both the models despite the slight under-estimation detected at 150 bar in the transition boiling regime. After the tuning of the splash exponent coefficient (Eq. (2-40), **Figure 2-10**) both the models have been considered validated even though the Senda model has shown a slightly better predicting performance.

Before moving on the effect of the back pressure, it is underlined that the sensitivity of the predicted liquid film mass by Senda and the Bai-ONERA models to the splash tuning exponent is significantly different. As reported in **Figure 2-28**, considering the case 150 vs 1 bar, 140°C ($T^* = 0.36$) the Senda model is more sensitive to the tuning of the splash ratio with respect to the Bai-ONERA model, thus, it is expected that the tuning of the Senda model by the user can be more effective to match experimental results in a wider range of conditions.

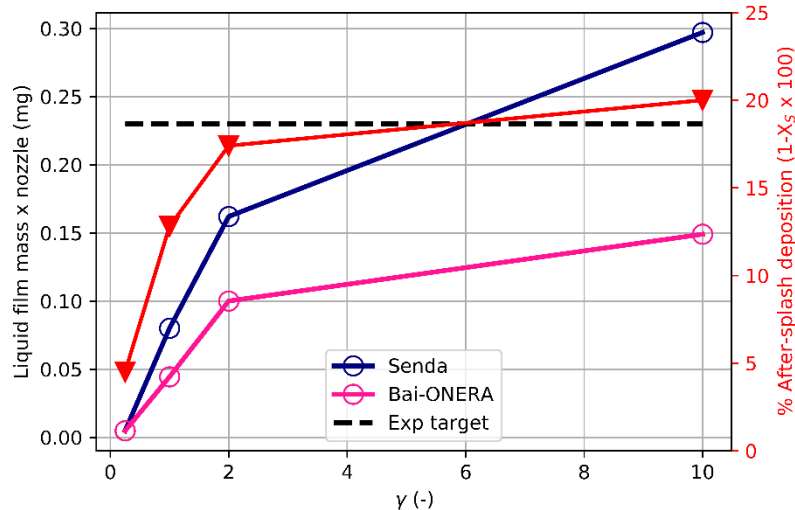


Figure 2-28: Liquid film mass (left y-axis) and After-splash deposited droplet mass (red, right y-axis) for different tested values of the splash tuning coefficient at given non-dimensional temperature ($T^* = 0.36$, transition boiling).

Influence of the back pressure

In the reference work [90] the test points of interest regarding the influence of the gas pressure were recorded at wall temperature of 80°C. Under those environmental conditions, the non-dimensional temperature and the associated expected evaporation regimes are listed in **Table 2-9**, where it is visible that the occurrence of the nucleate boiling regime only is expected for both the wall impingement models. It is underlined that at 6 bar the Leidenfrost temperature according to the Habchi correlation should be 219°C (footnote in **Table 2-9**). However, simulations have been run setting the Leidenfrost temperature at 1000°C (footnote in **Table 2-9**) since experiments [40] showed that the Leidenfrost effect for i-octane vanishes at gas pressure up to 4 bar, thus, a representative very high temperature value has been set in order to ensure that the non-dimensional temperature (Eq. (2-29)) does not exceed the film boiling threshold ($T^* = 1$) regardless to the wall temperature.

Table 2-9: Thermodynamics boundary of the wall impingement models at different gas pressure values.

Gas pressure @80°C					
i-Octane	0.4 bar	0.6 bar	1.0 bar	3.0 bar	6.0 bar
T_{sat} (°C)	69	83	99	143	177
T_N (°C)	90	104	120	159	189
T_L (°C)	145	159	180	200	1000* (219**)
T^* (-)	-0.18	-0.43	-0.72	-1.92	< 0
Regime	Nucleate boiling	Nucleate boiling	Nucleate boiling	Nucleate boiling	Nucleate boiling

* used in the code; **calculated with the Habchi correlation.

Figure 2-29, Figure 2-30 display the residual liquid film mass at 5 ms ASOI at different increasing environmental pressure values (0.4, 0.6, 1, 3, 6 bar) for injection pressure of 150 bar and 300 bar, respectively. It is visible that both the models reproduce the experimental bell-shaped behavior of the profile for each injection pressure, furthermore, the slope-change pressure as well (1 bar) has been captured.

With regards to the high-pressure branch of the curves (1-6 bar), it has been observed that the higher is the back pressure, the lower is the liquid film mass. The latter behavior depends on the fact that higher values of the back pressure lead to the increased resistance of the surrounding air to the spray penetration, which promotes a longer free-path time of the droplets. Thus, fewer droplets can reach the impact wall, and, as a consequence of the longer residence time into the gas, they show a reduced kinetic contribution.

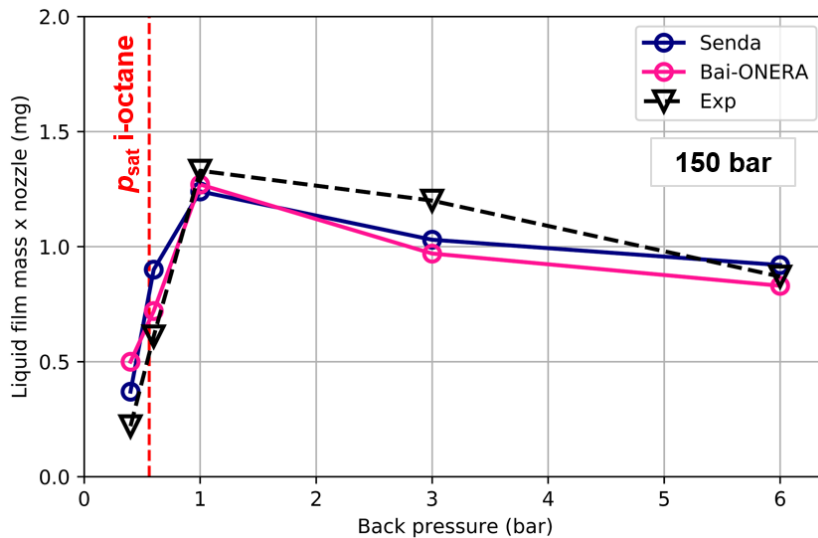


Figure 2-29: Experimental (dashed line) and simulated (solid lines) effect of the gas pressure on the liquid film formed at 80 °C, 150 bar injection pressure. The film mass is taken at 5 ms ASOI for a single footprint. The saturation pressure of the test fuel (i-octane, 0.56 bar) is also reported in red.

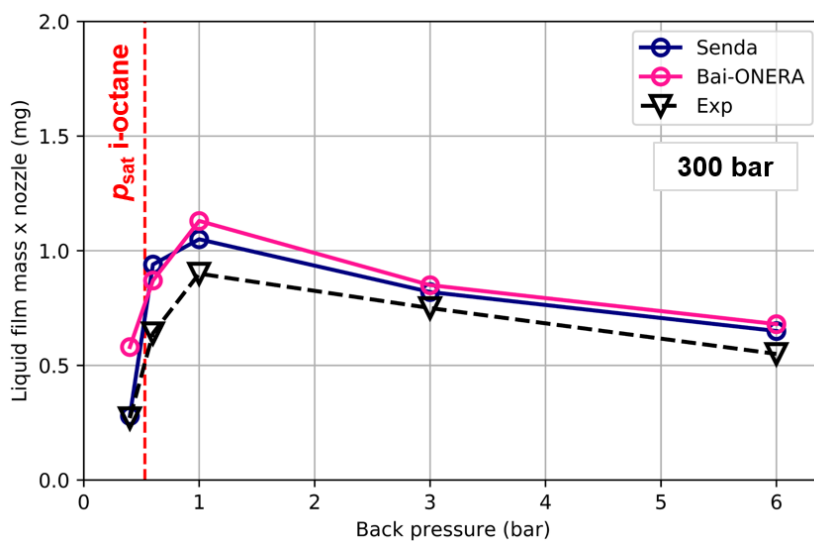


Figure 2-30: Experimental (dashed line) and simulated (solid lines) effect of the gas pressure on the liquid film formed at 80 °C, 300 bar injection pressure. The film mass is taken at 5 ms ASOI for a single footprint. The saturation pressure of the test fuel (i-octane, 0.56 bar) is also reported in red.

With regards to the low-pressure branch of the curves (0.4-0.6 bar), experiments highlighted that considering the saturation pressure of the injected fuel at given temperature, the lower is the back pressure, the lower is the liquid film mass. The decrease of the liquid film in spite of the longer spray penetration at low pressure is due to saturation-induced phase change of the deposited liquid. The simulation results suffer from the significant over-estimation of the film mass at 0.6 bar for both the injection pressures with respect to the experimental data. The mismatch is likely due to the fact that according to the NIST properties calculation, the deposited i-octane at 0.6 bar has not achieved the equilibrium conditions (0.56 bar).

Despite the results returned by the two models are almost comparable, the Senda model has shown a slightly improved overall predictive capability. The effect of the gas pressure on the liquid film at the reference condition 150 bar, 80°C has been also validated by comparing the macroscopic shape, area, and thickness distribution with respect to the LIF images recorded at 5 ms ASOI (**Figure 2-31**).

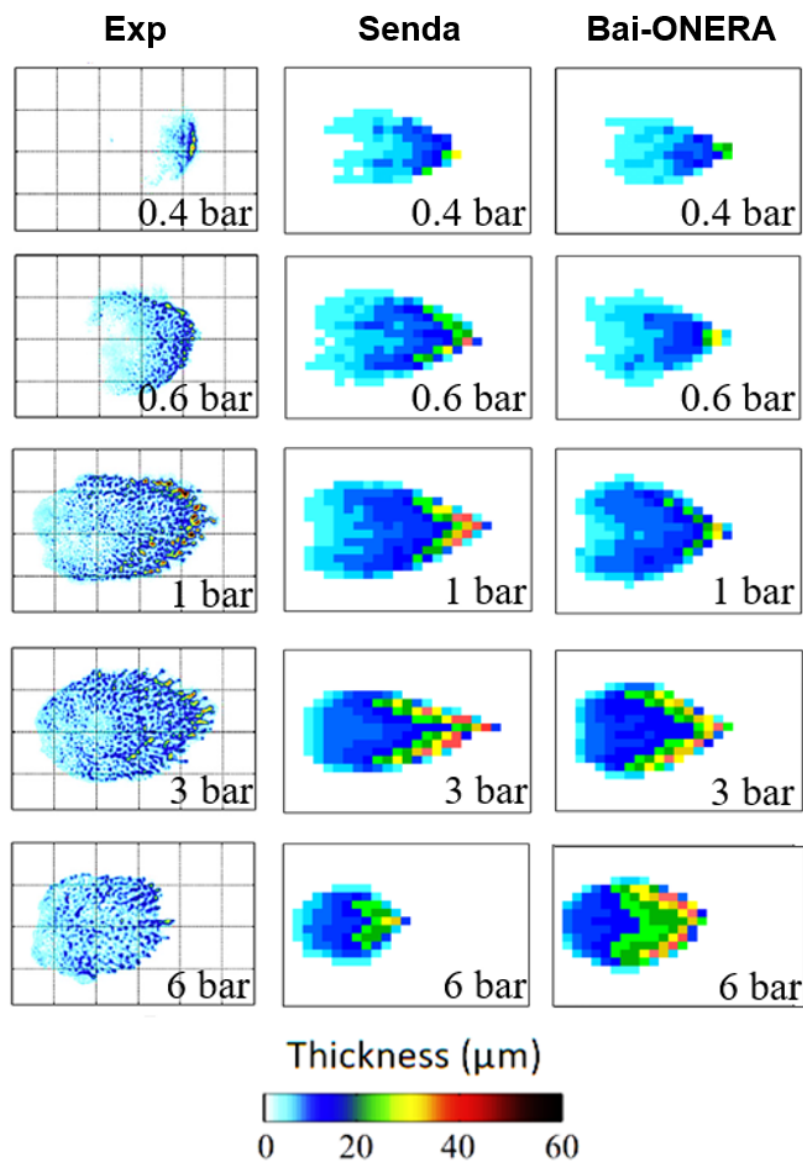


Figure 2-31: Liquid film morphology comparison between experiments (left column, LIF images) and simulation (central column: Senda, right column: Bai-ONERA) at 5 ms ASOI.

In **Figure 2-31** a general good agreement between the simulated and experimental shape of the footprint can be observed for the high-pressure branch of the profile. Regarding the results for the low-pressure branch (first two rows), the simulated footprints are larger than those recorded by the LIF mainly due to the presence of cells covered in fuel film of thickness in the range 1-8 μm (azure zones) whilst the liquid accumulation-induced rims (blue zones) have been reasonably reproduced. It is noteworthy that the Senda model can capture with greater accuracy the liquid film thickness distribution along the footprint, in particular for the high-pressure branch results around the accumulation rims.

As a result, the two models have been considered validated under different conditions, and the degree of accuracy on the liquid film mass and thickness distribution presented in this thesis is not present yet in the current state of the art. Considering the validated results concerning the liquid film mass and overall shape (representative of the liquid film exchange area) it is expected that the presented modeling settings allow for the prediction of the after-impingement liquid film formation and the consequent production of rich pockets from its evaporation.

3 After-impingement oil-fuel dilution simulation

3.1 State of the art and original contribution

In this section emphasis is posed on the effect of the fuel liquid film formation over the cylinder liner wall, which is wet by a layer of few micrometers of lubricant oil. As shown in **Figure 3-1**, for increasing back-pressure, considering three different temperatures representative of the cylinder liner wet wall at low (80°C) and high engine loads (140-180°C), the most likely vaporization regimes for impacting iso-octane are nucleate and transition boiling. As a result, according to the typical kinetics of the impacting fuel droplet, deposition-splash induced patches of liquid fuel may overlap to the lubricant oil layer.

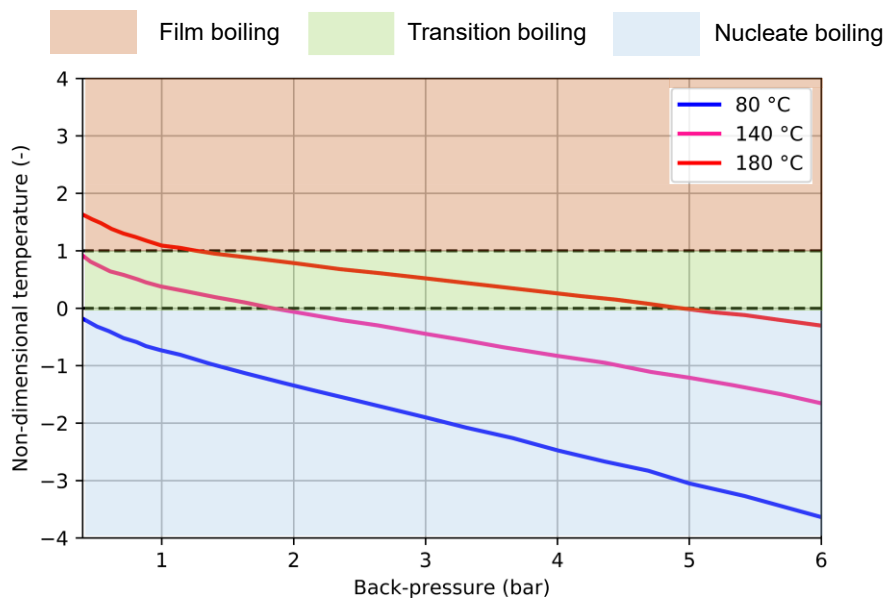


Figure 3-1: Pressure vs non-dimensional temperature maps of liquid iso-octane vaporization regimes for different wall temperatures.

As long as oil and fuel are in contact before the liquid fuel film is removed from the wall thanks to the continuous evaporation and the action of the piston top ring, the two liquids dilute each other due to diffusive mass transfer. As mentioned in 1.4 the dilution-induced oil-fuel mixture detachment and re-entrainment into the cylinder, may promote LSPI at high loads and soot formation at low loads. Therefore, the simulation of the after-impingement interaction between fuel in the continuum liquid phase and the lubricant oil can help to assess the risk of those phenomena for given engine operating configuration (engine load, spray pattern, spray timing, fuel and oil properties), avoiding the high time and cost requirements for comprehensive experimental campaigns, especially in the case of LSPI detection. Despite the fact that several significant works on oil induced LSPI experiments have been published, very few numerical works are available in the current literature because of the complexity of the problem and the lack of experimental data and validated

chemical kinetics schemes of the ignition properties of most of the heavy molecules that are representative of engine lubricant oils.

In [117] Zöbinger and Lauer have conducted an in-depth numerical analysis of the effect of different practical parameters on the ignition of oil-fuel droplets. In particular, the droplet ignitability boundaries for different oil-fuel shares, droplet initial temperature and initial diameter, droplet in-gas release time have been explored by using the Hieß ketohydroperoxide-induced based threshold criterion i.e., the ignition occurs if the near-droplet mixture shows the presence of oil mass fraction above 1×10^{-4} and has a temperature above 680 K. The Authors modelled both oil and fuel as multi-component mixtures of selected molecules based on Gas Chromatography data of real oils and on the distillation curve of real fuels, respectively. The models of the two liquids were implemented in a commercial CFD software which was used to perform three-dimensional simulations of the evaporative behavior of a single droplet placed into a quiescent box under engine-like time-variable pressure and temperature boundary conditions. For each of the tested aforementioned parameters, the ignitability of the droplet was assessed according to the Hieß criterion based on the simulated fields of temperature and mixture composition around the droplet. It is underlined that the direct simulation of oil-fuel dilution in three-dimensional CFD engine simulations is not viable due to high computation cost spent that would be necessary to account for the multi-fluid liquid film equations and to implement a fine mesh at the cylinder wall boundary. In fact, in common practice the cylinder wall boundary can be discretized with base cell size of ≈ 0.8 mm since neither particular low scale phenomena are involved in that zone (e.g., injection of high velocity parcels near the injector tip, flame kernel growth near the spark plug), nor the capture of particular geometric features is required (e.g. spark plug electrodes), however micrometric minimum size would be required in the impact regions in order to discretize the oil layer. Thus, the use of two-dimensional and one-dimensional external models for both stand-alone evaluation and offline integration with CFD codes is the most viable option to approach this problem. In [118] Yu and Min have presented a one-dimensional mathematical model for simulating the fuel vapor absorption and desorption from the engine oil film and the oil-liquid fuel dilution with the aim to model the contribution of these phenomena on the emission of unburnt HCs. With regards to the oil-fuel dilution modeling, the Authors implemented a two-liquids oil-fuel diffusion model by considering oil and fuel as two different pseudo-pure liquids characterized by the mean properties of commercial oils and fuels. The oil-fuel diffusion coefficient was predicted into two steps: i) firstly the Authors adopted the literature empirical correlation of Hayduk and Minhas [119] to estimate the diffusion coefficient at infinite dilution conditions i.e., solute molar concentration $< 10\%$, for oil-fuel as solute-solvent mixture and vice versa; ii) the two infinite dilution coefficients (D_0) are used to perform the runtime calculation of the effective diffusion coefficient according to the classical power-law formula depending on the liquid local concentration (x) of fuel (subscript F) and oil (subscript O) at each computation point along the film thickness (Eq. (3-1)). The liquid film temperature change caused by the fuel evaporation and the engine displacement was not taken into account, namely a uniform constant temperature was set along the film thickness.

$$D_{F-O} = D_{O-F} = (D_{0,F-O})^{x_F} \cdot (D_{0,O-F})^{x_O} \quad (3-1)$$

In [120] Zhang et al. improved the dilution model proposed in [118] by implementing additional modeling features in order to evaluate the oil-fuel composition of both the liquid mixture scraped by the piston and that left on the cylinder wall for the sake of considerations on frictions due to the oil viscosity reduction and providing a proof of concept of the possible

presence of significant oil amount into the gaseous phase due to mass diffusion as a cause of the LSPI. The Authors introduced a multi-component approach to model both oil and fuel, each component is traced over thickness and time. Infinite dilution conditions were considered for the diffusive mass transfer with the diffusion coefficient predicted by means of the classical literature empirical correlation of Wilke and Chang [121]. Furthermore, the liquid temperature change due to the heat transfer with the gaseous phase and the wall was included. However, the temperature dependence of the materials (solid, oil, fuel) was not accounted for.

In this research project, the model by Zhang et al. was taken as a reference and coded from scratch. The code aims at supporting the very early development stage of GDI engines, by performing sensitivity analysis to compare different engine relevant parameters such as film thickness, liquid fuel wall film location, injection timing and strategy, oil-fuel properties and additives, wall temperature, ranking them based on the resulting oil properties degradation and oil accumulation into the scraped liquid. Due to the high sensitivity of the pre-ignition conditions to temperature and oil-fuel composition, some improvements were implemented in order to increase accuracy and reliability in reproducing the oil-fuel mixing and distribution. Focusing on the numerical aspect, the main contributions regard the introduction of two numerical strategies aimed at refining the prediction of the final thickness and the temperature of the scraped liquid by means of a variable grid-size mesh, and the speed-up of the dilution simulation thanks to the decoupling of the solid wall and the liquid solvers. Moreover, the estimation of the liquid properties was upgraded by using more accurate mixing rules and an in-house developed methodology for the oil-fuel diffusion coefficient. It must be considered that as reported in [122], the comparison between different literature empirical correlations and experimental data on several solute-solvent combinations revealed that the use of correlations to estimate the liquid phase diffusion coefficient leads to values of the relative error from 13% to 20% for organic solutions and from 20% to 35% for aqueous solutions. Therefore, significant efforts were pushed towards the development of a new methodology to fill the gap.

3.2 Methodology

In this section the workflow of the mathematical oil-dilution model and its numerical implementation are firstly presented. Then, the methods adopted for the calculation of each property are reported, particular emphasis is posed on the liquid phase diffusion coefficient, being the latter one of the main contributions of this research on this topic.

3.2.1 Oil-Fuel dilution model

In this research project a one-dimensional transient numerical oil-fuel dilution model was coded in *Python* 3 environment. The computation domain develops along the engine cylinder radial direction accounting for the discretization of the liquid film thickness for a given punctual axial position. The domain is divided into two layers: i) the solid layer, which represents the cylinder liner wall; ii) the liquid layer, which represents the oil-fuel mixing domain. The liquid layer is initialized as the step overlap between the oil layer and the liquid fuel film, which are represented by pseudo-pure liquids of given thickness height (h_O , h_F). For the sake of simplicity, a Cartesian coordinates problem is considered, then the origin of the Cartesian reference system is placed between the two main layers at the so-called Solid-Liquid Interface (SLI). The interaction between the liquid film and the gaseous stream at the so-called Liquid-Gas Interface (LGI) is modelled by considering the time-varying liquid film depletion by means of a variable cell size moving boundary approach that will be discussed in the following. The scheme of the computation domain is shown in **Figure 3-2** for sample initial and final simulation times.

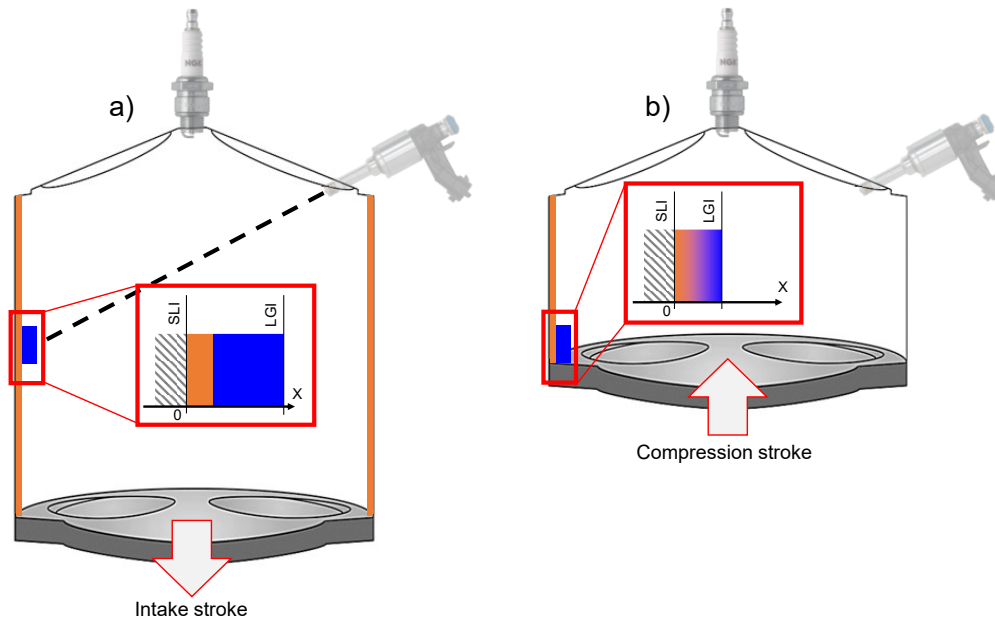


Figure 3-2: Sketch of the oil-fuel dilution domain at the simulation start (a) and stop (b) times.

The considered simulation time domain is the time span from the engine SOI, at which it is assumed that the liquid film forms instantaneously, to the piston arrival at the given liquid film stroke location according to the instantaneous piston speed. As shown in **Figure 3-2**, at the piston arrival the oil-fuel mixture present in the residual liquid film at $h(X) > h_0$ is subjected to scrap, and it can be analyzed in the perspective of LSPI risk potential. The oil-fuel mixture present at $h(X) \leq h_0$ can be analyzed for oil pollution and degradation evaluations.

Solid layer modeling

The cylinder wall modeling includes the conductive heat transfer through the solid wall (subscript S) according to the classical Fourier's law (Eq. (3-2)) under the assumptions of constant thermo-physical properties (thermal conductivity (k), density (ρ), specific heat (c_p), thermal diffusivity (α)) of the solid material and lack of heat sources.

$$\frac{\partial T_S}{\partial t} = \alpha_s \frac{\partial^2 T_S}{\partial X^2} \quad (3-2)$$

According to the X -positive direction, it is considered that the left-end of the solid layer is directly affected by the coolant. Therefore, due to both the high thermal capacity of the coolant and the high thermal inertia of the solid in comparison with the computation time (dozens ms at LSPI conditions i.e., 1200-2000 r/min) a temperature Dirichlet boundary condition is adopted at the coolant side i.e., the temperature at the solid left end is set at the constant value of the coolant temperature. With regards to the right-end of the solid layer (SLI), since gravity and shear forces on the liquid phase (subscript L) are not significant considering the typical simulation time, wall film mass and area, a zero liquid velocity is considered at the SLI. Therefore, being conduction the leading heat transfer mechanism at the SLI, the heat flux and temperature continuity (Eq. (3-3)) is adopted as boundary condition for the solid layer right-end. The cylinder wall is represented by a h_s thick solid layer, which is thinner than the cylinder liner height according to different computation tests performed to evaluate the maximum in-solid heat penetration depth assuming the maximum time interval available for the evolution of the 2-layer system, namely from SOI to the end of compression stroke (i.e., under the hypothesis of liquid fuel film location at the TDC).

$$\begin{cases} k_S \frac{\partial T_S}{\partial X} \Big|_{SLI} = k_L \frac{\partial T_L}{\partial X} \Big|_{SLI} \\ T_S \Big|_{SLI} = T_L \Big|_{SLI} \end{cases} \quad (3-3)$$

Considering the cylinder wall made of cast iron, the non-varying temperature height is in the order of 1-2 mm against the typical full liner thickness (≈ 5 mm), namely it was verified that the temperature profiles along the solid layer are not affected by thickness above 2 mm. This preliminary size-optimization analysis was applied to the solid layer in order to avoid waste of simulation time.

Liquid layer modeling

The modeling of the liquid film is performed under the following assumptions: i) thin film; ii) no viscous dissipations; iii) dilute binary oil-fuel mixture; iv) the two liquid compounds (oil and fuel) are considered as pseudo-pure liquids; v) evaporation is allowed for fuel only. In the liquid layer both heat and mass transfer are taken into account. It is considered that the heat transfer through the liquid layer relies on the conduction mechanism only, which is modelled by means of the Fourier's equation as shown in Eq. (3-2) for the solid layer. As mentioned before, the SLI boundary conditions are consistent with the one adopted at the solid side (Eq. (3-3)). It is considered that the liquid film depletion is caused by the liquid evaporation only, thus, a temperature Robin boundary conditions is adopted at the LGI in order to account for the convective heat transfer (Eq. (3-4)). In Eq. (3-4) H is the convective heat transfer coefficient between the liquid surface and the air stream, T_G^* is the free stream gas temperature reduced by the contribution of the fuel latent heat of vaporization (H_V) due to the liquid film evaporation rate (\dot{m}) (Eq. (3-5)).

$$k_L \frac{\partial T_L}{\partial X} \Big|_{LGI} = H \cdot (T_L \Big|_{LGI} - T_G^*) \quad (3-4)$$

$$T_G^* = T_G - \frac{\dot{m} \cdot H_V}{H} \quad (3-5)$$

The mass transfer through the liquid layer is driven by the diffusion mechanism, thus, the oil-fuel distribution changes along thickness can be described by the classical 2nd Fick's law (Eq. (3-6), considering mass concentration per volume (ξ)). Since the liquid mixture is binary due to the pseudo-pure liquids assumption, Eq. (3-6) is applied to solve the fuel concentration only, then the oil concentration is calculated as the complement to unity.

$$\frac{\partial \xi_F}{\partial t} = D_{F-o} \frac{\partial^2 \xi_F}{\partial X^2} \quad (3-6)$$

At the SLI a no slip and no penetration boundary condition is adopted in order to avoid mass flux through the solid layer, whilst at the LGI the convective-induced liquid depletion is represented by means of a concentration Robin boundary condition (Eq. (3-7)), where M is the mass transfer coefficient, and the term in the parenthesis on the right-hand side is the driving force of the mass flux, namely the concentration difference between the fuel vapor at the LGI ($\xi_F \Big|_{LGI}$), which is estimated by assuming the thermodynamic equilibrium of the fuel considered as a perfect gas (Eq. (3-8)) and the one into the gas free stream (ξ_G). Since the size of the fuel vapor released by the LGI condition at the computation location is negligible with respect to the size of the in-cylinder gas mixture, it is assumed that the fuel vapor concentration into the free stream remains constant according to the target engine air-fuel ratio.

$$D_{F-O} \left. \frac{\partial \xi_F}{\partial X} \right|_{LGI} = M \cdot (\xi_F|_{LGI} - \xi_G) = \dot{m} \quad (3-7)$$

$$\xi_F|_{LGI} = \frac{p_{sat,F}(T_L|_{LGI})}{R_F \cdot T_L|_{LGI}} \quad (3-8)$$

As a result, the instantaneous liquid film depletion per unit area is calculated according to Eq. (3-9), then, the thickness of the non-evaporated liquid film for the next computation step is given by $h_L(t+1) = h_L(t) - \delta(t)$. Once the evaporated liquid height is calculated and subtracted by the cell size, the liquid end cell is removed or it is not depending on the remaining liquid height in comparison with the full cell size. If one considers the fixed-space grid approach proposed in [120], given the evaporation-induced liquid mass loss while the solution volume (i.e., ΔX in this one-dimensional domain) remains fixed, the mass concentration in the liquid end cell would be underestimated until the motion of the LGI boundary towards the face of the neighbor cell.

$$\delta = \frac{\dot{m} \cdot \Delta t}{\rho_L} \quad (3-9)$$

Gas-liquid interface calculation

Applying variable-cell size at the liquid end cell, as the evaporated height is calculated, then the liquid end cell shrinks in its turn until the removal. Nevertheless, it must be underlined that the higher is the shrinking before the cell removal, the thinner becomes the liquid end cell. Therefore, as the effect of the evaporation develops for successive computation steps, the liquid end cell may collapse with concerns on the simulation steadiness. In order to accomplish both the requirements of accurate and steady simulations, in this research project an evaporation threshold criterion together with the cell resizing approach is proposed. For a given time-step, the ratio between the instantaneous evaporated height (Eq. (3-9)) and the cell size is named η , thus, the evaporation threshold is defined as the limiting value of η that must be exceeded to assume the liquid end cell as fully evaporated. Therefore, before reaching the evaporation threshold, the liquid end cell is maintained by reducing its size every time-step as $\Delta X_L - \delta$, and its concentration, namely $\xi_F \cdot \Delta X_L / (\Delta X_L - \delta)$. Once the evaporation threshold is exceeded, the liquid end cell is removed from the computation domain. It must be considered that the cumulative calculated evaporated height may exceed the η -threshold without exceeding the LGI boundary cell size. In order to comply with both mass conservation and evaporation rate calculation, in this case the liquid end cell is removed while the remaining non-evaporated liquid height is merged in the neighbor cell (the new liquid end cell) by updating its size as $2\Delta X_L - \delta$, and its concentration as $\xi_F \cdot \Delta X_L / (2\Delta X_L - \delta)$. A schematic view of the η evaporation threshold criterion for the liquid domain resize in reported in **Figure 3-3**.

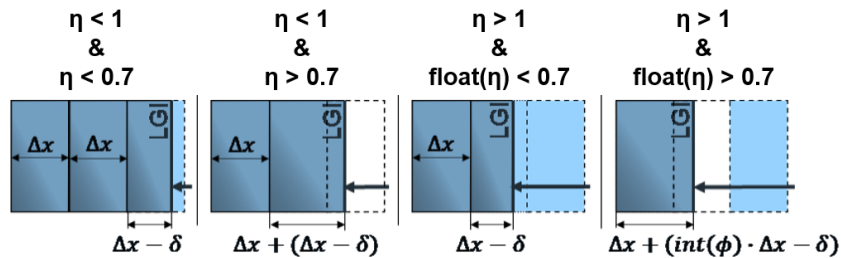


Figure 3-3: Scheme of the algorithm adopted to update the liquid boundary cell and the domain size because of the fuel evaporation.

Mixture properties calculation

As far as the oil-fuel mutual diffusion is concerned, each computation cell in the liquid layer may contain both oil and fuel, thus, the calculation of the mixture properties (subscript L) is needed. The mixing rules implemented in this research project for the liquid phase are the following: i) weighted mass average for density and specific heat; ii) the Filipov law [123] for thermal conductivity (Eq. (3-10)) of binary liquid mixtures; iii) the simplified Grunberg-Nissan law [124] for the dynamic viscosity (Eq. (3-11)). The Filipov law was developed based on steady state measurements of the thermal conductivity of both pure substances, including 83 organic liquids, and different binary mixtures, including 20 systems of non-associated liquids and 10 systems of a non-associated liquid mixed with an associated liquid. In [123] the analysis of the experimental data on binary mixtures revealed a parabolic behavior of the thermal conductivity with respect to the concentration. In particular, the quadratic term was found to be correlated to the difference between the thermal conductivity values of the two components by the constant of 0.72 tuned for non-associated binary mixtures, which is the case of the present study since both fuel and oil are non-polar liquids. The Grunberg-Nissan correlation is a classical and widely adopted method for the calculation of the viscosity in relatively low temperature liquid mixtures. In the current state of the art, this correlation has proven to return robust predictions in general while suffering from performance derating in the case of mixtures involving water or large differences in the molecules' size, however, both these circumstances are not present in this study, which is focused on hydrocarbons molecules with comparable size. The thermal diffusivity required in Eq. (3-2) is calculated according to its definition once the single liquid thermophysical properties of the mixture are predicted.

$$k_L = w_F \cdot k_F + w_O \cdot k_O - 0.72 \cdot (k_F - k_O) \cdot w_F \cdot w_O \quad (3-10)$$

$$\ln(\mu_L) = x_F \cdot \ln(\mu_F) + x_O \cdot \ln(\mu_O) \quad (3-11)$$

Numerical setting

In order to capture the liquid phase diffusion phenomena occurring in heights of few dozens of microns as that observed in GDI engines while optimizing the simulation time, a base grid-size (ΔX) of 0.1 μm has been adopted. Once the base grid-size has been determined based on the spatial scale constraints, the code was tested with different time-steps (Δt) with the aim of determining the best compromise between computing cost and numerical stability. Since several tests highlighted temperature divergence in the liquid layer close to the SLI and to the initial oil-fuel interface, the so-called Courant number (Co) from the Courant-Friedrichs-Lewy (CFL) stability condition for the heat equation is applied to define the maximum stable time-step (Eq. (3-13), [125]).

$$Co = \alpha \cdot \frac{\Delta t}{\Delta X^2} \leq 1 \quad (3-12)$$

As mentioned before, due to liquids diffusion each cell may contain a binary oil-fuel mixture, thus, the thermal diffusivity varies cell by cell. In order to ensure the stability condition throughout the simulation time, Eq. (3-12) is solved with respect to the time-step considering the liquid composition characterized by the higher thermal diffusivity, namely the pure lubricant oil in the case of oil-gasoline dilution as visible from the thermo-physical properties reported in **Figure 3-4** for a sample multigrade lubricant oil and commercial-like nowadays gasoline. As a result, depending on the specific liquids in exam, the simulation time-step

calculated at the simulation start by setting the CFL limiting condition at 0.9 (right-hand side of the inequality in (3-12)) is around 1×10^{-7} s.

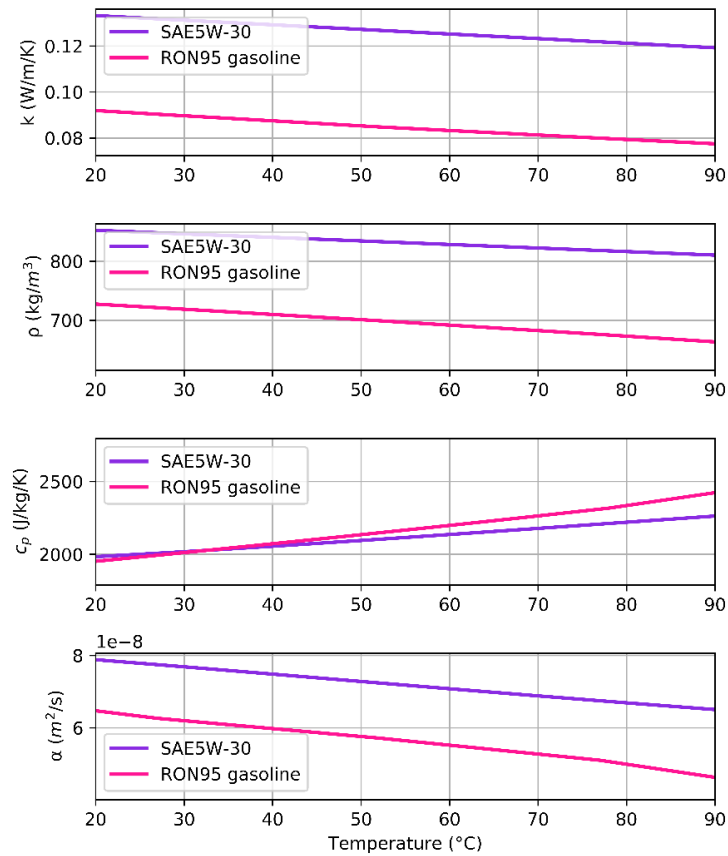


Figure 3-4: Comparison between different thermo-physical liquid properties (thermal conductivity, density, specific heat, thermal diffusivity) of sample lubricant oil and gasoline against temperature.

Comparing the thickness of the solid layer (order of millimeters) with the liquid height (order of dozens of micrometers) and considering that in the solid wall there are not mass diffusion phenomena, the grid-size along the solid layer was coarsened up to 0.1 mm in order to speed up the simulations. A further strategy that was implemented in order to reduce the computation time is the split of the solvers of the solid layer and the liquid layer, respectively. Due to the larger size of the mesh along the solid layer, greater values of the maximum stable time-step are allowed ($\approx 5 \times 10^{-5}$). Thus, the solution of the solid layer using its corresponding time-step is decoupled from the solution of the liquid layer, which requires a tighter stability condition. Thus, the solid layer is resolved around one time every 1000 iterations of the liquid solver. The two layers communicate between each other through the heat flux and temperature data provided from the solid layer to the liquid layer at the SLI.

Wall heat transfer coefficient

The coefficient for the convection-induced heat transfer (H) is calculated according to the well-known Woschni model [126], which is widely used in engine applications due to the simple usage. The model (Eq.s (3-13), (3-14)) relies on two different tuning coefficients for multiplying the pure convective (C_1) and the convective-like radiation (C_2) contributions respectively. Furthermore, an additional scaling coefficient (C_0) is introduced since it is known that the Woschni formulation is not able to predict the heat transfer rate at the walls accurately for nowadays gasoline engines because of the enhanced effect of turbulence with respect to the piston speed during the intake stroke in high tumble configurations and

the non-premixed nature of combustion in GDI operations [127], [128]. In Eq.s (3-13), (3-14) p is the in-cylinder pressure, B is the engine bore, U_P is the mean piston speed, V_C is the engine displacement, U_G is the estimate in-cylinder gas mean velocity, the subscript 'ref' indicates that the terms in parenthesis must be calculated at reference engine conditions, usually the Bottom Dead Center (BDC). The coefficients C_1 , C_2 are set in line with the values recommended in the original work [126], the coefficient C_0 is equal to a confidence value that was achieved by the match of experimental curves of modern engines. The tuning values adopted in the present calculation are reported in **Table 3-1**.

$$H = C_0 \cdot \frac{p^{0.8} \cdot U_G^{0.8}}{(T_G^*)^{0.53} \cdot B^{0.2}} \quad (3-13)$$

$$U_G = C_1 \cdot U_P + C_2 \cdot V_C \cdot \left(\frac{T_G^*}{V_C \cdot p} \right)_{@ref} \cdot (p - p|_{motored}) \quad (3-14)$$

Table 3-1: Tuning values for the coefficients of the Woschni heat transfer coefficient.

Coefficient	Measure unit	Value	Engine phase
C_0	(-)	1.2	any
C_1	(-)	6.18	Intake
		2.28	Compression
		2.28	Combustion
C_2	(m/K/s)	0	Intake
		0	Compression
		3.24×10^{-3}	Combustion

Interface mass transfer coefficient

The coefficient for the convection-induced mass transfer (M) is estimated according to the Chilton-Colburn j-factor analogy [129] for heat, mass and momentum transfer (Eq. (3-15)), which is a powerful method to estimate one of the transfer coefficients by knowing one of the other two transfer mechanisms and the fluid properties. In Eq. (3-15), U_G is the free stream gas velocity, Pr and Sc are the Prandtl and Schmidt non-dimensional number, C_f is the friction factor. Considering the so-called Chilton-Colburn factors for heat (j_H) and mass (j_M) transfer and assuming that the heat transfer coefficient is known thanks to the use of the Woschni model, the mass transfer coefficient is given by Eq. (3-16).

$$j_H = \frac{H}{\rho \cdot c_p \cdot U_G} \cdot Pr^{\frac{2}{3}} = j_M = \frac{M}{U_G} \cdot Sc^{\frac{2}{3}} = \frac{C_f}{2} \quad (3-15)$$

$$M = \frac{H}{\rho_{G,F} \cdot c_{p,G,F}} \cdot \left(\frac{1}{Le} \right)^{2/3} \quad (3-16)$$

In Eq. (3-16) the Lewis number (Le) is defined as the ratio between the gas thermal diffusivity (α_G) and the gaseous phase diffusion coefficient between fuel vapor (subscript F) and air (subscript a). The gas thermal diffusivity is calculated for pure air, the gaseous phase diffusion coefficient is estimated by means of the Fuller et al. [130] correlation (Eq. (3-17)), where MW is the molecular weight, v is the so-called diffusion volume, which is calculated according to the tabular guidelines provided in [130].

$$D_{G,A-F} = 1.01325 \times 10^{-7} \cdot \frac{(T_G^*)^{1.75}}{p} \cdot \left(\frac{1}{MW_A} + \frac{1}{MW_F} \right)^{0.5} \cdot (v_A^{1/3} + v_F^{1/3})^{-2} \quad (3-17)$$

Diffusion coefficient

3.3 Results

3.3.1 Predicting oil-fuel diffusion coefficient

It must be underlined that the current open literature presents several data on binary mixtures of pure hydrocarbons (light vs heavy), whilst it lacks experimental measures of the liquid phase diffusion coefficient between realistic gasolines and lubricant oils. As a consequence, a comprehensive quantitative validation was not applicable. Nevertheless, in order to provide a proof of reliability on engine applications of the predictions returned by the present methodology (0), two further prediction tests were performed.

Firstly, in order to trace the behavior of the predictive potential of the complete methodology, the BNN was applied to new solvent-solute combinations representative of real fuel-oil mixtures that were not included neither in the training set nor in the test set. To this aim, heptane was considered as a fuel solvent whilst a given number of saturated hydrocarbons with increasing number of carbons has been taken as oil solute. With regards to the solute, starting from reference hydrocarbons in the range C10-C16 (decane-hexadecane), for which experimental data on the dilution in heptane are available, the number of carbons was progressively increased up to C34, which is consistent with the experimental average number of carbons in engine oils [167]. As a result, from C16 to C34 conceptual heptane-CX combinations have been generated on purpose in order to extend the analysis of the BNN predictive behavior with respect to a pool of validated reference heptane-CX (C10-C16) points. As shown in **Figure 3-10**, the greater is the solute carbon number, the weaker is the liquid diffusivity as described by the Einstein-Stokes theory.

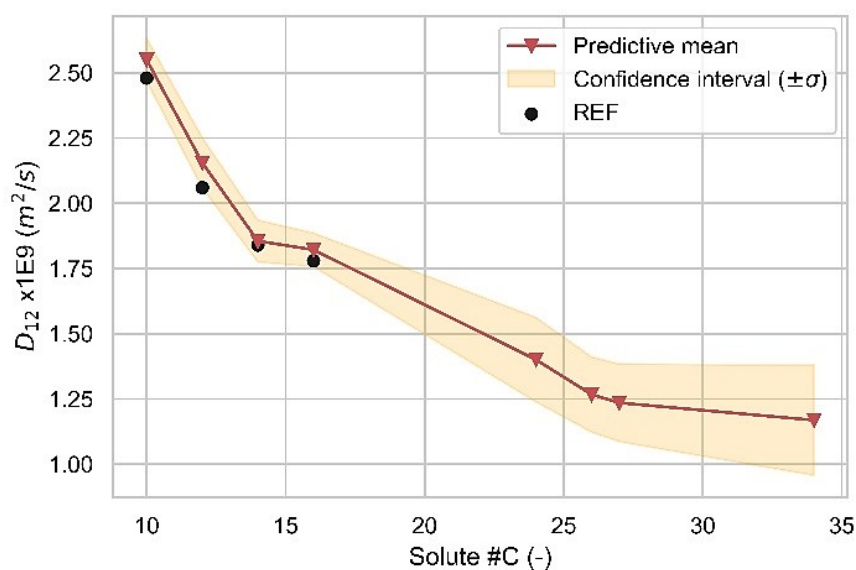


Figure 3-10: Bayesian neural network predicted value (red markers) and its confidence (yellow band) for different solutes identified by increasing number of carbons in n-heptane (solvent). Experimental reference values (black markers) are available for the first mixtures whilst x-axis points without reference represent conceptual mixtures.

Furthermore, it is visible that the confidence band (yellow) becomes wider moving towards C35, thus, given the predicted mean (red values) i.e., the estimated most likely value of the diffusion coefficient, it is ensured that the real value falls in the predicted confidence band. Considering both the lighter (C14-C16) and the heavier (C25-C35) components of oils, it is

shown that the predicted value may suffer from maximum relative errors between 10-15% with respect to the real value.

A further proof of concept was provided by taking under consideration the work by Hiss and Cussler [168]. In [168] the Authors measured the diffusion coefficient at ambient conditions of n-hexane and naphthalene, which played the role of solute, in different HC oils, which played the role of solvent. Those HC oils were characterized by molecular weight in the range 209-667 g/mol and dynamic viscosity in the range 3-5000 mPa·s. In [168] the experimental values of the diffusion coefficient of n-hexane diluted in HC oils are around $0.15-0.03 \times 10^{-9} \text{ m}^2/\text{s}$ considering HC oils with dynamic viscosity in the range 50-300 mPa·s that are selected since that viscosity range is representative of the most common SAE oils. As a validation test, the present neural network methodology was used to predict the diffusion coefficient of n-hexane (solute) through two different solvents, namely SAE 10W30 and SAE 30 engine lubricant oils, whose viscosity values are in line with those of the two HC oils tested in that range in the reference experiments. In **Figure 3-11** it is visible that both the predicted diffusion coefficient for the two SAE oils/n-hexane combinations are in solid agreement with the experimental values. It must be considered that slight differences could be expected due to the fact that the HC oils used in the reference case may exhibit different physical properties with respect to the chosen SAE oils in spite of the similar dynamic viscosity values.

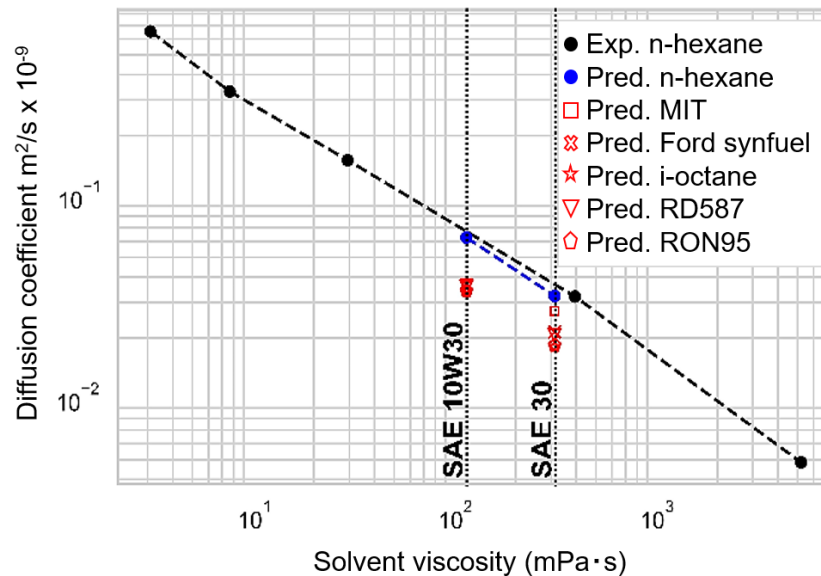


Figure 3-11: Diffusion coefficient against solvent viscosity for different solvent-solute combinations: generic HC oils-n-hexane experimental (black) and predicted (blue) data, SAE oils-gasolines/i-octane (red).

In comparison with n-hexane, real gasolines are characterized by higher number of carbons (C 7-8), larger molar volume and lower latent heat of vaporization, due to the consequent reduced molar volume ratio RV and θ correction factor lower values of the diffusion coefficients are expected considering the same solvent. In fact, as visible in Figure 3-11, the red markers associated to the SAE oils-gasolines and SAE oils-i-octane combinations lie below the reference experimental curve referred to n-hexane as a solute. Furthermore, the two SAE oils in the viscosity range under review were diluted with i-octane and four different gasolines from literature. Then, the values predicted for diffusion coefficient of the new ten mixtures (SAE 10W30 [120] + 4 gasolines [91], [120], [169], [170]/i-octane, SAE 30 [120] + 4 gasolines/i-octane) are placed in the same plot as that of the validation test in order to

discuss the results. The mixture properties of both the two engine oils and the four gasolines are calculated as reported in 3.2.1 according to their multi-component models listed in **Error! Not a valid bookmark self-reference.**, Table 3-7. Moreover, at the bottom of **Error! Not a valid bookmark self-reference.**, Table 3-7 the mixture properties used to generate the input features provided to the neural network are shown.

Table 3-6: Mass fraction composition % and relevant properties of the two tested engine oils.

Component	Formula	SAE 10W30 [120]	SAE 30 [120]
Pentadecane	C ₁₅ H ₃₂	0.3	0
Hexadecane	C ₁₆ H ₃₄	0.5	0
Heptadecane	C ₁₇ H ₃₆	0.7	0
Octadecane	C ₁₈ H ₃₈	1	0
Nonadecane	C ₁₉ H ₄₀	1.5	0
Eicosane	C ₂₀ H ₄₂	2	0.2
Heneicosane	C ₂₁ H ₄₄	3	0.3
Docosane	C ₂₂ H ₄₆	4.5	0.4
Tricosane	C ₂₃ H ₄₈	5.5	0.7
Tetracosane	C ₂₄ H ₅₀	6.5	1
Pentacosane	C ₂₅ H ₅₂	7.5	1.3
Hexacosane	C ₂₆ H ₅₄	8.5	1.5
Heptacosane	C ₂₇ H ₅₆	9	1.9
Octacosane	C ₂₈ H ₅₈	8.5	2.6
Nonacosane	C ₂₉ H ₆₀	8	3.5
Triacontane	C ₃₀ H ₆₂	7.5	3.7
Hentriacontane	C ₃₁ H ₆₄	6.5	4.3
Dotriacontane	C ₃₂ H ₆₆	5.5	5.1
Tritriacontane	C ₃₃ H ₆₈	4	5.6
Tettratriacontane	C ₃₄ H ₇₀	3	6.2
Pentatriacontane	C ₃₅ H ₇₂	3	6.5
Hexatriacontane	C ₃₆ H ₇₄	1.5	6.7
Heptatriacontane	C ₃₇ H ₇₆	1	6.6
Octatriacontane	C ₃₈ H ₇₈	0.5	6.4
Nonatriacontane	C ₃₉ H ₈₀	0.3	5.9
Tetracontane	C ₄₀ H ₈₂	0.2	5.3
1-Hentetracontene	C ₄₁ H ₈₂	0	4.8
1-Dotetracontanethiol	C ₄₂ H ₈₆ S	0	4
Tritetracontane	C ₄₃ H ₈₈	0	3.4
2-Methyl-Tritetracontane	C ₄₄ H ₉₀	0	2.9
2-Methyltetra-Tetracontane	C ₄₅ H ₉₂	0	2.4
n-Heptatetracontane	C ₄₇ H ₉₆	0	1.9
n-Octatetracontane	C ₄₈ H ₉₈	0	0.9
n-Nonatetracontane	C ₄₉ H ₁₀₀	0	0.7
n-Pentacontane	C ₅₀ H ₁₀₂	0	0.5
n-Henpentacontane	C ₅₁ H ₁₀₄	0	0.3
n-Dopentacontane	C ₅₂ H ₁₀₆	0	0.2
Tripentacontane	C ₅₃ H ₁₀₈	0	0.1
Input properties			

<i>MW</i> (g/mol)	387.5	497.9
ρ (kg/m ³)	875	890
<i>V</i> (cm ³ /mol)	442.8	559.5
μ (mPa·s)	113.7	311.5
<i>H_v</i> (kJ/kg)	257.4	221.2

Table 3-7: Mass fraction composition % and relevant properties of the four tested gasolines and i-octane.

Component	Formula	i-Octane	RON95 [91]	RD587 [169]	Ford-Synfuel [170]	MIT [120]
Cyclopentane	C ₅ H ₁₀	0	0	6.3736	0	0
i-pentane	C ₅ H ₁₂	0	0	0	16.61	20
n-Pentane	C ₅ H ₁₂	0	0	8.4304	0	0
Cyclohexane	C ₆ H ₁₂	0	0	0	24.05	0
1-Hexene	C ₆ H ₁₂	0	0	6.5558	0	0
n-Hexane	C ₆ H ₁₄	0	33.534	0	0	0
3-Methylpentane	C ₆ H ₁₄	0	0	0	0	10
Toluene	C ₇ H ₈	0	0	23.9247	17.65	13
n-Heptane	C ₇ H ₁₆	0	0	11.7079	0	5
m-Xylene	C ₈ H ₁₀	0	0	0	0	17
Ethylbenzene	C ₈ H ₁₀	0	0	0	12.93	0
i-Octane	C ₈ H ₁₈	100	45.24	43.0076	19.2	15
1,2,4-Trimethylbenzene	C ₉ H ₁₂	0	0	0	0	5
Naphthalene	C ₁₀ H ₈	0	0	0	1.09	0
n-Decane	C ₁₀ H ₂₂	0	21.226	0	8.47	3.5
i-Dodecane	C ₁₂ H ₂₆	0	0	0	0	1.5
Ethanol	C ₂ H ₆ O	0	0	0	0	10
Input properties						
<i>MW</i> (g/mol)		114.2	110.7	98.9	97.6	93.4
ρ (kg/m ³)		692	689	730	761	746
<i>V</i> (cm ³ /mol)		165.0	160.6	135.5	128.2	125.2
μ (mPa·s)		0.503	0.487	0.452	0.583	0.509
<i>H_v</i> (kJ/kg)		272	323.9	336.2	363.4	411.2

As a result, the final BNN methodology proved to capture the diffusive behavior of these fluids in the case of gasolines diluted in lubricant oils. Therefore, it is expected that the proposed methodology performs similarly in the case of lubricant oils diluted in gasolines, namely gasoline is the solvent and oil is the solute, which is the concentration ratio of interest for LSPI analysis in engines. Considering the RON95 gasoline among the four shown in **Figure 3-11**, which is consistent with typical nowadays gasoline characteristics, the predicted mean and confidence band listed in **Table 3-8** are predicted for the SAE 10W30 and the SAE 30 engine oils.

Table 3-8: Bayesian neural network prediction for the mean value and the confidence band of two gasoline-SAE oil mixtures.

Solvent/solute	Mean m ² /s x 10 ⁻⁹	Confidence band ($\pm 2\sigma$)
RON95/SAE 30	0.6885	0.1263
RON95/SAE 10W30	0.8864	0.2317

3.3.2 Oil-fuel dilution simulation

Since the validation of the implemented one-dimensional oil-fuel dilution code through quantitative data is not viable because of the lack of experimental measures of the oil mass scraped by the piston, a qualitative validation was performed in the attempt to capture the main experimental effects that were observed in literature works. In [48] Luo et al. conducted experiments on an in-line 4-cylinder TGDI engine with particular focus on the test of the mixture enrichment and the coolant heating up as promising strategies to mitigate the LSPI-induced mega knock frequency and intensity. The LSPI was identified by means of the indicating analysis of the magnitude of the peak firing pressure over many different engine cycles. The engine data and reference operating conditions used to setup the oil-fuel dilution simulation are listed in **Table 3-9**. Once the oil-fuel dilution has been simulated at the baseline engine conditions shown in **Table 3-9**, two different interesting variations and their effects are then simulated: i) use of a higher oil viscosity grade by implementing the SAE 10W30 lubricant oil properties in place of the ones of the reference SAE 5W30; ii) operation of the cylinder wall heating up by increasing the temperature of the solid layer from 90°C to 105°C.

Table 3-9: List of the relevant engine data of the reference validation case from [48].

Engine data	Test configuration
Engine type	TGDI
# Cylinder	4
Engine displacement	1500 cm ³
Bore x Stroke	79 x 76 mm
Geometric compression ratio	9.5:1
Engine speed	1500 r/min
Normalized air-fuel ratio (λ)	1.0
Injector position	Wide spacing, intake side
Injection pressure	100 bar
SOI-EOI	401.5-595.5 CA deg
Fuel	RON95 gasoline
Lubricant oil	SAE 5W30 synthetic
Coolant and oil temperature	90°C
Spark Advance	0 deg ATDC
Break Mean Effective Pressure	22 bar

Considering this case study, the 2-layer solution domain was setup as follows:

- the cylinder wall was modelled as 1 mm (maximum heat penetration depth) of cast iron, whose thermo-physical properties were taken from [171] and then maintained constant during the simulation.
- the oil layer, was modelled as a 4 μm layer of SAE 5W-30 synthetic oil under the assumption of pseudo-pure liquid. The oil thermo-physical properties were taken by the *Simscape™ Thermal Liquid* library [172] as temperature-dependent correlations.
- the liquid film, was modelled as a 20 μm layer of RON95 gasoline under the assumption of pseudo-pure liquid. The thermo-physical properties of the pseudo-pure liquid fuel were calculated as the weighted average of the properties of each single component reported in **Table 3-7**. The temperature-dependent behaviour of the properties of each pure component was evaluated according to the correlations in [113]. Since the saturation

pressure, which is fundamental to estimate the equilibrium condition at the LGI, is not an additive property, the value for the present mixture was calculated by using an in-house developed model provided with the name of the components and the mixture composition (molar/volume/mass fractions), that will be deeply described in the following section (4).

As a result, the initial computation grid comprises 250 cells, whilst the initial calculated time-step according to (3-12) is 4×10^{-8} s. The infinite dilution diffusion coefficient between the RON95 gasoline and the SAE 5W-30 oil was set to the predicted mean 1.4379×10^{-9} m²/s ($\pm 2\sigma = 0.0759$) according to the developed BNN methodology.

In order to provide the dilution model with the environmental gas conditions needed to solve the LGI, an in-house developed zero-dimensional engine model in *Matlab* environment was used. The model is based on the solution of the internal energy balance for the calculation of the gas temperature, accounting for the contribution of heat losses (tuned Woschni model) and combustion (tuned Wiebe correlation), and the use of the perfect gas law for the gas pressure. Those equations are solved for the in-cylinder gas transformation in the high part of the engine cycle, namely from IVC to EVO. The input required by the model are engine geometric data, engine speed, cylinder volumetric filling coefficient, target global lambda, EGR, spark timing, turbulence intensity. The cylinder volumetric filling coefficient and turbulent intensity were tuned in order to match the experimental pressure trace from IVC to the spark timing, then the models of Woschni and Wiebe were tuned to match the pressure trace during combustion. Once the tuning was accomplished, the BMEP (Break Mean Effective Pressure) of 22 bar and the pressure trace in **Figure 3-12** were achieved.

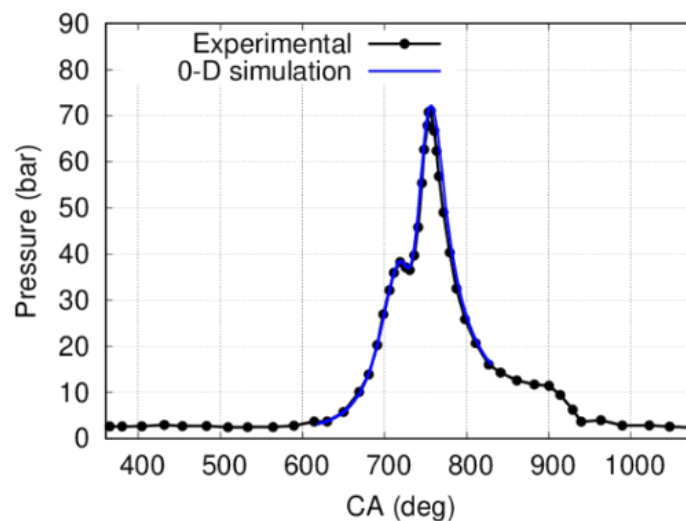


Figure 3-12: Comparison between calculated (solid blue, zero-dimensional model) and experimental (black dotted) pressure trace of the engine under review.

The main results of the code at the baseline conditions are listed in **Figure 3-13-Figure 3-15**. **Figure 3-13** shows that the deposited liquid fuel is quickly heated up by the cylinder wall, then, the fuel latent heat of vaporization causes a slight cool down. During the high half of the compression stroke the liquid temperature increases up to 200°C, which is close to the oil evaporation temperature. In this phase, the solid wall at SLI as well becomes slightly hotter.

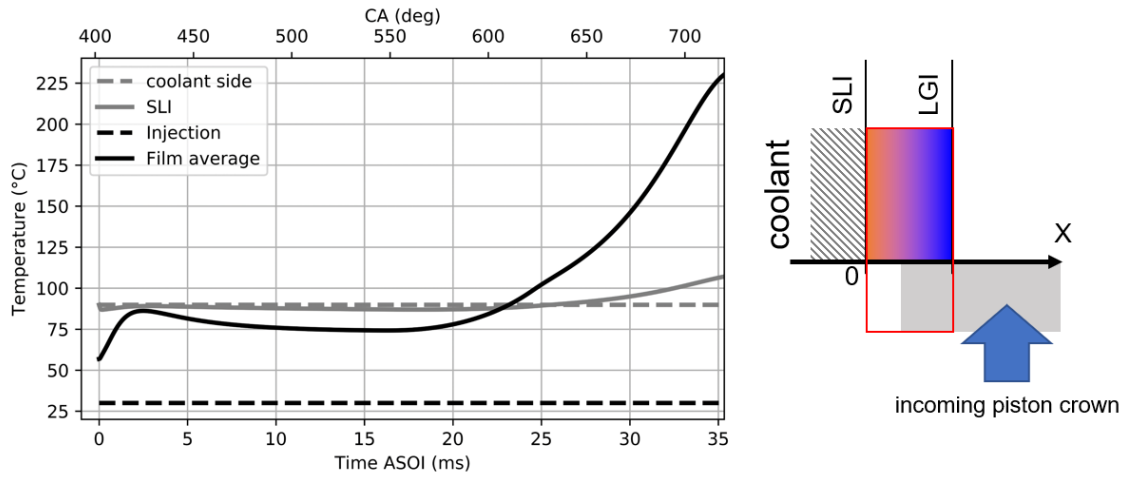


Figure 3-13: Predicted time temperature profile at the solid-liquid interface (solid gray) and for the average liquid film (solid black). Fixed coolant temperature and the film deposition (injection) temperature are also shown as a reference.

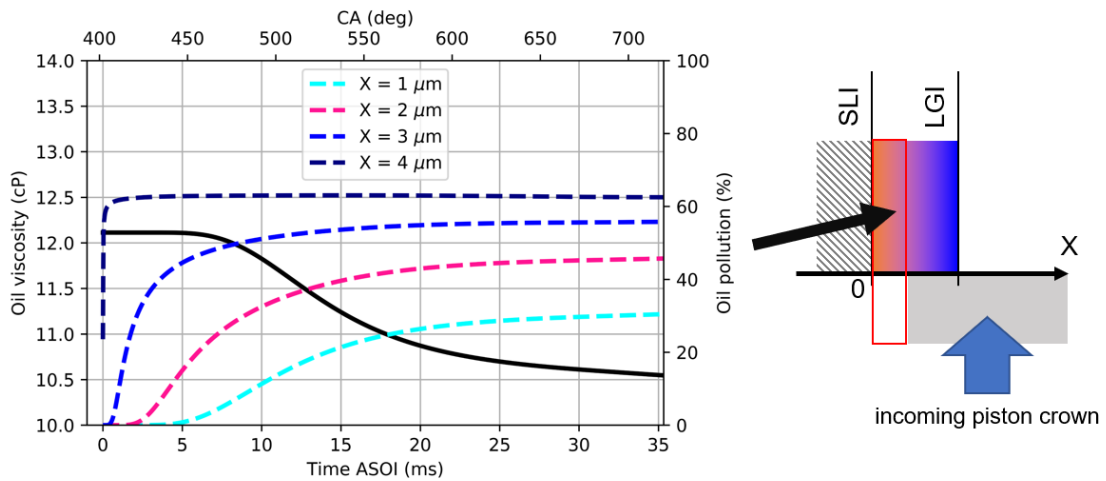


Figure 3-14: Predicted oil viscosity degradation (solid black) and oil pollution (dashed) at different x-location along the cylinder-piston clearance.

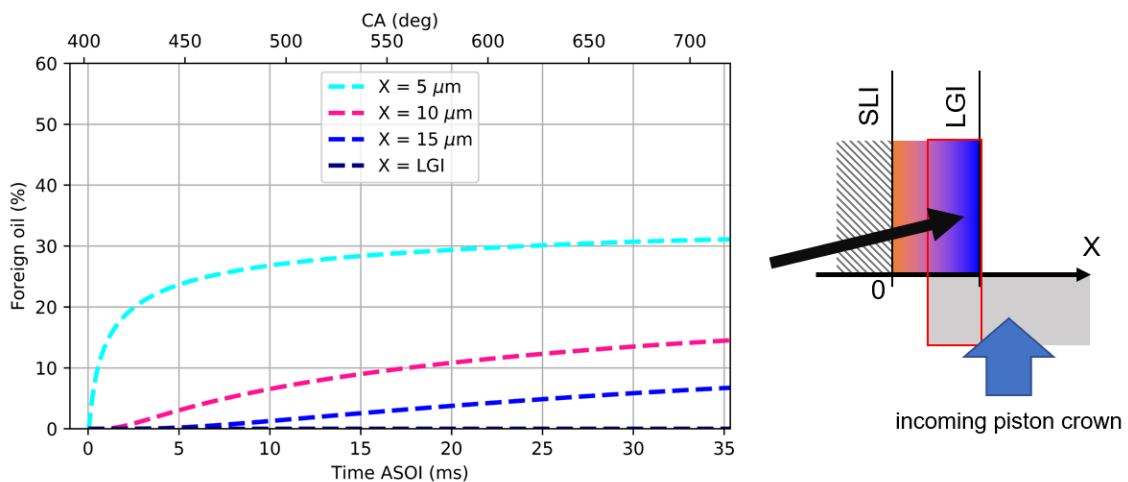


Figure 3-15: Predicted foreign oil presence in the non-evaporated liquid film, available to be scraped from the top land ring.

In **Figure 3-14** is displayed the not negligible oil viscosity degradation due to the oil pollution caused by the fuel penetration. It is visible that at the initial oil-fuel interface ($X = 4 \mu\text{m}$) 60% of the liquid is composed of fuel after the very early instants successive to the fuel deposition. Despite the oil pollution level decreases towards the cylinder wall, the level detected next to the wall ($X = 1 \mu\text{m}$) is still significant (30% fuel). **Figure 3-15** displays the concentration of foreign oil in the non-evaporated liquid film over time at different positions along the x-distance, which will be scraped by the piston up to the present liquid-gas interface. It can be noticed that in the time between the liquid fuel film creation and the SA, oil does not reach the interface with gases. However, the oil penetrates for a large distance leading to mixing levels up to 30%, which is a significant potentially auto-ignitable concentration that will be accumulated into the top land crevice at the piston arrival. The viscosity degradation and oil pollution, and the potential scraped amount of foreign oil will be considered for the comparative analysis between the baseline and the two validation configurations whose effect on LSPI has been studied in experimental literature works, which can be used as a benchmark. The simulated cases are: i) baseline, but the wall temperature is higher (105°C vs 90°C), which is named s-A; ii) baseline, but a higher oil viscosity grade is used (SAE 10W30 vs SAE 5W30), which is named s-B. Furthermore, an additional case (s-C) based on the joint use of both s-A and s-B was implemented. Simulations were performed assuming a spray pattern which causes fuel spray-wall impingement against the cylinder liner at half of the engine stroke. Thus, the final results are compared considering the piston arrival at half of the compression stroke.

In **Figure 3-16** is visible that the wall heating-up strongly reduces the oil penetration along the scrap film thickness with respect to the use of the higher oil grade. Despite the fact that the higher wall temperature promotes both the increasing of the liquid phase diffusion coefficient (Eq. (3-22)) and the mixing between the two fluids due to the viscosity reduction at higher temperature, the oil amount available for scrap is reduced of a third likely due to the higher evaporation rate with respect to the diffusion time scale, as reported in [48]. Moreover, consistently with the experimental observations of Yu et al. [173], who recorded extremely slight reduction of the LSPI frequency by replacing SAE 0W-30 with SAE 10W-30, the predicted oil amount available for scrap in the case of SAE 5W-30 (black curve) and SAE 10W-30 (green curve) is almost the same.

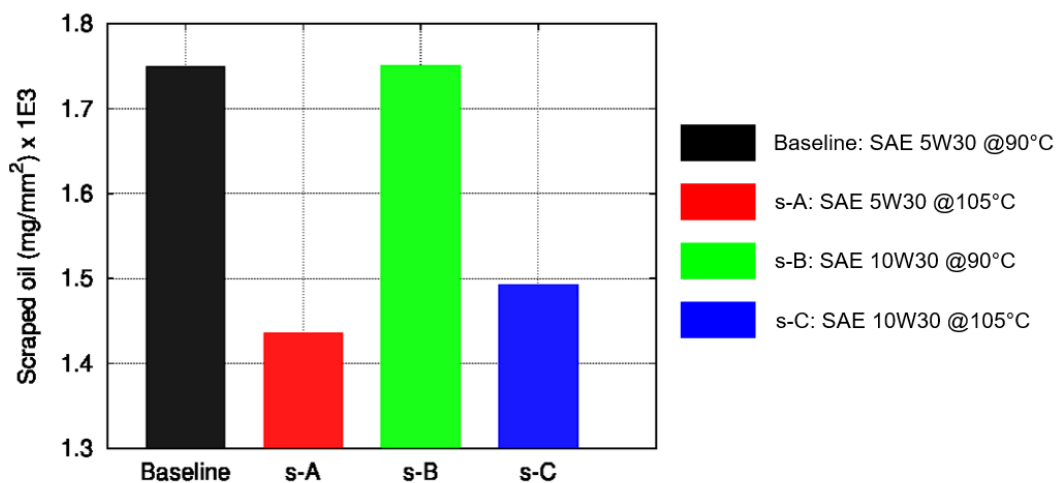


Figure 3-16: Potential oil scraped per unit film area recorded at half of compression stroke for baseline conditions and three different solution attempts to reduce LSPI.

As visible in the red curves in **Figure 3-17**, the application of the wall heating up with SAE 5W-30 oil leads to the significant viscosity reduction due to oil pollution from fuel (18%), with concerns on the enhancement of the film scrap and squeeze effects, which result in a larger oil mobility, and parts wear. On the one hand, the oil viscosity reduction to values around 10 cP may reduce the friction between the piston and the cylinder wall, promoting the dampen of friction losses [174]. On the other hand, it was proven that the lower is the oil viscosity, the higher are oil consumption and piston ring wear, which may increase up to dozens of $\mu\text{g/h}$ [175]. While the use of higher oil grades is not effective as the wall heating-up in reducing the LSPI frequency (**Figure 3-16**), it is demonstrated to be a powerful solution to slow down the oil layer degradation (**Figure 3-17**, green curve).

In fact, the viscosity degradation behavior of the SAE 10W-30 oil (green curve, reduction around 2%) is both delayed in time and weaker than that of the SAE 5W-30 oil (black curve, reduction around the 15%) due to the higher frictions between the molecules in oils with higher grades.

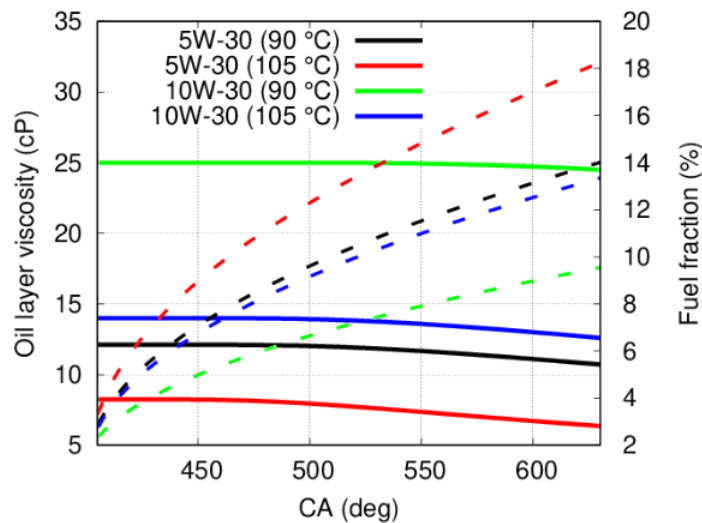


Figure 3-17: Oil viscosity degradation and average oil pollution recorded at half of compression stroke for baseline conditions and three different solution attempts to reduce LSPI.

In the view of the above, the results predicted by the model have been assessed in the case of a mixed solution, namely the wall heating-up to 105°C and the use of SAE 10W-30 oil have been implemented both, and named as s-C. As visible from the blue bar in **Figure 3-16**, the combination of those solutions leads to the significant reduction of the LSPI risk-driver (smaller oil concentration along the scrap thickness), which has been more than halved. Furthermore, the same baseline viscosity degradation behavior has been reached, which however relies on higher initial values, resulting in a slightly safer configuration. As a result, the tool provided results to evaluate a promising trade-off solution to comply with both combustion stability and engine parts saving.

4 Liquid fuel evaporative behaviour simulation

4.1 State of the art and original contribution

Once the numerical simulation of liquid fuel wall impingement and oil interaction has been addressed through the presented modeling approach, an in-depth analysis of the liquid evaporative behavior is necessary in order to forecast the real composition of the gasoline that can reach the engine walls as a dispersed liquid phase, the real liquid film depletion and spray evaporation. Firstly, the basic question that must be posed is ‘what is fuel in CFD simulations?’ It must be remembered that commercial gasolines are complex mixtures of hundreds of species, whose full reproduction in CFD simulations is not available since the exact composition of the real gasoline is not known and even so, the time spent for the tracing and resolution of that number of species would be unaffordable. Therefore, the common practice in CFD simulations is the representation of real gasolines by means of the so-called *surrogates*, namely mixtures of different well characterized pure components. The number, type and presence (mol/vol/mass) of the pure components comprised in the surrogate strongly depend on which aspects of the real gasoline must be emulated by the formulated surrogate [176].

In the recent past, the basic fuel surrogates were the so-called Primary Reference Fuels (PRF) i.e., binary mixtures of different shares of i-octane and n-heptane. In PRFs the role of i-octane is the emulation of the combustion behavior of the real gasoline, namely the match of laminar flame speed, auto-ignition delay time, octane rating, whilst the role of n-heptane is the emulation of the physical behavior of the liquid phase. As far as the GDI system is concerned, PRFs have become insufficient due to non-premixed nature of the combustion process in those engines with respect to that of PFI engines. As a result, the new basic fuel surrogate was identified in the so-called Toluene Reference Fuels (TRF), which are ternary mixtures of i-octane, n-heptane and toluene aiming at reproducing the late evaporation and soot formation caused by the aromatic share of gasolines, which are reproduced by introducing toluene. Finally, due to the recent wide spreading of oxygenate addition as a RON enhancer for new high thermal efficiency engines, the emulation of the effect of the oxygenates was necessary, being those components highly different with respect to hydrocarbons due to their molecule polarity. Therefore, the current minimal surrogate of real gasolines is the so-called Ethanol Toluene Reference Fuel (ETRF) i.e., a mixture of i-octane, n-heptane, toluene and ethanol. On the other hand, the maximum number of components comprised in a fuel surrogate mixture is around 6-8, which is driven by the need to avoid significant computational expense.

It is clear that once the target properties of the real gasoline are defined, the surrogate formulation in terms of number, type and presence of selected pure elements is a multi-objective optimization task. In the current literature the study of algorithms for the design of comprehensive fuel surrogates for practical gasolines is widely discussed. Most of the published works [177]–[181] are focused on the use of different searching techniques for the formulation of surrogates capable to mimic only the chemical aspect or both chemical and physical aspects of real gasolines. It must be underlined that, as reported in [182], the latter approach suffers from the current poor chemical kinetics characterization of different

essential pure compounds, for which kinetic mechanisms still need to be developed and validated. On the other hand, a wide number of reliable physical properties of the same pure compounds are commonly available. As shown by literature results [177]–[181] the mimic of physical and chemical properties at the same time with a single surrogate is extremely complex regardless of the searching strategy. The most common paradigm in the choice of the target properties (i.e., the properties that must be emulated), is the use of liquid density, carbon-to-hydrogen ratio, carbon, hydrogen, oxygen mass share (%w), lower heating value, octane rating, part of the distillation curve. In common practice the availability of the full gasoline distillation curve (%vol distilled vs temperature at which the associated X %vol has boiled (TX)) is quite rare, instead the value of T50 or the values of T10, T50, T90 are provided. In the open literature the surrogates achieved by many researchers show on the one hand good match with experiments for the values of liquid density, carbon-to-hydrogen ratio, chemical composition and lower heating value. On the other hand, poor representation of the boiling temperatures and octane rating were presented. Furthermore, it must be underlined that most of those surrogates were formulated with respect to gasoline RON values from 87 to 91, whilst pursuing the match of nowadays high RON gasolines (95-100) by using those methodologies would be extremely harder.

Very few works have approached the fuel surrogate formulation by using advanced optimization techniques such as machine learning and by posing emphasis on the emulation of only the physical properties. In [183] Pati et al. adopted a genetic algorithm to search surrogates representative of the distillation and vapor pressure curves of four gasolines with different levels of ethanol blending. The results showed the ability of that methodology to capture with decent accuracy the vapor pressure curve and the early distillation behavior (from 20% to 40% distilled volume). However, significant mismatches were reported for the very early distillation behavior (from 0% to 10% distilled volume) and for the TX at the right end-tail of the distillation curve for which temperature differences between 10-25°C were detected. In [184] Muelas et al. focused the efforts to capture the evaporative behavior and the soot tendency of a reference heating oil representative of the physicochemical complexity of fuels. A multi-objective regression algorithm was implemented to capture liquid density, carbon-to-hydrogen ratio, molecular weight, soot tendency and distillation curve by means of 2-components surrogate formulations. Errors around 15% were detected in reproducing the distillation curve, soot tendency and molecular weight likely due to the complexity of the multi-property optimization associated with the 2-component approximation. In [185] Zhu et al. applied a Bayesian multi kernel learning model to define surrogates capable to predict the soot tendency of fuels based on an in-house developed extensive experimental database. The work was focused on jet, diesel and bio-diesel fuels. The soot tendency of the surrogates presented by the Authors were in line with experiments, indeed coefficients of correlation over 0.95 were reported.

It must be underlined that according to the standard industrial practice in three-dimensional CFD engine simulation, two different gasoline surrogates can be used during the same calculation: i) firstly, a N1-components surrogate is adopted to simulate the mixture formation i.e. spray formation, spray evaporation, spray-wall impingement, liquid film evaporation; ii) then, the spatial distributions of pressure, temperature and mixture are given as input to correlations or models for laminar flame speed and ignition-delay time whose tuning parameters are taken from the chemical kinetic simulation of a different N2-components surrogate designed to simulate the combustion behavior of the same gasoline.

Since the detailed reproduction of the liquid fuel evaporative behavior in CFD simulations is crucial for implementing LTC modes successfully, investing resources in the development of new techniques aimed at tracing the physical properties and the liquid phase change of

new fuels together with few significant chemical features is of primary importance. To this aim, in this research project an advanced in-house developed machine-learning based methodology has been defined against the current common practice which relies on regression models and genetic algorithms. A Bayesian algorithm has been trained to provide the user with a multi-component fuel mixture resulted from an optimized searching strategy trade-off, which allows the minimum number of evaluations. As far as the prediction of the VLE features for iterative surrogate attempts is concerned, the Bayesian algorithm has been integrated with an in-house developed zero-dimensional model of a distillation test bench. Despite the fact that in the current literature on the present topic the VLE prediction task is usually performed by employing the commercial code *REFPROP* [186], the implementation of a custom model in open environment allows to avoid the cost spent for commercial licenses and the availability of a tailored database of components. The latter advantage is becoming increasingly important due to the need to test new engine fuels and additives while *REFPROP* was mainly developed for refrigerant fluids, thus, it lacks several key fluids such as i-butanol, prenol etc., which are promising RON enhancers in the perspective of high thermal efficiency engines. A further original contribution brought by this research project is the here called 'unicity analysis', which consists in the comparison between the optimum surrogate and the surrogate in the same solution pool that differs the most by the best surrogate formulation identified by the Bayesian algorithm and an equivalent valuable surrogate attempt stored in the solutions pool, with the aim of assessing whether an almost unique composition of gasoline surrogates is possible.

4.2 Methodology

The identification of the proper fuel surrogate of a real gasoline relies on three key methodological steps: i) selection of the set of pure compounds that can be used to fill the composition of the surrogate. This set is called 'palette'; ii) selection of the target properties that must be captured with high match with respect to the experimental values influencing the composition attempts and the searching process. This set is chosen such as to include those properties which are highly correlated to the evaporative behavior of the liquid, which must be emulated; iii) choice and training of a searching strategy for the formulation of surrogate attempts that are continuously improved based on the results of a tailored merit function. In this section the choices regarding the afore-mentioned three steps will be presented and discussed.

4.2.1 Palette definition

The definition of the initial palette composition (type of pure compounds) and size (number of pure compounds) has been based on literature Gas Chromatography gasoline data [187]–[191] and preliminary optimization tests. Once Gas Chromatography data have been reviewed, the following pattern can be clearly identified: i) the abundance of toluene and xylenes; ii) the relevance ethylbenzene, tri-substituted benzenes and light HCs (C5-C6) such as n-hexane, n-pentane, i-pentane, i-octane; iii) scarce presence of heavy HCs (> C8), which are usually n-nonane and n-decane. For the sake of illustration, the results of a sample Gas Chromatography analysis for a test gasoline from [191] is reported in **Figure 4-1**, where the x-axis shows the retention time in minutes (min) i.e., the time spent by the fuel gaseous phase into the column of the Gas Chromatography bench, whilst the y-axis shows the magnitude of the response of each molecule, which is proportional to its presence. The afore-mentioned pure compounds were used as guidelines to define the initial palette. Furthermore, 1-pentene and 1-hexene as well as cyclopentane and cyclohexane were added in order to ensure the choice among at least two representatives to include the presence of olefines and naphthenes, respectively. Moreover, as far as the simulation of

gasoline-ethanol blends is concerned, ethanol was added as oxygenate. As a result, the initial palette shown in **Table 4-1** has been assembled accounting for 14 pure compounds comprising one oxygenate, four n-paraffins, two i-paraffins, two olefins, two naphthenes and four aromatics. For the sake of illustration, the palette is shown in **Table 4-1** together with a set of representative properties, namely liquid density (ρ), vapor pressure (p_{sat}), boiling temperature (T_b) at normal conditions, octane numbers (Research Octane Number (RON), Motor Octane Number (MON)).

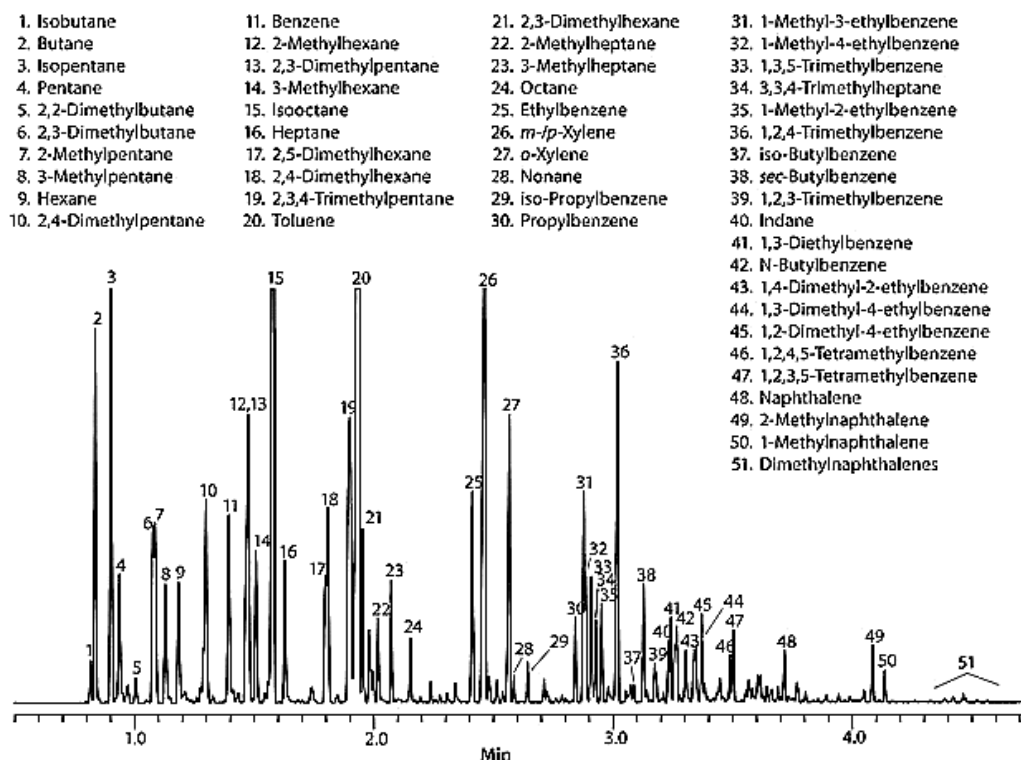


Figure 4-1: Example of gas chromatography data for gasoline [191].

Table 4-1: Compounds included in the initial palette for the surrogate definition and their properties.

Compound	Chemical class	ρ @20°C (kg/m ³)	p_{sat} @20°C (kPa)	T_b (°C)	RON/MON (-)
Ethanol (C ₂ H ₅ OH)	Oxygenate	791	5.85	78.3	109/90
n-Pentane (C ₅ H ₁₂)	n-Paraffins	627	56.3	36.2	62/62
n-Hexane (C ₆ H ₁₄)	n-Paraffins	661	16.1	68.9	19/26
n-Decane (C ₁₀ H ₂₂)	n-Paraffins	732	0.12	173.9	-41/-15
i-Pentane (C ₅ H ₁₂)	i-Paraffins	622	76.2	27.8	93.5/62
i-Octane (C ₈ H ₁₈)	i-Paraffins	695	5.11	99.2	100/100
1-Pentene (C ₅ H ₁₀)	Olefins	641	70.1	30.0	91/77
1-Hexene (C ₆ H ₁₂)	Olefins	674	19.2	63.3	76/63.4
Cyclopentane (C ₅ H ₁₀)	Naphthenes	746	34.4	48.9	101/84.9
Cyclohexane (C ₆ H ₁₂)	Naphthenes	778	10.3	79.9	83/85
Toluene (C ₇ H ₈)	Aromatics	869	2.9	110.7	116/103.5
<i>m</i> -Xylene (C ₈ H ₁₀)	Aromatics	865	0.83	138.9	118/115
Ethylbenzene (C ₈ H ₁₀)	Aromatics	868	0.57	136.1	101/98
1,2,4-trimethylbenzene (C ₉ H ₁₂)	Aromatics	876	0.20	167.9	111/124

4.2.2 Target properties

As pointed out in 4.1 the formulation of the proper fuel surrogate of a real gasoline is driven by the need to reproduce a specific behavior of the latter, which can be described by a set of its properties, namely the target properties. As far as the interest of this research project is the reproduction of the evaporative features of the gasoline liquid phase in order to improve the simulation of the mixture formation, the properties described in the following were selected as targets.

Density

The liquid density is considered since it is a physical property that is typically available in standard certification analysis. Moreover, considering the liquid density span for real gasolines (710-750 kg/m³ at 15°C), matching the liquid density value is helpful in order to capture the Weber number of impacting droplets, thus the impingement regime, and the liquid film boiling regime. The mixture liquid density measured at 15°C is calculated via mass weighted average according to Eq. (4-1). The liquid density of each of the components is estimated via temperature-dependent correlations taken from [113].

$$\rho(15^{\circ}\text{C}) = \frac{1}{\sum_i \frac{w_i}{\rho_i(15^{\circ}\text{C})}} \quad (4-1)$$

Macroscopic chemical composition

The macroscopic chemical composition is given as the presence in volume of alcohols (AL), n-paraffins (P), i-paraffins (I), olefins (O), naphthenes (N), aromatics (A), known as AL-PIONA. Targeting those chemical classes is fundamental due to their strong impact on key operating conditions of real engines e.g., n-paraffins accounting for 10-15% vol of real gasolines are typically light HCs (C4-C6) that can describe the early evaporative behavior of the injected liquid fuel, which can be fundamental for cold start and cat-heating simulations; aromatics are well known for being the evaporation tail of fuel mixtures, and their share is typically used to predict the soot tendency of gasolines. Considering the present palette, once the surrogate attempt has been formulated, AL-PIONA is directly calculated from its composition as the sum of the volumetric contribution (φ) of each component to its corresponding chemical class as listed in Eq.s (4-2)-(4-7).

$$\%AL = \varphi_{ethanol} \cdot 100 = \%E \quad (4-2)$$

$$\%P = (\varphi_{pentane} + \varphi_{hexane} + \varphi_{decane}) \cdot 100 \quad (4-3)$$

$$\%I = (\varphi_{i-pentane} + \varphi_{i-octane}) \cdot 100 \quad (4-4)$$

$$\%O = (\varphi_{1-pentene} + \varphi_{1-hexene}) \cdot 100 \quad (4-5)$$

$$\%N = (\varphi_{cyclopentane} + \varphi_{cyclohexane}) \cdot 100 \quad (4-6)$$

$$\%A = (\varphi_{toluene} + \varphi_{m-xylene} + \varphi_{ethylbenzene} + \varphi_{124TMB}) \cdot 100 \quad (4-7)$$

Distillation temperature

Distillation curves are powerful data to provide information on the fuel volatility and to fully describe its phase change features under reference conditions. Atmospheric distillation curves are given as monotonous increasing temperature values associated to increasing share of evaporated fuel from a liquid sample. The record of those pairs of values is conducted on a dedicated distillation test bench according to the ASTM-D86 procedure [192]. The in-depth analysis of the experimental recording of distillation curves is not the focus of the work, however, a brief description of the apparatus and the experimental results is given in order to pose the attention of the reader on some critical aspects regarding the numerical prediction of those curves. The liquid fuel distillation measurements are conducted by means of two communicating vessels of pyrex glass: the first vessel is a flask of sphere-shape bottom and cylinder-shape neck; the second is simply a collection vessel. The two vessels are connected by a pipe which is a side arm of the flask. A sample of liquid fuel at ambient conditions is placed at the bottom of the flask almost filling up the bottom sphere. The bottom of the flask is continuously heated up at atmospheric pressure and once the equilibrium temperature is achieved, the fuel vapors rise towards the neck of the flask, then fuel vapor pass through the connection pipe, which plays the role of chiller. As a result, while passing from the flask to the collection vessel the fuel vapors are subjected to the phase change back into liquid, thus, the condensed liquid is collected into the second vessel. The flask is supplied with time variable heat, which is adjusted in order to maintain a collection rate around 4-5 mL/min in the second vessel. In this framework, given the initial amount of liquid sample, the distillation temperature can be defined as the temperature measured in the flask at which a given share of the initial liquid has been transferred to the collection vessel. It must be underlined that fuel vapor phase change back into liquid may occur even into the liquid flask. In fact, during the rise towards the top of the flask, the fuel vapors exchange heat with both the surrounding air within the flask and the solid walls of the flask, furthermore the gaseous phase is cooled down by the latent heat of vaporization released by the fuel at the liquid surface. As a result, the fuel vapors may condensate before reaching the connection pipe and then fall down back into the liquid sample, promoting a sort of liquid internal reflux. The distillation temperature, which is indicated as T_X (temperature at which the X %vol of the initial liquid is evaporated and then collected out), can be measured by means of thermocouples at two different locations: i) at the bottom of the flask, thus, the probe is dipped into the liquid phase. In this case, the resulting distillation temperature is called 'kettle temperature' (T_K); ii) at the top of the flask neck as the fuel vapors hit the thermocouple before entering the connection pipe. In this case, the resulting distillation temperature is called 'head temperature' (T_H). Literature findings that report kettle temperature-based distillation curves or both kettle/head temperature-based distillation curves are very rare due to the complex data reported by the dipped probe, which is affected by the continuous liquid phase change, bubble formation and internal reflux. Therefore, the major part of literature works provide the measure of the head distillation temperature. For the sake of illustration, the sketch of a distillation test bench is reported in **Figure 4-2**. **Figure 4-3** displays the T_H experimental distillation curves (data from [193]) of a gasoline fuel and two ethanol-gasoline blends based on the same pure gasoline with two different levels of ethanol blending, namely 5%vol and 10%vol. With the perspective to the formulation of the proper fuel surrogate mixture, the use of both the full distillation curve and the chemical macro-composition of the real gasoline as target properties is attractive due to the strong mutual influence of those variables on each other. In fact, it is recognized that the right-end tail of gasoline distillation curves strongly depends on the aromatic composition of the gasoline under review since those compounds are the last that evaporate (T80-T90).

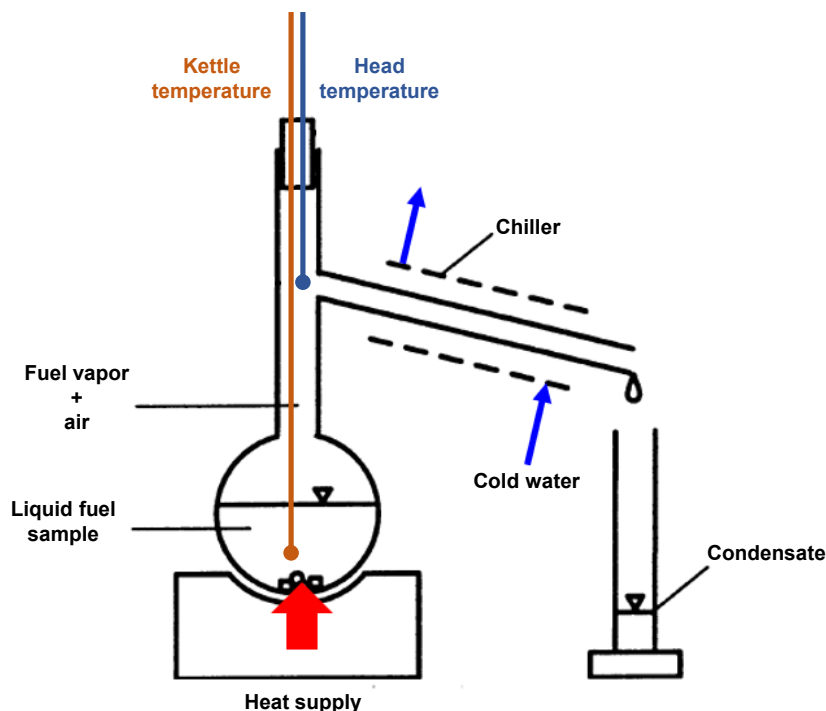


Figure 4-2: Sketch of an experimental distillation rig, measure probes placed for head temperature (dark blue) and kettle temperature (dark orange) recording.

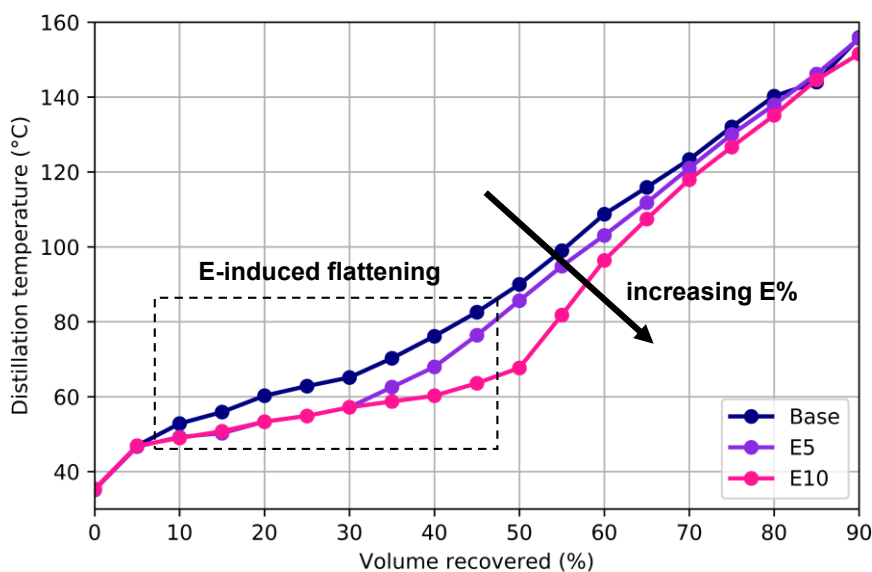


Figure 4-3: Sample experimental distillation curves [193] of a base gasoline and two of its blends with 5%vol (E5) and 10%vol (E10) ethanol.

Light HCs are responsible for the early evaporative behavior, thus, light n-paraffins affect the left-end tail of the distillation curve. Furthermore, in **Figure 4-3** it is visible that increasing ethanol addition (but oxygenates in general) induces the flattening of the evaporative behavior of the gasoline from T10 to T60 for E25 blends. Therefore, targeting the pursue of both the full distillation curve and the chemical macro-composition helps to address the surrogate formulation attempts. Since equilibrium properties are not additive, the prediction of the distillation curve of the mixtures formulated in searching the proper surrogate is addressed by means of a dedicated model. Despite the fact that in open literature it has

been deployed the modeling approach accounting for the numerical resolution of partial derivatives equations systems for the transient zero-dimensional representation of experimental distillation bench including VLE, fuel vapor escape and recondensation reflux [194], the use of the latter is not viable in this research project. In fact, since the distillation model would be called a number of times during the iterative searching of the surrogate, its solution time should be almost timeless in order to avoid the slowing down of the searching algorithm, which may need to perform hundreds of formulation attempts. Instead, based on the proposal of Slavinskaya et al. [195] and Abianeh et al. [196] a simplified approach which relies on the cumulative resolution of a number of selected volume recovered steps as steady state equilibrium problems was considered in order to save computing time. The model has been implemented into three steps in *Python* 3 environment and then validated against experimental data. The three modeling steps are: i) the estimation of the first kettle equilibrium temperature (T_0) by means of a pure thermodynamic model; ii) the calculation of the kettle temperature-based distillation curve ($T_0 < T_X \leq T_{90}$) by coupling the thermodynamic model of the first step with the resolution of the equations that describe a no-reflux simple batch distillation operation; iii) the resolution of a simplified energy balance applied to the flask wall-air-fuel vapor system aimed at determining the head temperature-based distillation temperature. It is underlined that the last step is simply charged to convert the predicted distillation curve from kettle-based to head-based temperatures, which is compulsory in order to test the final searching algorithm on a sufficient number of real gasolines for which only the head distillation temperatures are available. In **Figure 4-4** a scheme of the computation domain according to the three modeling steps is shown.

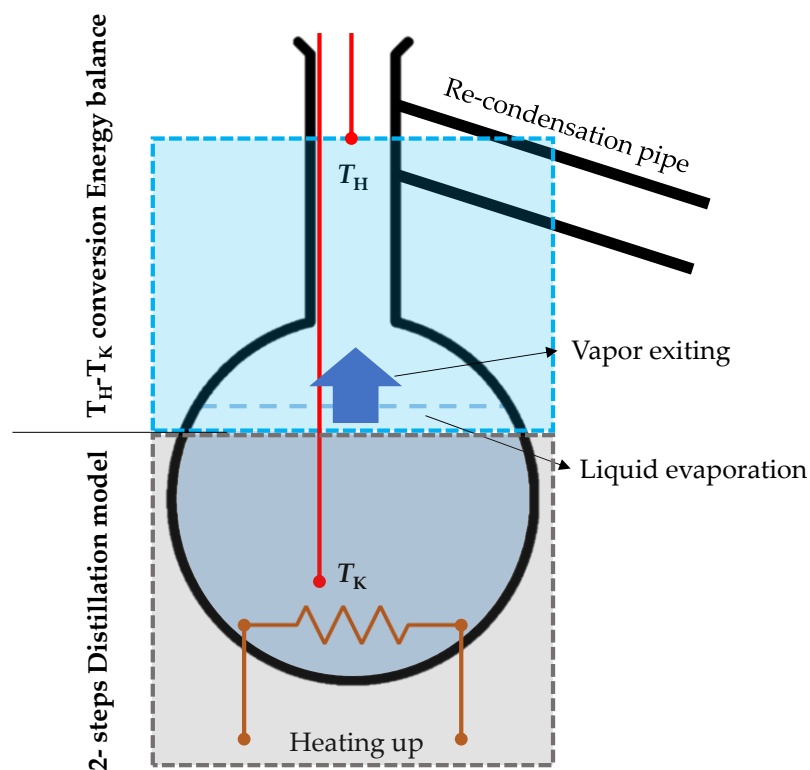


Figure 4-4: Scheme of the division of the distillation ambient into the three modeling steps.

The first kettle distillation temperature, which is the equilibrium temperature at atmospheric pressure of the original liquid fuel sample, is estimated according to the classical VLE bubble point temperature problem. In order to take into account the non-ideal behavior of real mixtures, the VLE is expressed by the equality between the so-called liquid and vapor fugacity in place of the classical Raoult's law. The estimation of the mixture fugacity is approached with the so called dual-fugacity method, which proposes the correlation of the fugacity (real fluid behavior) with the partial pressure (ideal fluid behavior) by means of the non-dimensional fugacity coefficient (ϕ) for both the phases, namely liquid (L) and vapor (V). As a result, the VLE of each component of the original mixture is written as in Eq. (4-8), in which p is the environmental pressure, x and y are the moles fractions of the i -th component in the liquid and in the vapor, respectively.

$$\phi_{V,i} \cdot (y_i \cdot p) = \phi_{L,i} \cdot (x_i \cdot p) \quad (4-8)$$

In order to simplify the initialization, Eq. (4-8) is adjusted by introducing the so-called equilibrium ratio (k) resulting in Eq. (4-9). Therefore, matching Eq.s (4-8), (4-9) the equilibrium ratios are calculated as the ratio between the liquid and the vapor fugacity coefficient.

$$y_i - k_i \cdot x_i = 0 \quad (4-9)$$

Fugacity coefficients are calculated via equation of state as in Eq. (4-10) according to the Soave-Redlich-Kwong (SKR) cubic equation of state [197], which is reported in Eq. (4-11) in a form that highlights the compressibility factor Z .

$$\phi_i = \exp \left[\beta_i \cdot (Z - 1) - \ln(Z - B) - \frac{A}{B} \cdot (\alpha_i - \beta_i) \cdot \ln \left(1 + \frac{B}{Z} \right) \right] \quad (4-10)$$

$$Z^3 - Z^2 + (A - B - B^2) \cdot Z - A \cdot B = 0 \quad (4-11)$$

In Eq. (4-10) A , B are coefficients that include constants, pressure, the implicit dependence from the equilibrium temperature, and the two characteristics parameters (a , b) of the chosen equation of state (SKR). The full expression of the coefficients A , B and the two SKR parameters a , b are reported in Eq.s (4-12), (4-13) and Eq.s (4-14), (4-15), respectively. With regards to the two SKR parameters reported in Eq.s (4-14), (4-15), the Van der Waals mixing rules were adopted, in particular the quadratic rule was applied to a whilst the linear rule was applied to b . It is underlined that A , B , a , b must be calculated separately for the liquid and the vapor phase, thus, in Eq.s (4-12)-(4-15) the subscript L or V should be reported. However, for the sake of simplicity no subscript is placed, instead a general form is presented accounting for the moles fraction z , which would be x for the liquid phase calculations whilst it would be y for the vapor phase calculations.

$$A = a \cdot \frac{p}{(R_0 \cdot T_{sat})^2} \quad (4-12)$$

$$B = b \cdot \frac{p}{R_0 \cdot T_{sat}} \quad (4-13)$$

$$a = \sum_{i=1}^N \sum_{j=1}^N (z_i \cdot z_j) \cdot \sqrt{a_i \cdot a_j} \cdot (1 - C_{ij}) \quad (4-14)$$

$$b = \sum_{i=1}^N z_i \cdot b_i \quad (4-15)$$

In Eq.s (4-12)-(4-15) R_0 is the universal gas constant, T_{sat} is the equilibrium temperature, which corresponds to T_0 in the first modeling step, a_i , b_i , are the SKR parameters for each of the N pure components of the mixture (Eq.s (4-16)-(4-18)), C_{ij} is a tuning coefficient implemented by the original Author with the aim of capturing the enhancement of the interactions between pairs of molecules that highly differ in terms of molecular size and polarity. Due to the lack of sufficient data on the fluids of interest and the complexity of the calculation, C_{ij} was set at zero since no significant improvements were observed on fuels comprising pure gasolines to E10 blends while sweeps of different C_{ij} values were tested.

$$a_i = 0.42747 \cdot \frac{(R_0 \cdot T_{C,i})^2}{p_{C,i}} \cdot \left[1 + f(\omega_i) \cdot \left(1 - \sqrt{\frac{T_{sat}}{T_{C,i}}} \right) \right]^2 \quad (4-16)$$

$$b_i = 0.08664 \cdot R_0 \cdot \frac{T_{C,i}}{p_{C,i}} \quad (4-17)$$

$$f(\omega_i) = 0.48508 + 1.55171 \cdot \omega_i - 0.15613 \cdot \omega_i^2 \quad (4-18)$$

In (4-16)-(4-18) T_c , p_c are the critical temperature and pressure respectively, ω is the so-called acentric factor, which was introduced by Pitzer in 1955 as an index of the configuration and non-sphericity shape of molecules. Finally, coefficients α , β in Eq. (4-10) are defined as in Eq.s (4-19), (4-20).

$$\alpha_i = \frac{2}{a} \cdot \sum_{j=1}^N z_j \cdot \sqrt{a_i \cdot a_j} \quad (4-19)$$

$$\beta_i = \frac{b_i}{b} \quad (4-20)$$

The estimation of the fugacity coefficients via equation of state were adopted due to the fact that the solution of cubic equation of states is simple and scarce time demanding. Among other options (e.g., the base Redlich-Kwong equation (RK) [198] and the Peng-Robinson (PR) equation [199]), the SKR equation was the first to introduce the dependence of the equation of state parameter a from both temperature and acentric factor (Eq.s (4-16), (4-18)) and the possibility of tuning the results based on experimental data by means of the aforementioned cross interaction coefficients C_{ij} . Furthermore, the comparative assessment of the three most popular equation of states (SKR, RK, PR) has shown that while ensuring comparable computational cost and vapor phase estimations, the SKR is able to provide greater accuracy against the RK and comparable against the PR in estimating the liquid phase characteristics. Moreover, the SKR equation shows the unique ability to perform accurate predictions for systems including polar substances, which can be attractive for the analysis of gasolines with high levels of oxygenates blending and any level of blending with hydrous ethanol ($\approx 5\%$ vol of water) i.e., ethanol produced by skipping the dehydration step (presence of water reduced to few tenths of %vol) in order to effectively reduce the well-to-wheel emission of CO_2 . It is underlined that the SKR equation (Eq. (4-11)) is solved twice to return the compressibility factors for the calculation of the fugacity coefficients by means of a standard root-finding algorithm: i) solving for the liquid phase, Z_L is the minimum real root considering the liquid moles fraction of each component ($z_i = x_i$) in Eq.s (4-14), (4-15), (4-19);

ii) solving for the vapor phase, Z_V is the maximum real root considering the vapor moles fraction of each component ($z_i = y_i$) in Eq.s (4-14), (4-15), (4-19).

Once the pressure is set at the atmospheric pressure and the initial liquid composition of the surrogate ($x_{i,0}$) is given, the solution is constrained by the fulfillment of vapor mass balance (Eq. (4-21)). As a result, adjusting the core equations in order to fit a root-finding problem a $N+3$ system of equations is obtained and then summarized in the objective function reported in Eq. (4-22) for the numerical solution.

$$\sum_{i=1}^N y_i = 1 \quad (4-21)$$

$$F_{obj} = \begin{cases} y_i - k_i(T_{sat}) \cdot x_{i,0} = 0 & [i = 1, \dots, N] \\ Z_L^3 - Z_L^2 + (A - B - B^2) \cdot Z_L - A \cdot B = 0 \\ Z_V^3 - Z_V^2 + (A - B - B^2) \cdot Z_V - A \cdot B = 0 \\ \sum_{i=1}^N y_i - 1 = 0 \end{cases} \quad (4-22)$$

The numerical solution of Eq. (4-22) requires an initial solution array composed of guessed values for equilibrium temperature, liquid and vapor compressibility, and composition of the first vapor. With regards to the initial value for the equilibrium temperature, the moles weighted average among the normal boiling temperature of the components of the original mixture is adopted. The initial guess for the first vapor composition is calculated from Eq. (4-9) by assuming that the equilibrium ratios can be estimated according to the correlation by Wilson [200] (Eq. (4-23)), which relies on the use of few information such as the critical properties and the acentric factor of fluids. As long as the pressure at which the VLE is around the atmospheric pressure, the results from Eq. (4-23) are proper first attempt values whilst they are affected by significant loss of accuracy as the environmental pressure increases. Since the predicted distillation curve is recorded at atmospheric pressure, the reliability in using Eq. (4-23) is ensured in this case.

$$k_i = \frac{p_{C,i}}{p} \cdot \exp \left[5.37 \cdot (1 + \omega_i) \cdot \left(1 - \frac{T_{C,i}}{T_{sat}} \right) \right] \quad (4-23)$$

Once reasonable values have been assigned to the initial equilibrium temperature and vapor mass fractions, these are used to compute the first attempt values for the coefficients A_V and B_V to solve the SKR equation of state for the vapor phase, which returns the first attempt value for the vapor compressibility factor. The initial equilibrium temperature and the original liquid composition are used to compute the first attempt values for the coefficients A_L and B_L to solve the SKR equation of state for the liquid phase, which returns the first attempt value for the vapor compressibility factor. The initial values for T_{sat} , y_i , Z_L , Z_V are provided to the numerical solver implemented in the SciPy Optimize *Python* open library that is a modified Powell's method accomplishing a multivariate root-finding. The solver is constrained to reach a relative tolerance of 1×10^{-9} whilst the number of iterative solution steps is limited to 5000.

The second modeling step deals with the prediction of the kettle temperature-based full distillation curve by means of the resolution of the VLE for the remaining liquid mixture, which continuously changes as the distillate volume increases. The full distillation curve was considered as the result of a given number of discrete atmospheric equilibrium status of as many different liquid mixtures whose composition is defined by updating that of the original mixture according to the progress of the distillate volume. Therefore, the distillation curve is

divided into a number of steps called distillate cuts, then for each cut the VLE is solved by applying the first $N+2$ equations from Eq. (4-22) whilst the liquid composition change is traced according to the Rayleigh's differential equation (Eq. (4-24)), which describes simple batch distillation operations with no external reflux. Furthermore, no vapor re-condensation and internal reflux are considered. In Eq. (4-24) R is the molar amount of residual liquid at the cut under analysis.

$$\frac{dR}{R} = \frac{dx_i}{x_i \cdot (k_i - 1)} \quad (4-24)$$

Once the distillate volume recovered range has been divided in the chosen number of discrete points, Eq. (4-24) is integrated from the first equilibrium temperature T_0 to the generic cut J under analysis. Introducing r_j as the residual liquid step change between two consecutive cuts ($r_j = R_j / R_{j-1}$), the integration of Eq. (4-24) leads to Eq. (4-25) in which the equilibrium ratio k is taken at a reference temperature T_j^* that should be an intermediate temperature between the distillate temperature of the cut under analysis (J) and the one of the previous cut ($J-1$). Thanks to the steady state discrete equilibrium points approach chosen for modeling the distillation process, the dedicated code is able to perform timeless computations. As a consequence, the user is allowed to divide the recovered volume range assuming increasing of 1% of distillate liquid, leading to 100 computation cuts. As a consequence, it is possible to assume that the j -th reference temperature needed by Eq. (4-25) is the distillate temperature of the previous cut increased by 0.5 K.

$$x_{i,J} = x_{i,0} \cdot \prod_{j=1}^J r_j^{k_i(T_j^*)-1} \quad (4-25)$$

Therefore, the second modeling step is based on a system of equations comprising $N+2$ equations for the solution of the VLE, N equations to trace the distillation-induced liquid consumption and composition change, and the liquid mass balance (Eq. (4-26)) as a constraint for the resolved liquid composition. The latter system of equations is rearranged in the objective function reported in Eq. (4-27), which is minimized numerically for each cut separately. At each cut, the initial solution to provide the numerical solver is given by the final values of vapor composition, liquid composition, and compressibility factors achieved in the previous cut whilst the initial equilibrium temperature is set at the intermediate temperature T_j^* . The same numerical solver and iterative setup as that used in predicting T_0 is adopted. It is underlined that since neither external reflux nor re-condensation internal reflux are considered, it is assumed that the resolved vapor composition of each cut (y_i) is the same as that of the collected liquid recovered volume.

$$\sum_{i=1}^N x_i = 1 \quad (4-26)$$

$$F_{obj} = \begin{cases} y_{i,J} - k_i(T_{sat}) \cdot x_{i,J} = 0 & [i = 1, \dots, N] \\ Z_L^3 - Z_L^2 + (A - B - B^2) \cdot Z_L - A \cdot B = 0 \\ Z_V^3 - Z_V^2 + (A - B - B^2) \cdot Z_V - A \cdot B = 0 \\ x_{i,J} - x_{i,0} \cdot \prod_{j=1}^J r_j^{k_i(T_j^*)-1} = 0 \\ \sum_{i=1}^N x_{i,J} - 1 = 0 \end{cases} \quad (4-27)$$

As mentioned before, the third modeling step is charged to convert the kettle temperature-based distillation curve to the head-based distillation curve. To this aim, the energy balance representing the fuel vapor cool-down caused by the heat exchange with both air and walls was implemented (Eq. (4-28)). In Eq. (4-28) m_V and m_A are respectively the mass of fuel vapor formed in a given cut J and the mass of air trapped into the flask, c_{p-V} and c_{p-A} the associated specific heats at constant pressure, C_W the heat capacity of the flask's walls.

$$m_V \cdot c_{p-V} \cdot (T_{K,J} - T_{H,J}) = (m_A \cdot c_{p-A} + C_W) \cdot (T_{H,J} - T_{H,J-1}) \quad (4-28)$$

The energy balance is applied to a variable-size control volume which comprises the fuel-air-walls system between the liquid height into the spherical bottom in the cut J and the position of the top thermocouple, which is assumed to be placed in line with the connection pipe. As a result, the mass of air and walls involved in the heat exchange increases with the distillation progress and must be updated during the computation. Regardless of the distillation progress, the air trapped in the flask's neck and the corresponding surrounding cylinder wall are fully available for the heat exchange, whilst the masses of air and solid that contribute to the energy balance at the bottom of the flask (spherical base) depends on the level of the remaining liquid. As a result, the volume of the flask that can affect the fuel vapor cool-down, named active volume, is calculated as the sum of two terms: a fixed term representing the flask's neck; and a variable increasing term representing the part of the spherical base that is not filled up by the liquid in the cut under analysis (**Figure 4-5**). It is assumed that in the J-th cut the empty volume increase corresponds to the distillate volume according to the recovered volume range discretization. The active volume is defined as in Eq.s (4-29), (4-30) (air (A) and walls (W)), in which t is the thickness of the flask, R_1 , R_2 are the internal and the external (R_1+t) radius of the spherical bottom, h is the height of the neck, φ_D is the cumulative distilled volume fraction from 0 to J cuts. Once the active volumes were defined, the gaseous masses involved in Eq. (4-28) were calculated according to the perfect gas law, whilst the solid mass was calculated as the product between density and active volume.

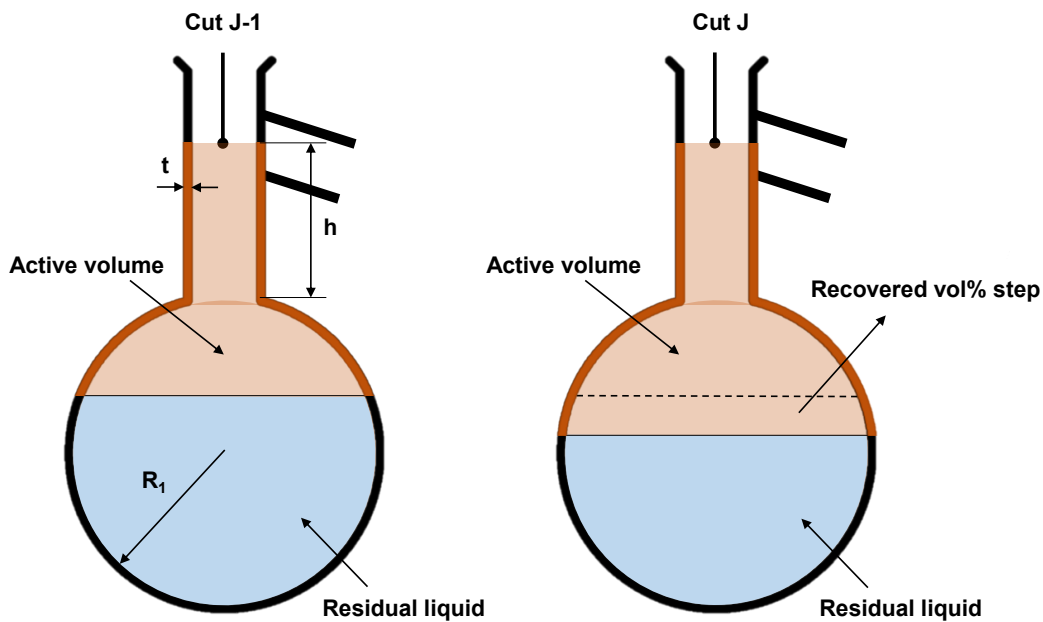


Figure 4-5: Schematic view of the fuel vapours heat exchange domain update.

$$V_{A-active} = V_{A,cyl} + V_{A,sph}(J) = \pi \cdot R_1^2 \cdot h + \frac{4}{3} \pi \cdot R_1^3 \cdot \varphi_{D,0-J} \quad (4-29)$$

$$V_{W-active} = V_{W,cyl} + V_{W,sph}(J) \\ = \pi[(R_1 + t)^2 - R_1^2] \cdot h + \frac{4}{3} \pi[(R_1 + t)^3 - R_1^3] \cdot \varphi_{D,0-J} \quad (4-30)$$

The geometrical data needed in Eq.s (4-29), (4-30) have been taken from the guidelines for distillation test bench reported in the ASTM-D86 regulation, and listed in **Table 4-2** together with the thermo-physical properties adopted for the solid walls of the flask.

Table 4-2: Geometrical data and thermo-physical properties of distillation flask.

Geometry	Value
Sphere diameter	69 mm
Neck diameter	19 mm
Neck height	70 mm
Glass thickness	2 mm
Initial liquid charge	100 mL
Property	Pyrex glass
Density	2230 kg/m ³
Specific heat	753 J/kg/K

Before applying the conversion to head distillation temperatures, the kettle temperature-based distillation curve returned by the first two modeling steps has been resampled in order to overcome two critical aspects of the match between experimental and numerical results. The two concerns in converting the distillation temperatures regard the end tails of the distillation curve: i) at the right-end tail of the curve, the sampling was limited to the T90 since in gasoline distillation experiments it is common to observe a non-evaporated residual which can be around 2%vol and 5%vol; ii) at the left-end tail of the curve, the sampling was applied starting from T5 due to the fact that the head T0 is difficult to define with respect to the other TX. This because T0 is the temperature at which the first vapor is formed, and its record in experiments is not based on the collection of a well-defined volume of liquid in the collection flask. Furthermore, the estimation of the head T0 via Eq. (4-28) requires the temperatures of air and walls at the first equilibrium, which depend on the heating up of the overall system from the ambient conditions to the T0 record time, which is not included in the present steady state-like modeling approach. Even in experiments, the measure of the first boiling temperature at the top of the flask is strongly affected by the heat exchange in the transient single-phase interval from ambient conditions to T0. In fact, the test of pure alcohols distillation in [201] has revealed a piecewise distillation curve characterized by a constant temperature value throughout the recovered volume range except for T0, which was slightly lower. Since it is well known that for a given pressure there is a single value of the equilibrium temperature for pure molecules, the piecewise curve for pure butanol shown in **Figure 4-6** (B100, data from [201]) is a clear evidence that the value of T0 measured at the top of the flask is not a well-defined point to compare experimental and numerical results.

In light of the above, finally, the full recovered volume range (0-100) provided by the kettle temperature-based distillation model is re-sampled from T5 to T90 by steps of 5%vol.

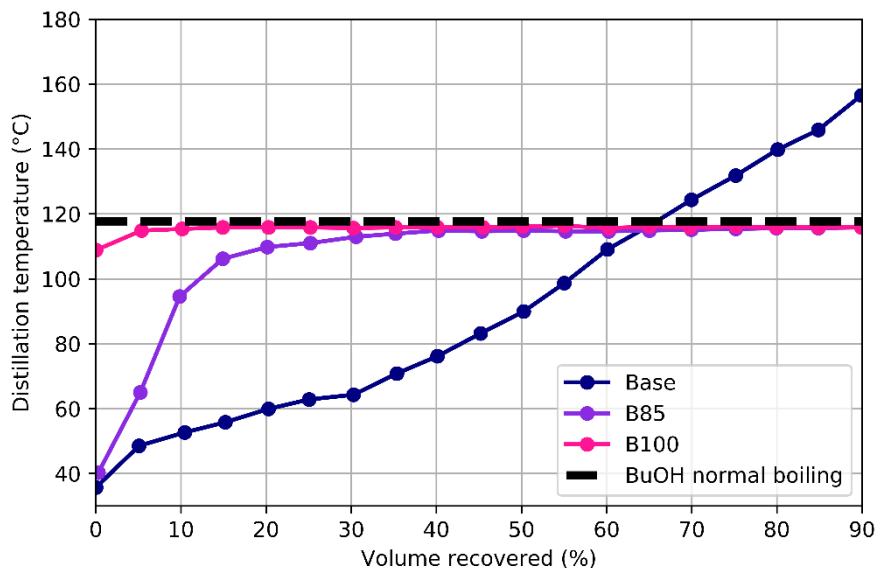


Figure 4-6: Experimental distillation curves [201] of a base gasoline, gasoline(15%vol)-butanol(85%vol) blend and pure butanol. The normal boiling temperature of butanol is also reported.

Reid vapor pressure

The Reid vapor pressure (RVP) i.e., the value of the absolute vapor pressure at 100°F (310 K), is a synthetic index representative of the volatility of fuel mixtures. Considering the typical injection temperature under early injection conditions in GDI engines (40-45°C), it is clear that RVP can describe the early evaporative behavior of real gasolines at the engine cold states, which are the most critical for the tailpipe emission under both WLTP and real driving conditions. As seen for the distillation temperatures, even the RVP is not additive and needs a dedicated modeling. In this research project, the RVP is predicted by using the same pure thermodynamic model adopted for T0 after adjustments to solve the classical bubble point pressure problem for non-ideal mixtures. Therefore, the same objective function shown in Eq. (4-22) was numerically minimized, however the temperature was set to the constant value of 310 K (100°F) instead of being the equilibrium unknown, whilst the pressure has been set as the implicit solution instead of being the environmental pressure. The initial solution guess was the same as that of the first distillation temperature except for the equilibrium unknown which was initially set as the moles weighted average among the saturation pressure values of the pure components at 310 K. It is underlined that as seen for T0, the initial values of the equilibrium ratios (k) were estimated by means of the Wilson correlation, which is still reliable due to the typical range of the gasolines RVP values.

Octane rating

Octane Numbers (ON), namely RON and MON values, were used as well to guide the surrogate searching process towards compositions that can be representative of nowadays high-octane rating, which are necessary in order to face off with the higher knock risk induced by higher in-cylinder pressure and engine thermal stress. However, RON and MON were not included in the target properties, instead, they were used as light constraints for the searching algorithm. Therefore, the searching algorithm was trained to check that RON and MON values of the surrogate formulation attempts lie in the acceptability range defined by the user as a threshold, instead of pursuing their punctual experimental reference values as required for the target properties. In the current literature, the prediction of RON and MON values of fuel mixtures by means of the moles weighted average is widely adopted. Despite

the fact that the latter estimation method produces reasonable results for PRF and TPRF mixtures, different correlations are necessary in order to take into account the non-linear increasing of the ONs with the addition of oxygenates. In the present research project, the correlation by Anderson et al. [202] was chosen. According to the Anderson et al. proposal, the ONs of a gasoline-oxygenate blend can be estimated as the sum of two terms: i) the moles weighted average ON including both oxygenates and hydrocarbons; ii) a term accounting for the quadratic dependence of the ON on the presence of oxygenates, then multiplied by the difference between the ON of the pure oxygenate (subscript AL) and the one of the unblended gasoline obtained as the moles weighted average including only hydrocarbons. According to the original Authors, the second term can be adjusted by means of the tuning coefficient which was set respectively at 0.45 for RON and at 0.94 for MON in line with the experimental guidelines given in [202]. Considering a surrogate formulation attempt including N components comprising N-1 hydrocarbons (N_{HC}) and one pure oxygenate as octane booster, the chosen reference correlation is written as in Eq.s (4-31), (4-32) and the resulting predicted effect on ON is shown in **Figure 4-7** for a generic RON95-MON85 base gasoline.

$$RON = \sum_{i=1}^N x_i \cdot RON_i + 0.45 \cdot x_{AL} \cdot (1 - x_{AL}) \cdot \left(RON_{AL} - \sum_{i=1}^{N_{HC}} RON_i \right) \quad (4-31)$$

$$MON = \sum_{i=1}^N x_i \cdot MON_i + 0.94 \cdot x_{AL} \cdot (1 - x_{AL}) \cdot \left(MON_{AL} - \sum_{i=1}^{N_{HC}} MON_i \right) \quad (4-32)$$

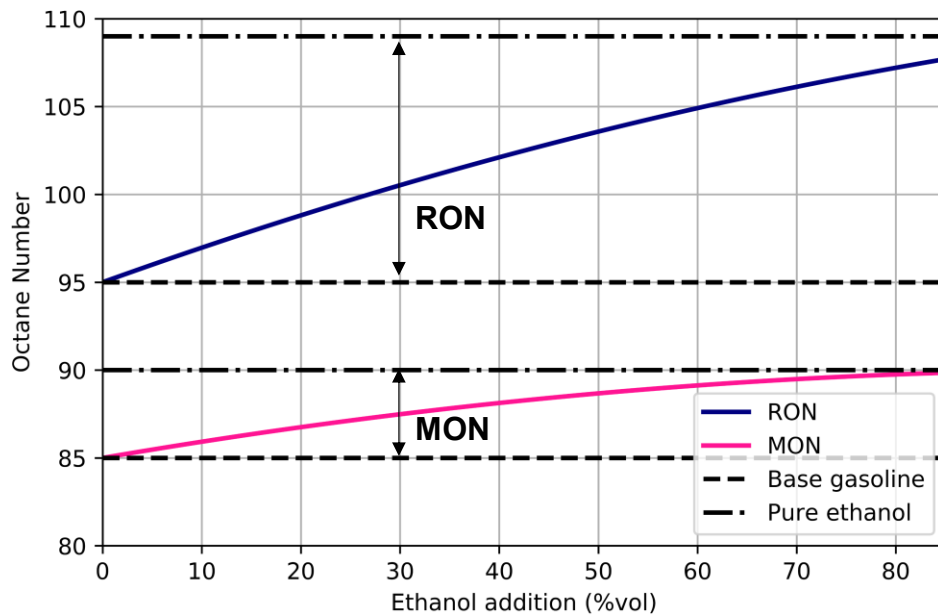


Figure 4-7: Effect of the oxygenate addition on a generic gasoline fuel considering predicted by the chosen tuned reference correlation by Anderson [202].

4.2.3 Searching strategy

Considering the large number of independent variables, equal to the size of the chosen palette i.e., 14 different fractions of pure fuels, and the non-linearity of some of the functions needed to reconstruct the target values, namely distillation temperatures, RVP, RON, MON, the optimization process cannot be addressed by a standard root-finding algorithm. Thus, it a more complex workflow was needed. State of the art optimization approaches have been successfully applied in literature to this aim. However, a customized implementation of the

distillation model with 100 discrete computation points in the perspective of mixture complexity around 6-9 components largely increases the amount of computing time required to run a number of evaluations sufficient to ensure a comprehensive exploration of the solution domain. In this framework, Bayesian optimization algorithms are attractive techniques to capture highly non-linear dependencies and minimize the number of evaluations due to optimized trade-off between exploration (searching phase during which the algorithm spend resources to test new distant points throughout the solution domain) and the exploitation (searching phase during which the algorithm pushes towards the refinement of a promising solution by evaluating the neighborhood points). The reason why Bayesian algorithms are usually employed in engineering application is that (in their classical form) they interpolate precisely the observations on which they were trained. Furthermore, they rely on a probabilistic algorithm that can simultaneously predict new values and their confidence intervals.

As far as an optimization task is concerned, an objective function must be defined and provided to the optimization algorithm. In common practice, the objective function can be cost functions (the optimization algorithm accomplishes a minimization task) or merit functions (the optimization algorithm accomplishes a maximization task). In this research project the merit function in Eq. (4-33) was defined as objective function in order to place the optimum surrogate mixture composition on a weighted Pareto-frontier according to the minimum Euclidian distance between the target properties of the surrogate and those of the reference real gasoline. In Eq. (4-33), given the number of the target properties (N_t) W are the weights assigned to each target property in order to enhance the importance of the match of some target properties with respect to others, e is the percentage absolute relative error between the predicted and the experimental values of each target property. As a result, the optimum mixture composition ($X = x_1, \dots, x_i, \dots, x_N$) is the one in the solution domain which produces the maximum value of the merit function F for given confidence on the sub-models adopted for the mixture properties prediction.

$$F = 100 - \frac{\sqrt{\sum_{i=1}^{N_t} W_i \cdot e_i^2}}{\sqrt{\sum_{i=1}^{N_t} W_i}} \quad (4-33)$$

It must be remembered that the optimum surrogate composition chosen by the searching algorithm is aimed at representing the real gasoline behavior in CFD engine simulations. Therefore, in order to avoid large computation expenses in CFD simulations, it was chosen to limit the number of components in the surrogate formulation attempts by including in the merit function a 'virtual' further target property called 'complexity'. The error associated with complexity needed to evaluate the merit function was defined as the ratio between the number of components in the surrogate formulation attempt (N) and the size of the initial palette (14). As a result, the value of the merit function that each surrogate would reach purely based on the match with the experimental target properties is penalized if the surrogate is too complex.

For the sake of clarity, the full expression of the merit function defined for the optimization of the surrogate composition is reported in Eq. (4-34). From Eq. (4-34) it can be seen that there is no term accounting for RON and MON values since those properties were considered light constraints instead of target properties. However, the impact of RON and MON values on the optimization algorithm is strong. In fact, regardless of the effective value of the merit function (target properties, net of complexity penalty) reached by any surrogate attempt, if RON and MON values differ from reference values by more than ± 3 units, the

merit function for that surrogate is set at zero. As a consequence, in the cases the penalty is applied, in the screening phase of the formulated surrogate options the algorithm is automatically discouraged in evaluating similar compositions, assuming that neighbor points are not able to comply with the threshold posed for the octane rating.

$$\begin{aligned}
 F = 100 - & \left[\frac{\sqrt{W_{density} \cdot \left(\frac{|\rho_{surr} - \rho_{exp}|}{\rho_{exp}} \right)^2}}{\sqrt{W_{density}}} + \frac{\sqrt{\sum_j^{AL-PIONA} W_{comp,j} \cdot \left(\frac{|\varphi_{j,surr} - \varphi_{j,exp}|}{\varphi_{j,exp}} \right)^2}}{\sqrt{\sum_j^{AL-PIONA} W_{comp,j}}} \right. \\
 & + \frac{\sqrt{W_{RVP} \cdot \left(\frac{|RVP_{surr} - RVP_{exp}|}{RVP_{exp}} \right)^2}}{\sqrt{W_{RVP}}} + \frac{\sqrt{\sum_j^{10:5:90} W_{temp,j} \cdot \left(\frac{|T_{j,surr} - T_{j,exp}|}{T_{j,exp}} \right)^2}}{\sqrt{\sum_{j=0}^{90} W_{temp,j}}} \\
 & \left. + \frac{\sqrt{W_{complexity} \cdot \left(\frac{N}{14} \cdot 100 \right)^2}}{\sqrt{W_{complexity}}} \right] \quad (4-34)
 \end{aligned}$$

Once the custom objective function is presented, the description of the searching algorithm needs to be revealed. Bayesian algorithms are machine-learning based optimization techniques focused on searching the global maximum of the expensive merit function F of unknown behavior with respect to the solution domain D (Eq. (4-35)), which in this work is the set of volume fractions of each component comprised in the initial palette (**Table 4-1**).

$$X_{opt} = (x_{1,opt}, \dots, x_{i,opt}, \dots, x_{N,opt}) = \operatorname{argmax}_{X \in D} (F(X)) \quad (4-35)$$

Bayesian optimization algorithms rely on two main features: i) the use of a method to introduce the statistical inference component; ii) the use of the so-called acquisition function, which is charged to decide the pattern for sampling the solution domain D . Both the method for statistical inference and the acquisition function are used iteratively in the searching process after initial evaluations of F on guessed domain-fillings that are typically chosen uniformly random. The implementation of these two components is presented in the following:

- In Bayesian-based methods the optimization of unknown expensive functions is accomplished via iterative steps by which the behaviour of the merit function on the composition domain is discovered by drawing ‘a picture’ of the so-called surrogate model, namely the evaluation of a function f that approximates the merit function F on a sequence of finite successive points based on priors (i.e., beliefs on the behaviour of the function on the composition domain) [203], [204]. In this research project, the chosen surrogate model is the Gaussian Process (GP), which is a Gaussian distribution over the functions domain, instead of that of variables, that is completely defined by a mean function $M(x)$ (expected behaviour of the surrogate function on the training points among the possible fitting options) and a covariance function $K(x,x')$. The covariance function called kernel describes the correlations between the evaluation of the surrogate function at each pair of points in the training set (x,x') assuming that closer points have the largest degree of correlation. Thus, the kernel encodes the belief that closer pairs of training points should have the more similar value of the surrogate function against distant points.

In other words, GP is a function that returns mean value and variance of a Gaussian distribution over possible values of the surrogate function f at a training point of the solution domain (Eq. (4-36)). As a result, the attractive feature of GPs is that they are able to infer the properties of the merit function over a large domain by providing both the expectation (mean) at a given point and the associated uncertainty (variance), which is fundamental for the algorithm to decide in which region of the solution domain the sampling for the next iterations should be applied. The kernel chosen for this task is the Matérn (Eq. (4-37)), in which ζ and ν are hyperparameters controlling the variance of the additional white noise on the training points and the smoothness of the function, respectively, Γ is the gamma function, K_ν is the modified Bessel function. At the first step of the Bayesian optimization, 30 uniformly distributed random points of the composition domain were selected as training set whilst a GP characterized by a zero mean function was chosen as a prior and then used to generate the posterior on those points. An example of the described GP can be seen in **Figure 4-8**.

$$f(x) = G(M(x), K(x, x')) \quad (4-36)$$

$$K(x, x') = \zeta \cdot \frac{2^{1-\nu}}{\Gamma(\nu)} \cdot (\sqrt{2\nu} \cdot \|x - x'\|)^\nu \cdot K_\nu \cdot (\sqrt{2\nu} \cdot \|x - x'\|) \quad (4-37)$$

- Once the GP has returned the posterior distribution over the solution domain, the predicted uncertainty is used to build-up the so-called acquisition function, which is charged to assess which new point in the composition multi-dimensional domain should be evaluated next. As acquisition function, the Upper Confidence Bound (UCB) form (Eq. (4-38)) has been adopted and then used in the searching strategy shown in Eq. (4-39) in order to minimize the regret over the optimization steps.

$$A_{UCB}(X, \{x_n, y_n\}, \theta) = M(X, \{x_n, y_n\}) - \theta \cdot \Sigma(X, \{x_n, y_n\}) \quad (4-38)$$

$$X_{next} = \operatorname{argmax}_X (A_{UCB}(x)) = X_{MAX} \quad (4-39)$$

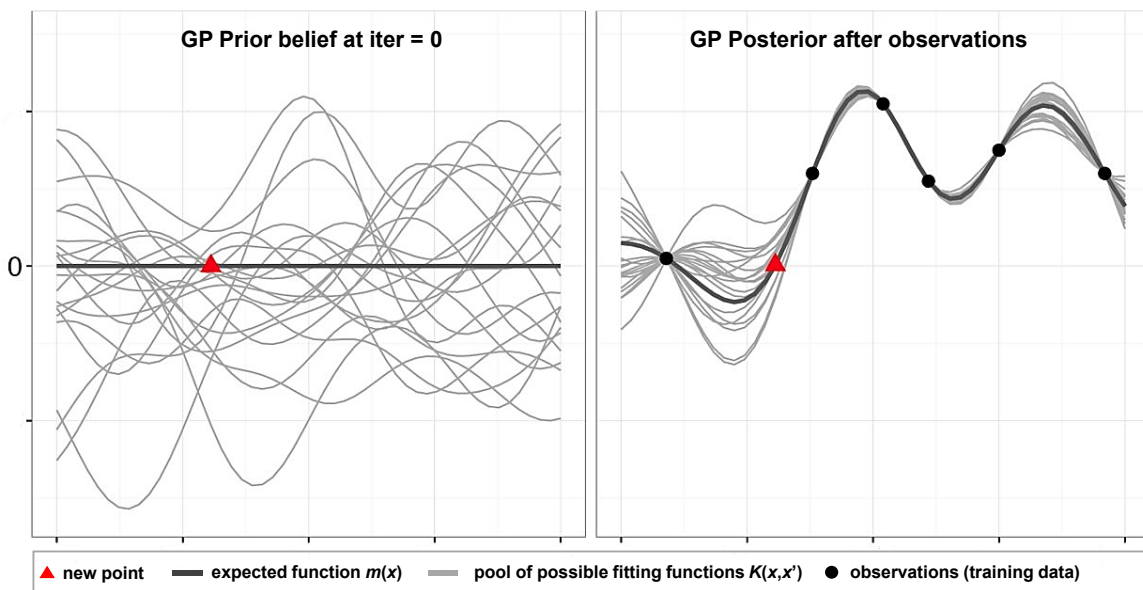


Figure 4-8: Example of prior and posterior distributions by a Gaussian Process on single variable.

At the right-hand side of Eq. (4-38), the first term accounting for the expected function emphasizes the exploitation phase, thus, points considered as promising for the next evaluation are neighbours of the point among the observations in the current posterior $\{x_n, y_n\}$ that reached the higher value of the expected merit function. In other words, the searching is guided towards the surrounding of the points at which the merit function is high with the belief that high merit points, including the global maximum, share the same space in the solution domain. Thus, a finer search in that space is applied. At the left-hand side of Eq. (4-38), the second term accounting for the uncertainty (pool of functions that fit given points from the posterior equally nice with respect to the expected mean) emphasizes the exploration phase. Thus, points considered as promising for the next evaluation are those that belong to spaces associated with interpolating functions that differ the most from the expectation $M(x)$ i.e., the space at which the uncertainty is maximum. Therefore, the searching is guided towards spaces in the solution domain that are still quite unknown. However, as a matter of fact in those unknown spaces lies the expectation of the derating of the merit function as well as the potential to discover significant improvements. In Eq. (4-38) θ is a tuning hyperparameter indicating the level of 'thrust' that is given to the GP. The hyperparameter is used as a leverage to balance exploitation and exploration, thus, according to the setting of the θ , UCB allows for a mixed searching strategy giving importance to spaces with significant high value of the merit function together with a decent perspective to discover new features of that which may lead to higher values. An example of the GP-UCB searching iterations is show in **Figure 4-9**. In **Figure 4-9** the dotted line is the merit function, black dots are observations, the black solid line and the dark gray band are the GP-predicted expected function and the uncertainty, respectively, the light gray curve (A_{UCB} pictures line) is the posterior-derived acquisition function, the black triangle is the worth new evaluation point according to Eq. (4-39), the white dot (GP pictures line) is the new observation. Pairs of successive iterations of the same sample optimization task are shown in rows.

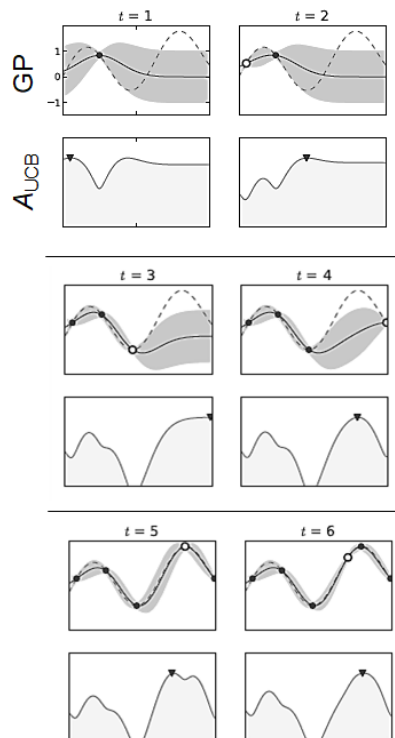


Figure 4-9: Example of Bayesian optimization by means of the joint use of Gaussian Process and Upper Confidence Bound driven searching strategy. Pictures edited from the original in [203].

Once the next evaluation point is determined by the UCB strategy, the posterior distribution of the last iteration is provided as prior to the next iteration, thus, the new posterior is computed based on the comparison between the new prior and the new training set (the previous observations + the new evaluation point). The complete algorithm, inspired from the fundamental application by Brochu et al. [203], can be summarized in the following points:

- a number of base combinations is initially evaluated, and the objective function (merit function) is calculated for them.
- the Gaussian Process priors are initially fit to those available data points.
- the objective function is evaluated in the point X_{MAX} that optimizes the acquisition function over the pre-trained Gaussian Process model.
- if successive iterations are expected, the Gaussian Process model is updated with the newly evaluated point, else the point X_{MAX} is returned.

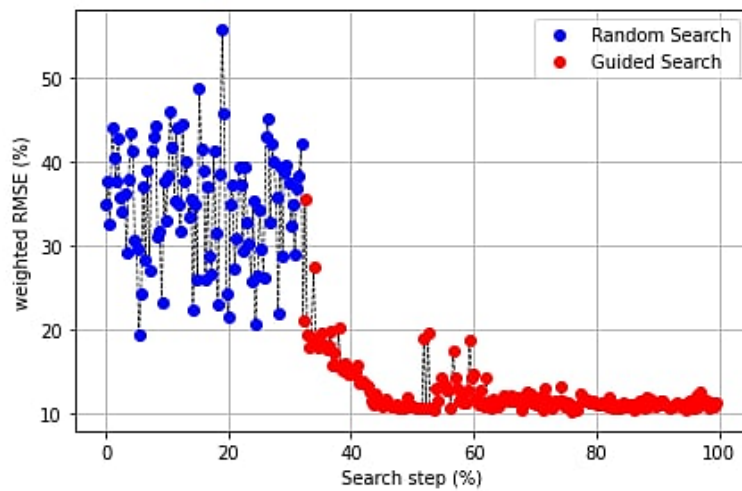


Figure 4-10: RSME profile in the searching process of the optimum surrogate composition according to the Gaussian Process - Upper Confidence Bound Bayesian optimization.

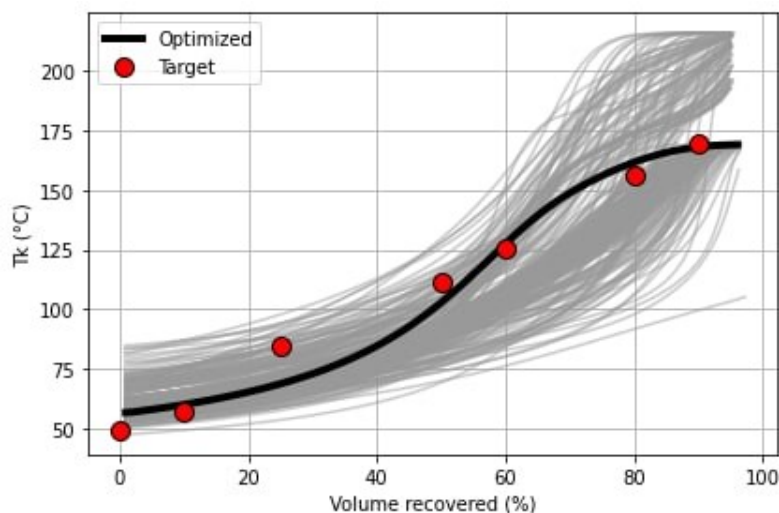


Figure 4-11: Evolution of the kettle distillation temperature for the surrogate formulation attempts (gray curves), optimized surrogate (black line) and reference experimental data (red markers).

Figure 4-10 displays the performance of the proposed algorithm for a sample test gasoline. Blue and red markers represent the exploration and the following exploitation phases, respectively. It is visible that the RSME approaches the asymptotic minimum value after around a half of the complete searching. In the second half the final solution is refined. The red peaks in the refinement step are caused by sporadic attempts of further exploration that are correlated to the set value of the degree of thrust θ . For the same sample optimization task, the evolution of the distillation properties during the iterative Bayesian optimization is reported in **Figure 4-11**.

Setup and convergence

The Bayesian optimization process is performed applying a 25%/75% split of random/guided search. As described in previous sections, the Bayesian algorithm must accomplish a multi-objective optimization task over the multi-dimensional (14-dimensional) space of the surrogate composition. In order to address the searching so that off-topic computations can be avoided, the infinite searching range of each of those dimensions was slightly limited between proper values with respect to the present application. Therefore, the presence of each of the 14 components of the original palette must range from 0 to 80%vol. Then, once the surrogate is defined, components with presence below 4%vol are automatically excluded, and the new composition is renormalized. Considering the dimension of the ethanol composition, it is underlined that: i) for non-oxygenate gasolines, the possibility to choose ethanol in the surrogate formulation is directly denied by the user i.e., the presence of ethanol is constrained at 0%vol, thus, the optimization task is reduced to a 13-dimensional problem. This device was necessary in order to avoid ethanol-blended formulations which could have been promoted to achieve easy match of RON and MON values for high octane pure hydrocarbon gasolines.

As shown in Eq. (4-34) the values of the weights in the merit function were grouped according to the associated type of properties. As a consequence, each chemical class of the macro-chemical composition (AL-PIONA) was associated to the same weight W_{comp} as well as each of the distillation temperature of the distillation curve (TX from T10 to T90 by step of 5) was associated to the same weight W_{temp} . On the other hand, different weights were assigned to density, RVP, and complexity. The values of the weights, presented in **Table 4-3**, were chosen according to the intrinsic difficulty to match equilibrium properties, thus, greater importance is given to the reference-surrogate distance of distillation temperatures and RVP. A lower value was assigned to macro-composition and density due to the fact that the first was intended as a complementary target property to increase the match of some distillation temperature and RVP as discussed in **4.2.2**, whilst the density can be easily matched by several combinations i.e., it shows a weak sensitivity to the variability present in the chosen palette. The assignment of greater importance (higher weights) to those properties which can be matched in a collateral manner, may lead to the 'over-constraint' of the optimization task resulting in the slowing down of computations and significant performance degradation of the algorithm. The optimum hyperparameters of GP and acquisition function as well are reported in **Table 4-3**.

With regards to the convergence criteria, in order to provide a tool able to perform timeless computations, it was decided to leave to the user the constraint of the maximum number of optimization iterations. As shown in **Table 4-3**, for this application the maximum number of iterations allowed before returning results was set to 200. The latter setting was achieved after testing different options i.e., 100, 200, 500 iterations, for a given target sample gasoline and setup of the algorithm. It must be remembered that even if slightly addressed by the user, the initial part of the searching process is random, and it is responsible for the results

of the following improvement. Therefore, for given conditions, each run of the code may produce different results.

In the development step, the convergence criterion adopted by the present Author relies on the fact that for a given maximum number of iterations, different runs of the code should produce similar RSME profile and asymptotic value as presented in **Figure 4-10**. Performing tests for 100 maximum iterations, the target RSME profile may or may not be achieved, thus, the achievement of the optimum solution at the end of the searching process is not ensured. Performing tests for 500 maximum iterations, no substantial differences with respect to the case of 200 were observed by comparing the results from different launches, however, the computation time was significantly higher. As a result, 200 was chosen as maximum number of iterations.

Table 4-3: List of the optimized setting of the Bayesian optimization algorithm.

Parameters	Setup
W_{density}	1.0
W_{comp}	1.5
W_{temp}	2.0
W_{RVP}	2.5
$W_{\text{complexity}}$	0.5
GP regressor kernel	Matérn
Target variables	Normalized
Kernel ν	5/2
Kernel ζ	1×10^{-6}
UCB θ	0.5
Initial evaluations	50
Max. iter	200

A further device added to the afore-described algorithm was a post-processing feature that allows the so-called unicity analysis. It is well known that for given reference gasoline and methodology, the optimum surrogate pursuing the chemical properties and that pursuing the physical properties are typically strongly different. However, the current literature lacks investigations on the comparison among different surrogates of a reference gasoline for given methodology and target properties as well. To this aim, at the end of the optimization task, the solution that reached the maximum value of the merit function (F_{MAX}) is signed as the optimum surrogate. Furthermore, a pool of other worth surrogate options is recorded according to a threshold criterion, namely solutions that reached an effective value of the merit function (i.e., the value of F after the screening step that checks that the composition complies with the RON and MON light constraint) that is sufficiently high ($F > 95\% F_{\text{MAX}}$). Among these solutions, the one associated to the most different composition with respect to that of the optimum surrogate is considered as equivalent-valuable surrogate (bounding surrogate), and the properties of those two (optimum and bounding) are compared in order to assess the surrogate composition unicity. **Figure 4-12** displays an example of the distribution of the scores obtained by the surrogate attempts formulated in successive iterations. The composition associated to the highest value of the objective function (blue square) is the optimum surrogate, whilst the black circle represents the score achieved by the trade-off composition between high value of the objective function and the larger composition difference with respect to the optimum option. Red circles represents surrogate attempts included that fall in the $F > 95\% F_{\text{MAX}}$ threshold, whilst green points are those that fall out of the threshold.

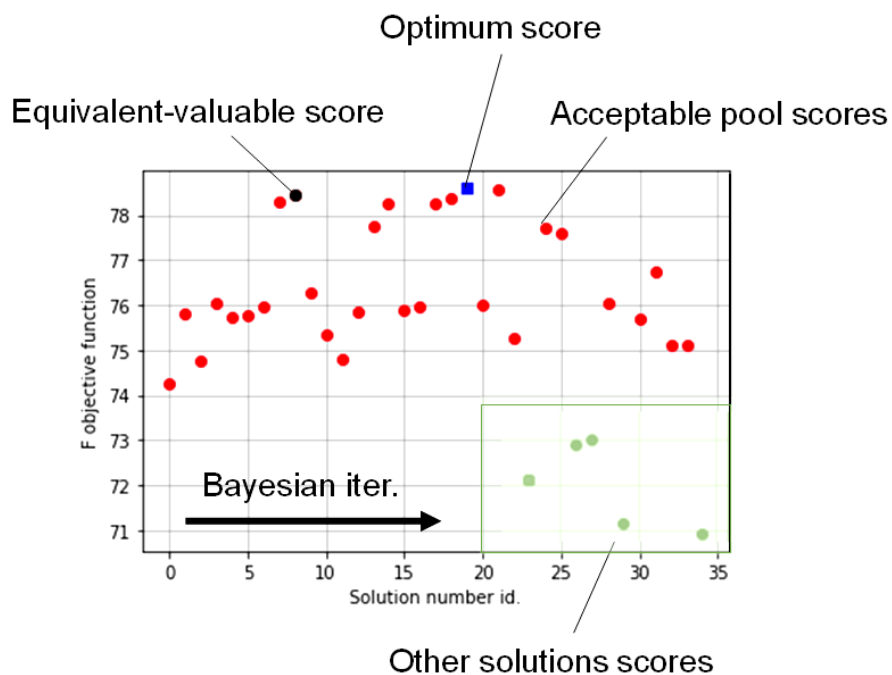


Figure 4-12: Example of the solutions pool returned by the Bayesian iterative algorithm reporting optimum surrogate (blue), bounding surrogate (black), acceptable surrogates pool (red), other minor surrogate options (green).

4.3 Results

4.3.1 Distillation model validation

In order to validate the in-house developed distillation model, experimental distillation curves of mixtures of known composition are necessary, thus, data from [205], [206] were considered as validation benchmark. The latter experimental references were chosen due to the fact that they provided the kettle distillation curve, which is very rare in the open literature, for mixtures of different complexity comprising different species. The experimental reference mixtures are reported in **Table 4-4**.

Table 4-4: Composition of six validation mixtures simulated at the distillation bench model.

Compound	Mix1 [205] %wt	Mix2 [205] %wt	Mix3 [206] %wt	Mix4 [206] %wt	Mix5 [206] %mol	Mix6 [206] %mol
n-Pentane	-	50	-	-	-	-
Methylcyclohexane	-	-	20	5	-	-
n-Heptane	-	50	-	-	-	-
i-Octane	-	-	-	5	-	-
n-Decane	50	-	60	25	80	-
n-Dodecane	-	-	-	25	-	80
n-Tetradecane	50	-	-	20	-	-
Toluene	-	-	20	20	-	-
124TMB	-	-	-	-	20	20

In **Figure 4-13** and **Figure 4-14** the experimental and predicted distillation curves and the associated errors are shown. In **Figure 4-13** it is visible that the model is able to capture the overall distillation behavior regardless of the mixture's complexity (i.e., number of components). A solid agreement with experiments is achieved for the heavier mixtures (Mix1, Mix5, Mix6) whilst a slight overestimation can be observed for more complex and lighter mixtures (Mix2, Mix3, Mix4) at the high half of the curve. In **Figure 4-14**, for the validation mixtures except Mix4 a bell-shaped error profile is visible with excellent prediction performance around the end tails of the distillation curves, which are significant indexes of the cold start behavior and the delayed evaporation tendency of the real gasoline as mentioned in **4.2.2**.

From the end tails of the curves, the error increase converging towards the middle distillation range with maximum values in the range T50-T70. The peak of the bell-shaped curve of Mix2 and Mix3 is associated to values of the error that are not negligible (>5%-8%), confirming the negative dependency of the prediction performance on the significant presence of light components (50% n-Pentane for Mix2, 20% Methylcyclohexane for Mix3). The latter is enhanced as the complexity of the mixture is lower (Mix2, 2-components with 8% peak absolute error) likely due to the need to trace the abrupt composition change from multicomponent to almost pure liquid. Except for the binary light mixture Mix2, the bell profiles are generally limited to error values around or below 5%, which can be acceptable aiming at high accuracy predictions. The most complex mixture (Mix4, 6-component) is characterized by a slight irregular error profile from T20 to T90 caused by the larger number of components that however oscillates around 4%, whilst the same excellent performance reported for the other mixtures is achieved at the right-end tail of the curve. Considering the composition and the typical number of components in gasoline surrogates for CFD application, prediction error profiles similar to that of Mix4 (blue curve) but shifted towards errors around 5-6% can be expected.

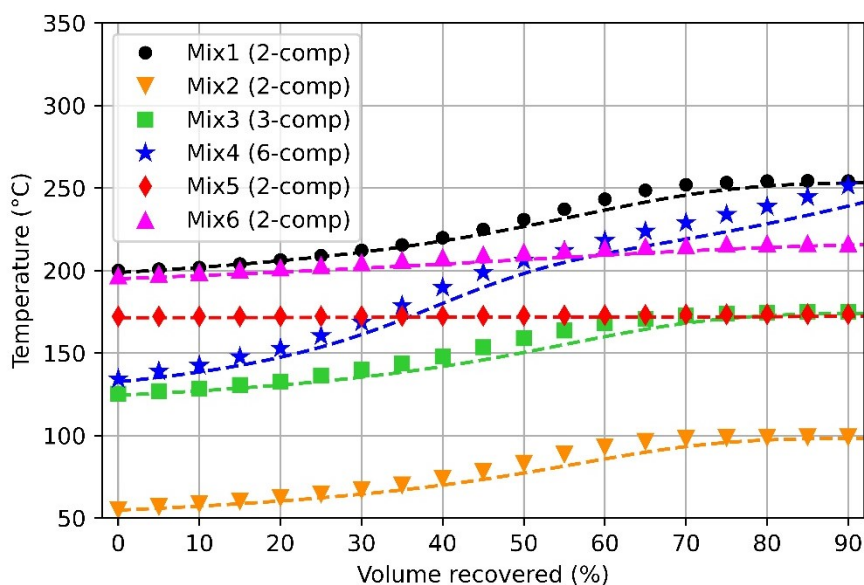


Figure 4-13: Comparison between experimental (markers) and predicted (dashed lines) kettle temperature-based distillation curves for the six validation mixtures.

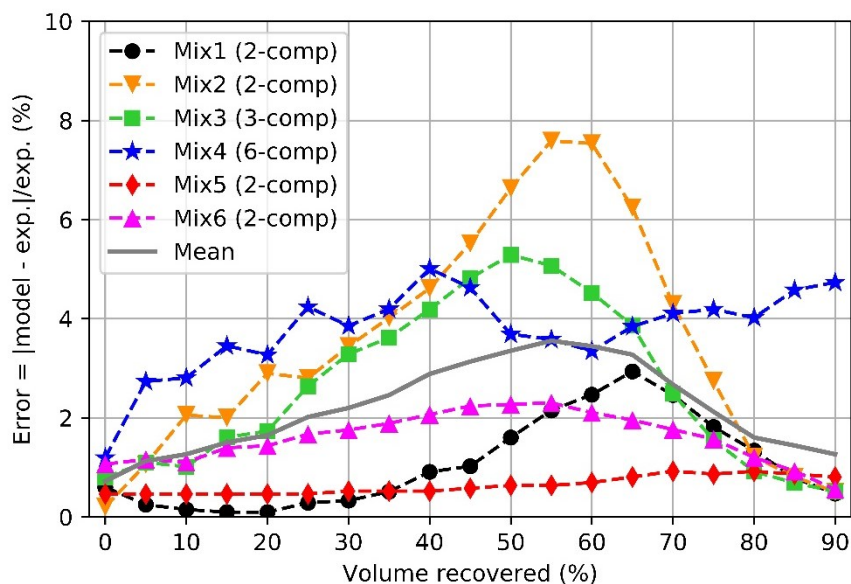


Figure 4-14: Absolute relative error profile in predicting the distillation curves of the six validation mixtures. Single profiles in dashed dotted lines, average profile in solid gray line.

In order to provide a fair validation of the proposed distillation model, even the simplified energy balance applied to convert the kettle distillation temperatures to head temperatures was validated against experimental data as a stand-alone model. For the sake of brevity, this validation step is shown only for Mix2 in order to give proof of reliability on the light mixture which showed the most challenging match. **Figure 4-15** shows the comparison between the experimental and the predicted head temperature-based distillation curve of Mix2, the experimental kettle temperature-based distillation curve which was provided as input to the iterative application of (4-28) is shown as well. It is visible from **Figure 4-15** that the chosen head temperature estimation approach returns a nice agreement with experiments throughout the distillate volume range except for a slight over-estimation at T60-T70.

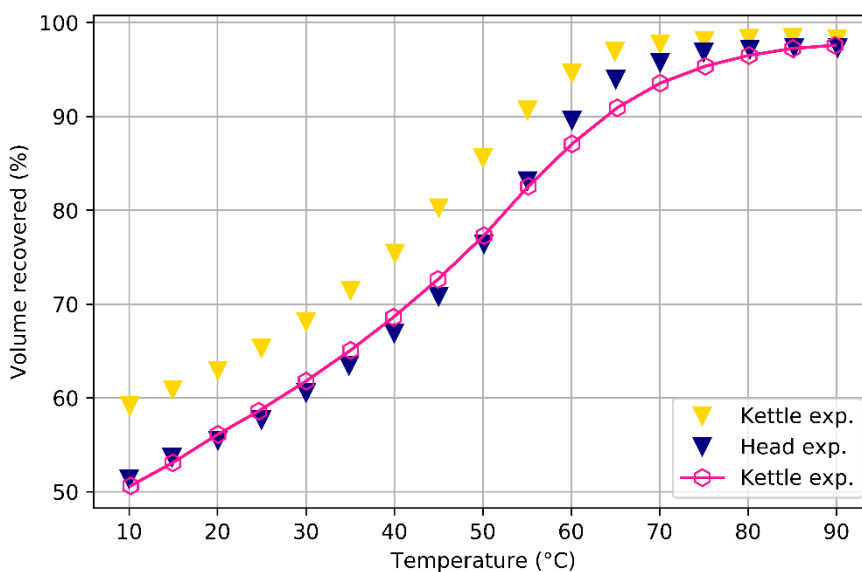


Figure 4-15: Comparison between experimental ([205], blue markers) and predicted (magenta dotted line) head distillation temperatures and the associated kettle temperatures (yellow markers).

Given the validation results, there was confidence in the fact that the modeling adopted for the mixture properties calculation did not suffer from relevant errors that can affect the formulation of surrogates.

4.3.2 Optimum surrogate identification

The implemented algorithm was applied to the formulation of surrogates for four real gasolines whose full experimental characterization is available in open literature. From [207], two Co-Optima gasoline fuels, namely the Aromatics-based Co-Optima gasoline and the Cycloalkanes-based Co-Optima gasoline were selected. From [208], the EU6 compliant gasolines Fuel-15 (additive-free gasoline with properties in line with the current commercial RON95 gasoline) and Fuel-11 (E10 gasoline-ethanol blend) were selected among the available fuels according to the following defined criteria: i) ethanol-blending $\leq 10\%$ vol; ii) RON ≥ 95 ; iii) olefins volume content $\leq 10\%$ vol. The main properties of the four validation gasolines collected from the reference works are listed in **Table 4-5**. It is underlined that the AL-PIONA of gasolines Fuel-11, Fuel-15 were calculated based on the Detailed Hydrocarbon Analysis (DHA) available in [208]. In the following, for the sake of simplicity the four validation gasolines are called A (Aromatics-based Co-Optima), B (Cycloalkanes-based Co-Optima), C (Fuel-15), D (Fuel-11). Firstly, the comparison between the real gasoline and their associated optima surrogates achieved is discussed.

Table 4-5: Available properties of the four validation gasolines.

Properties	A	B	C	D
RON	98.0	98.1	97.8	95.0
MON	87.1	87.8	85.6	84.9
Density @15°C (kg/m ³)	755.5	757.2	759.6	742.8
RVP (psi)	8.0	7.2	9.9	10.2
T10 (°C)	55.7	59.4	51.4	46.4
T20 (°C)	62.4	72.2	58.7	54.7
T30 (°C)	68.9	84.6	64.5	63.7
T40 (°C)	76.6	96.8	69.2	74.6
T50 (°C)	87.4	108.1	87.4	87.6
T60 (°C)	101.7	116.4	110.6	102.3
T70 (°C)	113.8	124.0	121.9	117.2
T80 (°C)	122.7	136.3	132.2	130.0
T90 (°C)	142.7	157.9	148.1	148.6
Carbon (%wt)	87.0	87.0	83.7	86.8
Hydrogen (%wt)	13.0	13.0	12.7	13.2
Oxygen (%wt)	0	0	3.7	0
Ethanol (%vol)	0	0	8.54	0
n-Paraffins (%vol)	6.9	6.7	15.66	17.81
i-Paraffins (%vol)	28.70	33.90	20.36	30.02
Olefins (%vol)	1.50	4.10	7.67	7.58
Naphthenes (%vol)	24.00	7.90	7.94	7.24
Aromatics (%vol)	38.40	45.80	38.62	36.11

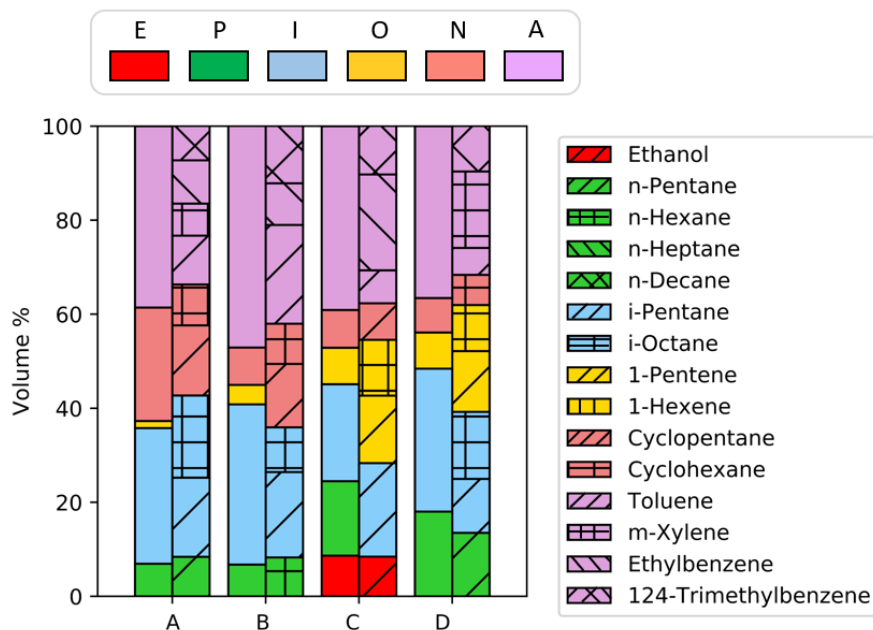


Figure 4-16: Volumetric composition of the four validation gasolines and their associated optima surrogates. Macro-composition is displayed via colours for both real and surrogate fuels, micro-composition is shown via patterns for surrogates only.

Figure 4-16 reports the macro-chemical classes considered in this project, which are indicated by the color of the bar, as well as the compounds included in the optima surrogates, which are indicated by different patterns of the bar. For each reference gasoline fuel, a pair of composition bars are presented: i) the macro-composition bar of the experimental fuel at the left (empty bars); ii) the macro and micro composition of the associated surrogate at the right (patterned bars). Since surrogates may include different compounds which belong to the same macro-chemical class, they would be filled with the same color. Thus, a unique pattern is assigned to each compound of a certain chemical class in order to distinguish among stacks of the same chemical class.

It can be seen that the surrogates of A, B gasolines lack olefins. Since A, B real gasolines are quite poor in olefins (1.57 %vol and 4.54 %vol, respectively) the setting of the Bayesian algorithm automatically removed the olefins available in the palette because their matched target presence would be below the chosen minimum threshold i.e., 4 %vol (**4.2.3**). The optima surrogates of C, D gasolines are characterized by the over-estimation of olefins, also a lack of n-paraffins can be observed in the surrogate of C gasoline. In **Figure 4-16** an overall nice agreement is visible, in particular with regards to i-paraffins, aromatics and ethanol. Despite the fact that the match of each chemical class is pursued with the same importance i.e., same weight value (**Table 4-3**), in the analysis of the results more emphasis should be placed on the excellent capture of ethanol, i-paraffins and aromatics with respect to others. This particular focus is due to the key role played by those chemical classes in determining fundamental features of the gasoline evaporation i.e., flattening of the distillation temperature profile in a significant distilled volume range due to the addition of oxygenates, average evaporative behavior mainly driven by i-paraffins, delayed evaporation with formation of rich pockets of mixture due to the presence of aromatics.

With regards to the species comprised in the optima surrogates, in **Figure 4-16** it is visible that heptane and decane are not included in any surrogate formulation because of their non-positive contribution to RON and MON values. Thus, surrogate options including those two components have been ignored likely due to the penalty posed on those formulations during

the screening phase by the algorithm ($F = 0$) if RON and MON values are not compliant with the corresponding light constraints. The components that are in common between the four optima surrogates are i-pentane, toluene, 1-2-4-trimethylbenzene. It must be highlighted that the representation of aromatics required the most various composition, giving proof of being the most complex part of real gasolines to mimic. As a results, four surrogates comprising from 8 to 9 components have been achieved. The detailed composition of the optima surrogates is released in **Table 4-6**. It must be underlined that even if the complexity of the present optima surrogates is slightly greater than that of state-of-the-art gasoline surrogates (8-9 components against 6-7 components), it was checked that the weight of this additional complexity on the engine cycle simulation time (order of 1-2 days) did not affect the overall computation cost significantly (order of 2-4 h of additional simulation time).

Table 4-6: Composition of the optimum surrogate for each of the four validation gasolines.

Compound (%mol)	A	B	C	D
Ethanol	-	-	15.44	-
n-Pentane	8.61	-	-	14.31
n-Hexane	-	7.34	-	-
n-Heptane	-	-	-	-
n-Decane	-	-	-	-
i-Pentane	17.06	18.12	18.31	12.06
i-Octane	12.52	6.71	-	10.58
1-Pentene	-	-	13.98	14.39
1-Hexene	-	-	10.14	9.58
Cyclopentane	18.70	16.61	8.83	-
Cyclohexane	9.47	9.15	-	7.21
Toluene	11.51	22.96	7.04	6.59
m-Xylene	6.55	-	-	16.15
Ethylbenzene	8.86	8.37	17.80	-
1-2-4-Trimethylbenzene	6.72	10.74	8.46	9.13

In **Figure 4-17**, **Figure 4-18**, **Figure 4-19**, **Figure 4-20** the results regarding the distillation curves are displayed. For each of the four validation gasolines, the experimental and the surrogate curves are compared, furthermore the normal boiling temperature of each component of the surrogate and the corresponding presence in terms of molar percentage are shown. **Figure 4-17-Figure 4-20** show that the shape of the distillation curve of the optima surrogates is in solid agreement with the experimental data along the whole distillation axis. The surrogates of A, C, D gasolines achieved an overall great match whilst a significant general under-estimation can be noticed for the surrogate of B gasoline. **Figure 4-21** shows the temperature difference between the predicted distillation temperature of the surrogate and the experimental value associated to the real gasoline. Dashed lines are placed at $\pm 7^\circ\text{C}$, which are here considered as acceptable temperature differences for this validation application. The surrogates of A, D gasolines show temperature differences with respect to experiments below 5°C along the whole distillation axis. The surrogate of C gasoline as well is characterized by overall acceptable temperature differences even though a predicting performance degradation is shown in the distillation interval T50-T60, where temperature differences out of the acceptability bounds are present. It must be underlined that experimental works in literature [193], [209], [210] have shown that the addition of oxygenates in light-duty gasolines particularly affects the range 30-60 %vol. Therefore, it is worth mentioning that accurate predictions (differences below 5°C) have been achieved in

this range for the E10 surrogate (C). Thus, a good performance of the algorithm in predicting the evaporation of oxygenates can be expected. The steep increase of the temperature difference in the T50-T60 interval can be caused by the lack of paraffins reported in **Figure 4-16** that affects the transition to ethanol-free mixture and the formation of the consequent first vapor of the next evaporating HC components.

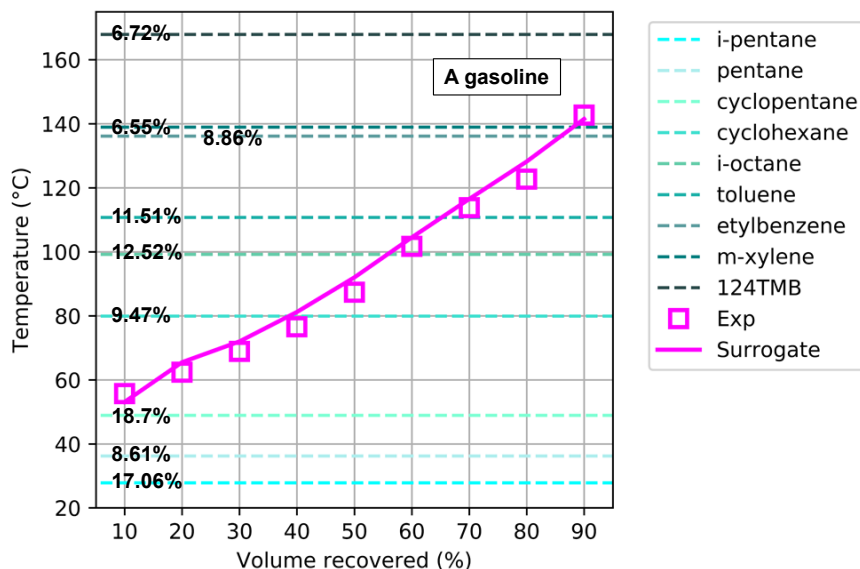


Figure 4-17: Comparison between experimental (markers) and surrogate (solid line) distillation curves for the validation gasoline A. Normal boiling temperature of the surrogate's components (dashed line) and their molar percentage are also reported.

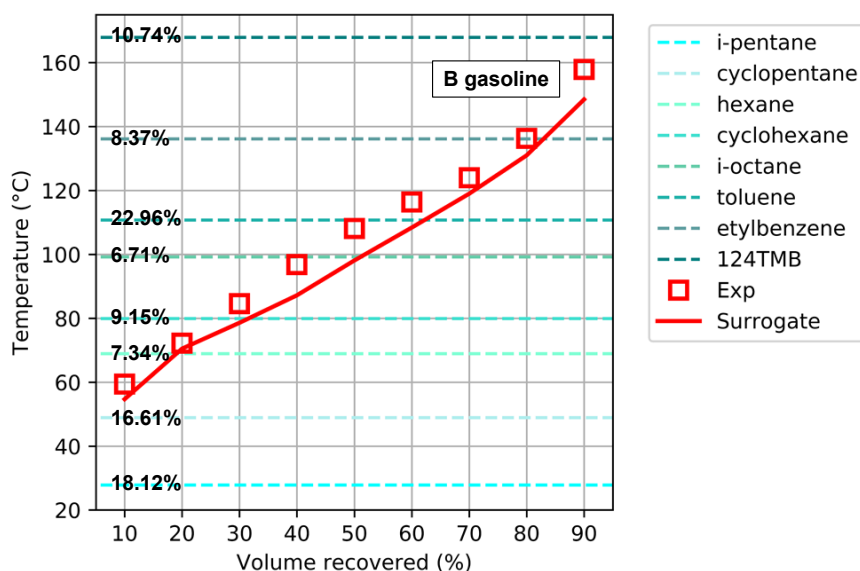


Figure 4-18: Comparison between experimental (markers) and surrogate (solid line) distillation curves for the validation gasoline B. Normal boiling temperature of the surrogate's components (dashed line) and their molar percentage are also reported.

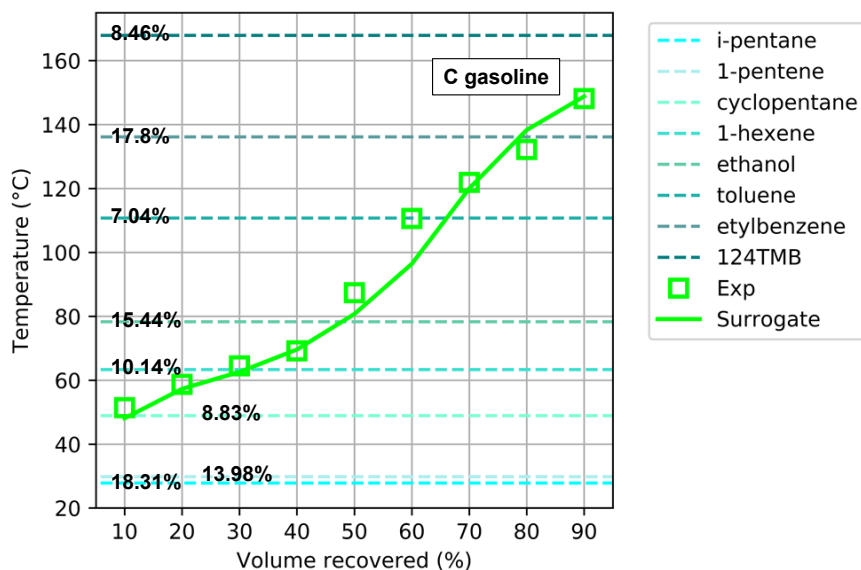


Figure 4-19: Comparison between experimental (markers) and surrogate (solid line) distillation curves for the validation gasoline C. Normal boiling temperature of the surrogate's components (dashed line) and their molar percentage are also reported.

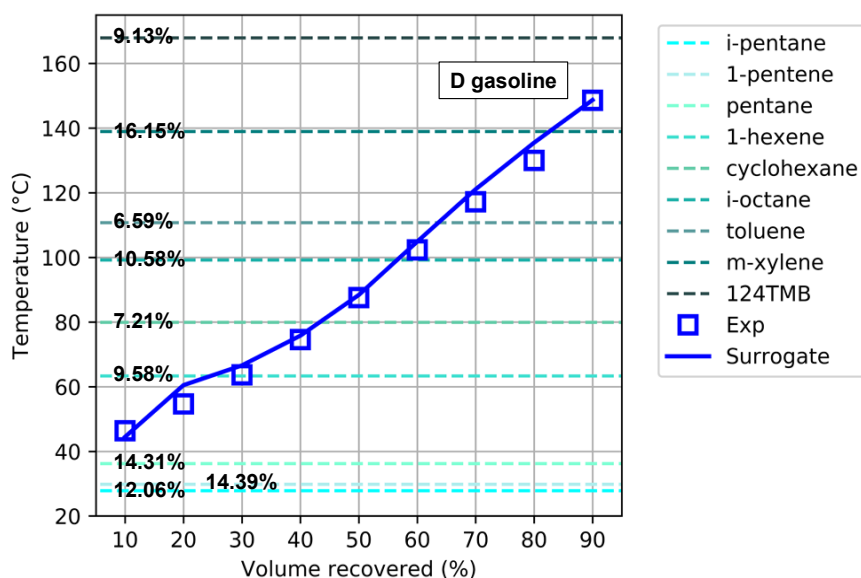


Figure 4-20: Comparison between experimental (markers) and surrogate (solid line) distillation curves for the validation gasoline D. Normal boiling temperature of the surrogate's components (dashed line) and their molar percentage are also reported.

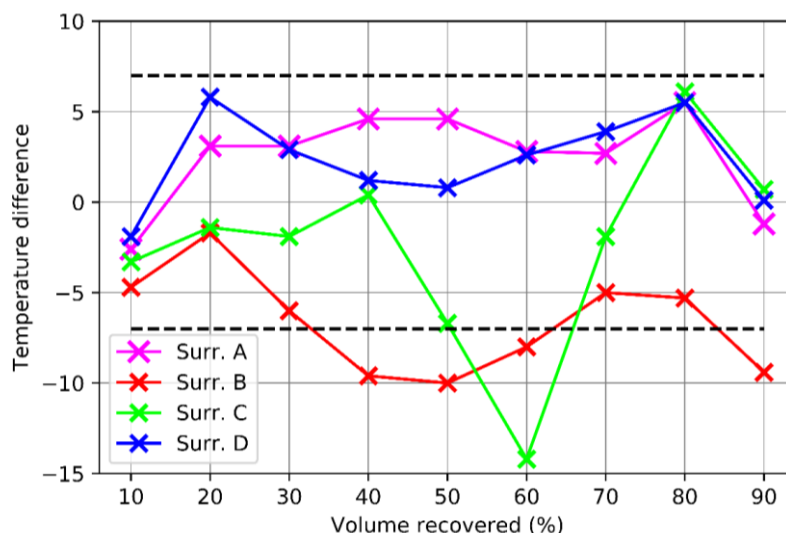


Figure 4-21: Temperature difference between experimental and surrogate distillation curve for the four validation gasolines.

A clear accuracy decrease is visible for the surrogate of B gasoline for which the temperature difference lies beyond the 5°C underestimation line over the distillation range with some points beyond the defined acceptability threshold (7°C) as well. The latter is correlated to the high aromatics content of gasoline B (46 %vol) with respect to that of gasolines A, C, D (30-35 %vol). It can be assumed that including additional aromatic species in the initial palette may help to improve the prediction of high aromatics gasoline fuels. However, it must be underlined that the aromatics content in nowadays commercial gasolines is limited at maximum values around those reported for A, C, D gasolines, thus, the predicted curves in **Figure 4-17**, **Figure 4-19**, **Figure 4-20** should be taken as reference results with the perspective of the next fuels.

The radar charts in **Figure 4-22**, **Figure 4-23**, **Figure 4-24**, **Figure 4-25** report the comparison between real gasolines and their associated optima surrogates with regards to RON and MON values, three key distillation temperatures (T10, T50, T90), two key components from E-PIONA i.e., ethanol and aromatics, density, and RVP. A general solid agreement can be seen for the surrogates of A, C gasolines (**Figure 4-22**, **Figure 4-24**). The general properties of gasoline D as well are in a good shape with experimental measures despite the relative error around 10% in predicting the RVP (**Figure 4-25**, **Figure 4-24**). It is worth mentioning that the bond between chemical (ethanol and aromatics volumes) and physical (density, RVP, key distillation temperatures) properties is well captured, furthermore RON and MON values are reasonably reproduced. In the current state of the art there is lack of methodologies performing the simultaneous accurate prediction of high-octane rating and evaporation features. Thus, the proven ability of the present algorithm to perform this task is worthwhile, in particular for gasolines whose properties are in line with nowadays RON95 and RON98 gasolines. As reported for the distillation validation, the surrogate of B gasoline suffers from a general loss of the predictivity of the selected evaporation features as visible in **Figure 4-23**, confirming further the sensitivity of the model to the aromatics content.

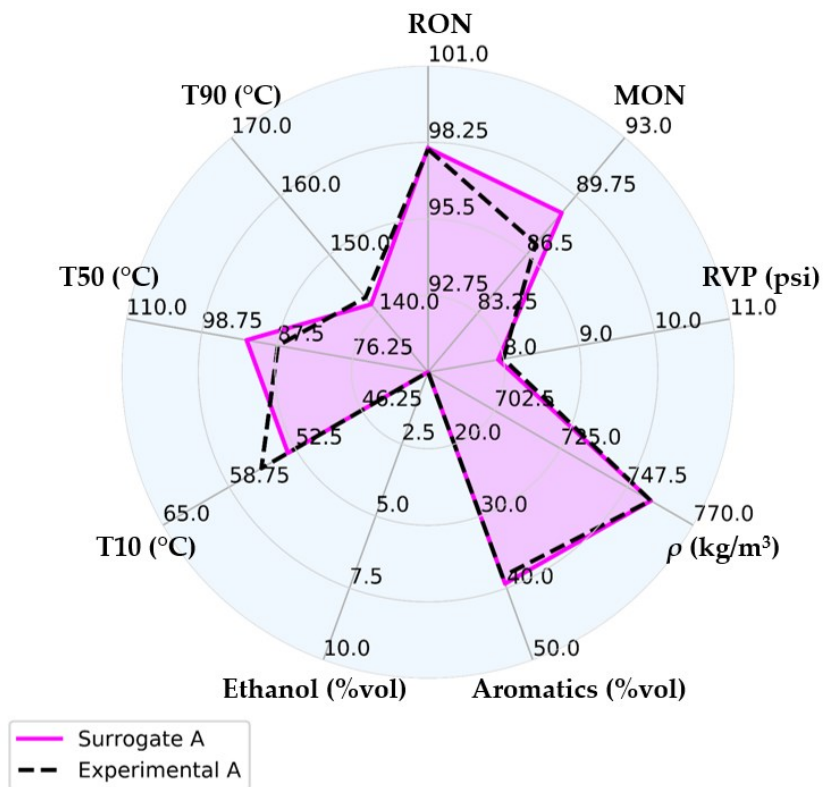


Figure 4-22: Comparison between different properties (RON, MON, RVP, density (ρ), aromatics volume, ethanol volume, T10, T50, T90) of the reference A gasoline (dashed polygon) and its optimum surrogate (filled polygon).

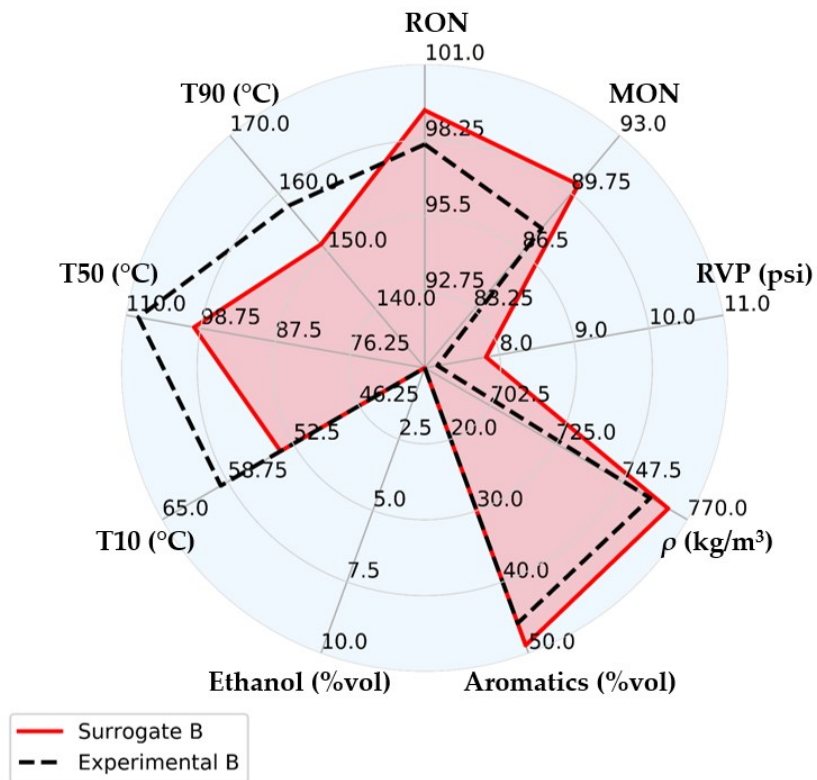


Figure 4-23: Comparison between different properties (RON, MON, RVP, density (ρ), aromatics volume, ethanol volume, T10, T50, T90) of the reference B gasoline (dashed polygon) and its optimum surrogate (filled polygon).

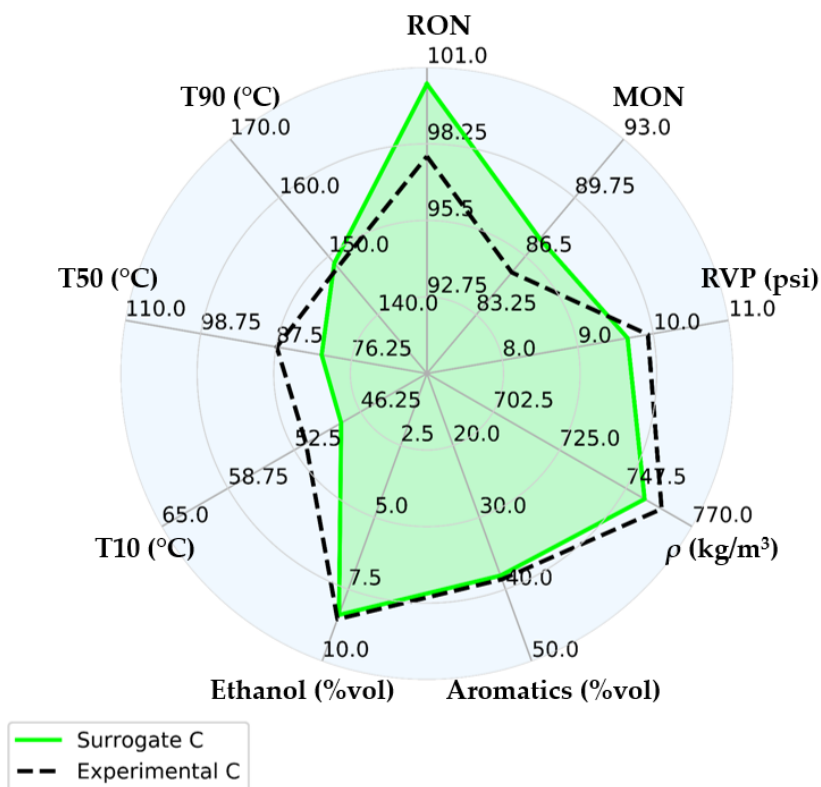


Figure 4-24: Comparison between different properties (RON, MON, RVP, density (ρ), aromatics volume, ethanol volume, T10, T50, T90) of the reference C gasoline (dashed polygon) and its optimum surrogate (filled polygon).

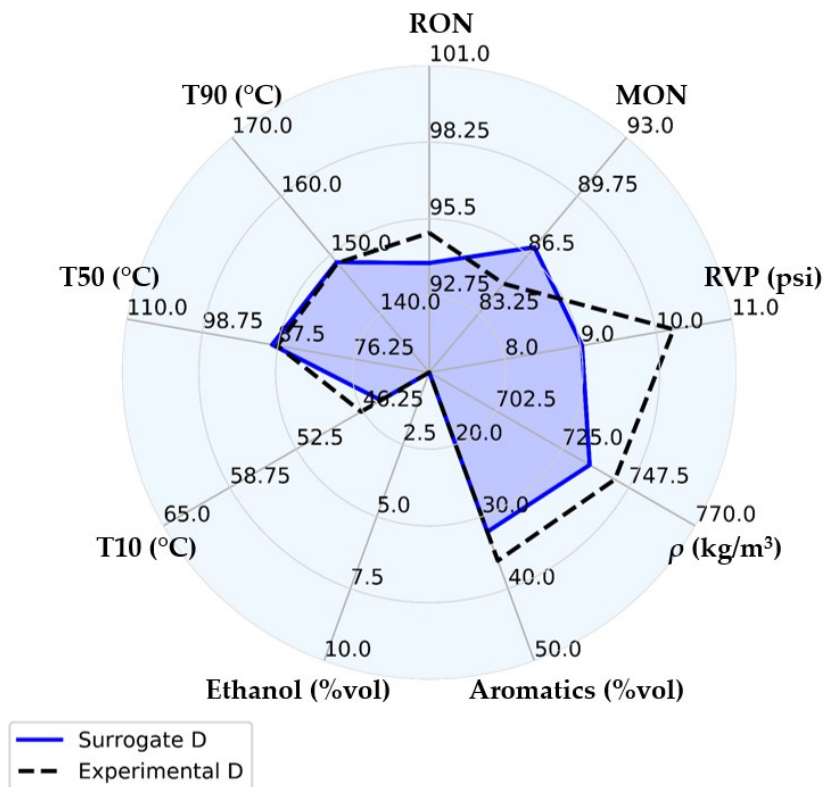


Figure 4-25: Comparison between different properties (RON, MON, RVP, density (ρ), aromatics volume, ethanol volume, T10, T50, T90) of the reference D gasoline (dashed polygon) and its optimum surrogate (filled polygon).

4.3.3 Surrogate unicity analysis

In this section, the properties achieved by the ‘winner’ surrogate (composition solution with maximum value of the merit function) are compared with those achieved by the bounding surrogate, namely the equivalent valuable surrogate (objective function $F \geq 0.95 \max(F)$) which had the most different composition with respect to the optimum surrogate. As mentioned in 4.2.3, the comparison is performed in order to discuss the ‘unicity’ of the surrogate composition assessed by means of the parameter called compatibility (γ), which is defined as in Eq. (4-40), where NP is the number of components in the initial palette (14), $x_{i,MAX}$ and $x_{i,BOUND}$ represent the volume fractions of the i -th compound in the palette between the optimum surrogate and the bounding surrogate, respectively.

$$\gamma = 100 - \sum_{i=1}^{NP} (x_{i,MAX} - x_{i,BOUND}) \cdot 100 \quad (4-40)$$

Figure 4-26 reports the results of both the overall and the class-by-class compatibility. It is underlined that the optimum surrogate and the bounding surrogate for A, B, D gasolines are fully compatible in ethanol a-priori since the presence of ethanol in those surrogates was constrained at zero by the user, since the real A, B, D gasolines lack oxygenates.

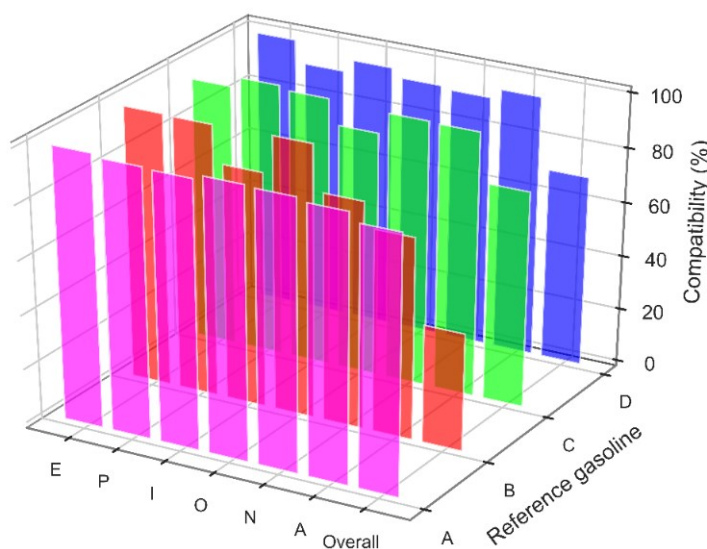


Figure 4-26: Overall and E-PIONA composition compatibility for optimum and bounding surrogates of the four validation gasolines.

As visible in **Figure 4-26**, an almost full compatibility is detected for the two most different surrogates of gasolines A (magenta, $\gamma = 95\%$) and C (green, $\gamma = 80\%$), confirming the solidity of the implemented Bayesian searching strategy. Therefore, it is observed that the need of accuracy in predicting the evaporative features of those gasolines converges towards an about unique possible composition. The high compatibility in ethanol ($\gamma = 96\%$) achieved by the two most different surrogate options of gasoline C is a further sign that the algorithm clearly identifies the role of the ethanol addition. A lower overall compatibility is detected between the two surrogates of gasoline D (blue, $\gamma = 70.5\%$) due to slight differences in the compatibility of each single chemical class and a significant n-paraffinic incompatibility caused by the replacement of n-pentane with n-hexane (**Table 4-6**). The composition variability between the two surrogates representing B gasoline (red) is large, indeed the overall compatibility of the bound surrogate is around 43%. The latter is mainly due to the

low aromatic compatibility, which is around 70%. As reported in **Table 4-6**, the properties of B gasoline and A gasoline are similar except for the aromatics content (45%vol against 38%vol), which in its turn affects the distillation temperature differences. The compatibility analysis suggests that the ‘unicity’ of the surrogate formulation as well is very sensitive to the presence of aromatics.

The sensitivity of the target properties to the discussed different levels of compatibility is shown in the parity plot figures **Figure 4-27-Figure 4-30**, where the value of compatibility is reported next to the bounding surrogate properties.

As expectable, the lower is the level of the compatibility, the larger is the bounding-optimum difference in predicting the properties. However, different sensitivities to the variability of the composition are experienced by different properties. In fact, regardless to the level of compatibility, an increasing sensitivity to the surrogate composition has been detected for RVP (**Figure 4-28**), distillation temperatures (**Figure 4-29**), macro-composition (**Figure 4-30**), density (**Figure 4-27**), respectively. Considering **Table 4-3**, it is clear that for similar ability of different surrogates to mimic a reference fuel, the higher is the importance (weight value) given to a given target property, the lower is its sensitivity to the composition variability of the surrogate. It must be noticed that a high level of compatibility is a sign of robustness and reliability of the surrogate solution. It can be observed that the compatibility recorded in a pool of surrogate solutions is correlated to the prediction performance. Indeed, the higher levels of compatibility (green, $\gamma = 80\%$ and magenta $\gamma = 95\%$) provide an improved prediction performance over the whole set of target properties, whilst lower levels of compatibility may result in good performance on some target properties and significant mismatch on others. As a result, one can assume that the high degree of accuracy equally distributed over the presented target properties relies on the ‘unicity’ of the surrogate composition (high compatibility).

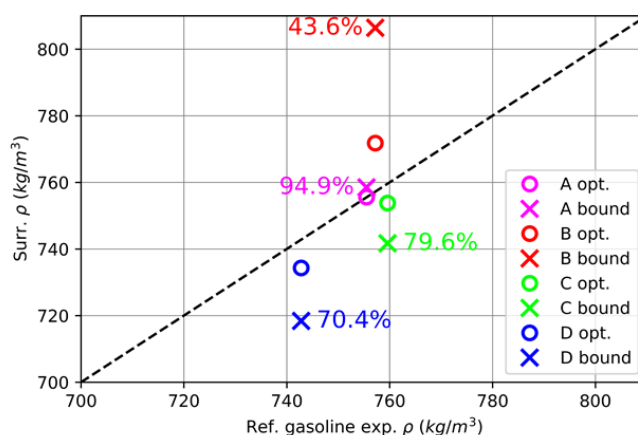


Figure 4-27: Parity plot between reference gasoline and surrogate density values for the four validation gasolines. The surrogate density is reported for both the optimum (circle) and the bounding (cross), for which the value of the compatibility is reported next.

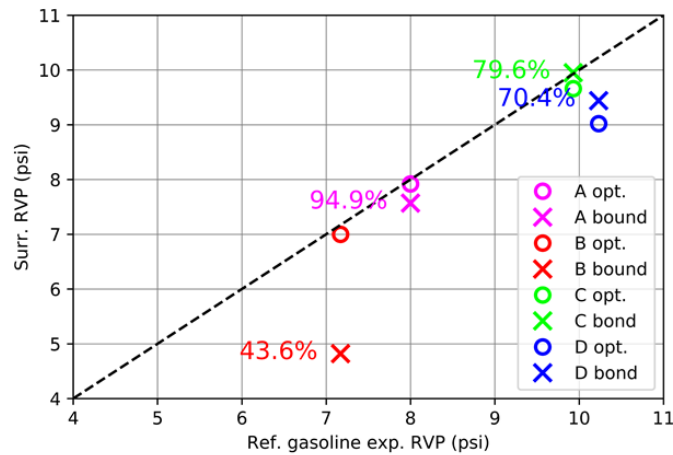


Figure 4-28: RVP parity plot between reference gasoline and surrogate RVP values for the four validation gasolines. The optimum (circle) and the bounding (cross, and associated compatibility) surrogates are shown.

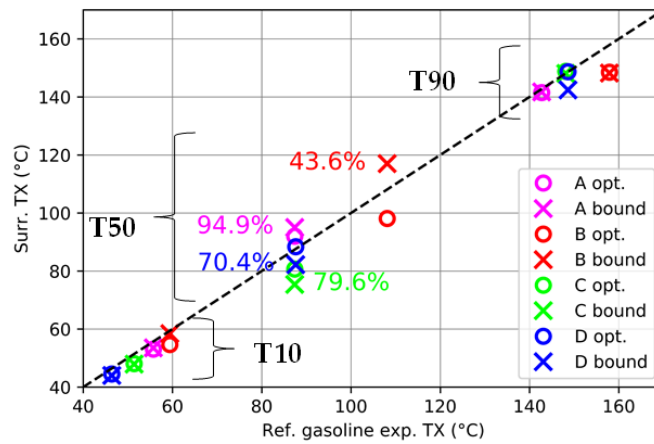


Figure 4-29: Distillation temperatures parity plot between reference gasoline and surrogate distillation temperatures values for the four validation gasolines. The optimum (circle) and the bounding (cross, and associated compatibility) surrogates are shown.

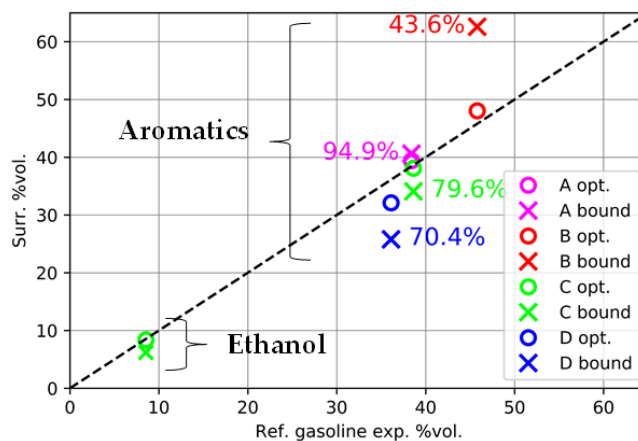


Figure 4-30: Chemical composition parity plot between reference gasoline and surrogate ethanol and aromatics volumes for the four validation gasolines. The optimum (circle) and the bounding (cross, and associated compatibility) surrogates are shown.

5 Conclusions and perspectives

The present research project aims at improving the current use of CFD engine simulations with focus on the fuel spray, the liquid fuel film evaporation, and the fuel spray-wall impingement, which are among the nowadays harder challenges for simulation engineers. These topics have been approached with a strong methodologic footprint since several development and analysis steps required implementation from scratch. The research activity has been carried out mainly by means of three-dimensional CFD simulations with the commercial code *STAR-CD* v4.28 and with *Python* programming. The final workflow of the project can be summarized into three different interconnected tasks i.e., CFD simulation and setting of reliable fuel spray wall impingement methodologies (T-1), one-dimensional modeling of the effect of the dilution between the wall impingement-induced liquid film on the cylinder liner and the lubricant oil layer upon it (T-2), zero-dimensional modeling of distillation apparatus to predict the evaporative behavior of fuel mixtures and its integration in a Bayesian statistical inference algorithm charged to identify the proper composition of mixtures able to mimic the phase change features of real gasolines to be provided as input to CFD simulations (T-3). For each task, results have been validated against experimental data from the literature. In the following, the main characteristics, home takes, and perspectives related to the accomplished tasks are presented.

- T-1: The punctual prediction of the in-cylinder mixture local distribution is gaining increasing importance in new combustion concepts. The latter can be strongly affected by the fuel spray-wall impingement, in particular because of the liquid fuel film formation which may lead to pool flames and delayed formation of rich mixture pockets. As a consequence, there are concerns on the combustion behaviour and soot emission. In the framework of engine CFD simulations, the literature critical analysis has shown that the simulation of spray-wall impingement is still backward with respect to that of many other relevant phenomena. This gap is likely due mainly to the effect of the approximation of real droplets with statistical representative samples (parcels) on the overall energy balance at the wall impingement, and the lack of strong bonds between models and experimental data in complex conditions such as dense sprays and droplets mutual interaction. Literature publications on topic are mostly limited to the validation of wall impingement settings at high wall temperature, and relatively low injection pressure (around or below 100 bar), aimed at reproducing the features of the scattered spray cloud. Detailed characterizations of the formed liquid fuel film are not typically accounted for, however if present, they suffer from poor accuracy in predicting the film mass. In this context, T-1 deals with the definition of best practice in choices and settings of the wall impingement modeling in CFD simulations by considering the features of the liquid film as a validation target.

In the current state of the art, the wall impingement models of Bai and Gosman, and Kuhnke are among the most popular choices. In this research project, two alternative models able to approach both high and low temperatures, namely the Bai-ONERA and the Senda models, have been tested and compared on an extensive simulation matrix. The matrix includes different nowadays engine relevant conditions that have been numerically investigated slightly in previous works e.g., negative gauge back pressure (0.4-0.6 bar, representative of early injection events), very high gauge back pressure (3-6 bar, representative of supercharged operations), high injection pressure (300 bar).

The model of Senda has shown the ability to produce morphologic features of the after-impingement liquid spray cloud that are consistent with experimental observations. On the other hand, the secondary spray cloud results from the Bai-ONERA model suffer from a significant over-estimation of the normal-to-wall bounce up of the dispersed liquid phase, of which no experimental evidence has been found in similar conditions.

The study of the predictive capability of the two models with respect to the surface temperature has highlighted that the performance of the two models at atmospheric pressure is comparable. The models are able to capture the main behaviour of the liquid film mass in the three liquid evaporation regimes i.e., nucleate boiling (convective-induced consumption), transition boiling (foam region, combined action of convection and pool boiling), film boiling (Leidenfrost effect, no liquid film). The simulated liquid mass-temperature profiles, in particular that predicted by the Senda model, are in nice agreement with respect to the reference experimental data. It is worth mentioning that at the highest tested wall temperature (180 °C), both the models return a zero liquid film mass, which is a clear sign that the occurrence of the Leidenfrost effect has been correctly reproduced. Analysing the effect of the wall temperature, the present Author suggests the use of the Senda model, although the use of the Bai-ONERA model is suitable as well. It is remembered that the results analysis has revealed that despite the implementation of the splash tuning coefficient to adjust the deposited mass in transition boiling conditions is the same, the tuning value and its effect are significantly different depending on the chosen model. In particular, the Senda model allows larger variation of the deposited mass by applying smaller variations of the splash tuning coefficient. On the other hand, if future investigators will choose the Bai-ONERA model, the weak variation of the after-splash formed film must be taken into account even applying the lower bound value of the tuning coefficient (i.e., 10). The study of the predictive capability of the two models with respect to the gas pressure at low load representative temperature has shown that both the wall impingement models can predict the liquid film bell-shaped profile with reliable results. In particular, on the one hand the Senda model has proven the ability to capture shape, thickness distribution and mass of the liquid film better than the Bai-ONERA model. On the other hand, it is reported that simulations run with the Senda model may require a significant longer computing time due to the complexity of its custom splash sub-models.

After the validation of different test engine relevant conditions, the Author of the present thesis suggests the use (if the built-in version is available) or the custom implementation of the Senda model to investigators that will approach the wall impingement simulation, in particular for relatively cold walls. As a result of the great match achieved for the liquid film mass and morphology in those conditions, promising predictions of the liquid film formation and delayed evaporation in engine simulations can be expected. Even though the Senda model has been underrated and poorly discussed in the recent literature on the topic, it should be considered for future works. The results in this thesis have shown that the main advantages of the Senda model are: i) the fact that its internal coefficients for the empirical correlation of the after-impingement characteristics were tuned on light vehicles' gasolines, whilst the coefficients of other models were typically obtained for pure fuels (e.g., i-octane as for the Bai-ONERA model), diesel fuels, urea, water; ii) the implementation of a comprehensive modeling of splash-like events; iii) the active use of the liquid film thickness in wet surface conditions in order to account for the film viscous damping effect on new incoming droplets.

- T-2: Thanks to the accomplishment of T-1, a validated methodology to model the fuel spray-wall impingement in CFD simulations has been provided. It must be remembered that in the framework of CFD simulations, in the case the fuel spray hits the cylinder wall the oil-fuel interaction is not simulated due to the several number of cells and equations that would be added in order to reproduce micrometric scales. T-2 deals with the development of an offline tool which supports CFD simulations with the additional modeling of the after-fuel wall impingement oil pollution and detachment. This research task has been pushed by the importance of predicting oil properties degradation tendency, flying oil-induced soot formation and low-speed pre-ignition events for given spray pattern and injection strategy.

A one-dimensional numerical model has been developed from scratch in *Python* environment in order to resolve the mutual diffusion between liquid fuel film and lubricant oil layer at engine relevant thermodynamics conditions. Considering a given fuel liquid film thickness deposited after the wall impingement, which can be provided by CFD three-dimensional results, the model simulates the evolution of the level of oil-fuel dilution in the time interval from the end of injection and the arrival of the piston at the liquid film position. As a final result, the presence of remaining fuel that has joined the lubricant layer and that of oil scraped by the piston which is available to be scattered out into the cylinder is predicted.

The reliability of the model is strongly based on the correct prediction of the oil-fuel diffusion coefficient, which is the transport property that mainly drives oil-fuel dilution. The literature review conducted on the topic revealed that the empirical correlations employed in common practice to estimate that key transport property suffer from severe errors (20-40% with respect to experiments) if applied to mixtures of light and heavy hydrocarbons, resulting in a poor representation of the phenomenon under review. To fill this gap, a neural network methodology based on the new concept of splitting the prediction of the output (diffusion coefficient) into two steps: i) interpretation of only the main dependencies (temperature and viscosity) by super-simplifying empirical correlations on purpose; ii) estimation of the most complex and highly non-linear dependencies (intermolecular forces) by means of a neural network trained on the induced mismatch between the super-simplified correlation and experimental data. It has been proven that the proposed methodology can replace both correlations and stand-alone neural networks as it has a greater accuracy with respect to both the alternative methods, and a weaker tendency to overfitting (i.e., a greater potential to generalize to new unseen data) with respect to stand-alone networks. Furthermore, the new hybrid methodology has been integrated with Bayesian inference statistics features, providing the user with additional information on the confidence band of the predicted diffusion coefficient i.e., the interval of values in which the real target must fall. As a proof of concept, the final methodology has been applied to conceptual mixtures between n-heptane and hydrocarbons with oil-like number of carbons (C30-C35). The resulting confidence band has shown that the most likely value of the diffusion coefficient cannot differ from the real value for more than 20%, which would still be an improvement with respect to the current state of the art.

The complete dilution model has been tested on a reference engine case once it has been provided with the predicted diffusion coefficient associated to the oil-gasoline combination of the study case by the Bayesian network. In spite of the fact that a straight validation of the code is not possible due to the lack of comparable experimental data, the model has shown the ability to reproduce complex effects of practical real solutions adopted to prevent oil-fuel dilution i.e., the application of higher wall temperature and

then the use of higher oil grade. With regards to the former, the model has captured the effect of the overall balance between the speed-up effect of the temperature on mutual diffusion and the greater fuel evaporation rate, resulting in the overall reduction of the scraped oil mass from the cylinder of about a third, which is consistent with the LSPI frequency decrease experienced by the real engine which is more than halved. With regards to the latter, the use of two different oil grades (SAE 5W-30 vs SAE 10W-30) has led to almost the same oil scrap that is in line with the experimentally observed negligible LSPI frequency decay caused by the replacement of SAE 10W-30 with SAE 30 (higher grade).

The proposed neural network methodology has been used to provide the scientific community with expected values of the diffusion coefficient between different engine oils and gasoline-like mixtures and their confidence degree, that are currently not available in the open literature. For given thermophysical properties of the test oil and fuel at reference conditions, the methodology allows the user to determine the dilution rate of any engine-like oil-fuel mixture with average expectable errors below 10%, which is a unique score at the time of writing of this project. For given engine configuration, the model can be used to evaluate the potential of molecules as additives for both oil and fuel to limit oil pollution and detachment. Furthermore, the model can be used to explore the effect of multiple injection strategies on the dilution evolution if oil-induced issues are present. Finally, in the perspective of a comparison against extensive experimental data, the oil amount into the top land crevice predicted by the model could be directly correlated with LSPI frequency and additional soot emission, contributing to enhance the role of CFD simulations as a device to address the complex multi-objective engine system optimization task.

- T-3: Since the first step towards the setup of reliable engine spray simulations and mixture formation is the implementation of the proper fuel phase change properties, it is necessary to identify a representative mixture to provide the CFD code, namely the so-called fuel surrogate. T-3 deals with the implementation of a methodology to perform the timeless definition of the proper fuel surrogate by exploring a wide space of possible composition combinations.

At the end of the development step, a powerful tool based on Bayesian optimization techniques has been provided. The tool requires the target values of liquid density, Reid vapor pressure, distillation temperatures, chemical macro-composition, RON, MON, and returns the optimum composition of the surrogate mixture based on the trade-off among: i) accuracy of the mixture's target properties, ii) number of components (which must be limited in order to ensure a light additional weight from the proposed tool on the overall CFD simulation time); iii) confidence in the sufficient extension of the composition space in which the solution has been drawn. It is underlined that the tool relies on an in-house distillation model that allows the full control on the reproduction of distillation curve and RVP.

The tool has been validated against four different gasolines representative of nowadays commercial gasolines, whose target properties are available in the open literature. The implemented algorithm has proven the potential to identify surrogate mixtures that match the reference experimental properties with overall relative errors below 6%. A fundamental result which makes the present tool attractive is the ability to formulate a single surrogate which can reproduce the phase change features (RVP, distillation curve) and the main chemical indexes (RON, MON) of the associated gasoline at the same time. Another home take from the proposed tool is the discovering of the correlation

between the predicting performance of the surrogate searching phase and the enhanced presence of aromatics in the reference gasoline. It has been shown that the higher is the target aromatics content, the weaker is the accuracy balance between the emulated phase change and chemical properties. The proposed tool was taken as a benchmark to investigate a fundamental issue regarding the formulation of fuel surrogates, namely attempt to answer the question: 'do fuel surrogates converge towards a unique composition at given gasoline, properties, and accuracy targets?'. Insights have been gained by performing a comparative analysis between the best surrogate and an alternative surrogate option evaluated during the Bayesian search which has a comparable accuracy together with the most different composition with respect to the best. Those pairs of surrogates have been compared via a novel synthetic index called compatibility calculated for the four validation gasolines. The compatibility analysis has revealed a strong bond between the similarity of different surrogate options and the maximum achievable accuracy. Thus, the compatibility as well as the accuracy suffers from the presence of large aromatics volume. In general, the higher is the value of the objective function evaluated by the Bayesian algorithm while drawing the solution on the composition space, the more similar are the surrogate options, thus, the convergence towards the unique surrogate is possible. Otherwise, lower levels of compatibility point out that the high compatibility solution sub-domain: i) does not belong to the implemented domain likely due to the lack of specific pure molecules in the initial palette that are of great importance for representing a given gasoline; ii) may lie in a zone of the solution space that was left blank by the drawing of the solution because of its unaffordable complexity (i.e., too large number of components with respect to that allowed for the CFD implementation).

In the current version, due to the choices made in the implementation of the custom distillation model, the code is able to approach successfully pure gasolines or anhydrous oxygenate-gasolines blends with blending level equal or below 10%. In order to gain the ability to approach a wider set of real nowadays fuels, especially considering the onset of new potential renewable oxygenate fuels and additives for light-duty vehicles such as MeFo (methyl formate), DMC (dimethyl-carbonate), MeOH (methanol), etc, the modelling of the azeotropic behaviour of liquids is mandatory. Therefore, a custom implementation of a chosen methodology to compute the activity coefficients of the liquid phase of each component must be introduced in order to account for high polarity differences between the components of the mixture. A further next update of the tool in view of what discussed about the compatibility analysis would be the implementation of a strategy to extend the size of the solution space by adding more test components in order to discover sub-domains which may comprise the high compatibility solution. To this aim, the tool should be aided by a pre-processing algorithm charged to determine correlations between the target properties in order to reduce the number of constraints and avoid redundant dependencies. As a result, the final tool would be subjected to a sort of pre-addressing and also to the save of computation cost that can be employed to extend the solution domain. It is worth mentioning that the proposed tool can be used in 'reverse mode'. In direct mode (standard), the task of the optimizer is the definition a known mixture which replaces a real fuel of properties known at reference conditions but unknown composition. In reverse mode the optimizer could be launched to provide the suppliers with guidelines to produce new real mixtures returned by the code based on a set of virtual properties that one needs to achieve. This application is particularly attractive with the perspective of the design of tailored mixtures from the synthesis of new e-fuels.

References

- [1] 'Database - Transport - Eurostat'. <https://ec.europa.eu/eurostat/web/transport/data/database> (accessed Oct. 13, 2021).
- [2] 'European Environment Agency's home page — European Environment Agency'. <https://www.eea.europa.eu/> (accessed Oct. 13, 2021).
- [3] 'Emission Standards: Europe: Cars and Light Trucks'. <https://dieselnet.com/standards/eu/ld.php#stds> (accessed Oct. 12, 2021).
- [4] D. Tsokolis *et al.*, 'Fuel consumption and CO2 emissions of passenger cars over the New Worldwide Harmonized Test Protocol', *Appl. Energy*, vol. 179, pp. 1152–1165, Oct. 2016, doi: 10.1016/j.apenergy.2016.07.091.
- [5] A. R. Varma and S. Thomas, 'Simulation, Design and Development of a High Frequency Corona Discharge Ignition System', SAE International, Warrendale, PA, SAE Technical Paper 2013-26-0014, Jan. 2013. doi: 10.4271/2013-26-0014.
- [6] D. I. Pineda, B. Wolk, J.-Y. Chen, and R. W. Dibble, 'Application of Corona Discharge Ignition in a Boosted Direct-Injection Single Cylinder Gasoline Engine: Effects on Combustion Phasing, Fuel Consumption, and Emissions', *SAE Int. J. Engines*, vol. 9, no. 3, Art. no. 2016-01-9045, Jan. 2016, doi: 10.4271/2016-01-9045.
- [7] A. Cimarello, C. N. Grimaldi, F. Mariani, M. Battistoni, and M. D. Re, 'Analysis of RF Corona Ignition in Lean Operating Conditions Using an Optical Access Engine', SAE International, Warrendale, PA, SAE Technical Paper 2017-01-0673, Mar. 2017. doi: 10.4271/2017-01-0673.
- [8] C. Hampe, H. Kubach, U. Spicher, G. Rixecker, and S. Bohne, 'Investigations of Ignition Processes Using High Frequency Ignition', SAE International, Warrendale, PA, SAE Technical Paper 2013-01-1633, Apr. 2013. doi: 10.4271/2013-01-1633.
- [9] Y. Li, H. Zhao, P. Stansfield, and P. Freeland, 'Synergy between Boost and Valve Timings in a Highly Boosted Direct Injection Gasoline Engine Operating with Miller Cycle', Apr. 2015, pp. 2015-01-1262. doi: 10.4271/2015-01-1262.
- [10] A. B. Dempsey, S. J. Curran, and R. M. Wagner, 'A perspective on the range of gasoline compression ignition combustion strategies for high engine efficiency and low NOx and soot emissions: Effects of in-cylinder fuel stratification', *Int. J. Engine Res.*, vol. 17, no. 8, pp. 897–917, Oct. 2016, doi: 10.1177/1468087415621805.
- [11] B. Lecointe and G. Monnier, 'Downsizing a Gasoline Engine Using Turbocharging with Direct Injection', SAE International, Warrendale, PA, SAE Technical Paper 2003-01-0542, Mar. 2003. doi: 10.4271/2003-01-0542.
- [12] N. Fraser, H. Blaxill, G. Lumsden, and M. Bassett, 'Challenges for Increased Efficiency through Gasoline Engine Downsizing', *SAE Int. J. Engines*, vol. 2, no. 1, Art. no. 2009-01-1053, Apr. 2009, doi: 10.4271/2009-01-1053.
- [13] 'FOTW# 1178, March 22, 2021: Gasoline Direct Injection was Installed on 55% of all Light-Duty Vehicles Produced in 2020 | Department of Energy'. <https://www.energy.gov/eere/vehicles/articles/fotw-1178-march-22-2021-gasoline-direct-injection-was-installed-55-all-light> (accessed Oct. 12, 2021).
- [14] 'Explained: Why Some Engines Have Both Port and Direct Injection'. <https://www.caranddriver.com/news/a15342328/explained-why-some-engines-have-both-port-and-direct-injection/> (accessed Oct. 12, 2021).
- [15] 'Is there a difference between PFI and GDI? | Afton Chemical'. https://www.aftonchemical.com/Generic/PFI-vs-GDI?__cf_chl_jschl_tk__=pmd_CWisfYDTaUHyyloQ6goGV0YSDZUm.NsK445hIPmsPAA-1634034005-0-gqNtZGzNAjucnBszQIR (accessed Oct. 12, 2021).

- [16] Y. Iwamoto, K. Noma, O. Nakayama, T. Yamauchi, and H. Ando, 'Development of Gasoline Direct Injection Engine', SAE International, Warrendale, PA, SAE Technical Paper 970541, Feb. 1997. doi: 10.4271/970541.
- [17] M. Sjöberg and J. E. Dec, 'Smoothing HCCI Heat-Release Rates Using Partial Fuel Stratification with Two-Stage Ignition Fuels', Apr. 2006, pp. 2006-01-0629. doi: 10.4271/2006-01-0629.
- [18] P. Priyadarshini, A. Sofianopoulos, S. Mamalis, B. Lawler, D. Lopez-Pintor, and J. E. Dec, 'Understanding partial fuel stratification for low temperature gasoline combustion using large eddy simulations', *Int. J. Engine Res.*, vol. 22, no. 6, pp. 1872–1887, Jun. 2021, doi: 10.1177/1468087420921042.
- [19] L. Zhou, J. Hua, H. Wei, K. Dong, D. Feng, and G. Shu, 'Knock characteristics and combustion regime diagrams of multiple combustion modes based on experimental investigations', *Appl. Energy*, vol. 229, pp. 31–41, Nov. 2018, doi: 10.1016/j.apenergy.2018.07.102.
- [20] 'Toyota Direct Injection? Port Injection? Why Not Both?' <https://www.import-car.com/toyota-direct-injection-port-injection-why-not-both/> (accessed Oct. 12, 2021).
- [21] F. Schulz, 'Private communication'. Aug. 2019.
- [22] E. Nakai, T. Goto, K. Ezumi, and Y. Tsumura, 'Mazda Skyactiv-X 2.0L gasoline engine', presented at the 28th Aachen Colloquium Automobile and Engine Technology, Aachen, Germany, Oct. 2019.
- [23] Q. Cheng, Z. Zhang, and N. Xie, 'Multi-Physical Fields Coupling Simulation and Performances Analysis of a Novel Heated-Tip Injector', *J. Thermophys. Heat Transf.*, vol. 30, no. 3, pp. 587–598, Jul. 2016, doi: 10.2514/1.T4872.
- [24] M. Jafari, 'Analysis of heat transfer in spray cooling systems using numerical simulations | Semantic Scholar'. <https://www.semanticscholar.org/paper/Analysis-of-heat-transfer-in-spray-cooling-systems-Jafari/016b390b2c419c8b07452a67140603fc30f1cbd9> (accessed Oct. 13, 2021).
- [25] P.-K. Wu, L.-K. Tseng, and G. Faeth, 'Primary breakup in gas/liquid mixing layers for turbulent liquids', presented at the 30th Aerospace Sciences Meeting and Exhibit, Reno, NV, U.S.A., Jan. 1992. doi: 10.2514/6.1992-462.
- [26] Z. Dai, W.-H. Chou, and G. M. Faeth, 'Drop formation due to turbulent primary breakup at the free surface of plane liquid wall jets', *Phys. Fluids*, vol. 10, no. 5, pp. 1147–1157, May 1998, doi: 10.1063/1.869639.
- [27] M. Chang, Z. Lee, S. Park, and S. Park, 'Characteristics of flash boiling and its effects on spray behavior in gasoline direct injection injectors: A review', *Fuel*, vol. 271, p. 117600, Jul. 2020, doi: 10.1016/j.fuel.2020.117600.
- [28] M. M. Khan, J. Hélie, M. Gorokhovski, and N. A. Sheikh, 'Experimental and numerical study of flash boiling in gasoline direct injection sprays', *Appl. Therm. Eng.*, vol. 123, pp. 377–389, Aug. 2017, doi: 10.1016/j.applthermaleng.2017.05.102.
- [29] F. Brusiani, S. Falfari, and C. Forte, 'The Role of Cavitation Inside High Pressure GDI Injector', *L'Aquila*, Sep. 2009, p. 9.
- [30] F. Payri, V. Bermúdez, R. Payri, and F. J. Salvador, 'The influence of cavitation on the internal flow and the spray characteristics in diesel injection nozzles', *Fuel*, vol. 83, no. 4–5, pp. 419–431, Mar. 2004, doi: 10.1016/j.fuel.2003.09.010.
- [31] S. Saito, Y. Abe, and K. Koyama, 'Flow transition criteria of a liquid jet into a liquid pool', *Nucl. Eng. Des.*, vol. 315, pp. 128–143, Apr. 2017, doi: 10.1016/j.nucengdes.2017.02.011.
- [32] J. Song and S. Park, 'EFFECT OF INJECTION STRATEGY ON THE SPRAY DEVELOPMENT PROCESS IN A SINGLE-CYLINDER OPTICAL GDI ENGINE', *At. Sprays*, vol. 25, no. 9, pp. 819–836, 2015, doi: 10.1615/AtomizSpr.2015012018.
- [33] M. Pilch and C. A. Erdman, 'Use of breakup time data and velocity history data to predict the maximum size of stable fragments for acceleration-induced breakup of a liquid drop', *Int. J. Multiph. Flow*, vol. 13, no. 6, pp. 741–757, Nov. 1987, doi: 10.1016/0301-9322(87)90063-2.
- [34] Y. Liu, X. Yan, and Z. Wang, 'Droplet dynamics on slippery surfaces: small droplet, big impact', *Biosurface Biotribology*, vol. 5, no. 2, pp. 35–45, Jun. 2019, doi: 10.1049/bsbt.2019.0004.
- [35] R. Lindgren and I. Denbratt, 'Influence of Wall Properties on the Characteristics of a Gasoline Spray After Wall Impingement', *SAE Trans.*, vol. 113, pp. 1202–1216, 2004.
- [36] C. Bai, 'Modelling of spray impingement process', PhD thesis, University of London, London, 1996.
- [37] *STAR-CD Methodology*. Siemens Product Lifecycle Management Inc., 2017.

- [38] T. Caswell, 'Dynamics of the vapor layer below a Leidenfrost drop', *Phys. Rev. E Stat. Nonlin. Soft Matter Phys.*, vol. 90, p. 013014, Jul. 2014, doi: 10.1103/PhysRevE.90.013014.
- [39] S. Moghtadernejad, C. Lee, and M. Jadidi, 'An Introduction of Droplet Impact Dynamics to Engineering Students', *Fluids*, vol. 5, no. 3, Art. no. 3, Sep. 2020, doi: 10.3390/fluids5030107.
- [40] R. W. Temple-Pediani, 'Fuel Drop Vaporization under Pressure on a Hot Surface', *Proc. Inst. Mech. Eng.*, vol. 184, no. 1, pp. 677–696, Jun. 1969, doi: 10.1243/PIME_PROC_1969_184_053_02.
- [41] S. Yao and K. Y. Cai, 'The dynamics and leidenfrost temperature of drops impacting on a hot surface at small angles', 1988, doi: 10.1016/0894-1777(88)90016-7.
- [42] M. Amann, T. Alger, B. Westmoreland, and A. Rothmaier, 'The Effects of Piston Crevices and Injection Strategy on Low-Speed Pre-Ignition in Boosted SI Engines', *SAE Int. J. Engines*, vol. 5, no. 3, pp. 1216–1228, Apr. 2012, doi: 10.4271/2012-01-1148.
- [43] C. Dahnz, K.-M. Han, U. Spicher, M. Magar, R. Schiessl, and U. Maas, 'Investigations on Pre-Ignition in Highly Supercharged SI Engines', *SAE Int. J. Engines*, vol. 3, no. 1, Art. no. 2010-01-0355, Apr. 2010, doi: 10.4271/2010-01-0355.
- [44] O. Welling, J. Moss, J. Williams, and N. Collings, 'Measuring the Impact of Engine Oils and Fuels on Low-Speed Pre-Ignition in Downsized Engines', *SAE Int. J. Fuels Lubr.*, vol. 7, no. 1, pp. 1–8, Apr. 2014, doi: 10.4271/2014-01-1219.
- [45] M. Raza, L. Chen, F. Leach, and S. Ding, 'A Review of Particulate Number (PN) Emissions from Gasoline Direct Injection (GDI) Engines and Their Control Techniques', *Energies*, vol. 11, no. 6, Art. no. 6, Jun. 2018, doi: 10.3390/en11061417.
- [46] R. Amirante *et al.*, 'Effects of lubricant oil on particulate emissions from port-fuel and direct-injection spark-ignition engines', *Int. J. Engine Res.*, vol. 18, no. 5–6, pp. 606–620, Aug. 2017, doi: 10.1177/1468087417706602.
- [47] M. Heiß, 'Approach for Modelling the Initiation Process of Low-Speed Pre-Ignition in Downsized SI-Engines', PhD thesis, Technischen Universität Wien, Wien, 2015. [Online]. Available: <https://repositum.tuwien.at/bitstream/20.500.12708/5959/2/Heiss%20Michael%20-%202015%20-%20Approach%20for%20modelling%20the%20initiation%20process%20of...pdf>
- [48] X. Luo, H. Teng, T. Hu, R. Miao, and L. Cao, 'An Experimental Investigation on Low Speed Pre-Ignition in a Highly Boosted Gasoline Direct Injection Engine', *SAE Int. J. Engines*, vol. 8, no. 2, pp. 520–528, Apr. 2015, doi: 10.4271/2015-01-0758.
- [49] M. Kassai *et al.*, 'Research on the Effect of Lubricant Oil and Fuel Properties on LSPI Occurrence in Boosted S. I. Engines', SAE International, Warrendale, PA, SAE Technical Paper 2016-01-2292, Oct. 2016. doi: 10.4271/2016-01-2292.
- [50] N. Zöbinger and T. Lauer, 'Numerical Investigation of the Influence of Oil Dilution on the Ability to Initiate a Pre-Ignition Combustion', *SAE Int. J. Adv. Curr. Pract. Mobil.*, vol. 2, no. 4, Art. no. 2020-01-0611, Apr. 2020, doi: 10.4271/2020-01-0611.
- [51] H. Kubach *et al.*, 'Investigations on the Influence of Fuel Oil Film Interaction on Pre-ignition Events in Highly Boosted DI Gasoline Engines', SAE International, Warrendale, PA, SAE Technical Paper 2018-01-1454, Apr. 2018. doi: 10.4271/2018-01-1454.
- [52] M. Lashkarbolooki, A. Z. Hezave, and M. Bayat, 'Thermal Diffusivity of Hydrocarbons and Aromatics: Artificial Neural Network Predicting Model', *J. Thermophys. Heat Transf.*, vol. 31, no. 3, pp. 621–627, Jul. 2017, doi: 10.2514/1.T5041.
- [53] S. Azizi, E. Ahmadloo, and M. M. Awad, 'Prediction of void fraction for gas–liquid flow in horizontal, upward and downward inclined pipes using artificial neural network', *Int. J. Multiph. Flow*, vol. 87, pp. 35–44, Dec. 2016, doi: 10.1016/j.ijmultiphaseflow.2016.08.004.
- [54] S. Azizi, M. M. Awad, and E. Ahmadloo, 'Prediction of water holdup in vertical and inclined oil–water two-phase flow using artificial neural network', *Int. J. Multiph. Flow*, vol. 80, pp. 181–187, Apr. 2016, doi: 10.1016/j.ijmultiphaseflow.2015.12.010.
- [55] L. Pulga, G. M. Bianchi, S. Falfari, and C. Forte, 'A machine learning methodology for improving the accuracy of laminar flame simulations with reduced chemical kinetics mechanisms', *Combust. Flame*, vol. 216, pp. 72–81, Jun. 2020, doi: 10.1016/j.combustflame.2020.02.021.

- [56] H. Ghanadzadeh, M. Ganji, and S. Fallahi, 'Mathematical model of liquid–liquid equilibrium for a ternary system using the GMDH-type neural network and genetic algorithm', *Appl. Math. Model.*, vol. 36, no. 9, pp. 4096–4105, Sep. 2012, doi: 10.1016/j.apm.2011.11.039.
- [57] S. L. Pandharipande, M. S. Anish, S. Ankit, and G. A. Sagar, 'Modeling Combined VLE of Ten Binary Mixtures using Artificial Neural Networks', Mumbai, India, Aug. 2012, vol. 1, pp. 30–33.
- [58] M. Mohadesi, G. Moradi, and H.-S. Mousavi, 'Estimation of Binary Infinite Dilute Diffusion Coefficient Using Artificial Neural Network', *J. Chem. Pet. Eng.*, vol. 48, no. 1, Jun. 2014, doi: 10.22059/jchpe.2014.5584.
- [59] A. Géron, *Hands-On Machine Learning with Scikit-Learn, Keras, and TensorFlow*, 2nd ed. O'Reilly Media, Inc., 2019.
- [60] S. Saitoh, H. Shibata, M. Ookuma, and M. Shigenaga, 'Evolution of Gasoline Direct Injection System for Reduction of Real Mode Emission', SAE International, Warrendale, PA, SAE Technical Paper 2019-01-0265, Apr. 2019. doi: 10.4271/2019-01-0265.
- [61] R. Lindgren and I. Denbratt, 'Modelling Gasoline Spray-wall Interaction -a Review of Current Models', SAE International, Warrendale, PA, SAE Technical Paper 2000-01-2808, Oct. 2000. doi: 10.4271/2000-01-2808.
- [62] C. Bai and A. D. Gosman, 'Development of Methodology for Spray Impingement Simulation', SAE International, Warrendale, PA, SAE Technical Paper 950283, Feb. 1995. doi: 10.4271/950283.
- [63] C. X. Bai, H. Rusche, and A. D. Gosman, 'MODELING OF GASOLINE SPRAY IMPINGEMENT', *At. Sprays*, vol. 12, no. 1–3, pp. 1–28, 2002, doi: 10.1615/AtomizSpr.v12.i123.10.
- [64] M. Gavaises, A. Theodorakakos, and G. Bergeles, 'Modeling wall impaction of diesel sprays', *Int. J. Heat Fluid Flow*, vol. 17, no. 2, pp. 130–138, Apr. 1996, doi: 10.1016/0142-727X(95)00097-A.
- [65] Chr. Mundo, M. Sommerfeld, and C. Tropea, 'Droplet-wall collisions: Experimental studies of the deformation and breakup process', *Int. J. Multiph. Flow*, vol. 21, no. 2, pp. 151–173, Apr. 1995, doi: 10.1016/0301-9322(94)00069-V.
- [66] C. Mundo, C. Tropea, and M. Sommerfeld, 'Numerical and experimental investigation of spray characteristics in the vicinity of a rigid Wall', *Exp. Therm. Fluid Sci.*, vol. 15, no. 3, pp. 228–237, Oct. 1997, doi: 10.1016/S0894-1777(97)00015-0.
- [67] C. Mundo, M. Sommerfeld, and C. Tropea, 'On the modeling of liquid sprays impinging on surfaces', *At. Sprays*, vol. 8, pp. 625–652, Nov. 1998, doi: 10.1615/AtomizSpr.v8.i6.20.
- [68] J. Senda and H. G. Fujimoto, 'Multidimensional Modeling of Impinging Sprays on the Wall in Diesel Engines', *Appl. Mech. Rev.*, vol. 52, no. 4, pp. 119–138, Apr. 1999, doi: 10.1115/1.3098930.
- [69] J. Senda, T. Kanda, M. Al-Roub, P. V. Farrell, T. Fukami, and H. Fujimoto, 'Modeling Spray Impingement Considering Fuel Film Formation on the Wall', SAE International, Warrendale, PA, SAE Technical Paper 970047, Feb. 1997. doi: 10.4271/970047.
- [70] J. Senda, T. Takahashi, T. Tanaka, K.-H. Lee, and H. Fujimoto, 'Spray-Wall Interaction Model Considering Superheating Degree of the Wall Surface.', *Trans. Jpn. Soc. Mech. Eng. Ser. B*, vol. 66, no. 642, pp. 604–611, 2000, doi: 10.1299/kikaib.66.604.
- [71] J. Senda, M. Kobayashi, S. Iwashita, and H. Fujimoto, 'Modeling of Diesel Spray Impinging on Flat Wall.', *JSME Int. J. Ser. B*, vol. 39, no. 4, pp. 859–866, 1996, doi: 10.1299/jsmeb.39.859.
- [72] T. Matsuda and J. Senda, 'Modeling on Spray-Wall Interaction for Direct Gasoline Injection Engines', *Trans. Jpn. Soc. Mech. Eng. Ser. B*, vol. 69, pp. 2698–2705, Dec. 2003, doi: 10.1299/kikaib.69.2698.
- [73] D. W. Stanton and C. J. Rutland, 'Multi-dimensional modeling of thin liquid films and spray-wall interactions resulting from impinging sprays', *Int. J. Heat Mass Transf.*, vol. 41, no. 20, pp. 3037–3054, Oct. 1998, doi: 10.1016/S0017-9310(98)00054-4.
- [74] H. Xu, Y. Liu, P. He, and H. Wang, 'The TAR Model for Calculation of Droplet/Wall Impingement', *J. Fluids Eng.*, vol. 120, no. 3, pp. 593–597, Sep. 1998, doi: 10.1115/1.2820705.
- [75] A. L. N. Moreira, A. S. Moita, and M. R. Panão, 'Advances and challenges in explaining fuel spray impingement: How much of single droplet impact research is useful?', *Prog. Energy Combust. Sci.*, vol. 36, no. 5, pp. 554–580, Oct. 2010, doi: 10.1016/j.pecs.2010.01.002.

- [76] R. Lindgren and I. Denbratt, 'Modeling Gasoline Spray-Wall Interactions and Comparison to Experimental Data', SAE International, Warrendale, PA, SAE Technical Paper 2004-01-3003, Oct. 2004. doi: 10.4271/2004-01-3003.
- [77] Z. Han, Z. Xu, and N. Trigui, 'Spray/wall interaction models for multidimensional engine simulation', *Int. J. Engine Res.*, vol. 1, no. 1, pp. 127-146, Feb. 2000, doi: 10.1243/1468087001545308.
- [78] D. Kuhnke, 'Spray Wall Interaction Modeling by Dimensionless Data Analysis', PhD thesis, Technische Universität Darmstadt, Aachen, Germany, 2004.
- [79] A. Montanaro, L. Allocca, G. Meccariello, and M. Lazzaro, 'Schlieren and Mie Scattering Imaging System to Evaluate Liquid and Vapor Contours of a Gasoline Spray Impacting on a Heated Wall', SAE International, Warrendale, PA, SAE Technical Paper 2015-24-2473, Sep. 2015. doi: 10.4271/2015-24-2473.
- [80] A. Montanaro, L. Allocca, M. Lazzaro, and G. Meccariello, 'Impinging Jets of Fuel on a Heated Surface: Effects of Wall Temperature and Injection Conditions', SAE International, Warrendale, PA, SAE Technical Paper 2016-01-0863, Apr. 2016. doi: 10.4271/2016-01-0863.
- [81] A. Montanaro, S. Malaguti, and S. Alfuso, 'Wall Impingement Process of a Multi-Hole GDI Spray: Experimental and Numerical Investigation', SAE International, Warrendale, PA, SAE Technical Paper 2012-01-1266, Apr. 2012. doi: 10.4271/2012-01-1266.
- [82] A. Montanaro, M. Costa, U. Sorge, and L. Allocca, 'GDI Spray-Wall Interaction with Numerical Characterization: Wall Temperature Influence', SAE International, Warrendale, PA, SAE Technical Paper 2015-01-0917, Apr. 2015. doi: 10.4271/2015-01-0917.
- [83] F. Catapano, M. Costa, G. Marseglia, P. Sementa, U. Sorge, and B. M. Vaglieco, 'An Experimental and Numerical Investigation of GDI Spray Impact over Walls at Different Temperatures', SAE International, Warrendale, PA, SAE Technical Paper 2016-01-0853, Apr. 2016. doi: 10.4271/2016-01-0853.
- [84] F. Köpple, P. Jochmann, A. Kufferath, and M. Bargende, 'Investigation of the Parameters Influencing the Spray-Wall Interaction in a GDI Engine - Prerequisite for the Prediction of Particulate Emissions by Numerical Simulation', *SAE Int. J. Engines*, vol. 6, no. 2, Art. no. 2013-01-1089, Apr. 2013, doi: 10.4271/2013-01-1089.
- [85] D. Maligne and G. Bruneaux, 'Time-Resolved Fuel Film Thickness Measurement for Direct Injection SI Engines Using Refractive Index Matching', SAE International, Warrendale, PA, SAE Technical Paper 2011-01-1215, Apr. 2011. doi: 10.4271/2011-01-1215.
- [86] H. Luo, K. Nishida, S. Uchitomi, Y. Ogata, W. Zhang, and T. Fujikawa, 'Effect of temperature on fuel adhesion under spray-wall impingement condition', *Fuel*, vol. 234, pp. 56-65, Dec. 2018, doi: 10.1016/j.fuel.2018.07.021.
- [87] H. Luo, Y. Ogata, and K. Nishida, 'Effects of Droplet Behaviors on Fuel Adhesion of Flat Wall Impinging Spray Injected by a DISI Injector', SAE International, Warrendale, PA, SAE Technical Paper 2019-24-0034, Sep. 2019. doi: 10.4271/2019-24-0034.
- [88] F. Schulz and J. Schmidt, 'Investigation of Fuel Wall Films using Laser-Induced-Fluorescence', May 2012.
- [89] F. Schulz, J. Schmidt, and F. Beyrau, 'Development of a sensitive experimental set-up for LIF fuel wall film measurements in a pressure vessel', *Exp. Fluids*, vol. 56, no. 5, p. 98, May 2015, doi: 10.1007/s00348-015-1971-1.
- [90] F. Schulz, W. Samenfink, J. Schmidt, and F. Beyrau, 'Systematic LIF fuel wall film investigation', *Fuel*, vol. 172, pp. 284-292, May 2016, doi: 10.1016/j.fuel.2016.01.017.
- [91] F. Schulz and F. Beyrau, 'Systematic Investigation of Fuel Film Evaporation', SAE International, Warrendale, PA, SAE Technical Paper 2018-01-0310, Apr. 2018. doi: 10.4271/2018-01-0310.
- [92] F. Schulz and F. Beyrau, 'The effect of operating parameters on the formation of fuel wall films as a basis for the reduction of engine particulate emissions', *Fuel*, vol. 238, pp. 375-384, Feb. 2019, doi: 10.1016/j.fuel.2018.10.109.
- [93] R. O. Grover, T. D. Fansler, A. Lippert, M. C. Drake, and D. N. Assanis, 'A numerical-experimental assessment of wall impingement models for spark-ignition direct-injection engines', *Int. J. Engine Res.*, vol. 21, no. 2, pp. 281-301, Feb. 2020, doi: 10.1177/1468087419863966.
- [94] G. E. Cossali, A. Coghe, and M. Marengo, 'The impact of a single drop on a wetted solid surface', *Exp. Fluids*, vol. 22, no. 6, pp. 463-472, Apr. 1997, doi: 10.1007/s003480050073.

- [95] S. Malaguti, S. Fontanesi, and G. Cantore, 'A numerical characterization of new high-pressure multi-hole GDI injector', presented at the 23rd Annual Conference on Liquid Atomization and Spray Systems, Brno, Czech Republic, Sep. 2010.
- [96] D. Piazzullo, M. Costa, L. Allocca, A. Montanaro, and V. Rocco, 'A 3D CFD Simulation of GDI Sprays Accounting for Heat Transfer Effects on Wallfilm Formation', *SAE Int. J. Engines*, vol. 10, no. 4, Art. no. 2017-24-0041, Sep. 2017, doi: 10.4271/2017-24-0041.
- [97] S. Paltrinieri, F. Mortellaro, N. Silvestri, L. Rolando, M. Medda, and D. Corrigan, 'Water Injection Contribution to Enabling Stoichiometric Air-to-Fuel Ratio Operation at Rated Power Conditions of a High-Performance DISI Single Cylinder Engine', SAE International, Warrendale, PA, SAE Technical Paper 2019-24-0173, Sep. 2019. doi: 10.4271/2019-24-0173.
- [98] F. Brusiani, G. M. Bianchi, and A. Tiberi, 'Primary Breakup Model for Turbulent Liquid Jet Based on Ligament Evolution', Apr. 2012, pp. 2012-01-0460. doi: 10.4271/2012-01-0460.
- [99] R. Reitz, 'Modeling atomization processes in high-pressure vaporizing sprays', *At. Spray Technol.*, vol. 3, pp. 309-337, Jan. 1987.
- [100] K. Y. Huh and A. D. Gosman, 'A Phenomenological Model of Diesel Spray Atomisation', presented at the Proceedings of the International Conference on Multiphase Flows, Tsukuba, Japan, 1991.
- [101] F. Obermeier and H. Chaves, 'Initial modelling of splashing phenomena'. IDEA Project, Subprogram A3, Mar. 1991.
- [102] P. J. O'Rourke and A. A. Amsden, 'A Particle Numerical Model for Wall Film Dynamics in Port-Injected Engines', SAE International, Warrendale, PA, SAE Technical Paper 961961, Oct. 1996. doi: 10.4271/961961.
- [103] P. J. O'Rourke and A. A. Amsden, 'A Spray/Wall Interaction Submodel for the KIVA-3 Wall Film Model', SAE International, Warrendale, PA, SAE Technical Paper 2000-01-0271, Mar. 2000. doi: 10.4271/2000-01-0271.
- [104] G. N., P. Villedieu, D. J., and G. Lavergne, *A new droplet-wall interaction model*. 2008.
- [105] P. Spiegler, J. Hopenfeld, M. Silberberg, C. F. Bumpus, and A. Norman, 'Onset of stable film boiling and the foam limit', *Int. J. Heat Mass Transf.*, vol. 6, no. 11, pp. 987-989, Nov. 1963, doi: 10.1016/0017-9310(63)90053-X.
- [106] D. Fardad and N. Ladommatos, 'Evaporation of hydrocarbon compounds, including gasoline and diesel fuel, on heated metal surfaces', *Proc. Inst. Mech. Eng. Part J. Automob. Eng.*, vol. 213, no. 6, pp. 625-645, Jun. 1999, doi: 10.1243/0954407991527152.
- [107] C. Habchi, 'A Comprehensive Model for Liquid Film Boiling in Internal Combustion Engines', *Oil Gas Sci. Technol.*, vol. 65, pp. 331-343, Mar. 2010, doi: 10.2516/ogst/2009062.
- [108] C. Habchi, *New Correlations for Leidenfrost and Nukiyama Temperatures with Gas Pressure Application to Liquid Film Boiling Simulation*. 2010. doi: 10.13140/2.1.1699.4242.
- [109] R. H. Stanglmaier, C. E. Roberts, and C. A. Moses, 'Vaporization of Individual Fuel Drops on a Heated Surface: A Study of Fuel-Wall Interactions within Direct-Injected Gasoline (DIG) Engines', SAE International, Warrendale, PA, SAE Technical Paper 2002-01-0838, Mar. 2002. doi: 10.4271/2002-01-0838.
- [110] A. Mills and J. Fry, 'Rate of evaporation of hydrocarbons from a hot surface: Nukiyama and Leidenfrost temperatures', *Eur. J. Phys.*, vol. 3, p. 152, Dec. 2000, doi: 10.1088/0143-0807/3/3/005.
- [111] M. Frasso, A. Oliveira, and R. Gonçalves dos Santos, *Determination of Nukiyama and Leidenfrost Temperatures for Hydrocarbons using the Droplet Evaporation Method*. 2018.
- [112] M. Frasso, A. Oliveira, and R. Gonçalves dos Santos, *Droplet Vaporization of Ethanol, n-Heptane, and iso-Octane on Heated Surfaces of Different Metals*. 2018. doi: 10.26678/ABCM.ENCIT2018.CIT18-0642.
- [113] R. H. Perry and D. W. Green, *Perry's Chemical Engineers' Handbook*, 8th ed. McGraw-Hill, 2008.
- [114] 'Properties: Silica - Fused Silica (Silicon Dioxide)'. <https://www.azom.com/properties.aspx?ArticleID=1387> (accessed Oct. 20, 2021).
- [115] M. Durat, M. Kapsiz, E. Nart, F. Ficici, and A. Parlak, 'The effects of coating materials in spark ignition engine design', *Mater. Des. 1980-2015*, vol. 36, pp. 540-545, Apr. 2012, doi: 10.1016/j.matdes.2011.11.053.

- [116] H. X. Li *et al.*, 'Influence of Liquid Core Reduction on Stress-strain Distribution and Strand Deformation in a Thin Slab Caster', *ISIJ Int.*, vol. 56, no. 9, pp. 1616–1624, 2016, doi: 10.2355/isijinternational.ISIJINT-2016-242.
- [117] N. Zöbinger, T. Schweizer, T. Lauer, H. Kubach, and T. Koch, 'Experimental and Numerical Analysis on Two-Phase Induced Low-Speed Pre-Ignition', *Energies*, vol. 14, no. 16, Art. no. 16, Jan. 2021, doi: 10.3390/en14165063.
- [118] S. Yu and K. Min, 'Effects of the oil and liquid fuel film on hydrocarbon emissions in spark ignition engines', *Proc. Inst. Mech. Eng. Part J. Automob. Eng.*, vol. 216, no. 9, pp. 759–771, Sep. 2002, doi: 10.1243/09544070260340853.
- [119] W. Hayduk and B. S. Minhas, 'Correlations for prediction of molecular diffusivities in liquids', 1982, doi: 10.1002/CJCE.5450600213.
- [120] Q. Zhang, V. T. Kalva, and T. Tian, 'Modeling the Evolution of Fuel and Lubricant Interactions on the Liner in Internal Combustion Engines', SAE International, Warrendale, PA, SAE Technical Paper 2018-01-0279, Apr. 2018. doi: 10.4271/2018-01-0279.
- [121] C. R. Wilke and P. Chang, 'Correlation of diffusion coefficients in dilute solutions', *AIChE J.*, vol. 1, no. 2, pp. 264–270, Jun. 1955, doi: 10.1002/aic.690010222.
- [122] M. A. Siddiqi and K. Lucas, 'Correlations for prediction of diffusion in liquids', *Can. J. Chem. Eng.*, vol. 64, no. 5, pp. 839–843, Oct. 1986, doi: 10.1002/cjce.5450640519.
- [123] L. P. Filippov, 'Liquid thermal conductivity research at Moscow University', *Int. J. Heat Mass Transf.*, vol. 11, no. 2, pp. 331–345, Feb. 1968, doi: 10.1016/0017-9310(68)90161-0.
- [124] L. Grunberg and A. H. Nissan, 'Mixture Law for Viscosity', *Nature*, vol. 164, no. 4175, pp. 799–800, Nov. 1949, doi: 10.1038/164799b0.
- [125] J. Crank and P. Nicolson, 'A practical method for numerical evaluation of solutions of partial differential equations of the heat-conduction type', *Adv. Comput. Math.*, vol. 6, no. 1, pp. 207–226, Dec. 1996, doi: 10.1007/BF02127704.
- [126] G. Woschni, 'A Universally Applicable Equation for the Instantaneous Heat Transfer Coefficient in the Internal Combustion Engine', SAE International, Warrendale, PA, SAE Technical Paper 670931, Feb. 1967. doi: 10.4271/670931.
- [127] T. Tabatabaie, M. A. Ehteram, and V. Hosseini, 'Investigating the effect of the heat transfer correlation on the predictability of a multi-zone combustion model of a hydrogen-fuelled spark ignition engine', *Proc. Inst. Mech. Eng. Part J. Automob. Eng.*, vol. 230, no. 1, pp. 70–81, Jan. 2016, doi: 10.1177/0954407015578047.
- [128] C. Schubert, A. Wimmer, and F. Chmela, 'Advanced Heat Transfer Model for CI Engines', SAE International, Warrendale, PA, SAE Technical Paper 2005-01-0695, Apr. 2005. doi: 10.4271/2005-01-0695.
- [129] T. H. Chilton and A. P. Colburn, 'Mass Transfer (Absorption) Coefficients Prediction from Data on Heat Transfer and Fluid Friction', *Ind. Eng. Chem.*, vol. 26, no. 11, pp. 1183–1187, Nov. 1934, doi: 10.1021/ie50299a012.
- [130] E. N. Fuller, P. D. Schettler, and J. Calvin. Giddings, 'NEW METHOD FOR PREDICTION OF BINARY GAS-PHASE DIFFUSION COEFFICIENTS', *Ind. Eng. Chem.*, vol. 58, no. 5, pp. 18–27, May 1966, doi: 10.1021/ie50677a007.
- [131] C. J. King, L. Hsueh, and K.-W. Mao, 'Liquid Phase Diffusion of Non-electrolytes at High Dilution.', *J. Chem. Eng. Data*, vol. 10, no. 4, pp. 348–350, Oct. 1965, doi: 10.1021/je60027a014.
- [132] M. T. Tyn and W. F. Calus, 'Diffusion coefficients in dilute binary liquid mixtures', *J. Chem. Eng. Data*, vol. 20, no. 1, pp. 106–109, Jan. 1975, doi: 10.1021/je60064a006.
- [133] Y. Wen, J. Bryan, and A. Kantzas, 'Estimation of Diffusion Coefficients in Bitumen Solvent Mixtures as Derived From Low Field NMR Spectra', *J. Can. Pet. Technol.*, vol. 44, Apr. 2013, doi: 10.2118/2003-017.
- [134] E. S. Saltzman, D. B. King, K. Holmen, and C. Leck, 'Experimental determination of the diffusion coefficient of dimethylsulfide in water', *J. Geophys. Res.*, vol. 98, no. C9, p. 16481, 1993, doi: 10.1029/93JC01858.
- [135] L. Sun, W. Meng, and X. Pu, 'New method to measure liquid diffusivity by analyzing an instantaneous diffusion image', *Opt. Express*, vol. 23, no. 18, p. 23155, Sep. 2015, doi: 10.1364/OE.23.023155.

- [136] P. Schatzberg, 'Diffusion of water through hydrocarbon liquids', *J. Polym. Sci. Part C Polym. Symp.*, vol. 10, no. 1, pp. 87–92, 1965, doi: 10.1002/polc.5070100108.
- [137] R. L. Olson and J. S. Walton, 'Diffusion Coefficients of Organic Liquids in Solution from Surface Tension Measurements', *Ind. Eng. Chem.*, vol. 43, no. 3, pp. 703–706, Mar. 1951, doi: 10.1021/ie50495a037.
- [138] K. A. Reddy and L. K. Doraiswamy, 'Estimating Liquid Diffusivity', *Ind. Eng. Chem. Fundam.*, vol. 6, no. 1, pp. 77–79, Feb. 1967, doi: 10.1021/i160021a012.
- [139] J. W. Moore and R. M. Wellek, 'Diffusion coefficients of n-heptane and n-decane in n-alkanes and n-alcohols at several temperatures', *J. Chem. Eng. Data*, vol. 19, no. 2, pp. 136–140, Apr. 1974, doi: 10.1021/je60061a023.
- [140] A. Vignes, 'Diffusion in Binary Solutions. Variation of Diffusion Coefficient with Composition', *Ind. Eng. Chem. Fundam.*, vol. 5, no. 2, pp. 189–199, May 1966, doi: 10.1021/i160018a007.
- [141] Y. Fan, R. Qian, M. Shi, and J. Shi, 'Infinite Dilution Diffusion Coefficients of Several Aromatic Hydrocarbons in Octane and 2,2,4-Trimethylpentane', *J. Chem. Eng. Data*, vol. 40, no. 5, pp. 1053–1055, Sep. 1995, doi: 10.1021/je00021a004.
- [142] L. Rodwin, J. A. Harpst, and P. A. Lyons, 'Diffusion in the System Cyclohexane—Benzene', *J. Phys. Chem.*, vol. 69, no. 8, pp. 2783–2785, Aug. 1965, doi: 10.1021/j100892a503.
- [143] S. A. Sanni, C. J. D. Fell, and H. Peter. Hutchison, 'Diffusion coefficients and densities for binary organic liquid mixtures', *J. Chem. Eng. Data*, vol. 16, no. 4, pp. 424–427, Oct. 1971, doi: 10.1021/je60051a009.
- [144] M. A. Matthews and A. Akgerman, 'Diffusion coefficients for binary alkane mixtures to 573 K and 3.5 MPa', *AIChE J.*, vol. 33, no. 6, pp. 881–885, 1987, doi: 10.1002/aic.690330602.
- [145] T. Funazukuri, N. Nishimoto, and N. Wakao, 'Binary Diffusion Coefficients of Organic Compounds in Hexane, Dodecane, and Cyclohexane at 303.2–333.2 K and 16.0 MPa', *J. Chem. Eng. Data*, vol. 39, no. 4, pp. 911–915, Oct. 1994, doi: 10.1021/je00016a062.
- [146] H. Y. Lo, 'Diffusion coefficients in binary liquid n-alkane systems', *J. Chem. Eng. Data*, vol. 19, no. 3, pp. 236–241, Jul. 1974, doi: 10.1021/je60062a014.
- [147] J. J. C. Shieh and P. A. Lyons, 'Transport properties of liquid n-alkanes', *J. Phys. Chem.*, vol. 73, no. 10, pp. 3258–3264, Oct. 1969, doi: 10.1021/j100844a017.
- [148] J. H. Dymond, 'Limiting diffusion in binary nonelectrolyte mixtures', *J. Phys. Chem.*, vol. 85, no. 22, pp. 3291–3294, Oct. 1981, doi: 10.1021/j150622a016.
- [149] T. K. Kett and D. K. Anderson, 'Ternary isothermal diffusion and the validity of the Onsager reciprocal relations in nonassociating systems', *J. Phys. Chem.*, vol. 73, no. 5, pp. 1268–1274, May 1969, doi: 10.1021/j100725a016.
- [150] H. T. Cullinan and H. L. Toor, 'Diffusion in the Three-Component Liquid System Acetone-Benzene-Carbon Tetrachloride', *J. Phys. Chem.*, vol. 69, no. 11, pp. 3941–3949, Nov. 1965, doi: 10.1021/j100895a050.
- [151] D. K. Anderson, J. R. Hall, and A. L. Babb, 'Mutual Diffusion in Non-ideal Binary Liquid Mixtures', *J. Phys. Chem.*, vol. 62, no. 4, pp. 404–408, Apr. 1958, doi: 10.1021/j150562a006.
- [152] K. McKeigue and E. Gulari, 'Effect of molecular association on diffusion in binary liquid mixtures', *AIChE J.*, vol. 35, no. 2, pp. 300–310, 1989, doi: 10.1002/aic.690350215.
- [153] F. O. Shuck and H. L. Toor, 'DIFFUSION IN THE THREE COMPONENT LIQUID SYSTEM METHYL ALCOHOL-n-PROPYL ALCOHOL-ISOBUTYL ALCOHOL', *J. Phys. Chem.*, vol. 67, no. 3, pp. 540–545, Mar. 1963, doi: 10.1021/j100797a002.
- [154] P. Chang and C. R. Wilke, 'Some Measurements of Diffusion in Liquids.', *J. Phys. Chem.*, vol. 59, no. 7, pp. 592–596, Jul. 1955, doi: 10.1021/j150529a005.
- [155] M. J. M. te Riele, E. D. Snijder, and W. P. M. van Swaaij, 'Diffusion Coefficients at Infinite Dilution in Water and in N-Methylpyrrolidone', *J. Chem. Eng. Data*, vol. 40, no. 1, pp. 34–36, Jan. 1995, doi: 10.1021/je00017a009.
- [156] C. J. Vadovic and C. P. Colver, 'Infinite dilution diffusion coefficients in liquids', *AIChE J.*, vol. 19, no. 3, pp. 546–551, 1973, doi: 10.1002/aic.690190320.
- [157] W. Baldauf and H. Knapp, 'Experimental Determination of Diffusion Coefficients, Viscosities, Densities and Refractive Indexes of 11 Binary Liquid Systems', *Berichte Bunsenges. Für Phys. Chem.*, vol. 87, no. 4, pp. 304–309, 1983, doi: 10.1002/bbpc.19830870407.

- [158] B. E. Poling, J. M. Prausnitz, and J. P. O'Connell, *The Properties of Gases and Liquids*, 5th ed. McGraw-Hill, 2000.
- [159] 'PubChem'. <https://pubchem.ncbi.nlm.nih.gov/> (accessed Oct. 12, 2021).
- [160] C. L. Yaws, *Thermophysical Properties of Chemicals and Hydrocarbons*, 2nd ed. Gulf Professional Publishing, 2014.
- [161] W. Schotte, 'Prediction of the molar volume at the normal boiling point', *Chem. Eng. J.*, vol. 48, no. 3, pp. 167–172, Apr. 1992, doi: 10.1016/0300-9467(92)80032-6.
- [162] I. S. Panidi, V. A. Trofimov, and N. S. Lepikhina, 'Calculation of the molar volume of liquid hydrocarbons', *Chem. Technol. Fuels Oils*, vol. 42, no. 6, pp. 440–445, Nov. 2006, doi: 10.1007/s10553-006-0104-1.
- [163] J. Kukačka, V. Golkov, and D. Cremers, 'Regularization for Deep Learning: A Taxonomy', *ArXiv171010686 Cs Stat*, Oct. 2017, Accessed: Oct. 13, 2021. [Online]. Available: <http://arxiv.org/abs/1710.10686>
- [164] F. Chollet, 'Keras'. 2015. [Online]. Available: <https://keras.io/>
- [165] M. Abadi *et al.*, 'TensorFlow: A system for large-scale machine learning', *ArXiv160508695 Cs*, May 2016, Accessed: Oct. 13, 2021. [Online]. Available: <http://arxiv.org/abs/1605.08695>
- [166] C. Blundell, J. Cornebise, K. Kavakcuoglu, and D. Wierstra, 'Weight uncertainty in neural networks', Lille, France, 2015, pp. 1613–1622.
- [167] Z. Liang *et al.*, 'Comprehensive chemical characterization of lubricating oils used in modern vehicular engines utilizing GC × GC-TOFMS', *Fuel*, vol. 220, pp. 792–799, May 2018, doi: 10.1016/j.fuel.2017.11.142.
- [168] T. G. Hiss and E. L. Cussler, 'Diffusion in high viscosity liquids', *AIChE J.*, vol. 19, no. 4, pp. 698–703, 1973, doi: 10.1002/aic.690190404.
- [169] C. K. Westbrook, M. Sjöberg, and N. P. Cernansky, 'A new chemical kinetic method of determining RON and MON values for single component and multicomponent mixtures of engine fuels', *Combust. Flame*, vol. 195, pp. 50–62, Sep. 2018, doi: 10.1016/j.combustflame.2018.03.038.
- [170] S. Malaguti, G. Bagli, A. Montanaro, S. Piccinini, and L. Allocca, 'Experimental and Numerical Characterization of Gasoline-Ethanol Blends from a GDI Multi-Hole Injector by Means of Multi-Component Approach', Sep. 2013, pp. 2013-24-0002. doi: 10.4271/2013-24-0002.
- [171] 'Thermophysical Properties'. <https://materialsdata.nist.gov/handle/11115/166?show=full> (accessed Oct. 13, 2021).
- [172] *Simscape Matlab Toolbox*. Massachusetts, USA: The MathWorks Inc.
- [173] Y. Yu *et al.*, 'Characteristics of Auto-Ignition for Lubricants and Lubricant/Gasoline Based on an Innovative Single Droplet Test System', SAE International, Warrendale, PA, SAE Technical Paper 2020-01-1428, Apr. 2020. doi: 10.4271/2020-01-1428.
- [174] D. K. W. Leong, P. J. Shayler, I. G. Pegg, and M. Murphy, 'Characterizing the effect of viscosity on friction in the piston assembly of internal combustion engines', *Proc. Inst. Mech. Eng. Part JJ. Eng. Tribol.*, vol. 221, no. 4, pp. 469–478, Apr. 2007, doi: 10.1243/13506501JET261.
- [175] T. Ohmori, M. Tohyama, M. Yamamoto, K. Akiyama, K. Tasaka, and T. Yoshihara, 'Influence of Engine Oil Viscosity on Piston Ring and Cam Face Wear', SAE International, Warrendale, PA, SAE Technical Paper 932782, Oct. 1993. doi: 10.4271/932782.
- [176] S. M. Sarathy, A. Farooq, and G. T. Kalghatgi, 'Recent progress in gasoline surrogate fuels', *Prog. Energy Combust. Sci.*, vol. 65, pp. 67–108, Mar. 2018, doi: 10.1016/j.pecs.2017.09.004.
- [177] M. Mehl, J. Y. Chen, W. J. Pitz, S. M. Sarathy, and C. K. Westbrook, 'An Approach for Formulating Surrogates for Gasoline with Application toward a Reduced Surrogate Mechanism for CFD Engine Modeling', *Energy Fuels*, vol. 25, no. 11, pp. 5215–5223, Nov. 2011, doi: 10.1021/ef201099y.
- [178] O. S. Abianeh, M. A. Oehlschlaeger, and C.-J. Sung, 'A surrogate mixture and kinetic mechanism for emulating the evaporation and autoignition characteristics of gasoline fuel', *Combust. Flame*, vol. 162, no. 10, pp. 3773–3784, Oct. 2015, doi: 10.1016/j.combustflame.2015.07.015.
- [179] A. Ahmed, G. Goteng, V. S. B. Shankar, K. Al-Qurashi, W. L. Roberts, and S. M. Sarathy, 'A computational methodology for formulating gasoline surrogate fuels with accurate physical and chemical kinetic properties', *Fuel*, vol. 143, pp. 290–300, Mar. 2015, doi: 10.1016/j.fuel.2014.11.022.

- [180] S. R. Daly, K. E. Niemeyer, W. J. Cannella, and C. L. Hagen, 'FACE Gasoline Surrogates Formulated by an Enhanced Multivariate Optimization Framework', *Energy Fuels*, vol. 32, no. 7, pp. 7916–7932, Jul. 2018, doi: 10.1021/acs.energyfuels.8b01313.
- [181] T. Grubinger, G. Lenk, N. Schubert, and T. Wallek, 'Surrogate generation and evaluation of gasolines', *Fuel*, vol. 283, p. 118642, Jan. 2021, doi: 10.1016/j.fuel.2020.118642.
- [182] S. Cheng *et al.*, 'Autoignition and preliminary heat release of gasoline surrogates and their blends with ethanol at engine-relevant conditions: Experiments and comprehensive kinetic modeling', *Combust. Flame*, vol. 228, pp. 57–77, Jun. 2021, doi: 10.1016/j.combustflame.2021.01.033.
- [183] A. Pati, S. Gierth, P. Haspel, C. Hasse, and J. Munier, 'Strategies to Define Surrogate Fuels for the Description of the Multicomponent Evaporation Behavior of Hydrocarbon Fuels', SAE International, Warrendale, PA, SAE Technical Paper 2018-01–1692, Sep. 2018. doi: 10.4271/2018-01-1692.
- [184] Á. Muelas, D. Aranda, and J. Ballester, 'Alternative Method for the Formulation of Surrogate Liquid Fuels Based on Evaporative and Sooting Behaviors', *Energy Fuels*, vol. 33, no. 6, pp. 5719–5731, Jun. 2019, doi: 10.1021/acs.energyfuels.9b00737.
- [185] L. Zhu, Z. Gao, X. Cheng, F. Ren, and Z. Huang, 'An assessment of surrogate fuel using Bayesian multiple kernel learning model in sight of sooting tendency', *Front. Energy*, Apr. 2021, doi: 10.1007/s11708-021-0731-6.
- [186] E. W. Lemmon, I. H. Bell, M. L. Huber, and M. O. McLinden, *REFPROP Standard Reference Database*. Boulder, Colorado, USA: National Institute of Standards and Technology, 2018.
- [187] W. Spielsma, 'Prediction of ASTM Method D86 Distillation of Gasolines and Naphthas according to the Fugacity-Filmmodel from Gas Chromatographic Detailed Hydrocarbon Analysis', *J. Chromatogr. Sci.*, vol. 36, no. 9, pp. 467–475, Sep. 1998, doi: 10.1093/chromsci/36.9.467.
- [188] L. S. Moreira, L. A. d'Avila, and D. A. Azevedo, 'Automotive Gasoline Quality Analysis by Gas Chromatography: Study of Adulteration', *Chromatographia*, vol. 58, no. 7, pp. 501–505, Oct. 2003, doi: 10.1365/s10337-003-0065-z.
- [189] U. Dorgerloh, R. Becker, and I. Nehls, 'Volatile Hydrocarbons in Contaminated Soil: Robustness of Fractional Quantification Using Headspace Gas Chromatography-Mass-Spectrometry', *Soil Sediment Contam. Int. J.*, vol. 27, pp. 1–12, Jan. 2018, doi: 10.1080/15320383.2018.1418287.
- [190] T. Sherlock and E. Taylor, 'Determination of the ethanol level in commercial gasolines by gas chromatography', *J. Undergrad. Chem. Res.*, vol. 2010, Mar. 2010.
- [191] S. Ito, 'Analysis of Aromatic Hydrocarbons in Gasoline and Naphtha with the Agilent 6820 Series Gas Chromatograph and a Single Polar Capillary Column: Application'. 2003. [Online]. Available: <https://www.agilent.com/cs/library/applications/5988-9261EN.pdf>
- [192] D02 Committee, 'Test Method for Distillation of Petroleum Products and Liquid Fuels at Atmospheric Pressure', ASTM International. doi: 10.1520/D0086-20B.
- [193] Q. Jiao, Y. Ra, and R. D. Reitz, 'Modeling the Influence of Molecular Interactions on the Vaporization of Multi-component Fuel Sprays', SAE International, Warrendale, PA, SAE Technical Paper 2011-01–0387, Apr. 2011. doi: 10.4271/2011-01-0387.
- [194] M. L. Greenfield, G. A. Lavoie, C. S. Smith, and E. W. Curtis, 'Macroscopic Model of the D86 Fuel Volatility Procedure', SAE International, Warrendale, PA, SAE Technical Paper 982724, Oct. 1998. doi: 10.4271/982724.
- [195] N. A. Slavinskaya, A. Zizin, and M. Aigner, 'On Surrogate Fuel Formulation', in *Volume 2: Combustion, Fuels and Emissions*, Orlando, Florida, USA, Jan. 2009, pp. 759–771. doi: 10.1115/GT2009-60012.
- [196] O. Samimi Abianeh, C. P. Chen, and R. L. Cerro, 'Batch Distillation: The Forward and Inverse Problems', *Ind. Eng. Chem. Res.*, vol. 51, no. 38, pp. 12435–12448, Sep. 2012, doi: 10.1021/ie300710s.
- [197] G. Soave, 'Equilibrium constants from a modified Redlich-Kwong equation of state', *Chem. Eng. Sci.*, vol. 27, no. 6, pp. 1197–1203, Jun. 1972, doi: 10.1016/0009-2509(72)80096-4.
- [198] Otto. Redlich and J. N. S. Kwong, 'On the Thermodynamics of Solutions. V. An Equation of State. Fugacities of Gaseous Solutions.', *Chem. Rev.*, vol. 44, no. 1, pp. 233–244, Feb. 1949, doi: 10.1021/cr60137a013.
- [199] D.-Y. Peng and D. B. Robinson, 'A New Two-Constant Equation of State', *Ind. Eng. Chem. Fundam.*, vol. 15, no. 1, pp. 59–64, Feb. 1976, doi: 10.1021/i160057a011.

- [200] G. Wilson, 'A modified Redlich-Kwong equation of state applicable to general physical data calculations', presented at the 65th AIChE National Meeting, Cleveland, OH, USA, May 1968.
- [201] V. Hönig, S. Hornickova, and J. Hromádko, 'Analysis of the Distillation Curves of Mixtures of BioButanol with Gasoline', *Adv. Mater. Res.*, vol. 1030–1032, pp. 25–28, Sep. 2014, doi: 10.4028/www.scientific.net/AMR.1030-1032.25.
- [202] J. E. Anderson *et al.*, 'Octane Numbers of Ethanol-Gasoline Blends: Measurements and Novel Estimation Method from Molar Composition', SAE International, Warrendale, PA, SAE Technical Paper 2012-01–1274, Apr. 2012. doi: 10.4271/2012-01-1274.
- [203] E. Brochu, V. M. Cora, and N. de Freitas, 'A Tutorial on Bayesian Optimization of Expensive Cost Functions, with Application to Active User Modeling and Hierarchical Reinforcement Learning', *ArXiv10122599 Cs*, Dec. 2010, Accessed: Oct. 12, 2021. [Online]. Available: <http://arxiv.org/abs/1012.2599>
- [204] P. I. Frazier, 'A Tutorial on Bayesian Optimization', *ArXiv180702811 Cs Math Stat*, Jul. 2018, Accessed: Oct. 13, 2021. [Online]. Available: <http://arxiv.org/abs/1807.02811>
- [205] A. M. Ferris and D. A. Rothamer, 'Methodology for the experimental measurement of vapor–liquid equilibrium distillation curves using a modified ASTM D86 setup', *Fuel*, vol. 182, pp. 467–479, Oct. 2016, doi: 10.1016/j.fuel.2016.05.099.
- [206] T. J. Bruno and B. L. Smith, 'Evaluation of the Physicochemical Authenticity of Aviation Kerosene Surrogate Mixtures. Part 1: Analysis of Volatility with the Advanced Distillation Curve', *Energy Fuels*, vol. 24, no. 8, pp. 4266–4276, Aug. 2010, doi: 10.1021/ef100496j.
- [207] F. D.F. Chuahy, T. Powell, S. J. Curran, and J. P. Szybist, 'Impact of fuel chemical function characteristics on spark assisted and kinetically controlled compression ignition performance focused on multi-mode operation', *Fuel*, vol. 299, p. 120844, Sep. 2021, doi: 10.1016/j.fuel.2021.120844.
- [208] 'EPAAct/V2/E-89 Tier 2 Gasoline Fuel Effects Study | US EPA'. <https://www.epa.gov/moves/epactv2e-89-tier-2-gasoline-fuel-effects-study> (accessed Oct. 12, 2021).
- [209] C. Stan, C. Andreescu, A. Dobre, and D. Iozsa, 'Experimental Study on the Distillation Capacity of Alcohol-Gasoline Blends', *IOP Conf. Ser. Mater. Sci. Eng.*, vol. 252, p. 012069, Oct. 2017, doi: 10.1088/1757-899X/252/1/012069.
- [210] V. F. Andersen, J. E. Anderson, T. J. Wallington, S. A. Mueller, and O. J. Nielsen, 'Distillation Curves for Alcohol–Gasoline Blends', *Energy Fuels*, vol. 24, no. 4, pp. 2683–2691, Apr. 2010, doi: 10.1021/ef9014795.